UNIVERSITY OF Southampton

University of Southampton Research Repository
ePrints Soton

Copyright © and Moral Rights for this thesis are retained by the author and/or other copyright owners. A copy can be downloaded for personal non-commercial research or study, without prior permission or charge. This thesis cannot be reproduced or quoted extensively from without first obtaining permission in writing from the copyright holder/s. The content must not be changed in any way or sold commercially in any format or medium without the formal permission of the copyright holders.

When referring to this work, full bibliographic details including the author, title, awarding institution and date of the thesis must be given e.g.

AUTHOR (year of submission) "Full thesis title", University of Southampton, name of the University School or Department, PhD Thesis, pagination

http://eprints.soton.ac.uk

UNIVERSITY OF SOUTHAMPTON

FACULTY OF ENGINEERING AND THE ENVIRONMENT

Institute of Sound and Vibration Research

Efficient Finite Element Methods for Aircraft Engine Noise Prediction

by

Albert Gerrard Prinn

Thesis for the degree of Doctor of Engineering

July 2014

UNIVERSITY OF SOUTHAMPTON

ABSTRACT

FACULTY OF ENGINEERING AND THE ENVIRONMENT
Institute of Sound and Vibration Research

Doctor of Engineering

EFFICIENT FINITE ELEMENT METHODS FOR AIRCRAFT ENGINE NOISE PREDICTION

by Albert Gerrard Prinn

Aircraft noise has a negative environmental impact. One of the ways in which it can be mitigated is by placing acoustic liners inside the aircraft's engines. These liners can be optimised for noise reduction. A cost effective way to optimise acoustic liners is to make use of numerical modelling. However, there is room for improvement of the efficiency of current modelling methods. This thesis is concerned with the efficient numerical prediction of noise emitted from modern aircraft engines. Four high order finite element methods are used to solve the convected wave equation, and their performances are compared. The benefit of using the hierarchic Lobatto finite element method to solve this type of problem is demonstrated. A scheme which optimises the efficiency of the high order method is developed. The scheme automatically chooses the most efficient order for a given element, depending on the element size, and the problem parameters on that element. The computational cost of using the standard quadratic finite element method to solve a typical engine intake noise problem, is compared to the cost of the proposed adaptive-order method. A significant improvement in terms of efficiency is demonstrated when using the proposed method over the standard method. Furthermore, a new formulation based on potential flow theory for the solution of vortex sheet problems (typically encountered when dealing with exhaust noise problems) is presented.

Contents

List of Figures

LIST OF FIGURES

List of Tables

Academic Thesis: Declaration of Authorship

I, Albert Gerrard Prinn, declare that this thesis, and the work presented in it, are my own and has been generated by me as the result of my own original research.

Efficient Finite Element Methods for Aircraft Engine Noise Prediction.

I confirm that:

1. This work was done wholly or mainly while in candidature for a research degree at this University;

2. Where any part of this thesis has previously been submitted for a degree or any other qualification at this University or any other institution, this has been clearly stated;

3. Where I have consulted the published work of others, this is always clearly attributed;

4. Where I have quoted from the work of others, the source is always given. With the exception of such quotations, this thesis is entirely my own work;

5. I have acknowledged all main sources of help;

6. Where the thesis is based on work done by myself jointly with others, I have made clear exactly what was done by others and what I have contributed myself;

7. Either none of this work has been published before submission, or parts of this work have been published as: [please list references below]:

Signed:

Date:

Acknowledgements

I would like to acknowledge the Engineering and Physical Sciences Research Council and LMS International for funding this project.

Nomenclature

List of Variables

(x, y, z)	= Cartesian coordinates
(r, θ, z)	= Cylindrical coordinates
(η, ζ, ξ)	= Reference space coordinates

Roman Letters

a	= Unknown coefficient
$\boldsymbol{a}$	= Unknown coefficient vector
A	= Admittance, or Complex amplitude
$\boldsymbol{A}$	= Global matrix
B	= Number of fan blades
c	= Speed of sound
C	= Constant
d	= Dimension
D_λ	= Number of degrees of freedom per wavelength (includes flow effect)
E	= Error (calculated)
E_d	= Dispersion error
E_i	= Interpolation error
E_{H^1}	= Error in the H^1 norm
E_{L^2}	= Error in the L^2 norm
E_τ	= Error (desired)
f	= Frequency
$\boldsymbol{f}$	= Source vector

h = Element size
i = $\sqrt{-1}$
$\boldsymbol{I}$ = Acoustic intensity
$\boldsymbol{J}$ = Bessel function, or Jacobian
k = Effective wavenumber (flow dependent)
k_0 = Free-field wavenumber (no flow)
$\tilde{k}$ = Hydrodynamic wavenumber
$\boldsymbol{k}$ = Wavenumber vector
kH = Helmholtz number
K = Constant
L_w = Sound power level
m = Azimuthal mode order
M = Mach number
n = Radial mode order
$\boldsymbol{n}$ = Normal vector
N_λ = Number of elements per wavelength (no flow effect)
N_{nz} = Number of non-zero entries
p = Pressure
P = Polynomial order
$\mathcal{P}$ = Power
N_{nz} = Number of non-zero entries
R = Duct radius
R_0 = Inner duct radius
R_1 = Outer duct radius
s = Entropy
S = Surface
S_0 = Source surface
S_w = Hard-walled surface
S_z = Impedance surface
t = time
T = Temperature
$\boldsymbol{T}$ = Viscous stress tensor
v_0 = Velocity

$\boldsymbol{v}$ = Velocity vector
V = Enrichment function
W = Test function associated with velocity potential
$\boldsymbol{x}$ = Vector of spatial coordinates
Y = Neumann function
Z = Impedance

Greek Letters

α = Absorption function
β = Upwinding parameter
γ = Ratio of specific heats
Γ = Boundary
ζ = A physical quantity
η = Effectivity index, or Test function associated with displacement
κ = Condition number, or Wavenumber
λ = Wavelength
ν = Normal displacement in the absence of flow
ξ = Displacement
ρ = Density
σ = Test function associated with velocity
$\boldsymbol{\sigma}$ = Stress tensor
φ = Basis function
ϕ = Velocity potential
$\hat{\phi}$ = Trial function
χ = Partition of unity function
ψ = Shape function
Ψ = Mode shape function
α = Absorption function
ω = Angular frequency
Ω = Domain
Ω_s = Shaft rotation speed

Superscripts

$()^*$	= Complex conjugate
$\overline{()}$	= Complex conjugate transpose
$()'$	= Derivative with respect to dependent variable
$()^t$	= Total quantity
$\tilde{()}$	= Transformed variable
$()^P$	= Polynomial order
$()^T$	= Transpose

Subscripts

$()_0$	= Base flow quantity
$()_a$	= Analytic solution
$()_e$	= Belonging to an element
$()_h$	= Discrete variable
$()_{\text{opt}}$	= Optimal variable
$()_\lambda$	= Per wavelength

Acronyms

ACARE	= Advisory Council for Avaiation Research and Innovation in Europe
APE	= Acoustic Perturbation Equations
DEM	= Discontinuous Enrichment Method
DGM	= Discontinuous Galerkin Method
FEM	= Finite Element Method
GFEM	= Generalised Finite Element Method
GGLS	= Galerkin Gradient Least Squares
GLS	= Galerkin Least Squares
GTS	= Gradient Term Suppression
LEE	= Linearised Euler Equations
LU	= Lower Upper

MUMPS	= Multifrontal Massively Parallel Sparse direct Solver
NURBS	= Non-Uniform Rational B-Splines
PML	= Perfectly Matched Layer
P-PUM	= Polynomial Partition of Unity Method
PUFEM	= Partition of Unity Finite Element Method
SUPG	= Streamlined Upwind Petrov-Galerkin
UVWF	= Ultra Weak Variational Formulation

1

Introduction

Commercial aviation has many social and economic benefits. It provides shorter travel times, and a plethora of employment opportunities. However, aviation has a noticeable environmental impact. Modern turbofan engines still rely heavily upon fossil fuels, and the gasses and particulates they emit contribute to global climate change. Despite the development of more fuel efficient engines, the environmental impact of aviation is increasing due to the growth of the aviation industry.

Although consideration of gas and particulate emissions is very important, to those people living and working close to airports the more evident environmental impact is noise pollution. Community noise caused by aircraft during take-off and landing can lead to high levels of annoyance and may cause adverse health effects [15, 61, 133]. Furthermore, flyover noise can affect aesthetic evaluations of natural landscapes [26, 136], and adversely affects wildlife [23, 72].

To protect people subjected to aviation noise, international standards, which place limits on noise emission and aircraft noise levels, were introduced in the 1960s. In response, noise reducing technologies have advanced considerably, as can be seen in Figure 1.1. Current aircraft are significantly quieter than first generation turbofan aircraft - roughly 20 to 30 dB quieter - but the number of flights has increased. The forecast growth of aviation is 4.25 % per annum [112]. Although current designs meet Chapter 4 certification requirements, future targets are very ambitious, *e.g.* the ACARE target which aims to reduce the current noise emissions by 10 dB between 2000 and 2020. Novel noise reduction technologies will be needed in order to meet these targets.

1.1 Project Motivation

Numerical modelling can be used to design quieter aircraft. It can be employed to enhance the three main aircraft noise reduction techniques: 1. Controlling noise source mechanisms, *e.g.* making use of novel fan blade designs for quieter aircraft engines, or minimising the aerodynamic noise created by the airframe. 2. Noise reduction through the use of acoustic liners inside the engines which absorb acoustic energy, thus reducing noise emission levels. 3. Land planning, restricting flight operations, and flight path design. Numerical modelling can be used to reduce the uncertainty in new designs, and can enable the selection of quieter designs at an early stage. It can then be used to optimise designs, and may even be used to demonstrate that minor design changes will not affect existing certification.

There are other benefits to be gained from numerical modelling. Monetary savings can be made in terms of prototype manufacture and flight test costs. It also serves as an enabler for low-carbon emission technologies, like for example the contra-rotating fan designs which are more fuel efficient than current designs for short flights [106] but are still at the design stage for optimal noise emissions. Using modelling to find designs which easily comply with certification limits can provide headroom for the improvement of aerodynamic efficiency, and other design criteria. Also, numerical modelling can provide insights into the underlying physics of a problem.

However, the time and computational resources needed to obtain noise predictions depend on the problem size and the required accuracy. As an example of the limitation imposed by the available resources, it is not currently possible to model a fully three-dimensional turbofan engine. The problem must be separated into intake and exhaust problems, but even obtaining solutions to these problems can be very demanding. As will be shown in this work, using a standard quadratic finite element method to solve an intake noise problem, up to a frequency of 1.6 kHz, takes approximately 10 hours. This is bad news for design optimisation as many iterations are required. To make design optimisation feasible it must be possible to run many test cases within a reasonable time frame. Thus, there is room for improvement of the computational efficiency of the modelling methods currently employed for the solution of such problems.

The main objective of this work is to develop more efficient modelling techniques that outperform those currently employed for commercial aeroacoustic prediction codes.

This project has been carried out in collaboration with an industrial partner, LMS International, a provider of acoustic prediction software. The company's software, VirtualLab (driven by the acoustic solver SysNoise), makes use of the finite element method for the solution of convected wave propagation problems in the frequency domain. A typical application is the prediction of aircraft engine noise, with a view to the optimisation of acoustic liner performance. It is this type of problem that is studied in this work. Although the main focus of this project is the prediction of noise emission from turbofan engines, it should be noted that the methodology developed here can be extended to other applications, *e.g.* noise reduction in the automotive industry or in heating, ventilating, and air conditioning systems.

The problem is approached by investigating finite element methods that make use of high order polynomial interpolating functions, and by comparing the preferred method to the standard method when used to obtain solutions for a typical application.

1.2 Outline of the Thesis

This thesis is organised as follows. In Chapter 2 the mathematical models used in this work to describe acoustic waves in moving media are introduced. In Chapter 3 a review of finite element methods for wave problems is presented; this chapter includes descriptions of the candidate methods for more efficient solution of such problems. Chapter 4 presents an assessment of the candidate methods, and concludes with the identification of the hierarchic Lobatto method as the most efficient of the methods investigated. In Chapter 5 a scheme which adaptively chooses the optimal order of the Lobatto functions to be used on a given element is developed, and its performance is analysed.

A choice has been made to delay the presentation of the application of the method to an industrial problem in the hope that the foundations of the proposed method are clear to the reader. The application of the proposed adaptive-order method to a simplified turbofan intake noise problem is presented in Chapter 6, and the improved efficiency of the new adaptive-order method over the standard quadratic method is demonstrated. In Chapter 7 a new formulation for the prediction of the acoustic refraction present in exhaust noise problems is proposed, and compared to two existing formulations and an analytic solution. The thesis is concluded, and future work is discussed, in Chapter 8.

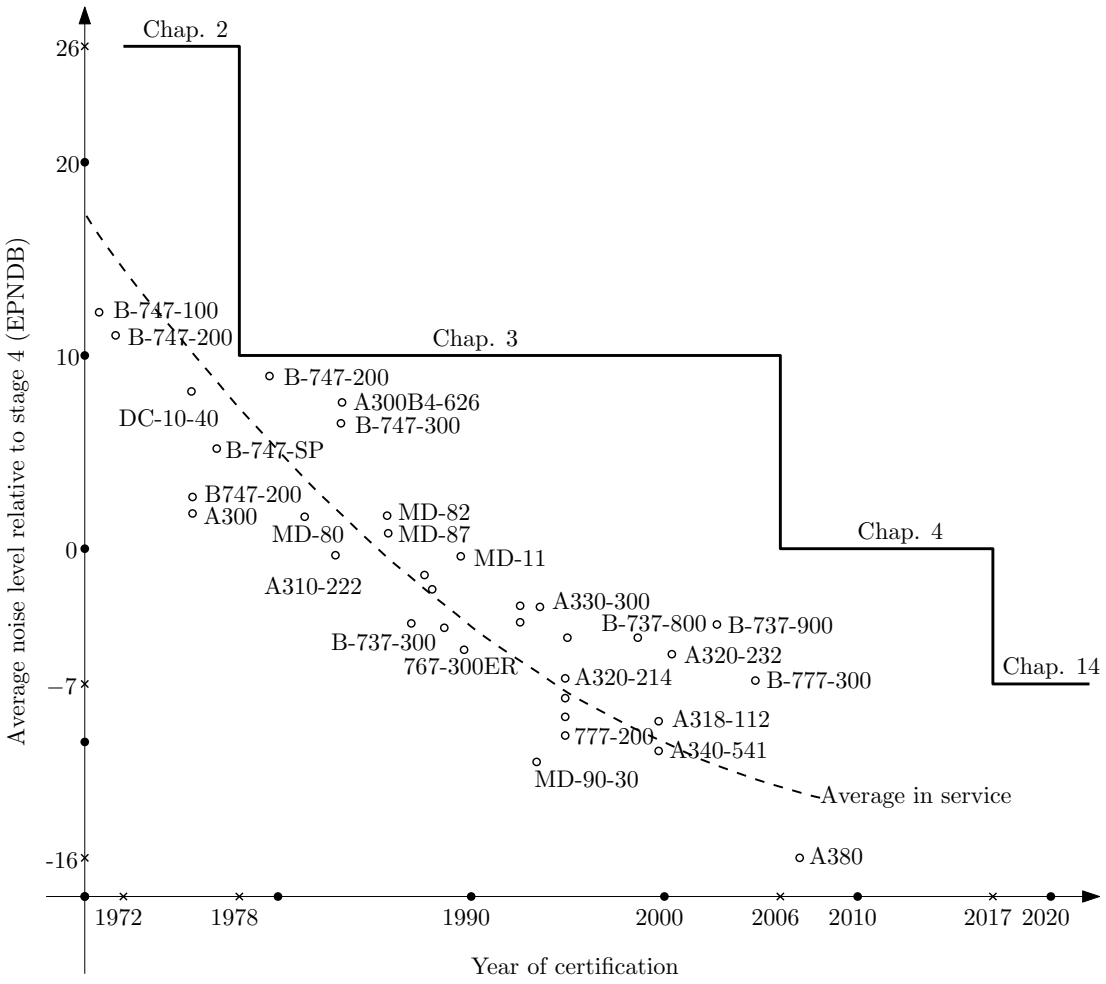

Figure 1.1: Progression of noise certification limits (Adapted from [81]). In this figure the EPNdB (Effective Perceived Noise decibel) relative to Stage 4 is plotted against time (in years).

2

Acoustic Waves in Moving Media

In this chapter, the governing equations used to model convected acoustic waves are introduced. The linearised Euler equations, which govern the linear motion of inviscid fluids, are derived. Bernoulli's equation and the assumption of irrotationality are put to use to derive a convected wave equation, given in terms of the velocity potential. The linearised Euler equations are further simplified to give a convected wave equation in terms of acoustic pressure, valid for uniform flows. This simplification provides an illustration of the typical properties of acoustic waves in moving media. The boundary conditions required to complete the mathematical models are described. These include a boundary condition to represent duct modes, an impedance condition for modelling acoustic liners, and two non-reflecting boundary conditions used to minimise unwanted reflections in domains of finite extent. Finally, the Kirchhoff formula, which is used to extrapolate solutions to the far-field, is discussed.

2.1 Governing Equations

The laws of mass and momentum conservation, and an equation of state, will be introduced in this section. It will be assumed that the flow field can be decomposed into base flow quantities and perturbed variables to arrive at the linearised Euler equations.

2.1.1 Conservation Equations

The mass continuity and momentum conservation laws that govern a fluid's motion, in the absence of external sources, are given by the equations [66]:

$$\frac{\partial \rho^t}{\partial t} + \nabla \cdot \left(\rho^t \boldsymbol{v}^t\right) = 0 \qquad \text{(mass)}\,, \tag{2.1}$$

$$\rho^t \left[\frac{\partial \boldsymbol{v}^t}{\partial t} + \left(\boldsymbol{v}^t \cdot \nabla\right) \boldsymbol{v}^t\right] = \nabla \cdot \boldsymbol{\sigma} \qquad \text{(momentum)}\,. \tag{2.2}$$

In these equations ρ^t is the fluid density, $\boldsymbol{v}^t$ is the flow velocity vector field, and $\boldsymbol{\sigma}$ is the stress tensor.

The mass continuity equation (2.1) can be rewritten in the form:

$$\frac{\mathrm{D}\rho^t}{\mathrm{D}t} + \rho^t \nabla \cdot \boldsymbol{v}^t = 0\,, \tag{2.3}$$

where we have made use of the material derivative: $\mathrm{D}/\mathrm{D}t = \partial/\partial t + \boldsymbol{v}^t \cdot \nabla$. This operator establishes a link between the Eulerian and Lagrangian descriptions of fluid motion; it describes the evolution of some property of the fluid as it travels along a streamline.

The divergence of the stress tensor can be written as: $\nabla \cdot \boldsymbol{\sigma} = -\nabla p^t + \nabla \cdot \boldsymbol{T}^t$, where p^t is the pressure, and $\boldsymbol{T}$ is the viscous stress tensor. If we ignore viscosity we obtain, from the momentum equation (2.2), the equation:

$$\rho^t \frac{\mathrm{D}\boldsymbol{v}^t}{\mathrm{D}t} + \nabla p^t = \boldsymbol{0}\,. \tag{2.4}$$

2.1.2 Equation of State

An equation of state is required to relate the thermodynamic variables within the fluid. It is assumed that the fluid may be treated as an ideal fluid. The assumptions made by this approximation are that: 1. No energy is lost in collisions between the molecules, or in their motion. 2. Attractive and repulsive forces betweens the molecules, and between the molecules and their surroundings, may be neglected. These assumptions are reasonable at low pressure and density, and at moderate temperature. The ideal fluid law provides us with the equation of state [37]:

$$\frac{\mathrm{D}p^t}{\mathrm{D}t} = \left(\frac{\partial p^t}{\partial \rho^t}\right)_s \frac{\mathrm{D}\rho^t}{\mathrm{D}t} + \left(\frac{\partial p^t}{\partial s}\right)_{\rho^t} \frac{\mathrm{D}s}{\mathrm{D}t}\,, \tag{2.5}$$

where s is the entropy.

Instating the isentropic assumption, *i.e.* that the entropy of a fluid element remains constant, yields: $\mathrm{D}s/\mathrm{D}t = 0$. The equation of state (2.5) is reduced to:

$$\frac{\mathrm{D}p^t}{\mathrm{D}t} = \left(c^2\right)^t \frac{\mathrm{D}\rho^t}{\mathrm{D}t}\,, \quad \text{where} \quad \left(c^2\right)^t = \left(\frac{\partial p^t}{\partial \rho^t}\right)_s \tag{2.6}$$

is the speed of sound. It may vary over the fluid.

The speed of sound is a function of the bulk modulus (or compressibility) of a fluid, and the inverse of its density. When an ideal fluid is used, the bulk modulus may be replaced with the product of the pressure and the ratio of specific heats, γ. The speed of sound in an isentropic flow is given by:

$$\left(c^2\right)^t = \gamma \frac{p^t}{\rho^t}\,. \tag{2.7}$$

An energy equation can be arrived at by combining the mass equation (2.3) and the equation of state (2.6), and is written as [12]:

$$\frac{\mathrm{D}p^t}{\mathrm{D}t} + \rho^t \left(c^2\right)^t \nabla \cdot \boldsymbol{v}^t = 0\,. \tag{2.8}$$

The Euler equations consist of the continuity of mass (2.3), the conservation of momentum (2.4), and the energy equation (2.8).

2.1.3 Linearised Euler Equations

The Euler equations can be linearised by assuming that the flow field may be decomposed into base flow quantities and perturbed variables, as follows:

$$\rho^t = \rho_0 + \rho, \qquad \boldsymbol{v}^t = \boldsymbol{v}_0 + \boldsymbol{v}, \qquad p^t = p_0 + p, \qquad \text{and} \qquad \left(c^2\right)^t = c_0^2 + c^2,$$

where the subscript represents a steady quantity in the base flow, and the unscripted variable indicates an unsteady perturbation. The decomposed variables are substituted into the Euler equations, and non-linear terms (which are assumed have a negligible effect on the acoustic field) are identified and omitted.

This produces two sets of equations; those which describe the behaviour of the base flow, and those which describe all linear disturbances of the fluid. These sets of equations are often solved separately, with the solutions of the former being used as inputs for the latter.

For the base flow we obtain the steady Euler equations:

$$\begin{aligned} \nabla \cdot (\rho_0 \boldsymbol{v}_0) &= 0 && \text{(mass)}\,, \\ \rho_0 \frac{\mathrm{d}_0 \boldsymbol{v}_0}{\mathrm{d}t} + \nabla p_0 &= \mathbf{0} && \text{(momentum)}\,, \\ \boldsymbol{v}_0 \cdot \nabla p_0 + \rho_0 c_0^2 \nabla \cdot \boldsymbol{v}_0 &= 0 && \text{(energy)}\,. \end{aligned}$$

Here we have introduced the material derivative in terms of the base flow only: $\mathrm{d}_0/\mathrm{d}t = \partial/\partial t + \boldsymbol{v}_0 \cdot \nabla$. These equations are non-linear, and can be solved using computational fluid dynamics. In this work, the software package FLUENT has been used to solve the steady Euler equations for an inviscid, compressible flow.

The unsteady linearised Euler equations are:

$$\frac{\mathrm{d}_0 \rho}{\mathrm{d}t} + \boldsymbol{v} \cdot \nabla \rho_0 + \rho_0 \nabla \cdot \boldsymbol{v} + \rho \nabla \cdot \boldsymbol{v}_0 = 0 \qquad \text{(mass)}\,, \tag{2.9}$$

$$\rho_0 \frac{\mathrm{d}_0 \boldsymbol{v}}{\mathrm{d}t} + \rho_0 \left(\boldsymbol{v} \cdot \nabla\right) \boldsymbol{v}_0 + \rho \left(\boldsymbol{v}_0 \cdot \nabla\right) \boldsymbol{v}_0 + \nabla p = \mathbf{0} \qquad \text{(momentum)}\,, \tag{2.10}$$

$$\frac{\mathrm{d}_0 p}{\mathrm{d}t} + \boldsymbol{v} \cdot \nabla p_0 + \rho_0 c_0^2 \nabla \cdot \boldsymbol{v} + \rho_0 c^2 \nabla \cdot \boldsymbol{v}_0 = 0 \qquad \text{(energy)}\,. \tag{2.11}$$

The linearised Euler equations support acoustic, entropy, and vorticity modes. Solving them can be computationally expensive, as five unknown variables must be computed. Furthermore, if solved in the time domain they can exhibit linear instability modes, a typical example of which is the Kelvin-Helmholtz instability. However, these first order equations can be further manipulated to give a second order wave equation, which involves only one unknown (acoustic) variable. In formulating these equations, the following have not taken into account: viscosity, heat-transfer, non-linearity, and feedback between the base flow and the perturbation field.

2.2 Potential Flow Theory

This section will introduce an unsteady version of Bernoulli's equation, which will be used to derive a wave equation, given in terms of the velocity potential. The use of potential flow is valid for most non-uniform flows, but the limitations of the theory will be discussed. The acoustic energy, intensity and power will also be briefly introduced.

2.2.1 Bernoulli's Equation

Bernoulli's equation is a special form of the momentum equation. It relates the pressure, velocity, and the velocity potential of a fluid element travelling along a streamline. In essence it states that the sum of the kinetic and potential energies along a streamline remains constant. To begin with, the flow is assumed to be irrotational: $\boldsymbol{v}^t = \nabla\phi^t$, where ϕ^t is the velocity potential. (This assumption holds for the base flow and the perturbed field.) For a compressible, inviscid, irrotational, unsteady flow, Bernoulli's equation states [129]:

$$\frac{\partial\phi^t}{\partial t} + \frac{\boldsymbol{v}^t \cdot \boldsymbol{v}^t}{2} + \int \frac{1}{\rho^t}\mathrm{d}p^t = f(t)\,.$$

The integral is evaluated along any streamline. For a perfect gas, we can make use of the relation $p^t = K\left(\rho^t\right)^\gamma$ (where K is a constant) and the sound speed definition (2.7) to write the integral as $\int 1/\rho^t\,\mathrm{d}p^t = \left(c^t\right)^2/(\gamma-1)$. Assume that at infinity the base flow is steady, to obtain:

$$\frac{\partial\phi^t}{\partial t} + \frac{\boldsymbol{v}^t \cdot \boldsymbol{v}^t}{2} + \frac{\left(c^t\right)^2}{\gamma-1} = \text{constant}.$$

By linearisation, *i.e.* $\phi^t = \phi_0 + \phi$, we arrive at a more practical form of Bernoulli's equation:

$$\rho = -\frac{\rho_0}{c_0^2}\left(\frac{\partial\phi}{\partial t} + \boldsymbol{v}_0 \cdot \nabla\phi\right)\,, \tag{2.12}$$

where the relation: $c^2 = c_0^2(\gamma-1)\rho/\rho_0$ has been used.

2.2.2 Velocity Potential Wave Equation

Substitution of (2.12) into the linearised mass equation (2.9) yeilds:

$$\frac{\partial}{\partial t}\left(-\frac{\rho_0}{c_0^2}\frac{\mathrm{d}_0\phi}{\mathrm{d}t}\right) + \nabla\cdot\left(\rho_0\nabla\phi - \frac{\rho_0}{c_0^2}\frac{\mathrm{d}_0\phi}{\mathrm{d}t}\boldsymbol{v}_0\right) = 0\,.$$

This can be rewritten to give a convected wave equation in terms of the velocity potential:

$$\frac{\mathrm{d}_0}{\mathrm{d}t}\left(\frac{\rho_0}{c_0^2}\frac{\mathrm{d}_0\phi}{\mathrm{d}t}\right) - \nabla\cdot(\rho_0\nabla\phi) + \frac{\rho_0}{c_0^2}\frac{\mathrm{d}_0\phi}{\mathrm{d}t}\nabla\cdot\boldsymbol{v}_0 = 0\,. \tag{2.13}$$

This mathematical model can provide solutions, in the absence of vorticity in both the base flow and the perturbed flow, for a fraction of the cost that would be incurred if the linearised Euler equations were to be solved. It enables faster solutions and makes provision for acoustic predictions at higher frequencies.

This model may be solved in either the time or the frequency domain. If we consider a noise problem in which a source has been generating acoustic waves for a period of time long enough for the initial conditions not to be of concern, then we can assume that the solution behaviour is time harmonic. We seek solutions of the form: $\phi \sim \mathrm{e}^{+\mathrm{i}\omega t}$, where $\omega = 2\pi f$ is the angular frequency, and f is the frequency. The sponsoring company solves this model in the frequency domain, and thus for the work carried out here we will consider only time harmonic solutions. From this point onwards, the definition of the material derivative will be: $\mathrm{d}_0/\mathrm{d}t = (\mathrm{i}\omega + \boldsymbol{v}_0 \cdot \nabla)$.

2.2.3 Acoustic Energy, Intensity, and Power

A quantity of interest in acoustic measurements is the acoustic power. To present the power we must introduce an energy equation which describes the energy density, E, and the energy flux, $\boldsymbol{F}$. The energy equation for a homentropic (uniform entropy) and irrotational field (in both the base flow and the perturbation) is [104]:

$$\frac{\partial E}{\partial t} + \nabla \cdot \boldsymbol{F} = 0\,,$$

where

$$E = \frac{p\rho}{2\rho_0} + \frac{\rho_0 v^2}{2} + \rho \boldsymbol{v} \cdot \boldsymbol{v}_0\,,$$

and

$$\boldsymbol{F} = \left(\frac{p}{\rho_0} + \boldsymbol{v} \cdot \boldsymbol{v}_0\right)(\rho_0 \boldsymbol{v} + \rho \boldsymbol{v}_0)\ .$$

The acoustic intensity is defined as the time averaged energy flux, which gives:

$$\boldsymbol{I} = \frac{1}{2}\Re\left\{p\boldsymbol{v}^*\right\} + \frac{1}{2}\Re\left\{\rho_0\left(\boldsymbol{v}_0 \cdot \boldsymbol{v}\right)\boldsymbol{v}^*\right\} + \frac{|p|^2}{2\rho_0 c_0^2} + \frac{1}{2c_0^2}\Re\left\{p^*\left(\boldsymbol{v}_0 \cdot \boldsymbol{v}\right)\boldsymbol{v}_0\right\}\ .$$

The power crossing a surface, S, which completely surrounds any acoustic sources, is obtained by integrating the normal intensity over the surface:

$$\mathcal{P} = \int_S \boldsymbol{I} \cdot \boldsymbol{n}\ \mathrm{d}S\,,$$

where $\boldsymbol{n}$ is the outwardly pointing unit vector perpendicular to the surface. This integral can then be used to obtain the acoustic power radiated to the far field.

2.3 Uniform Flow

If the base flow quantities have no gradient profiles, then the flow is said to be uniform. Applying this simplification to equation (2.13) results in a convected wave equation valid for uniform flow:

$$\frac{\mathrm{d}_0^2\phi}{\mathrm{d}t^2} - c_0^2\nabla^2\phi = 0\,. \tag{2.14}$$

A possible solution of equation (2.14) is the free-field plane wave: $\phi = A\mathrm{e}^{-\mathrm{i}\boldsymbol{k}\cdot\boldsymbol{x}+\mathrm{i}\omega t}$, where A is a complex amplitude, and $\boldsymbol{k} = k\boldsymbol{n}$ is the wavenumber vector which indicates the direction of propagation of the wave, where $\boldsymbol{n}$ is the unit normal. The wavenumber is given by:

$$k = \frac{\omega}{c_0\left(M\cos\theta \pm 1\right)} = \frac{k_0}{\left(M\cos\theta \pm 1\right)}\,,$$

where k_0 is the free-field wavenumber, $M = v_0/c_0$ is the Mach number, and θ is the angle of the flow. It can be seen that the direction of the flow has an effect on the wavenumber. For downstream flow the acoustic wavelength is lengthened, whereas it is shortened in the upstream case. The wavenumber is related to the wavelength by: $k = 2\pi\lambda^{-1}$.

2.4 Boundary Conditions

Boundary conditions are required to supplement the convected wave equation (2.13). Here we introduce an admittance condition which can be used to describe the behaviour of acoustic liners, which may form part of the problem specification, present a source condition based on the modal decomposition of a duct and discuss two non-reflecting boundary conditions which will be used. A far field radiation condition is also discussed.

2.4.1 Impedance Condition

At a hard wall the gradient of the velocity potential vanishes, $\nabla\phi\cdot\boldsymbol{n} = 0$. At an acoustically lined surface a portion of the energy of an impinging acoustic wave is absorbed. A complex frequency-dependent impedance, $Z(\omega)$, can be used to write a boundary condition which describes the effect of the lined surface on the acoustic field. Myers [110] derived an acoustic boundary condition in the presence of an inviscid flow, which is convenient to implement using Eversman's method [50].

The derivation begins with the decomposition of the impedance surface into a steady part and an unsteady part. The response of the unsteady part to an incident acoustic wave is considered. The condition can be written in terms of the normal particle displacement, ξ, at the surface to give:

$$\boldsymbol{v} \cdot \boldsymbol{n} = \mathrm{i}\omega\xi + \boldsymbol{v}_0 \cdot \nabla\xi - \xi\boldsymbol{n} \cdot (\boldsymbol{n} \cdot \nabla\boldsymbol{v}_0) \ .$$

The impedance of the liner may also be written in terms of its admittance, $A(\omega)$, which is the inverse of the impedance. The admittance is related to the normal acoustic particle displacement by:

$$A(\omega)p = \mathrm{i}\omega\xi \ .$$

Using the admittance, the acoustic velocity normal to the surface can be related to the acoustic pressure by:

$$\boldsymbol{v} \cdot \boldsymbol{n} = \left[\mathrm{i}\omega + \boldsymbol{v}_0 \cdot \nabla - \boldsymbol{n} \cdot (\boldsymbol{n} \cdot \nabla\boldsymbol{v}_0)\right] \frac{A(\omega)p}{\mathrm{i}\omega} \ . \tag{2.15}$$

The first term inside of the square brackets represents the impedance relation in the absence of flow, the second term represents the convective effect of the grazing flow, and the third term is related to the curvature of the surface. In the case of a plane surface the third term vanishes.

In essence, this condition models the behaviour of a boundary layer at the surface using an infinitely thin shear layer (referred to as a vortex sheet). When solved in the time domain the vortex sheet can exhibit an instability mode that will overwhelm the acoustic field, if left untreated. The Myers boundary condition is ill-posed in the time domain [129]. In the frequency domain, however, instabilities are not expected [2].

2.4.2 Duct Modes

This work is predominantly concerned with the prediction of noise radiated from turbofan engines. The engine inlet and exhaust are ducts along which noise propagates from the source plane to the exterior flow. The sound field within a duct can be decomposed into an infinite sum of duct modes. Here we use the concept of duct modes to describe the acoustic source at the source plane.

We begin by considering a straight duct, with hard walls, which carries a uniform subsonic flow with axial velocity v_0; the flow is aligned with the duct axis. An example of such a duct, with an arbitrary cross-section, is given in Figure 2.1.

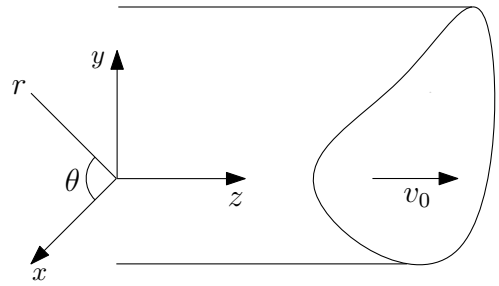

Figure 2.1: A straight, hard-walled duct with arbitrary cross-section, carrying an axial flow with velocity v_0.

The convected wave equation (2.14) governs the acoustic behaviour of the fluid. The modal decomposition can be written as:

$$\phi(r,z,\theta,t) = \sum_{m=-\infty}^{+\infty}\sum_{n=0}^{+\infty}\left(A^+_{mn}e^{-\mathrm{i}k^+_{zmn}z} + A^-_{mn}e^{-\mathrm{i}k^-_{zmn}z}\right)\Psi_{mn}(r)e^{\mathrm{i}\omega t-\mathrm{i}m\theta}\,, \tag{2.16}$$

where r is the radial coordinate, z is the axial coordinate, θ is the azimuth, Ψ_{mn} is the mode shape function, and A_{mn} is the amplitude of mode (m,n). A^+ implies a right-going wave, and A^- a left-going mode. The circumferential mode order is m, and the radial mode order is n. The axial wavenumber is given by:

$$k^\pm_{zmn} = \frac{\pm c_0\sqrt{\omega^2 - (c_0^2 - v_0^2)k^2_{rmn}} - v_0\omega}{c_0^2 - v_0^2}\,, \tag{2.17}$$

where k_{rmn} is the radial wavenumber.

2.4.2.1 Propagating and Evanescent Modes

Duct modes may be either propagating or evanescent (*i.e.* exponentially decaying). A critical frequency can be defined, above which modes propagate and are said to be cut-on, and below which modes are evanescent and are referred to as cut-off. The cut-off frequency is given by:

$$f_c = \frac{1}{2\pi}\sqrt{c_0^2 - v_0^2}k_{rmn}\,. \tag{2.18}$$

We note that the axial wavenumber (2.17) may be either real or complex imaginary, depending on the frequency and the radial wavenumber; this determines the behaviour of the mode (either propagating or evanescent).

Evanescent modes decay rapidly away from the source, and as a result they do not carry acoustic energy far along the duct. In contrast, the amplitude of a propagating

mode remains constant along the duct. This means that, far from the source, evanescent modes do not contribute to the soundfield, and so they are generally omitted from the source description.

The mean flow has an effect on the cut-off frequency; as the flow velocity increases the cut-off frequency is reduced, thus creating many more cut-on modes.

2.4.2.2 Annular and Circular ducts

Let us now consider the modal decomposition of two types of ducts used in this work. These are circular and annular ducts; their cross-sections are shown in Figure 2.2.

For an annular duct the mode shape function is of the form:

$$\Psi_{mn}(r) = \mathrm{Y}'_m(k_{rmn}R_0)\mathrm{J}_m(k_{rmn}r) - \mathrm{J}'_m(k_{rmn}R_0)\mathrm{Y}_m(k_{rmn}r)\,,$$

where R_0 is the inner radius of the duct, J_m is the Bessel function of order m, Y_m is the Neumann function of order m, and the prime indicates the derivative with respect to the argument. At the hard walls of the duct we have the equation:

$$\mathrm{Y}'_m(k_{rmn}R_0)\mathrm{J}'_m(k_{rmn}R_1) - \mathrm{J}'_m(k_{rmn}R_0)\mathrm{Y}'_m(k_{rmn}R_1) = 0\,, \tag{2.19}$$

where R_1 is the outer radius of the duct. This is the characteristic equation of the annular duct; it must be solved numerically to find admissible values for the radial wavenumber. For a circular duct R_0 vanishes, and the mode shape function becomes:

$$\Psi_{mn}(r) = \mathrm{J}_m(k_{rmn}r)\,,$$

where R is the duct radius. In this case, the radial wavenumbers are solutions of the characteristic equation:

$$\mathrm{J}'_m(k_{rmn}R) = 0\,. \tag{2.20}$$

Modes with $m = 0$ are called axisymmetric, as they are independent of θ, and all other modes for which $m \neq 0$ are called spinning modes. Examples of the modes in a circular duct are given in Figure 2.3; we see that n controls the number of radial oscillations, and m controls the circumferential oscillations.

If the duct walls are not acoustically hard the modal source description becomes more complex.

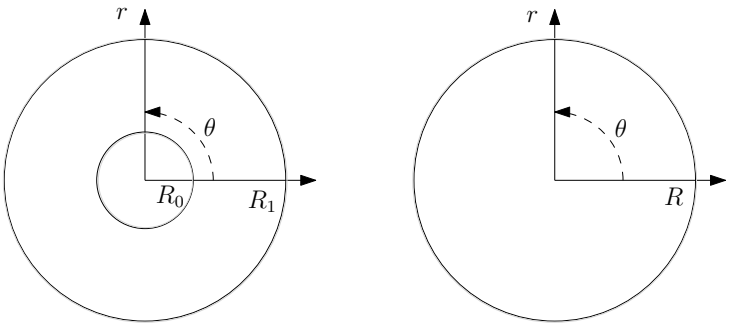

Figure 2.2: Cross-sections of the annular (left) and circular ducts. R_0 is the inner duct radius, and R_1 and R are the outer duct radii.

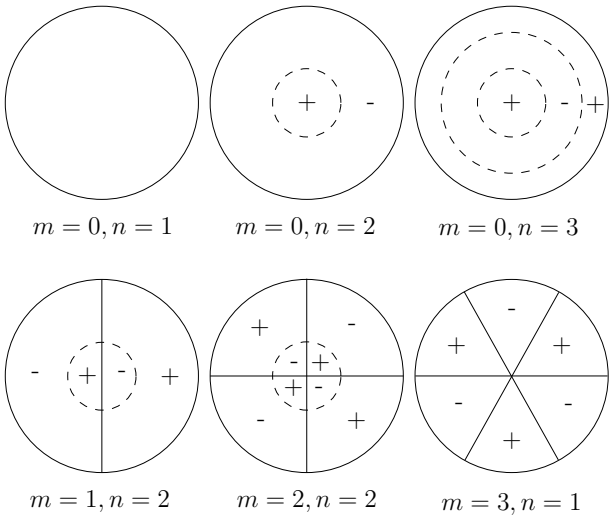

Figure 2.3: Examples of circular duct modes. Top: axisymmetric modes, with the plane wave mode (0,0) on the far left. Bottom: spinning modes.

2.4.3 Non-reflecting Conditions

The physical domain considered in this work is unbounded. This infinite domain must be truncated using an artificial boundary. The artificial boundary must allow propagating waves to leave the domain without creating unphysical waves which are reflected back into the domain. However, constructing such a non-reflecting boundary for complex, multidimensional geometries is not straightforward.

Hixon [75] compared three such conditions, when used to solve the linearised Euler equations in the time domain. He compared boundary conditions based on a one-dimensional (1D) characteristic analysis, a decomposition of the solution into Fourier

modes, and an asymptotic analysis of the governing equation. He found that the most robust boundary condition was obtained using an asymptotic expansion to enforce the asymptotic behaviour of the solution at infinity. An example of an asymptotic condition is the Sommerfeld radiation condition, which ensures that waves do not radiate from infinity. It may be expressed mathematically as:

$$\lim_{|\boldsymbol{x}|\to\infty} |\boldsymbol{x}|^{\frac{d-1}{2}} \left(\frac{\partial}{\partial |\boldsymbol{x}|} + \mathrm{i}k_0 \right) \phi = 0,$$

where d is the dimension of the space.

Radiation and outflow boundary conditions for the accurate simulation of acoustic and flow disturbances in non-uniform mean flows were proposed by Tam & Dong [143]. A more recent review of computational aeroacoustics for turbofan engines [12] states that it is currently common to find non-reflecting boundary conditions based on 1D characteristics, asymptotic expansion, or absorption zones which surround the computational domain. In this work, we make use of two types of non-reflecting condition: boundary conditions based on 1D characteristics, and an absorption zone referred to as a perfectly matched layer.

2.4.3.1 Characteristic Boundary Conditions

This approach was first proposed by Thompson [146] for the solution of hyperbolic systems in the time domain. This method is presented by Hixon [74] in his review of radiation and wall boundary conditions for computational aeroacoustics.

Begin by considering the Euler equations, which support acoustic, entropy, and vorticity modes. At computational boundaries these modes must be correctly specified if unwanted reflections are to be avoided. The modes at a boundary are depicted in Figure 2.4; in essence this is a 1D wave propagation problem in which the waves are perpendicular to the boundary. The Euler equations are rewritten as a 1D problem, and eigenvectors and eigenvalues are identified.

To implement the characteristic boundary condition the incoming and outgoing solutions at the boundaries must be correctly specified or be part of the solution, *i.e.* the amplitude of the incoming wave should be specified, and the amplitudes of the outgoing waves must be determined by the system being solved.

To clarify our implementation of the characteristic condition, we choose a simple duct problem, which more closely resembles the test cases considered in this work. We

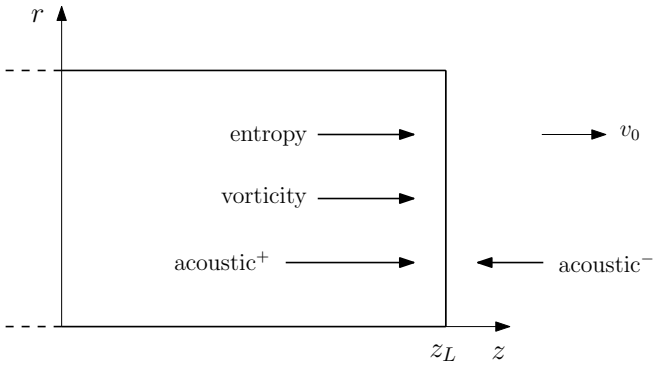

Figure 2.4: Permitted solutions at an outflow boundary: incoming and outgoing characteristics in the presence of subsonic flow [74].

choose to model the propagation of a right-going acoustic wave along a hard-walled duct of infinite extent, which carries a subsonic uniform flow. The domain has been truncated at the planes $z = 0$ and $z = z_L$.

We safely neglect to include entropy and vorticity modes, as we are solving the convected wave equation for the velocity potential. The acoustic field within the duct is governed by the convected wave equation (2.14), which is valid for uniform flows. A general solution of the wave equation is of the form:

$$\phi = f(z - (v_0 - c_0)t) + g(z - (v_0 + c_0)t)\,,$$

which is the sum of a left-going wave and a right-going wave, respectively. We see that we have $-c_0$ and $+c_0$ characteristics. If we consider the boundaries of the problem, we obtain:

$$\begin{aligned} \frac{\mathrm{d}_0\phi}{\mathrm{d}t} - c_0\frac{\partial\phi}{\partial z} &= -2c_0 g' && \text{at } z = 0\,, \text{and} \\ \frac{\mathrm{d}_0\phi}{\mathrm{d}t} + c_0\frac{\partial\phi}{\partial z} &= +2c_0 f' && \text{at } z = z_L\,. \end{aligned}$$

To impose the characteristic condition we must specify the amplitude of the incoming waves, and allow the outgoing waves to be set by the system being solved. To create an acoustic wave that travels from left to right (in the domain shown in Figure 2.4), and which is anechoically terminated at the end of the domain, we specify that $f = 0$ at $z = z_L$. This ensures that a wave travels into the computational domain at $z = 0$, and that (theoretically) there is no reflection at $z = z_L$.

The characteristic condition is only accurate when the wave is normal to, or tangent to, the boundary, see, for example, Hixon & Shih [75]. Results are not optimal for curved boundaries as there are no genuine characteristics for multidimensional problems [142]. In this work, this condition will be used in test cases in which the wave direction is perpendicular to the boundary only. When curved boundaries are present we will rely on a perfectly matched layer.

2.4.3.2 Perfectly Matched Layers

The technique of replacing the boundary conditions with an absorbing region, called a Perfectly Matched Layer (PML), was first proposed by Bérenger [27]. He applied this method to Maxwell's equations, and used a finite difference approximation to find electromagnetic wave solutions in the time domain. Hu [77] studied the use of a PML for the solution of the linearised Euler equations, in two dimensions and subject to a uniform flow. He reported good results, and noted that errors were associated with the discretisation process.

Bécache *et al.* [25] employed the PML method to solve the convected Helmholtz equation. They developed a PML which can handle inverse upstream modes, which are unstable when the phase velocity, ω/k, and the group velocity, $\partial\omega/\partial k$ of a propagating wave have opposite signs. Hu [78] solved the linearised Euler equations, subject to a non-uniform flow, using a PML. He showed that the PML works well for subsonic compressible shear flows, and found that grid-stretching suppresses unstable modes.

Ozgun & Kuzuoglu [116] developed a PML for the finite element method. They made use of a coordinate transformation, which replaces real-valued node coordinates with complex-valued coordinates, and analytically continued the field variables to the complex domain. It is this approach that we will follow in this work.

To construct the PML, the solutions and equations must be analytically continued into the complex space. The computational domain boundary is extended, and a complex transformation is applied. The extended region is truncated, and a boundary condition is applied to the end of the extended region. In practice waves travelling along the extended region should be sufficiently damped at the end of the region so that a Dirichlet boundary condition will suffice; any reflections from the end of the extended region will be attenuated further on their return journey.

We shall demonstrate the method with a simple 1D wave propagation example. Here, the governing equation is the quiescent wave equation ($v_0 = 0$). Let our transform be:

$$z \to \tilde{z} : \tilde{z} = z - \mathrm{i}\alpha(z)\,,$$

where the absorption function is given by:

$$\alpha(z) = \begin{cases} (z - z_L)^3/k & \text{if } |z| \geq z_L\,, \text{and} \\ 0 & \text{if } |z| < z_L\,, \end{cases}$$

where z_L is the boundary of the computational domain. The transformation changes the derivatives of the governing equation:

$$\frac{\partial}{\partial \tilde{z}} = \frac{1}{1 - \mathrm{i}\alpha'(z)} \frac{\partial}{\partial z}\,. \tag{2.21}$$

We see that inside the computational domain the original derivatives are retained. A solution of the governing equation is now of the form:

$$\phi = \mathrm{e}^{-\mathrm{i}k[z - \mathrm{i}\alpha(z)]}\,.$$

When $\alpha \neq 0$ the solution becomes evanescent, *i.e.* beyond the boundary, z_L, the solution decays exponentially. As the PML width increases, the propagating wave converges to the solution at infinity. This method is easily extended to higher dimensions.

The method does have some limitations. The PML is only reflectionless for the exact equations, upon discretisation of the equations the interface between the computational domain and the PML is no longer reflectionless. This source of error can be minimised through the use of a slowly varying absorption function.

Also, the attenuation rate is proportional to the angle of incidence of the propagating wave; as the angle approaches the tangent, reflections can appear. High angle reflections which occur can be minimised by placing the PML sufficiently far from sources and internal boundaries - as in the far field propagating waves begin to resemble plane waves.

2.4.4 Far-field Predictions

The position of an observer of the noise emitted from a turbofan engine is quite likely to be far away from the engine itself. Numerical solutions obtained on the artificial boundary must therefore be extrapolated to the far field. This is achieved by computing an integral over a control surface which encloses all acoustic sources and flow effects. Two integral methods are available: the Kirchhoff integral formulation and the Ffowcs Williams-Hawkings equation.

For the Kirchhoff method a surface integral of the pressure, its normal derivative, and its time derivative, is performed. When the flow is non-zero a moving frame of reference is used [105]. Farassat & Myers [54] present a derivation of the Kirchhoff formula for a surface moving subsonically. The Ffowcs Williams-Hawkings formula allows for non-linearities on the surface, but is more expensive as it requires pressure, density, and the velocity vector for its solution. When the control surface is placed in a region of uniform flow the two formulas are equivalent (see Brentner & Farassat [34], in which an analytic comparison of the formulas is presented).

Thus, the Kirchhoff formulation performs well for inlet noise extrapolations, whereas for exhaust noise problems (in which shear layers are present) the Ffowcs Williams-Hawkings equation is more accurate. In this work we make use of the Kirchhoff formulation; this is acceptable as we will only present far field data for intake noise predictions. A full derivation is provided by Farassat [53].

3

Finite Element Methods for Wave Problems

In this chapter, the standard finite element method is applied to a convected acoustic wave propagation problem, in order to present its basic construction and notable features. The most relevant advanced methods, which have been designed to tackle wave problems, are then reviewed. The remainder of the chapter is devoted to descriptions of four advanced finite element methods, which have been identified as candidates for producing more efficient convected wave solutions.

3.1 The Standard Method

The standard version of the finite element method makes use of Lagrange interpolation functions to generate predictions of the behaviour of some physical system. We will use this section to develop the core concepts of the standard method.

3.1.1 Physical Problem

A turbofan engine intake noise problem is to be solved, using the finite element method. This is an exterior acoustic problem, in which a body with a closed surface is placed within a moving fluid of infinite extent. The mean flow field, $\boldsymbol{v}_0$, has sound speed, c_0, and density, ρ_0. It is assumed that a solution for the flow field is available, and thus that only a solution for the acoustic field is required. Furthermore, in this example

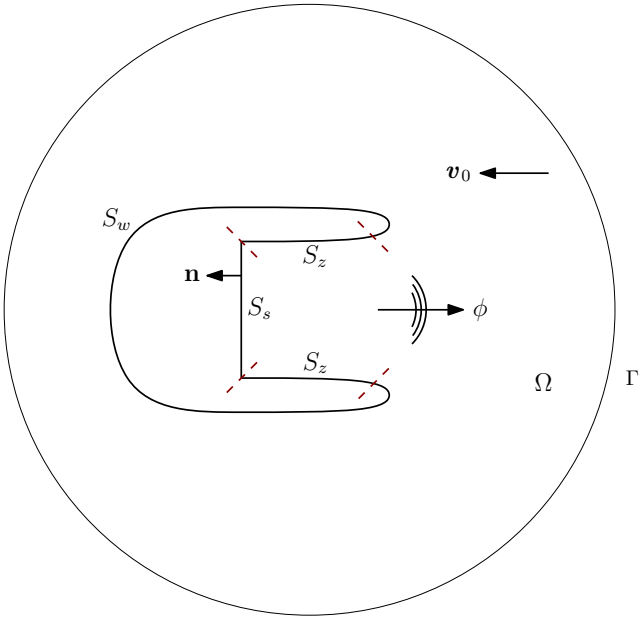

Figure 3.1: Example of an exterior acoustic problem (an axisymmetric engine intake).

sheared flows are not considered. In such problems, the convected wave equation given in terms of the velocity potential (2.13) is solved [129].

The physical problem geometry is shown in Figure 3.1. The surface of the engine comprises a vibrating section which emits acoustic waves, S_s, sections which absorb acoustic energy, S_z, and a section which is acoustically hard, S_w.

The source surface, S_s, is modelled using the duct mode definition given in Section 2.4.2. The sound absorbing surfaces, S_z, are described by their acoustic impedance, which is given by Eversman's implementation of the Myers condition (2.15). On the hard wall, S_w, the velocity potential gradient normal to the surface is zero. The mean flow is tangent to the impedance surfaces and the hard wall. Γ is a non-reflecting boundary.

3.1.2 Weak Variational Formulation of the Governing Equation

The method of weighted residuals is used to solve the convected wave equation (2.13). The solution, ϕ, is approximated using a trial function: $\phi \approx \hat{\phi}$. From this approximation there will be an error, which is referred to as a residual. With the aim of minimising the residual the equation is set equal to zero. The equation is multiplied by a test

function, W, and integration is performed over domain Ω. This gives a weak variational formulation:

$$\int_\Omega \overline{W} \left[\frac{\mathrm{d}_0}{\mathrm{d}t} \left(\frac{\rho_0}{c_0^2} \frac{\mathrm{d}_0 \hat{\phi}}{\mathrm{d}t} \right) - \nabla \cdot \left(\rho_0 \nabla \hat{\phi} \right) + \frac{\rho_0}{c_0^2} \frac{\mathrm{d}_0 \hat{\phi}}{\mathrm{d}t} \nabla \cdot \boldsymbol{v}_0 \right] \mathrm{d}\Omega = 0 \,, \qquad \forall W \,,$$

where the overbar denotes the complex conjugate. Using integration by parts and Green's theorem, the weak formulation can be rewritten as:

$$\int_\Omega -\frac{\rho_0}{c_0^2} \frac{\overline{\mathrm{d}_0 W}}{\mathrm{d}t} \frac{\mathrm{d}_0 \hat{\phi}}{\mathrm{d}t} + \rho_0 \nabla \overline{W} \cdot \nabla \hat{\phi} \, \mathrm{d}\Omega = \int_S -\frac{\rho_0}{c_0^2} \boldsymbol{v}_0 \cdot \mathbf{n} \left(\overline{W} \frac{\mathrm{d}_0 \hat{\phi}}{\mathrm{d}t} \right) + \rho_0 \overline{W} \nabla \hat{\phi} \cdot \mathbf{n} \, \mathrm{d}S \,, \quad (3.1)$$

where the integral on the right hand side is to be evaluated along each of the surfaces: $S = S_s + S_z + S_w$. Formulas (2.16) and (2.15) are used on the source and impedance surfaces, respectively, and the integral vanishes on the hard wall. A perfectly matched transformation (Section 2.4.3.2) is used on the non-reflecting boundary, Γ.

3.1.3 Discretisation

The continuous domain is divided into non-overlapping elements. The average spacing between the nodes of the elements determines the element size, h. The resulting mesh of elements, which approximates the problem geometry, may be either structured or unstructured. When modelling complex geometries unstructured meshes are preferred, however, in some cases structured meshes may be more suitable, like for example when a perfectly matched layer is used [29]. In this work both types of mesh will be considered, although more attention will be given to unstructured meshes. Meshes may be either conformal, *i.e.* nodes, edges, and faces are perfectly matched, or they may be non-conformal, in which case hanging nodes or overlapping zones may be present. In this study, we restrict ourselves to conformal meshes only.

Now that the problem geometry has been discretised, the Galerkin method is employed to define the trial and test functions. We write the discrete functions as: $\phi_h = \sum_{j=1}^{n} a_j \varphi_j$ and $W_h = \varphi_i$, for $i = 1, ..., n$, where the subscript h indicates a discrete variable, n is the number of unknown coefficients a, φ are the global shape functions, and the briefly introduced 'hat' notation has been dropped. A global matrix is constructed, with entries defined by:

$$A_{ij} = \int_{\Omega_h} -\frac{\rho_0}{c_0^2} \frac{\overline{\mathrm{d}_0 \varphi_i}}{\mathrm{d}t} \frac{\mathrm{d}_0 \varphi_j}{\mathrm{d}t} + \rho_0 \nabla \overline{\varphi_i} \cdot \nabla \varphi_j \; \mathrm{d}\Omega_h - \int_{S_{zh}} \rho_0 \overline{\varphi_i} \nabla \varphi_j \cdot \mathbf{n} \; \mathrm{d}S_{zh} \,,$$

as can a source vector:

$$f_j = \int_{S_{sh}} -\frac{\rho_0}{c_0^2}\boldsymbol{v}_0 \cdot \mathbf{n}\left(\overline{\varphi_i}\frac{\mathrm{d}_0\varphi_j}{\mathrm{d}t}\right) + \rho_0\overline{\varphi_i}\nabla\varphi_j \cdot \mathbf{n}\ \mathrm{d}S_{sh}\,.$$

This can be written more succinctly as the linear system: $\boldsymbol{A}\boldsymbol{a} = \boldsymbol{f}$. The system is solved to obtain the unknown coefficient vector $\boldsymbol{a} = [a_1, ..., a_n]^T$ using a direct method, in this case LU factorisation. Note that that the perfectly matched transformation is not explicitly included in the formulation given here.

Certain requirements must be met by the method if the numerical solution is to converge towards an analytic solution. To begin with, we note that a weak variational formulation will have derivatives ranging from zeroth order up to some maximum order. The first requirement is completeness: within each element the shape functions must have an order of continuity equivalent to the highest order derivative present in the weak formulation. Second, the elements must be compatible: at element interfaces the order of continuity of the shape functions must be no less than one order below the highest order derivative [80]. Lastly, the method must have stability. This requires that the problem is well-posed, meaning that it has a unique solution that depends continuously on the input parameters.

A model that is both complete and compatible is said to be consistent. For a consistent model as $h \to 0\,,\ \phi_h \to \phi$.

3.1.4 Reference Elements

An integral must be computed over each element. Numerical quadrature is used to approximate the integrals. To facilitate the use of quadrature, reference elements are used. Coordinate mapping is used to transform the physical space, (x, y), to a reference space, (η, ζ); this transformation is depicted in Figure 3.2.

The Jacobian used in the coordinate mapping is given by:

$$\boldsymbol{J} = \begin{bmatrix} \frac{\partial x}{\partial \eta} & \frac{\partial x}{\partial \zeta} \\ \\ \frac{\partial y}{\partial \eta} & \frac{\partial y}{\partial \zeta} \end{bmatrix}.$$

The integral over the physical space, Ω, is related to the reference space, $\tilde{\Omega}$, by: $\int_\Omega(\cdots)\,\mathrm{d}\Omega = \int_{\tilde{\Omega}}(\cdots)|\boldsymbol{J}|\,\mathrm{d}\tilde{\Omega}$, where the details of the integrand have been omitted (represented by the ellipses), and $|\boldsymbol{J}|$ is the determinant of the Jacobian. A function

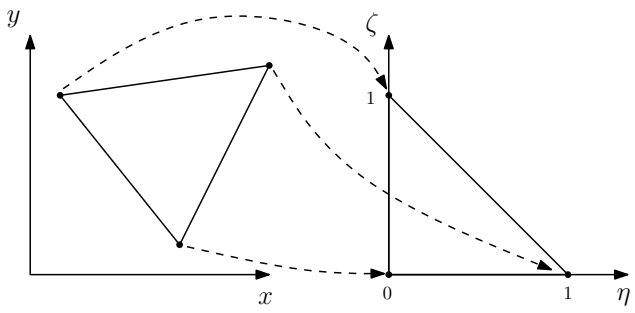

Figure 3.2: Coordinate mapping from physical space to reference space.

present in the transformed weak formulation is given by: $f(x, y) = \tilde{f}(\eta, \zeta)$, and its gradient is given by: $\nabla f(x, y) = \boldsymbol{J}^{-1} \cdot \tilde{\nabla} \tilde{f}(\eta, \zeta)$.

Gauss-Legendre quadrature is used to evaluate the integral over the reference element, using a finite sum:

$$\int_{\tilde{\Omega}} g(\eta) \, \mathrm{d}\tilde{\Omega} = \sum_{i=1}^{n} w_i g(\eta_i) \,,$$

where g is a function, w are weighting coefficients, and η_i are the locations of evaluation points. The numerical quadrature is exact for functions of polynomial order $P = 2n-1$.

3.1.5 Shape Functions

The global shape functions are defined as:

$$\varphi_i(x_j) = \begin{cases} 1 & \text{if } i = j \,, \\ 0 & \text{if } i \neq j \,, \end{cases}$$

where i, j are nodes within a given mesh. The global functions are composed of element shape functions, ψ, which are defined on each element that supports a specific global function.

The shape functions can be taken from various members of the set of mathematical functions. Some popular choices are Bessel, exponential, trigonometric, or polynomial functions. The use of polynomials can facilitate faster frequency sweeps; more will be said of this in Section 3.2.2. As such, only polynomial shape functions will be considered in this work. There are many different kinds of polynomial functions to choose from, like for example Chebyshev, Lagrange, or Legendre polynomials.

As an example, we will briefly introduce the linear triangular Lagrange shape functions. There are three shape functions associated with the linear triangular functions,

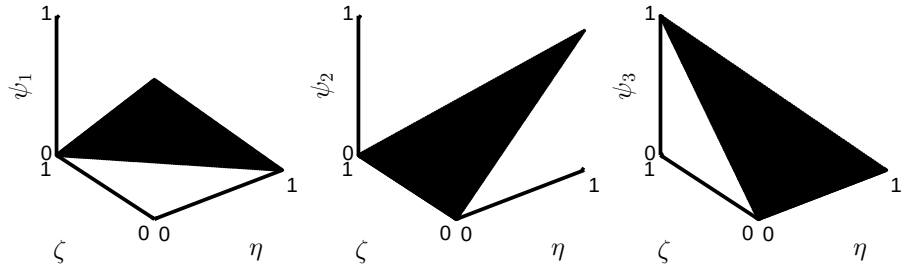

Figure 3.3: The three shape functions associated with linear triangular elements.

and these are given by:

$$\psi_1 = 1 - \eta - \zeta\,, \qquad \psi_2 = \eta\,, \qquad \text{and} \qquad \psi_3 = \zeta\,. \tag{3.2}$$

These functions are defined on the reference element shown in Figure 3.2. The functions are depicted in Figure 3.3. The shape functions are unity at one vertex, and have zero value at the remaining vertices. This property ensures interelement continuity.

A discussion of the key properties of shape functions follows.

3.1.5.1 Continuity

Let us consider the continuity requirements of the problem to be modelled. To satisfy the weak formulation of the problem, the shape functions must be C^{G-1} continuous between the elements, and C^G differentiable inside the elements, where G is the highest order derivative in the weak formulation [80].

For a second order differential equation, like the convected wave equation, the functions used must be C^0 continuous between the elements. This implies that the solution field is constructed using a continuous function whose first derivative is discontinuous at element interfaces. Some structural mechanics models require C^1 continuity, in that case the shape function and its first derivative must be continuous, and its second derivative may be discontinuous between the elements.

Most of the methods considered in this work are equipped with C^0 continuity, but note that we will also consider the Hermite method (to be introduced in Section 3.5) which ensures C^1 continuity.

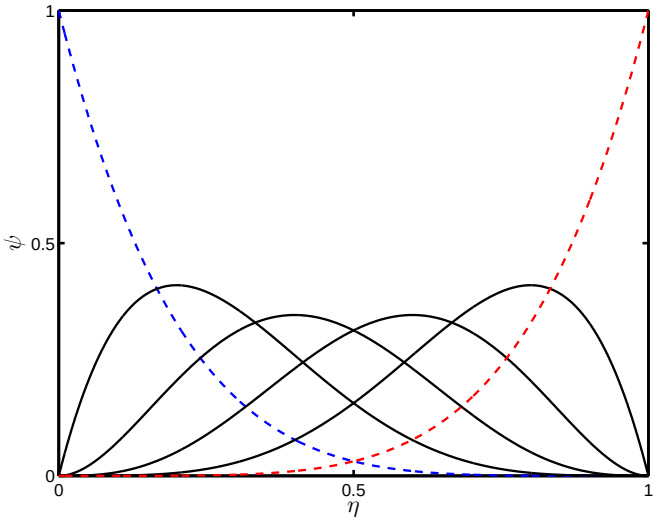

Figure 3.4: Modal shape functions on a one-dimensional element with two nodes. The shape function which is non-zero on the left node is given by the dashed blue line, and the function which is non-zero on the right node is shown using the dashed red line. Four bubble functions are shown.

3.1.5.2 Higher Order Modal Expansion

The accuracy of the finite element solution can be improved either by increasing the number of elements used, this is referred to as h-refinement, or by increasing the polynomial order of the shape functions, which is referred to as P-refinement. Increasing the polynomial order of the shape functions can be carried out in two ways. One method is to increase the number of nodes in the elements, higher order shape functions are then introduced using these nodes. These kinds of shape functions are called nodal, and an example is the high order Lagrange functions. The other method is to use a modal expansion of the nodes which are already available; such functions are called modal. The shape functions which will be investigated in this work are of the modal type.

In one dimension , as the interpolation order P is increased, *i.e.* for $P \geq 2$, bubble functions are added to the approximation space. Bubble functions are zero at both nodes, but have non-zero amplitudes inside the element. This property of the shape functions is demonstrated in Figure 3.4, which shows the one-dimensional modal Bernstein shape functions. In this case, the polynomial order of the shape functions is 5, and thus two nodal functions and four bubble functions are found. A higher order shape

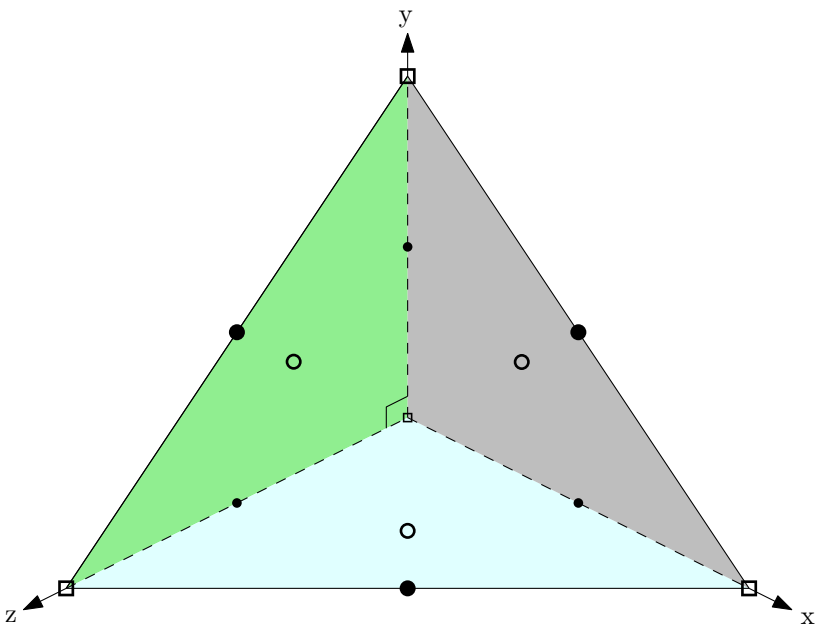

Figure 3.5: Degrees of freedom of a four-noded tetrahedral element with modal shape functions. Node functions □, edge functions •, face functions ○.

function, given in terms of a modal expansion, can be written as:

$$\psi(\eta) = a_1\psi_1(\eta) + \sum_{i=2}^{P} a_i\psi_i(\eta) + a_{P+1}\psi_{P+1}(\eta)\,,$$

where a_n is the coefficient multiplied by function ψ_n, and $\psi_1 = (1-\eta)/2$ and $\psi_{P+1} = (1+\eta)/2$ are the linear nodal functions attached to the first and last node, respectively. ψ_i are bubble functions, where $\psi_i(\eta) = 0$ for $\eta = \pm 1$.

In two dimensions, node, edge and face (or 2D bubble) functions are found. For three-dimensional elements, node, edge, face and volume (3D bubble) functions are found. As an example, consider Figure 3.5, which depicts the degrees of freedom different types of functions on a tetrahedral element with four nodes. Node functions are zero on all nodes but one, edge functions are zero on all other edges, face functions are zero on all other faces, and bubble functions vary only within the element. As will be seen in Section 3.1.5.4, bubble functions can be removed from the final system to be solved without loss of accuracy, but with the added benefit of improved conditioning (*e.g.* [97]).

3.1.5.3 Hierarchic Functions

A disadvantage of using high order nodal functions is the need to construct a new set of shape functions when the polynomial order is increased. This has implications for P-refinement; increasing the order will require the construction of a new mesh. If instead modal shape functions are used, the polynomial order can be increased without re-meshing. Although this is clearly an improvement in terms of efficiency, it still requires the construction of new element matrices when the order is changed. If modal shape functions which do not change with the order are used instead, further savings can be made; as higher order functions can be included in the existing approximation space without changing lower order shape functions. Such shape functions are called hierarchic.

This property is ideal for P-adaptive schemes, in which case a local estimator could be used to determine the optimum interpolation order required in different regions of a problem, and the necessary shape functions sets could then be appended to the element matrices. All of the functions, up to the highest order required, could then be stored and accessed as needed by the global system assembly procedure. This property enables a very efficient implementation of the finite element method. In this work, the Lobatto method (to be introduced in Section 3.6) makes use hierarchic functions.

3.1.5.4 Static Condensation

As the polynomial order of the shape functions is increased, the number of bubble functions increases. Bubble functions only contribute to the solution locally - they have no connectivity with neighbouring elements. The bubble functions can be removed from the final system using a technique called static condensation, which involves removal of the internal degrees of freedom from the set of global degrees of freedom, at the element level. Making use of this technique means that only the degrees of freedom which are shared between elements are included in the final global matrix. The solution values interior to the elements can be recovered during post-processing.

Using condensation has two advantages. Firstly, it reduces the size of the final system, thus reducing the computational cost of solving the system. Secondly, it improves the conditioning of the system, particularly for higher order polynomial approximations

[137]. It is worth noting that this process does not affect the final solution. Condensation is performed by decomposing the element matrix and the unknown solutions into exterior and interior components, as follows:

$$\begin{bmatrix} \boldsymbol{A}_{ee} & \boldsymbol{A}_{ei} \\ \boldsymbol{A}_{ie} & \boldsymbol{A}_{ii} \end{bmatrix} \left\{ \begin{array}{c} \boldsymbol{a}_e \\ \boldsymbol{a}_i \end{array} \right\} = \begin{bmatrix} \boldsymbol{B}_{ee} & \boldsymbol{0} \\ \boldsymbol{0} & \boldsymbol{0} \end{bmatrix} \left\{ \begin{array}{c} \boldsymbol{a}_e \\ \boldsymbol{a}_i \end{array} \right\}$$

where $(\cdot)_e$ are the external degrees of freedom, and $(\cdot)_i$ are the internal degrees of freedom. This can be simplified to give $\boldsymbol{B}_{ee} = \boldsymbol{A}_{ee} - \boldsymbol{A}_{ei}\boldsymbol{A}_{ii}^{-1}\boldsymbol{A}_{ie}$, the condensed matrix, where $\boldsymbol{A}_{ee} - \boldsymbol{A}_{ei}\boldsymbol{A}_{ii}^{-1}\boldsymbol{A}_{ie}$ is the Schur complement. The final system to be solved is then $\boldsymbol{B}_{ee}\boldsymbol{a}_e = \boldsymbol{f}$. A more rigorous description of the condensation technique can be found in Reference [150].

3.2 Review of Advanced Methods for Wave Propagation Problems

When used for wave problems, the standard finite element method becomes inaccurate at high frequencies due to dispersion error. The error occurs due to a phase shift between the numeric and exact solutions. The error is cumulative, and results in what is referred to as pollution error. The only way to tackle this when using standard finite elements is to reduce the element size, but this can become very computationally expensive. To remedy this drawback, advanced methods that aim to improve the accuracy and efficiency of the finite element method have been developed. In this section, the advanced methods for wave problems are reviewed, and the requirements of the candidate methods considered in this work are stated.

3.2.1 Advanced Methods

Since the first textbook on the finite element method (FEM) was published by Zienkiewicz & Cheung [160], many variations of the method have been investigated.

Rose [130] proposed the weak element method for the construction of smooth solutions of elliptic differential equations. The method makes use of elements in which enrichment functions are added to the local shape functions. Interelement continuity is enforced by imposing continuity conditions based on the average value of local approximate solutions and their normal derivatives. Goldstein [65] used this method to solve

the Helmholtz equation. He used a sum of exponentials to approximate the solution within each element.

Hughes *et al.* [84] introduced a least squares approach, called the Galerkin Least Squares (GLS) method, for the solution of advective-diffusive equations. The method involves adding residuals from the strong form of the boundary value problem to the variational form. The method is closely related to the streamline upwind Petrov Galerkin method proposed by Brooks & Hughes [35], but it is more general. In the same year, and in the same vein, Franca & Carmo [59] proposed the Galerkin Gradient Least Squares (GGLS) method. In this method the term added to the standard variational formulation is obtained from a least squares form of the gradient of the strong form of the problem. They applied the method to a singular diffusion problem, and demonstrated the method's stability and accuracy. Harari & Hughes [71] compared the standard Galerkin, the GLS, and the GGLS methods, when used to solve the Helmholtz equation on exterior domains. They found the GLS method to be more efficient than the Galerkin and GGLS methods. Monk & Wang [102] also applied the GLS method to the Helmholtz equation. They used plane waves and Bessel functions as shape functions to prove convergence theorems for the method, and suggest that it may be more efficient than standard FEM.

Hughes [82] presented a variational multiscale approach, which requires dividing the problem into large and small (subgrid) scales. Large scales are solved using standard elements, while the subgrid scales are accounted for by using the residual of the large resolvable scales. The method makes use of bubble functions to approximate the subgrid scales. The use of bubble functions enables static condensation. Hughes employed the method for the solution of the Helmholtz equation. Hughes *et al.* [83] presented a multiscale method which makes use of a hierarchic basis for approximation of the subgrid scales. The multiscale method is equivalent to the residual-free bubbles method proposed by Franca *et al.* [60], which uses finite elements enriched with bubble functions to solve the Helmholtz equation. They showed that the enriched method outperforms the standard FEM and the GLS method.

Després [45] proposed an Ultra Weak Variational Formulation (UWVF). The method uses discontinuous shape functions, with continuity between elements being enforced through impedance boundary conditions. The system is solved using an iterative algorithm. Cessenat & Després [38] employed the UWVF for solution of the Helmholtz

equation. They made use of a plane wave basis with equally spaced angles of propagation, and demonstrated that the UWVF converges faster than standard FEM. Huttunen *et al.* [85, 86] also considered the use of a plane wave basis, but found conditioning problems for coarse elements and unstructured grids. They presented an improved basis with better conditioning, and showed that the UWVF enables the solution of problems at higher frequencies.

A Partition of Unity Finite Element Method (PUFEM) was introduced by Melenk & Babuška [98]. This method uses partition of unity functions, to which enrichment functions are appended to produce new approximation functions. The partition of unity functions ensure interelement continuity, and the enrichment functions are tailored to provide improved local approximations. Generalized FEM (GFEM) is an extension of the PUFEM, in which only the fine scales are solved using enrichment. Strouboulis *et al.* [140] applied this method to the Laplace operator, and used enrichment functions which contained *a priori* information of the problem to be solved (*i.e.* functions obtained from an asymptotic expansion of the exact solution). They identified a linear dependency issue in their interpolation functions. An advantage of the PUFEM and the GFEM is that both methods can be easily implemented into existing standard FEM codes, without the need for changing the underlying structure of the solver.

A Discontinuous Enrichment Method (DEM) was proposed by Farhat *et al.* [55]. The standard FEM is enriched by the addition of solutions to the differential equation of the problem being solved to the standard polynomial functions. The enrichment functions represent the fine scales of the problem. Interelement continuity is enforced through the use of Lagrange multipliers, and static condensation can be applied at an element level prior to assembly. This method was used to solve the Helmholtz equation, using plane wave enrichment functions. Arnold *et al.* [11] presented an analysis of the various versions of the Discontinuous Galerkin Method (DGM), which was first proposed by Reed & Hill [126]. This method uses discontinuous shape functions, and continuity of the solution at the element boundaries is weakly enforced through the variational formulation. The DGM allows for solution discontinuities between elements and lends itself easily to hP-adaptivity, which is a combination of h-refinement and P-refinement for optimal performance.

Another advanced FEM is the spectral element method, which makes use of high order functions. The method was first proposed by Patera [120], who used it for the so-

lution of the incompressible Navier-Stokes equations. Stanescu *et al.* [139] have applied the method to a turbofan engine inlet problem, using quadrilateral spectral elements based on Chebyshev polynomials, and an iterative solver. Bao *et al.* [22] used a local spectral method, the Discrete Singular Convolution algorithm, to solve the Helmholtz equation. They investigated the pollution effect, and demonstrated that the method is a dispersion vanishing scheme. They found that the spectral element method is efficient and accurate when used to solve the Helmholtz equation for high wavenumbers. Unfortunately, the method requires the discretisation of the elements into a set of quadrature points, which means boundary curves might not be properly represented by boundary elements [139]. This property complicates the use of commercial meshing codes, as a quadrature point mesh generator is required.

The spectral element method makes use of elements with interior nodes, a different approach is to construct higher order interpolation functions on elements without interior nodes. Dey *et al.* [46] used higher-order finite elements with a hierarchic polynomial basis. Their method uses blending functions to ensure global continuity of the interpolated field variable. The method is similar to the PUFEM in that the shape functions contain partition of unity functions dedicated to interelement continuity, and a set of functions which can be varied to modify the order of approximation. They demonstrated the ability of the higher-order approximations to control the pollution error in 3D. Listerud & Eversman [93] also made use of higher-order methods to reduce the nodal density of potential theory simulations of exterior acoustic problems. They considered both fan intake and exhaust problems, for the latter they used a penalty method first proposed by Eversman & Okunbor [51]. They compared cubic serendipity elements (elements without interior nodes) to quadratic elements, and found the cubic elements more efficient; specifically, at the post-processing phase in which the acoustic pressure is retrieved from the velocity potential.

3.2.2 Requirements of Candidate Methods

For a method to be considered in this work it must satisfy three requirements.

1. For each source frequency considered a new linear system must be assembled and solved (for each cut-on mode at a certain frequency only a new right-had side must be assembled). A significant computational saving can be made if the shape functions are independent of frequency. Then the element matrices can be constructed and stored. For each frequency the pre-computed matrices are recalled, and the linear system is built and solved. The advantage is that the element matrices need only to be computed once, thus reducing solution times. As we are interested in high order methods, which can be increasingly costly to construct (with increasing order), faster frequency sweeps can vastly improve efficiency. To ensure that the element matrices are frequency independent, we will consider only polynomial shape functions. This requirement means that methods which make use of local solutions, like for example those with a plane wave basis, will not be considered.

2. The finite element method can be optimised through the combination of mesh and polynomial order refinement. In regions of significant geometrical complexity, mesh refinement must be relied upon, but in regions where description of the geometry is not important polynomial order refinement is more efficient. Thus, the second requirement is that the method must lend itself easily to hP adaptivity. Methods which make use of interelement nodes, *e.g.* high order Lagrange methods, will be rejected since P-refinement would require mesh regeneration, which would incur additional expense. Instead, we will consider only methods which make use of modal expansion (Section 3.1.5.2) for the construction of shape functions in which case there is no need for mesh regeneration.

3. Lastly, the method must be easy to include in an existing code.

Using this list of requirements, four candidate methods have been identified. These are: a partition of unity method with a polynomial basis, and the use of a Bernstein basis, a Hermite basis, and a Lobatto basis. Each method will now be introduced, and its strengths and/or weaknesses will be identified.

3.3 Partition of Unity Method

The partition of unity method permits the construction of a conforming space from any local approximation space, and thus separating the issues of interelement continuity, and of locally approximating a smooth function using polynomials. By way of enrichment functions, the local approximation order can be varied according to the problem requirements without the need for mesh refinement. The choice of enrichment functions is problem dependent. These can be used to include *a priori* knowledge of the local solution behaviour, *e.g.* the use of plane wave enrichment for wave problems. The choice of enrichment function will ultimately determine the properties of the resulting global matrix, *i.e.* the cost of construction and the system condition number. Conditioning is dependent on the resulting shape functions [16].

Melenk & Babuška [98], considered generalised harmonic functions and plane waves as enrichment functions for the PUFEM. They used this method to solve the Helmholtz, Laplace, and elasticity equations. The PUFEM has since gained much popularity in computational modelling research, *e.g.* Bacuta *et al.* [19] used PUFEM on non-matching grids for the solution of a Stokes problem, Bacuta & Sun [20] used PUFEM and overlapping domains to solve the Poisson equation, and Kumar *et al.* [90] used the method to solve the stationary Fokker-Planck equation.

The PUFEM is often used to model structural mechanics problems. Oden *et al.* [111] used hierarchic enrichment functions to solve a linear elasticity problem subject to a corner singularity. In terms of P-adaptivity, they found the method to be quite versatile. Taylor *et al.* [144] also used hierarchic enrichment functions, and applied the method to a linear elasticity problem. They investigated the stability of the resulting system, and found that their system had an excess of zero eigenvalues. Duarte *et al.* [49] solved elasticity problems in 3D using the PUFEM.

The method has also been used to tackle wave propagation problems. Laghrouche *et al.* [91] solved the Helmholtz equation using plane waves as enrichment functions. The number of plane waves, and their angles of incidence, at each node were varied. They showed that the PUFEM could be used to solve high frequency problems more efficiently than using the standard FEM. Astley & Gamallo [13, 63] used plane wave enrichment functions to solve the convected wave equation for flow problems, in the context of noise prediction methods for aircraft engines. Huttunen *et al.* [85] compared

the PUFEM, with plane wave enrichments, to an ultra weak variational formulation. They considered the singular problem of an L-shaped domain, and found that both methods were highly accurate, but ill-conditioned. Mohamed *et al.* [100] presented an investigation of 'q-adaptivity', in which the number of plane wave enrichments was varied according to element size. They employed this method to solve the Helmholtz equation, but found it ill-conditioned.

To introduce the method, we consider a domain Ω covered with elements Ω_e. A set of functions form a partition of unity on Ω_e if:

$$\sum_i \chi_i(\eta) \equiv 1\,, \qquad \forall \eta \in \Omega_e\,.$$

The approximated solution on a single element is written as:

$$\phi_e = \sum_{i=1}^{n} \sum_{j=1}^{P} \chi_i V_i^{(j)} a_{i,j}\,,$$

where e identifies an element, i identifies the nodes, V are the enrichment functions, j is the enrichment function order, and a are the unknown coefficients. The shape functions are given by $\psi_i^{(j)} = \chi_i V_i^{(j)}$.

3.3.1 Polynomial Partition of Unity Method

In this work, we consider the use of polynomial enrichment functions only, as this relieves the dependence on frequency of the elementary matrices, and requires fewer quadrature points than plane wave enrichment. Han & Liu [70] presented a brief overview of the Polynomial Partition of Unity Method (P-PUM). Rajendran & Zhang [122] proposed a quadrilateral element based on P-PUM for the solution of linear elastic problems. Their enrichment functions are the so-called point interpolation method polynomials [94]. Hazard & Bouillard [73] demonstrated the efficiency of P-PUM for the modelling of viscoelastic sandwich plates, using polynomial enrichment functions. Oh *et al.* [114] used polynomial enrichment to solve second order and fourth order differential equations.

The only group to have published an investigation of the performance of the P-PUM when applied to convected acoustic problems is Mertens *et al.* [99]. They solved the convected Helmholtz equation for the velocity potential in the frequency domain. In some circumstances, they found the P-PUM to be more efficient than the standard

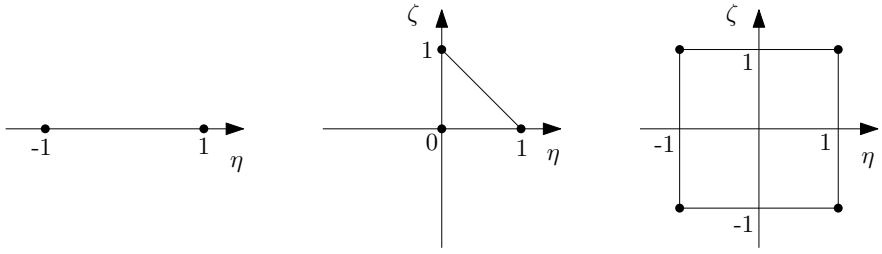

Figure 3.6: Reference elements for the polynomial partition of unity method. From left to right: linear, triangular, and quadrilateral.

FEM, and claimed that the method avoided the high condition numbers generally associated with conventional finite elements. We now leave the general description of the method to provide more specific details of the method used in this work.

The linear Lagrange functions form a partition of unity; in 1D they are:

$$\chi_1 = \frac{1-\eta}{2}\,, \qquad \text{and} \qquad \chi_2 = \frac{1+\eta}{2}\,,$$

on the interval [-1 , 1] (see Figure 3.6). The polynomial enrichment functions are taken from the space:

$$V_i = \left\{1\,,\,(\eta-\eta_i)\,,\,(\eta-\eta_i)^2\,,\,\ldots\,,\,(\eta-\eta_i)^{P-1}\right\}\,,$$

where η_i are the coordinates of the nodes. For example, using an enrichment order of 3 gives the approximated solution:

$$\phi_e = \boldsymbol{\psi}\boldsymbol{a}\,, \tag{3.3}$$

where the shape functions are given by the combination of the partition of unity functions and the enrichment functions:

$$\boldsymbol{\psi} = \frac{1}{2}\begin{bmatrix}1-\eta & 1+\eta\end{bmatrix}\begin{bmatrix}1 & \eta+1 & (\eta+1)^2 & 0 & 0 & 0\\ 0 & 0 & 0 & 1 & \eta-1 & (\eta-1)^2\end{bmatrix}\,,$$

and the unknown coefficients are:

$$\boldsymbol{a} = \begin{bmatrix}a_{1,1} & a_{1,2} & a_{1,3} & a_{2,1} & a_{2,2} & a_{2,3}\end{bmatrix}^T\,.$$

The complete one dimensional approximation functions, up to order 3, are presented in Figure 3.7.

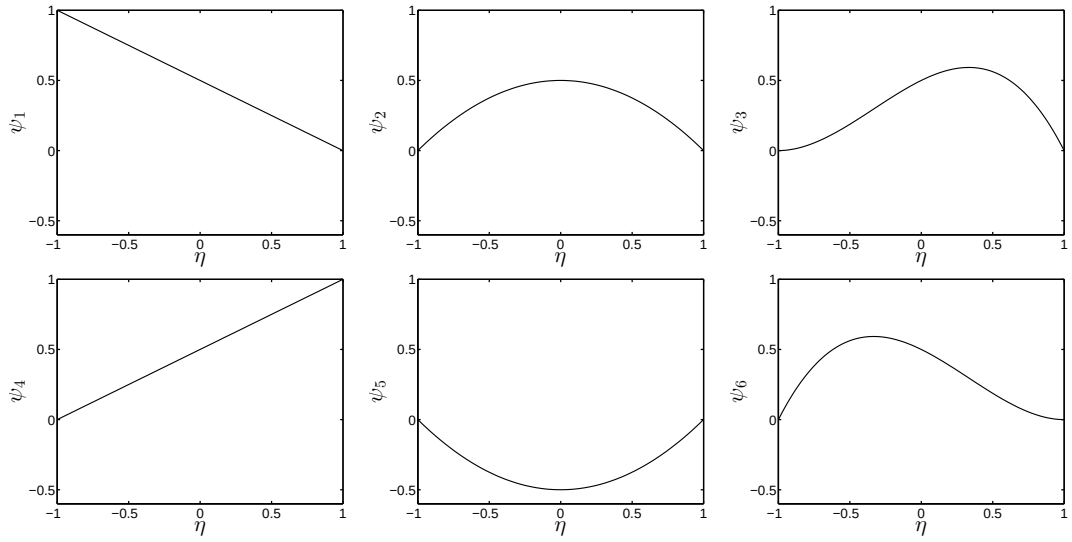

Figure 3.7: One-dimensional polynomial partition of unity functions, up to order 3. Top: shape functions attached to node 1, bottom: shape functions attached to node 2.

3.3.2 Two-Dimensional Shape functions

In 2D, the linear Lagrange functions form a partition of unity. The quadrilateral shape functions are constructed using the tensor product of the 1D functions: $\psi_i^{(j)}(\eta) \otimes \psi_i^{(j)}(\zeta)$. The partition of unity functions and higher order functions for quadrilateral elements (Q4) are given in Figure 3.8.

For triangular elements (T3) the partition of unity functions are the linear Lagrange functions (3.2). The 2D enrichment functions are taken from Pascal's triangle; see Figure 3.9. The triangular shape functions are constructed by following the same technique used in equation (3.3).

3.3.3 Linear Dependency

Decomposition of the 1D shape functions, $\boldsymbol{\psi}^{(j)} = \boldsymbol{\chi} \boldsymbol{V}^{(j)}$, into a polynomial space and a coefficient matrix, for $P = 3$, gives:

$$\boldsymbol{\psi}^{(3)} = \frac{1}{2} \begin{bmatrix} 1 & \eta & \eta^2 & \eta^3 \end{bmatrix} \begin{bmatrix} 1 & 1 & 1 & 1 & -1 & 1 \\ -1 & 0 & 1 & 1 & 0 & -1 \\ 0 & -1 & -1 & 0 & 1 & -1 \\ 0 & 0 & -1 & 0 & 0 & 1 \end{bmatrix}. \tag{3.4}$$

Let us take a moment to analyse the resulting coefficient matrix on the far right. If column 5 is multiplied by -1 we retrieve column 2, and if column 6 is added to column

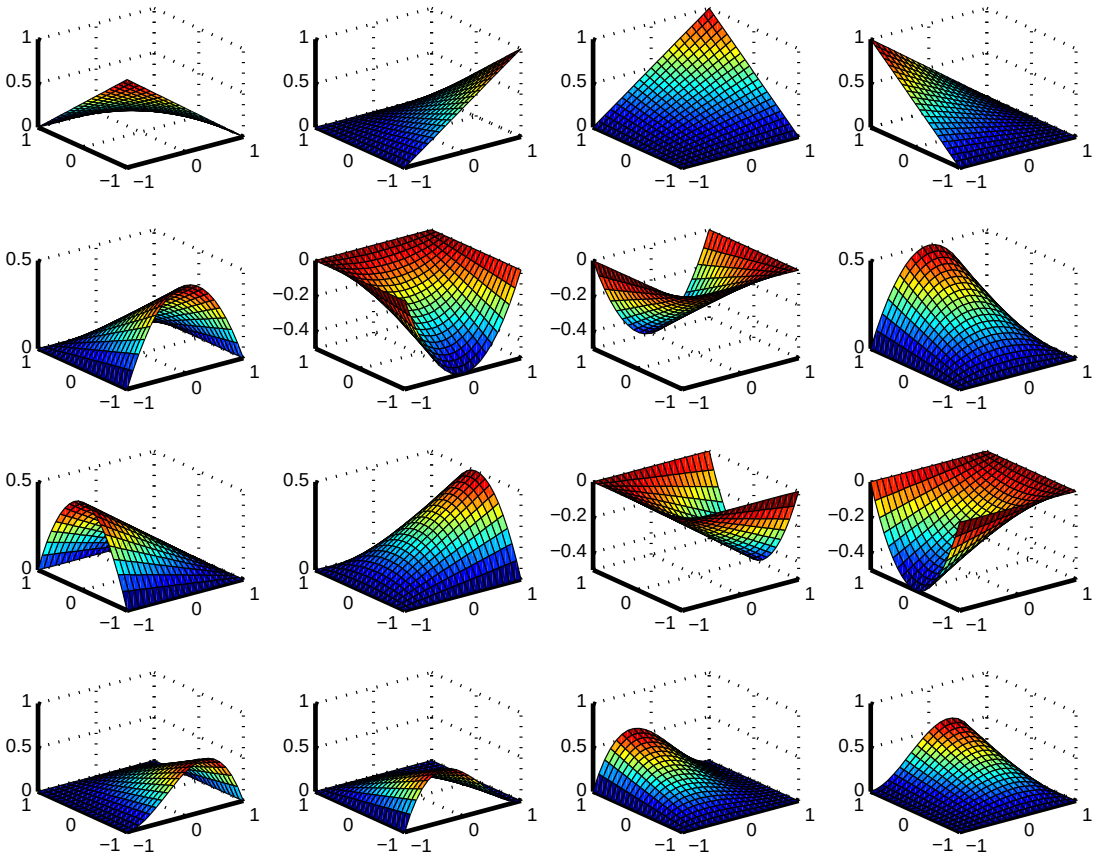

Figure 3.8: Two-dimensional polynomial partition of unity functions on quadrilateral elements. Top row: partition of unity / first order functions, remaining rows: examples of the second order functions.

3 we obtain column 2 multiplied by 2. The matrix in equation (3.4) contains linear dependencies.

Melenk & Babuška [98] first identified the linear dependency problem. For 1D problems, they suggest changing the partition of unity functions at the boundaries in order to remove the linear dependency problem. Taylor *et al.* [144] carried out patch tests to determine the stability of the system. They considered patches with varying numbers of elements, and evaluated the number of zero eigenvalues in each of the resulting systems, but found an excess of zero eigenvalues. They eliminated the first order terms from the local approximation (enrichment) space and in this way obtained a system which was not rank deficient. Oden *et al.* [111] removed the enrichment functions at the boundaries, and suggested that components common to both the partition of unity

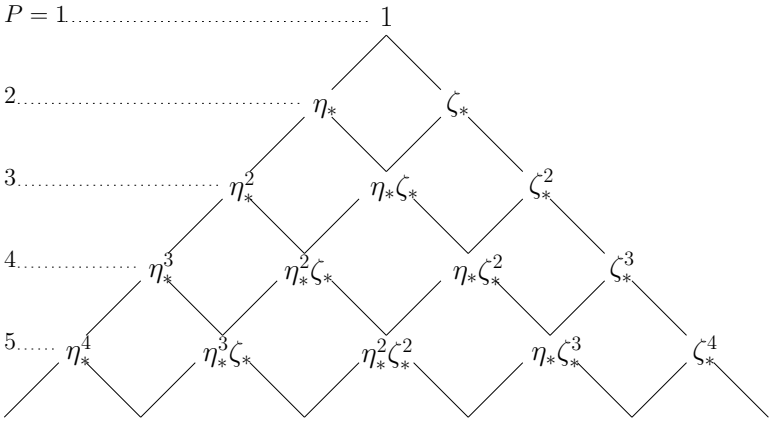

Figure 3.9: Demonstration of the two-dimensional polynomial partition of unity functions, using Pascal's triangle. $\eta_* = \eta - \eta_i$ and $\zeta_* = \zeta - \zeta_i$.

space and the enrichment space should be removed from the system.

Tian *et al.* [148] have shown that the enrichment functions must not be used at boundary nodes. Oh *et al.* [115] made use of flat top partition of unity functions, which resulted in a lower condition number for the global matrix. Oh *et al.* [114] proved the relation between linear independence and the condition number of the global matrix, while An *et al.* [9] suggested that the linear dependency problem is reflected in the rank deficiency of the global approximation space (as was shown in the coefficient matrix given in Definition 3.4).

In conclusion, according to the literature, either enrichment must not be used at the boundaries, or the boundaries should be treated in a manner which avoids linear dependency issues, see for example the work carried out by Cai *et al.* [36]. The former approach has been adopted in this work. When using one-dimensional elements this approach improves the method, although the condition number is still very high for higher orders, and it rises for increasingly smaller elements as the method fails to differentiate between different portions of the same wave. In two dimensions, the approach remedies the linear dependency issue for unstructured meshes, but not for structured meshes. This will be shown in more detail in the next chapter, in which the performance of all of the methods described here will be compared.

3.4 Bernstein Finite Elements

The Bernstein polynomial basis was developed by Sergei Natanovich Bernstein, and was first published in 1912 [31] as a proof of the Weierstrass theorem (approximation theorem). The basis then sunk into obscurity until the 1960's, when it was resurrected by De Casteljau & Bezier [57]. They used it to construct complex shapes for Citroën, using digital computers. Since then the basis has flourished among the computer aided design community. Recently, the basis has been considered for the construction of interpolation functions, in the context of computer modelling of continuum mechanics, *e.g.* [64].

Zumbusch [163] compared various polynomial shape functions, for solution of the Laplace operator (∇^2), and showed that using Bernstein polynomials resulted in a lower system condition number than using Lagrange polynomials. Roth [131] used the Bernstein basis to generate C^1 continuous shape functions, and subsequently made facial surgery simulations using finite elements with Bernstein-Bezier shape functions. He found that accurate results could be obtained using these functions, but concluded that for facial surgery simulations h-refinement using quadratic elements is preferable in terms of computational costs.

One significant advantage of using this basis is that Bernstein polynomials are defined for most commonly used element types. For example, Farouki *et al.* [57] presented a scheme used to construct orthogonal Bernstein polynomials on triangular elements, which could be generalised for the construction of orthogonal bases on simplexes. More recently, Farouki [56] has published a centennial retrospective review of the Bernstein polynomial basis, which provides a wealth of information on the subject.

To date, it seems that the only published work in which the Bernstein basis is used to solve an acoustic problem is provided by Peterson *et al.* [121]. They investigated the use of Bernstein polynomials as shape functions for the solution of the standard Helmholtz equation for interior acoustic simulations, and investigated their performance in an L-shaped domain. They found the polynomials to be the most efficient in their comparison, for the problems investigated, when using an iterative solver, and specifically at higher frequencies. In 3D simulations they found that using the Bernstein polynomials instead of Lagrange polynomials significantly reduced the overall computational costs. They concluded that higher-order shape functions can be used

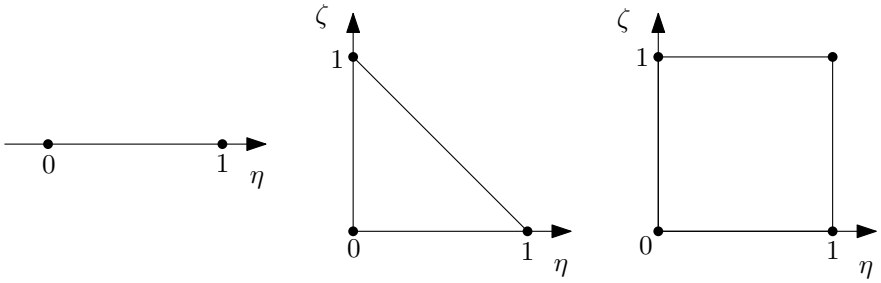

Figure 3.10: Reference elements for the Bernstein functions. From left to right: linear, triangular, and quadrilateral.

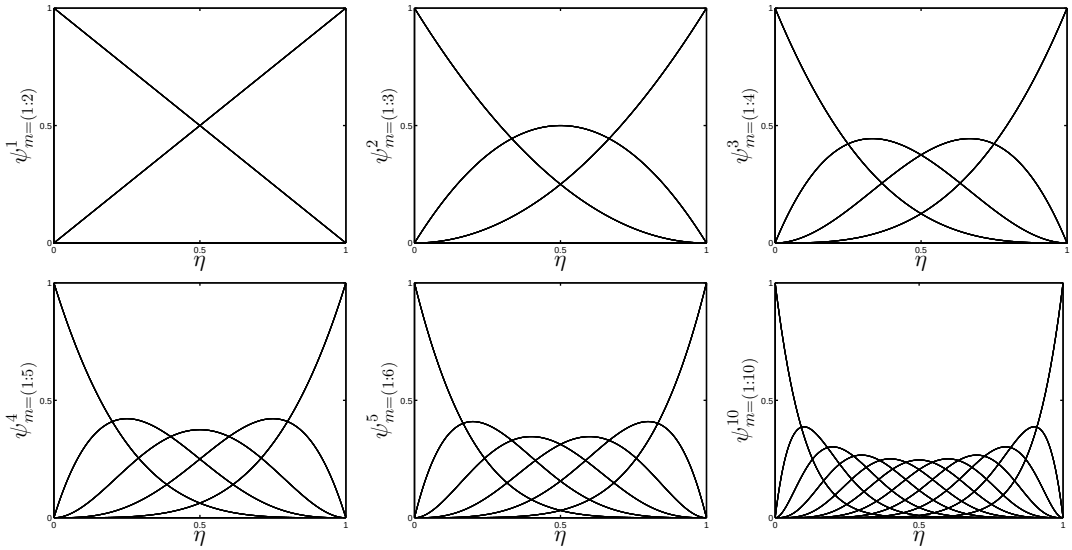

Figure 3.11: One-dimensional Bernstein functions of polynomial order 1 (top left) to 5, and 10 (bottom right).

to effectively control the pollution error and can be used to provide more accurate and efficient simulations.

Polynomials in Bernstein form are non-negative on the interval [0 , 1] (we refer the reader to Figure 3.10 for the reference element used). In one dimension the polynomials are given by:

$$\psi^P_m(\eta) = \frac{P!}{m!(P-m)!}\eta^m\,(1-\eta)^{P-m}\,,$$

where $m = 1, 2, ..., P+1$ and P is the highest polynomial order; there are $P+1$ polynomials. The 1D Bernstein shape functions, for polynomial orders $P = 1$ to 5, and 10, are shown in Figure 3.11.

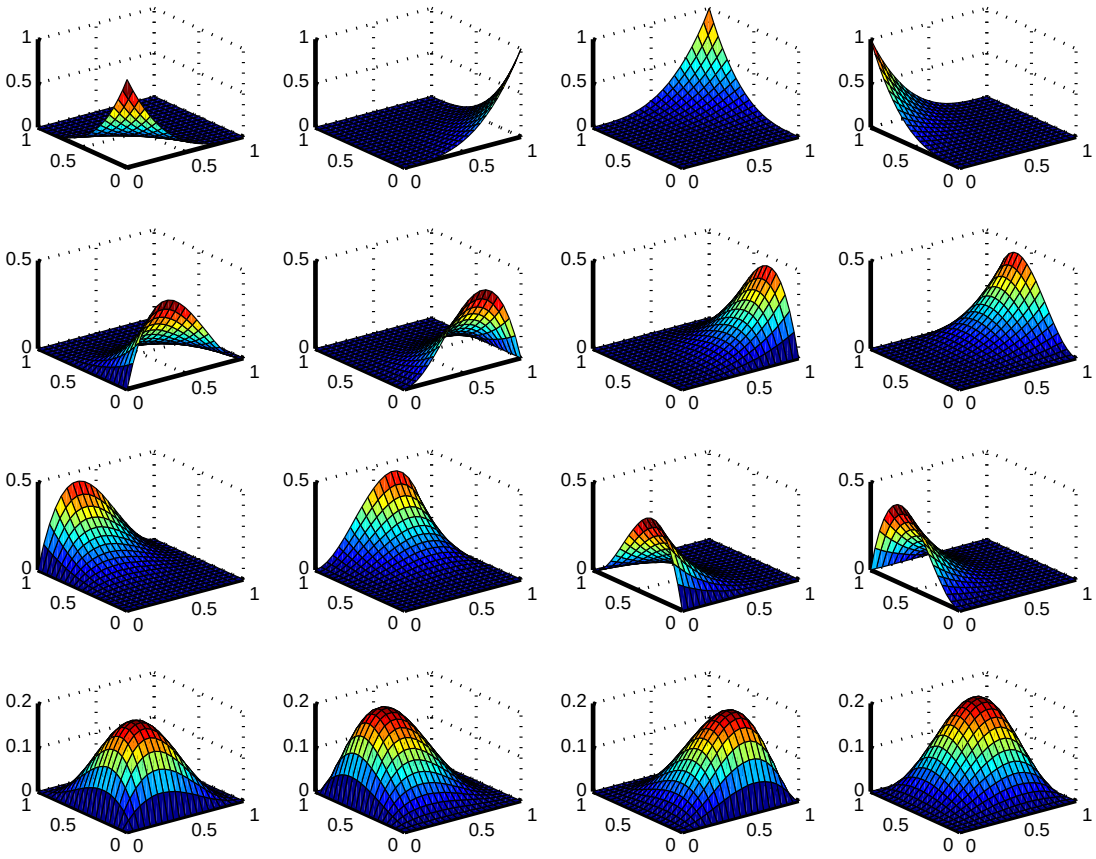

Figure 3.12: Two-dimensional Bernstein functions of order 3, on Quadrilateral elements. Top row: first order functions, remaining rows: second order functions.

For $P = 1$ the linear Lagrange functions are recovered, but it can be seen that all of the shape functions change as the polynomial order changes, *i.e.* the functions are not hierarchic. The result of this that as the polynomial order is increased, which is the case when P-refinement is used, the elementary matrices need to be re-computed.

3.4.1 Higher-Dimensional Shape Functions

Higher-dimensional shape functions are quite easy to construct. The hexahedral element (Q8) shape functions are given by the tensor product of the one-dimensional shape functions: $\psi_m^P(\eta) \otimes \psi_m^P(\zeta) \otimes \psi_m^P(\xi)$. To retrieve the Q4 shape functions the ξ-dimension is neglected. The Q4 shape functions for order $P = 3$ are shown in Figure 3.12.

The different types of Q4 functions can be clearly seen in the figure: the top row shows the vertex functions, the second and third rows show the edge functions, and the face (2D-bubble) functions can be seen in the last row.

The tetrahedral element (T4) shape functions are given by:

$$\psi^P_{i,j,k,l}(\eta,\zeta,\xi) = \frac{P!}{i!j!k!l!}\nu^i\eta^j\zeta^k\xi^l,$$

where $\nu = 1-\eta-\zeta-\xi$. To obtain the 2D basis (T3 elements) the ξ-dimension is omitted. The triangular (and tetrahedral) shape functions also exhibit the different types of functions, *i.e.* vertex, edge, and face (and, in three dimensions, volume).

3.5 Hermite Finite Elements

Hermite polynomials are named after the French mathematician Charles Hermite. C^1 continuity can be achieved when using Hermite polynomials as shape functions, *i.e.* not only are the approximated solutions globally continuous, but so are the first order derivatives of the solutions (see Section 3.1.5.1). Due to this property it is more common to find Hermite shape functions employed for the solution of biharmonic operators (Δ^2) than for the solution of the Laplace operator (Δ).

Augarde [14] showed that Hermite polynomials could be constructed from Lagrange polynomials. Šolín & Segeth [153] proposed hierarchic Hermite polynomials for triangular and quadrilateral elements. However, they found that the resulting triangular element face functions have poor conditioning properties. Li *et al.* [92] considered the conditioning properties of Hermite finite elements used for the solution of biharmonic equations. They found that, for small elements, the condition number of the system was much greater than when used for the solution of the Poisson equation.

It is possible to construct 1D shape functions of variable order in either a nodal or a modal hierarchic fashion. Šolín & Segeth have designed hierarchic Hermite shape functions for 1D elements [152], and their hierarchic 1D Hermite bubble functions, up to order 12, are used in this work. They also provide a hierarchic basis for triangular and quadrilateral elements [153]. However, they found the triangular elements to be poorly conditioned.

At the time of writing, a variable-order set of shape functions for simplex elements is not readily available, although there are sets of functions available for specific orders.

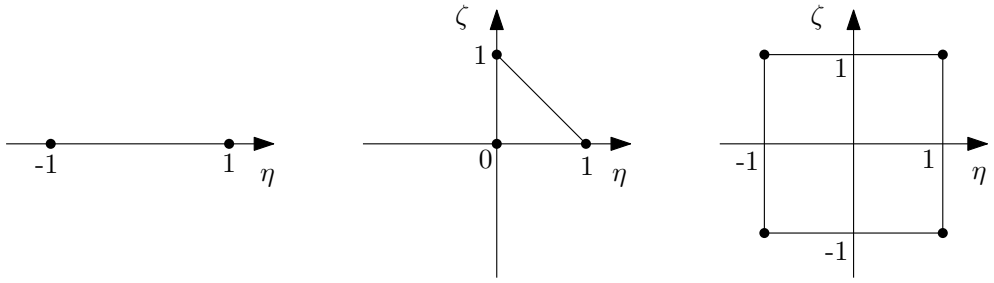

Figure 3.13: Reference elements for the Hermite functions. From left to right: linear, triangular, and quadrilateral.

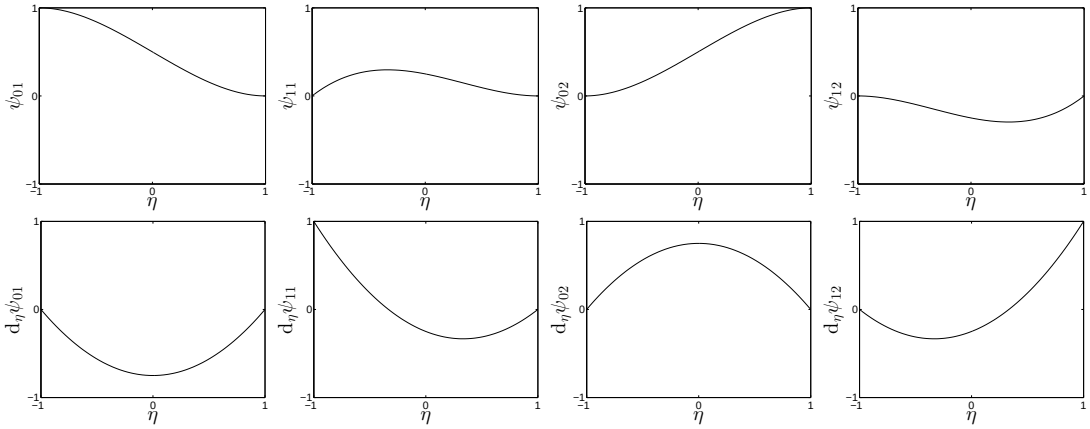

Figure 3.14: One-dimensional Hermite functions of polynomial order 3 (top row), and their gradients (bottom row).

Shi & Liang [138] developed a quadratic Hermite triangular element. Chien & Shih [41] used cubic quadrilateral elements to solve the von Kármán equations. Tabata & Ueda [141] proposed a family of tetrahedral shape functions which could be controlled to 'morph' from Lagrange elements to Hermite elements. They used these to solve Poisson problems. From the literature it appears that constructing well conditioned variable order tetrahedral elements may not be a simple task.

The Hermite basis has been applied to fluid dynamics and acoustic problems. Holdeman [76] used Hermite elements to solve incompressible flow problems, and Agut *et al.* [3] used them to solve the wave equation. Apellö *et al.* [10] used a hybrid discontinuous Galerkin - Hermite method to solve aeroacoustic problems in the time domain. They compared the method to a finite difference method, and found the hybrid method to be more efficient.

Let the Hermite shape functions be denoted by $\psi_{mi}^{(n)}$, where n is the Hermite order, m is the order of the derivative, and i is the node of interest. The polynomial order of the functions are given by $P = n + 2$, it follows that the lowest order Hermite shape functions are cubic. The approximated solution and its first derivative are defined at the nodes. The shape functions are labelled $\psi_{01}^{(1)}$ and $\psi_{11}^{(1)}$ at the first node, and $\psi_{02}^{(1)}$ and $\psi_{12}^{(1)}$ at the second node.

The finite element solution can be written as:

$$\phi_e(\eta) = \psi_{01}^{(1)}(\eta)a_{01} + \psi_{11}^{(1)}(\eta)a_{11} + \psi_{02}^{(1)}(\eta)a_{02} + \psi_{12}^{(1)}(\eta)a_{12}\,,$$

where the 1D Hermite shape functions, on the interval $[-1, 1]$ (see Figure 3.13 for the reference element), are given by:

$$\begin{aligned}
\psi_{01}^{(1)} &= \tfrac{1}{2} - \tfrac{3}{4}\eta + \tfrac{1}{4}\eta^3, \\
\psi_{11}^{(1)} &= \tfrac{1}{4} - \tfrac{1}{4}\eta - \tfrac{1}{4}\eta^2 + \tfrac{1}{4}\eta^3, \\
\psi_{02}^{(1)} &= \tfrac{1}{2} + \tfrac{3}{4}\eta - \tfrac{1}{4}\eta^3, \\
\psi_{12}^{(1)} &= \tfrac{1}{4} - \tfrac{1}{4}\eta + \tfrac{1}{4}\eta^2 + \tfrac{1}{4}\eta^3.
\end{aligned}$$

These shape functions are given in Figure 3.14. It can be seen that the shape functions are continuous, as are their derivatives. This illustrates the C^1 continuity property of the Hermite shape functions. Šolín and Segeth have designed hierarchic Hermite shape functions for 1D elements [152]. Their hierarchic 1D Hermite bubble functions, from order 5 to 12, are given in Appendix A.1.

3.5.1 Two-Dimensional Shape functions

The quadrilateral element has four nodes, and each node has four degrees of freedom so that:

$$\boldsymbol{\phi}_i = \left[\begin{array}{cccc} \phi_i & \dfrac{\partial \phi_i}{\partial \eta} & \dfrac{\partial \phi_i}{\partial \zeta} & \dfrac{\partial^2 \phi_i}{\partial \eta \partial \zeta} \end{array} \right]^T,$$

where $i = 1, 2, 3, 4$. The complete space with C^1 continuity is given by

$$\boldsymbol{P} = \{\eta^m \zeta^n \;;\; m = 0, 1, 2, 3 \;;\; n = 0, 1, 2, 3\}\;.$$

The quadrilateral shape functions are constructed by using the tensor product of the 1D shape functions. The approximated solution can be written as

$$\phi(\eta, \zeta) = \sum_{i=1}^{2} \sum_{j=1}^{2} \left[\psi_{0i}^{(1)} \psi_{0j}^{(1)} a_{ij} + \psi_{1i}^{(1)} \psi_{0j}^{(1)} a_{ij} + \psi_{0i}^{(1)} \psi_{1j}^{(1)} a_{ij} + \psi_{1i}^{(1)} \psi_{1j}^{(1)} a_{ij} \right]\;.$$

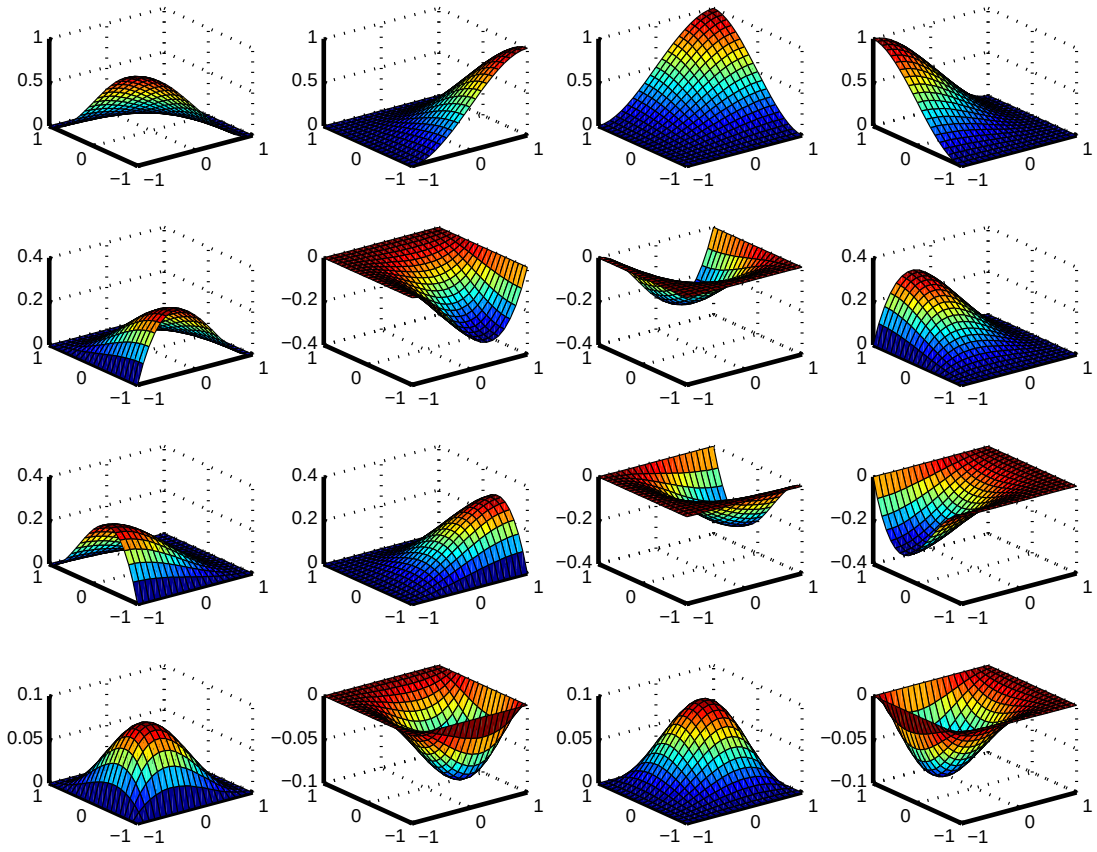

Figure 3.15: Two-dimensional third-order Hermite functions on a quadrilateral element.

The quadrilateral shape functions are given in Figure 3.15. As previously seen in the Bernstein shape functions, we observe different types of functions, namely: vertex, edge, and face. Note that the function gradients are smoother than those of the Bernstein functions. Hexahedral shape functions can also be constructed using the tensor product of the 1D functions, but they have not been used in this work.

The triangular functions are far more complex to define, and a detailed description of the functions is not included in this section; for conciseness the triangular Hermite shape functions are given in Appendix A.2. In the triangular element case each node has 6 degrees of freedom, and the set of shape functions is fourth order convergent in the L^2 error norm [47]. The approximated solution at each node is:

$$\boldsymbol{\phi}_i = \left[\begin{array}{cccccc} \phi_i & \dfrac{\partial \phi_i}{\partial \eta} & \dfrac{\partial \phi_i}{\partial \zeta} & \dfrac{\partial^2 \phi_i}{\partial \eta^2} & \dfrac{\partial^2 \phi_i}{\partial \eta \partial \zeta} & \dfrac{\partial^2 \phi_i}{\partial \zeta^2} \end{array} \right]^T,$$

where $i = 1, 2, 3$. The behaviour of tetrahedral functions has not been investigated in this work due to the lack of a robust construction method.

3.6 Lobatto Finite Elements

The Lobatto basis is obtained from the integrated Legendre polynomials, and can be used to construct higher-order hierarchic functions, *i.e.* the higher-order function sets contain sets of lower-order functions.

Thompson & Pinsky [147] compared the hierarchic Legendre basis, the hierarchic Fourier basis, and the Lagrange basis for solution of the Helmholtz equation. They found that the hierarchic basis outperforms the Lagrange basis by reducing the dispersion error. (They concluded that higher-order elements give greater phase accuracy than lower-order elements for the same number of degrees of freedom.) Adjerid *et al.* [1] described a new hierarchic basis for simplexes, and compared its conditioning properties to existing hierarchic bases. They found that hierarchic functions in multiple dimensions suffer from poor conditioning caused by the interaction of face and volume functions with themselves and with other functions. They reduced the coupling between the shape functions by orthogonalising the face functions, and showed that their new basis exhibited an algebraically growing condition number (with increasing order) for the Laplace operator. Šolín & Vejchodský [155] considered the conditioning of the Lagrange functions, the Lobatto functions and generalised functions (based on eigenfunctions of the Laplace operator). Šolín *et al.* [156] used a modified Gram-Schmidt procedure to construct an orthonormal basis for the bubble functions. They found this new basis to be better conditioned than the Lobatto basis. It is this basis we consider in this work.

The main advantage of using hierarchic functions is that they lend themselves easily to efficient hP adaptivity. Vos *et al.* [151] investigated the run times of various combinations of h and P refinements to solve a system to a predefined accuracy. They found that for elliptic operators with smooth solutions the mesh size should be kept constant and the polynomial order increased. For non-smooth solutions (they used an L-shaped domain with a corner singularity) they found that the order should be held constant and mesh refinement should be used, but stated that using a high polynomial order is optimal.

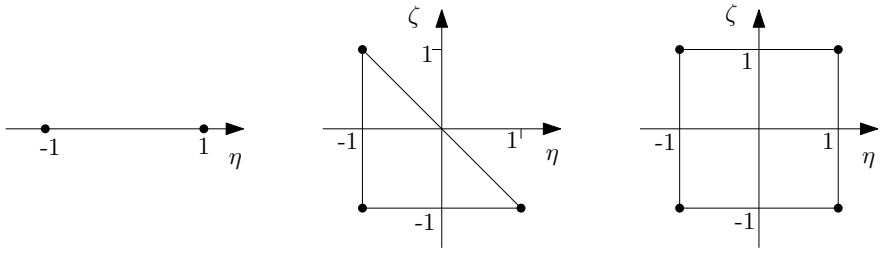

Figure 3.16: Reference elements for the Lobatto functions. From left to right: linear, triangular, and quadrilateral.

It is common to find investigations of higher order elements applied to the Helmholtz operator, but of these (to the best of the author's knowledge) only Petersen *et al.* [121] have considered using Lobatto elements to solve acoustic problems. They solved the Helmholtz equation for high wavenumbers, and demonstrated that the Bernstein basis and Lobatto basis are more efficient than the Lagrange basis.

To derive the basis we begin with the Legendre polynomials:

$$L_n(\eta) = \frac{2n-1}{n}\eta L_{n-1}(\eta) - \frac{n-1}{n}L_{n-2}(\eta)\,,$$

where $n = 1, 2, 3, ...,\ -1 \leq \eta \leq 1$ (see Figure 3.16 for reference element), $L_0(\eta) = 1$ and $L_1(\eta) = \eta$. These polynomials have the orthogonality relation:

$$\int_{-1}^{1} L_n(\eta)L_m(\eta)\,\mathrm{d}\eta = \begin{cases} \frac{2}{2n+1} & \text{for } n = m \\ 0 & \text{otherwise} \end{cases}$$

Lobatto polynomials are based on modified integrated Legendre polynomials. The nodal modes of the basis are given by:

$$\psi_0 = \frac{1-\eta}{2}, \quad \text{and} \quad \psi_1 = \frac{1+\eta}{2}\,.$$

These shape functions are the linear Lagrange functions; they ensure interelement continuity. The internal modes, or 1D bubble functions, are given by

$$\psi_n(\eta) = \sqrt{\frac{2n-1}{2}}\int_{-1}^{\eta} L_{n-1}(\tilde{\eta})\,\mathrm{d}\tilde{\eta}\,,$$

Note that $\psi_n(\pm 1) = 0$, which once again ensure that interelement continuity is maintained. A list of these polynomials, and more details of the basis, can be found in the book by Šolín [154]. The Lobatto 1D shape functions, up to polynomial order 9, are shown in Figure 3.17.

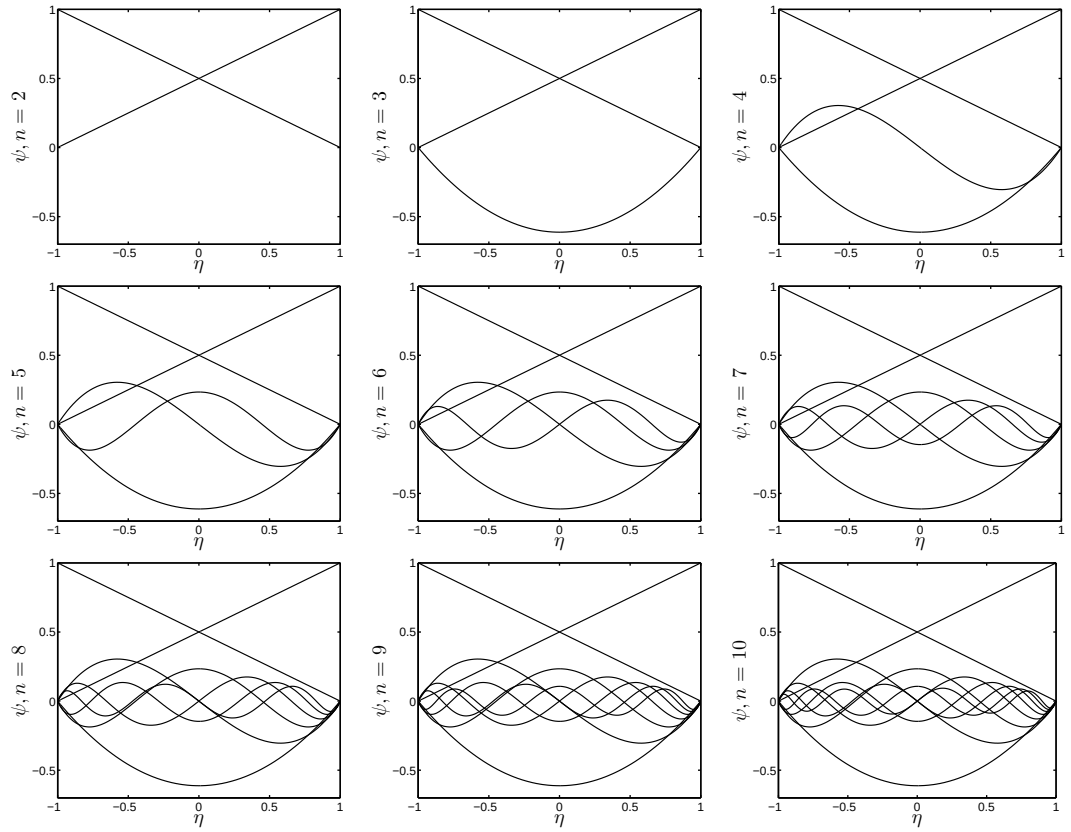

Figure 3.17: One-dimensional Lobatto function, from polynomial order 1 (top left) to 9 (bottom right).

3.6.1 Higher-Dimensional Shape Functions

We consider the reference elements presented in Figure 3.16. The quadrilateral and hexahedral shape functions are constructed using the tensor product of the 1D polynomials: $\psi_i(\eta) \otimes \psi_j(\zeta) \otimes \psi_k(\xi)$. The 2D shape functions up to order 3 for quadrilateral elements (Q4) are given in Figure 3.18. Once again, different types of shape functions can be identified as the polynomial order is increased, these functions are: vertex functions, edge functions, and face functions. The vertex functions can be see in the top row of Figure 3.18, edge functions can be seen in the second and third rows, and bubble functions can be seen in the last row. The existence of face (or 2D-bubble) functions implies that condensation can be applied to the system to be solved, which reduces the computational cost of the method, as explained in Section 3.1.5.4.

The triangular and tetrahedral shape functions are formulated in terms of affine

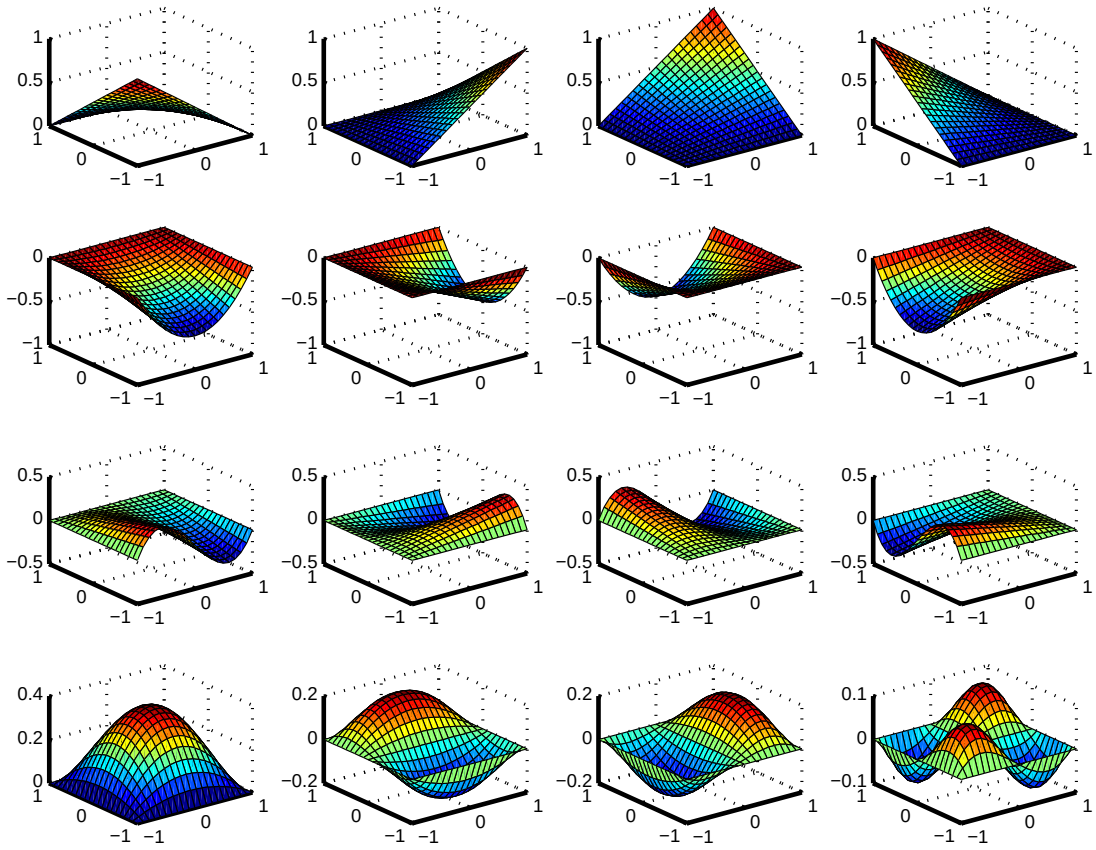

Figure 3.18: Two-dimensional Lobatto functions of order 3 on Quadrilateral elements. Top row: first order functions, remaining rows: second order functions.

coordinate transformation, and constructed from a tensorial type basis. The description of these functions is quite lengthy, and the interested reader is referred to Reference [154] where an extremely detailed description of the functions is given.

3.7 Chapter Summary

The standard finite element method has been introduced. A weak variational formulation of the convected wave equation has been developed for a turbofan engine intake noise problem. The most notable properties of the shape functions have been described (continuity, high order modal expansion, hierarchy, and static condensation).

The advanced methods which have been developed to tackle high frequency problems have been reviewed, and the requirements of the candidate methods have been stated; the shape functions must be based on polynomial functions, they must make use of a high order modal expansion, and the candidate methods must be easy to implement into an existing finite element code. Following the review of the literature, and after taking the method requirements into account, four candidate methods have been identified.

The polynomial partition of unity method comprises the addition of enrichment functions to the approximation space. The method suffers from a linear dependency issue, which has been discussed. The rank deficiency of a single one-dimensional element has been demonstrated. The method has poor conditioning.

Shape functions for the Bernstein basis exist for most commonly used element types. These functions exhibit good conditioning properties. The functions are modal, but not hierarchic.

The Hermite basis exhibits C^1 continuity and is well conditioned. However, its use for variable order shape functions is not well established, and as a result interpolation order refinement in multiple dimensions may not be possible for all commonly used element types.

The Lobatto basis generates hierarchic functions, which lend themselves easily to a combination of element (h) and polynomial order (P) adaptivity. Shape functions for all commonly used element types are readily available.

4

Assessment of High Order Methods

In this chapter, the performances of the candidate high order methods are assessed. Our aim is to find the most computationally efficient method. The efficiency of the methods will be determined from comparisons of accuracy against various measures of cost.

The chapter begins with a description of the test case that will be used. This will be followed by a comment on the possible sources of numerical error, and definitions of the various measures of performance to be used. Convergence results of one-dimensional and two-dimensional solutions will be presented. Finally, the selected method - the use of Lobatto shape functions - will be further analysed in two and three dimensions.

4.1 Preliminary Notions

In this section, we will introduce: the test case which will be used to assess the performances of the candidate methods, the numerical errors of the finite element method which may be encountered, and the measures of cost that will be used.

4.1.1 Test Case

The test case is a hard-walled duct, which carries a uniform axial flow, v_0. The acoustic field inside the duct is governed by the convected wave equation (2.13). Two test case

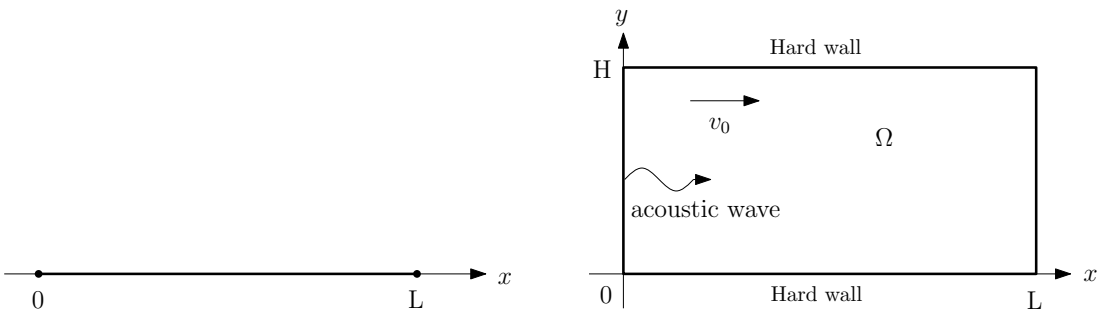

Figure 4.1: Test case geometries for the one-dimensional and two-dimensional analyses. Left: 1D domain. Right: 2D duct.

geometries are given in Figure 4.1. Note that a one-dimensional version of the test case will also be used.

An acoustic plane wave is excited at the beginning of the duct, at $x = 0$. It propagates from left to right, and passes through an anechoic boundary at the end of the duct, at $x = L$. Characteristic boundary conditions (see Section 2.4.3.1) are used to specify the incoming wave and the anechoic termination. On the hard walls, at $y = 0$ and $y = H$, the gradient of the velocity potential is set to zero. For this version of the test case, the duct length is $L = 2$ and the duct width is $H = 1$.

The problem is normalised by the density, sound speed, and the duct width to give a non-dimensional angular frequency, ω, and the non-dimensional Helmholtz number, kH, where k is the effective wavenumber which includes the flow effect. For both the one-dimensional and two-dimensional analyses, only an upstream flow case is considered. This flow direction is considered as the 'worst case scenario', because the upstream flow increases the Helmholtz number (for a fixed frequency), thus this case requires the highest number of elements per wavelength to adequately resolve the acoustic waves (when compared to the no flow and the downstream flow cases).

4.1.2 Numerical Errors

Various types of error may be encountered when attempting to build a numerical model of a physical problem. A very important error is the difference between the physical problem and the theoretical model of it; however, this is beyond the scope of the work presented here. We will concern ourselves only with the differences between the theoretical model and the numerical one, *i.e.* with verifying the numerical method.

Generally, the physical problem geometry is discretised using either linear or quadratic elements. If the geometry is under-discretised erroneous solutions may be obtained; it is important to respect the geometry description to ensure that the discretisation does not introduce an error. Also, the properties of the medium (*i.e.* density, flow velocity, and sound speed) may vary over the size of an element. Under-discretisation with respect to the medium properties is another potential source of error that a mesh designer should be aware of.

In exterior problems, the truncation of an infinite domain can introduce artificial waves that are reflected back into the computational domain. In this chapter, characteristic boundary conditions (see Section 2.4.3.1) are used to ensure that acoustic waves leave the computational domain without generating any significant reflections.

Errors may be caused by the improper use of numerical integration techniques, machine precision, or conditioning problems. Obviously, care must be taken when designing the model. Furthermore, the finite element method has inherent errors. For convected acoustics problems the inherent aliasing, dispersion, and interpolation errors can lead to solutions which deviate significantly from an exact solution to a given problem.

In both the no flow and downstream flow cases, and when using quadratic or higher-order shape functions, error peaks emerge in convergence plots (which are obtained by comparing the numeric solution to an exact solution while reducing the element size). The peaks are caused by aliasing error [108]. Internal numerical resonances along an element create this aliasing effect. However, in practical applications, a mesh is often designed to resolve the highest Helmholtz number, *i.e.* the upstream flow case, in which case the aliasing error does not manifest itself (see Beriot *et al.* [28]). Taking this into consideration, the dispersion and interpolation errors are of the most concern in this work.

Discretisation of the geometry introduces a dependence of the numerical solution on the element size. A consequence of this dependence is a drift of the numerical phase speed relative to an exact solution. The difference between the phase speeds results in dispersion error. The numerical phase error accumulates as a wave propagates along a computational domain, resulting in a pollution effect. The pollution effect is a function of the frequency, domain size, and the number of degrees of freedom, D,

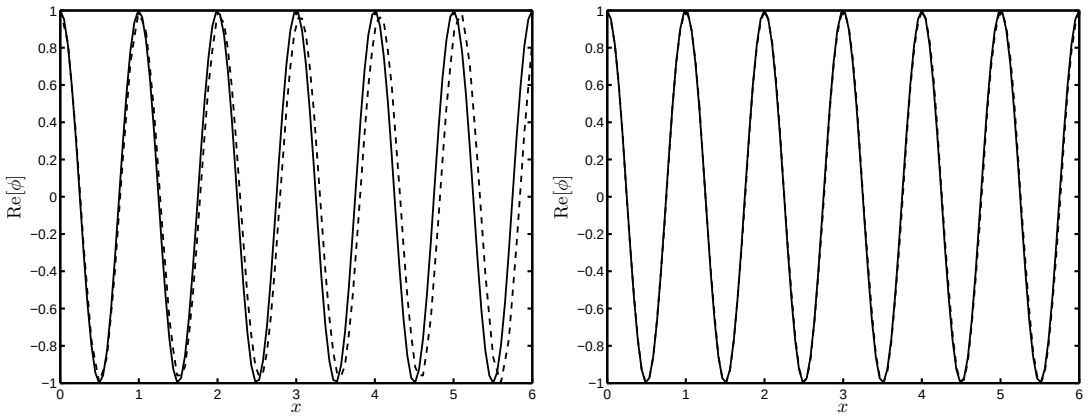

Figure 4.2: Demonstration of the pollution effect (accumulation of dispersion error): $M = 0$, $\omega = 2\pi$, $D = 61$. Analytic (—), numeric (- - -). Left: linear element solution, right: quadratic element solution.

used to obtain the solution. The error introduced by the pollution effect converges like $O\left(k[kh/(2P)]^{2P}\right)$ [87].

An example of the pollution effect is given in Figure 4.2. A one-dimensional finite element model of a right going wave has been solved using linear and quadratic elements. The number of elements used has been varied between the two solutions to ensure that the same number of degrees of freedom are used in both cases. The pollution error is clearly visible when linear elements are used. It can be seen that the dispersion error is significantly reduced when quadratic elements are used. The pollution error becomes increasingly more prohibitive as the frequency is increased; it can be eliminated in one dimension, but Babuška & Sauter have shown that it is impossible to fully eliminate the pollution error in higher dimensions [18]. The dispersion properties of higher-order elements have been investigated by Ainsworth [5]. Higher-order elements tackle dispersion error more effectively than lower-order elements, as can be seen from the order of magnitude estimate given above.

The interpolation error is the difference between the interpolating function and the best approximation of the exact solution. This error dominates the convergence of the numerical solution to the exact solution in the asymptotic range, and it is of the order of $O\left([kh/(2P)]^{P}\right)$ [87]. The interpolation error is local (it does not accumulate) and it can be controlled by keeping kh constant.

4.1.3 Measures of Performance

In this section, we introduce the measures of performance that will be used to evaluate the efficiency of the higher order methods, which were introduced in Chapter 3.

To measure the error incurred, the L^2 norm will be used. The relative L^2 error is given, in percent, by:

$$E = 100\,\frac{\|\phi_a - \phi_h\|_{L^2}}{\|\phi_a\|_{L^2}}\,, \qquad \text{where} \qquad \|f\|_{L^2} = \left(\int |f|^2\,\mathrm{d}\boldsymbol{x}\right)^{1/2}\,,$$

$\phi_a = \exp(-\mathrm{i}k\boldsymbol{x})$ is the exact solution, and ϕ_h is the approximated (numerical) solution.

Since we are dealing with engineering problems, we will be interested in obtaining a certain level of accuracy from the numerical model. A typical error level for engineering problems is 1 %. The computational resources required to reach such an error level are of specific interest in this work.

A possible measure of the computational resources required is the time taken to solve the linear system $\boldsymbol{A}\boldsymbol{a} = \boldsymbol{f}$. However, this is not a reliable measure due to differences in computer architectures and algorithm implementations. The time taken to solve will not be considered as a dependable measure of performance in this work, although it will be included for the sake of interest.

A better indicator of the computational resources required is the amount of computer memory needed to store and factorise the sparse matrix. The sparsity of the matrix is quantified by its number of non-zero entries. The number of non-zero entries is directly correlated with the amount of memory needed to store the matrix. The amount of memory needed to factorise the matrix is dependent on the number of non-zero entries, but also (as will be shown) on the order of the (hierarchic) polynomials used. The sparse matrix system is solved using LU factorisation, and the memory needed represents the number of arithmetic operations used to factorise the matrix.

A measure of the stability of the linear system is the condition number. Given the system $\boldsymbol{A}\boldsymbol{a} = \boldsymbol{f}$, the condition number quantifies the sensitivity of $\boldsymbol{a}$ to changes in $\boldsymbol{A}$ or $\boldsymbol{f}$ [68]. The number is given by $\kappa = \|\boldsymbol{A}\|_1 \cdot \|\boldsymbol{A}^{-1}\|_1$, and in this work the number is estimated using the 1-norm, given by:

$$\|\boldsymbol{A}\|_1 = \max_j \sum_{i=1}^{n} |A_{ij}|\,,$$

where A_{ij} is the element in row i and column j, and n is the matrix dimension.

The parameters varied in order to produce the comparisons which follow are the frequency, element size, and polynomial order. The input frequency and element size can be used to describe the resulting system in terms of the number of elements per wavelength, $N_\lambda = 2\pi/(k_0 h)$. This measure is a useful criteria for mesh design, *i.e.* from the frequency, the required element size can be determined by assuming that a constant number of elements per wavelength will maintain a certain level of accuracy (note, however, that this assumption neglects pollution error).

When using higher order shape functions, more information is conveyed by using the number of degrees of freedom per wavelength. The definitions of the number of degrees of freedom per element that follow have been obtained from asymptotic analyses. For the polynomial partition of unity shape functions the number of degrees of freedom in a given 1D domain are $(N+1)P$, where N is the number of elements in the domain. The length of the domain is given by Nh, and thus the number of degrees of freedom per wavelength is given by $(N+1)P\lambda/(Nh)$, where $\lambda = 2\pi/k$. Asymptotically, as $N \to \infty$, we obtain:

$$D_\lambda = \frac{2\pi}{k\,h} P\,. \tag{4.1}$$

For the Bernstein and Lobatto shape functions the number of degrees of freedom in a given 1D domain are $NP + 1$. The number of degrees of freedom per wavelength are then: $(NP + 1)\lambda/(Nh)$. Asymptotically this gives the same definition for the number of degrees of freedom per wavelength as for the polynomial partition of unity functions.

For the Hermite shape functions the number of degrees of freedom are $N(P - 1)$ (bearing in mind that the first shape function in the set is of polynomial order 3). Thus, in this case, the number of degrees of freedom per wavelength is given by:

$$D_\lambda = \frac{2\pi}{k\,h}(P-1)\,.$$

4.2 One-Dimensional Analysis

Here, we compare the efficiency and condition number of the shape functions when they are used to solve the convected wave problem in 1D. This is carried out by conducting convergence tests, and an engineering accuracy (introduced in Section 4.1.3) analysis.

4.2.1 Convergence and Conditioning Properties

In this section we present the performances of the methods in one dimension. For each method we will consider:

1. The L^2 error as a function of the number of degrees of freedom per wavelength,
2. The L^2 error as a function of the number of non-zero entries in the sparse matrix,
3. The condition number as a function of the number of degrees of freedom per wavelength,
4. The L^2 error as a function of the condition number.

Convergence plots for the upstream case ($M = -0.6$) are generated by holding the frequency constant, at $\omega = 20$, while the element size and polynomial order are varied. The polynomial order is varied from 1 to 10, except in the case of the Hermite shape functions, for which only orders 3 to 10 are available. The number of degrees of freedom per wavelength is varied from 1 to 100, by varying the element size.

In the convergence plots that follow, three distinct regions are generally visible: an oscillatory region in which there is no convergence, a transition region controlled by the dispersion error, and an asymptotic convergence region that is dependent on the interpolation error [5].

4.2.1.1 Error Against Number of Degrees of Freedom per Wavelength

In this section we investigate the convergence properties of the methods. The L^2 error as a function of the number of degrees of freedom per wavelength is shown in Figure 4.3. Asymptotically, the numerical solution should converge towards the exact solution like $O\left(D_\lambda^{-(P+1)}\right)$ [24].

The polynomial partition of unity functions display poor convergence properties. The error of the linear functions converges as expected, *i.e.* like $O\left(D_\lambda^{-2}\right)$, as does the quadratic function ($P = 2$) error, which behaves like $O\left(D_\lambda^{-3}\right)$. For polynomial orders higher than 2 the numerical solution does not converge as expected. Furthermore, as the order is increased the performance of the numerical solutions deteriorates, this is evidenced by the occurrence of error peaks for order 5 and higher. Poor conditioning is to blame for this behaviour; this will be demonstrated shortly. (Note that in an attempt

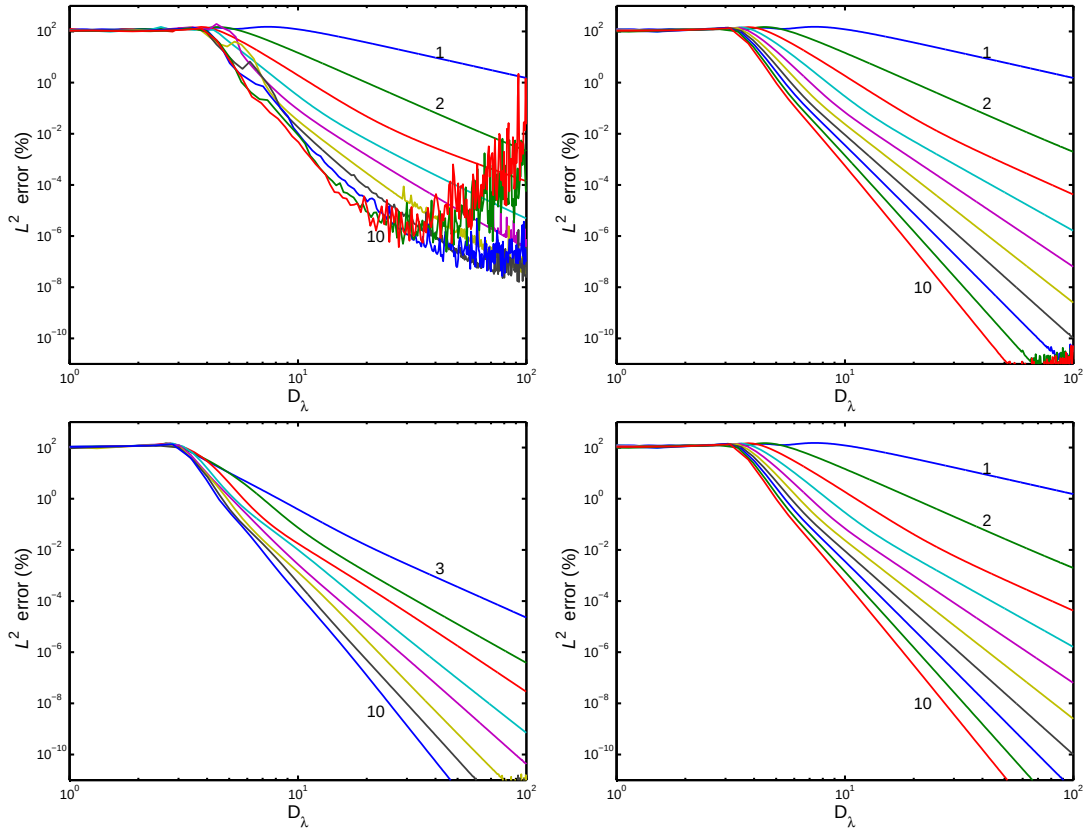

Figure 4.3: The L^2 error as a function of the number of degrees of freedom per wavelength ($\omega = 20, M = -0.6$). Top left: partition of unity, top right: Bernstein, bottom left: Hermite, and bottom right: Lobatto.

to remedy the linear dependency issue the enrichment functions at the boundaries have been removed from the global matrix.)

The Bernstein and Lobatto results are identical. Let us consider the decomposition of their second order shape functions into a polynomial space and a coefficient matrix. The Bernstein shape functions are given by:

$$\psi = \begin{bmatrix} 1 & \eta & \eta^2 \end{bmatrix} \begin{bmatrix} 1 & 0 & 0 \\ -2 & 0 & 2 \\ 1 & 1 & -2 \end{bmatrix}, \tag{4.2}$$

while the Lobatto shape functions are given by:

$$\psi = \frac{1}{2} \begin{bmatrix} 1 & \eta & \eta^2 \end{bmatrix} \begin{bmatrix} 1 & 1 & -\sqrt{3/2} \\ -1 & 1 & 0 \\ 0 & 0 & \sqrt{3/2} \end{bmatrix}. \tag{4.3}$$

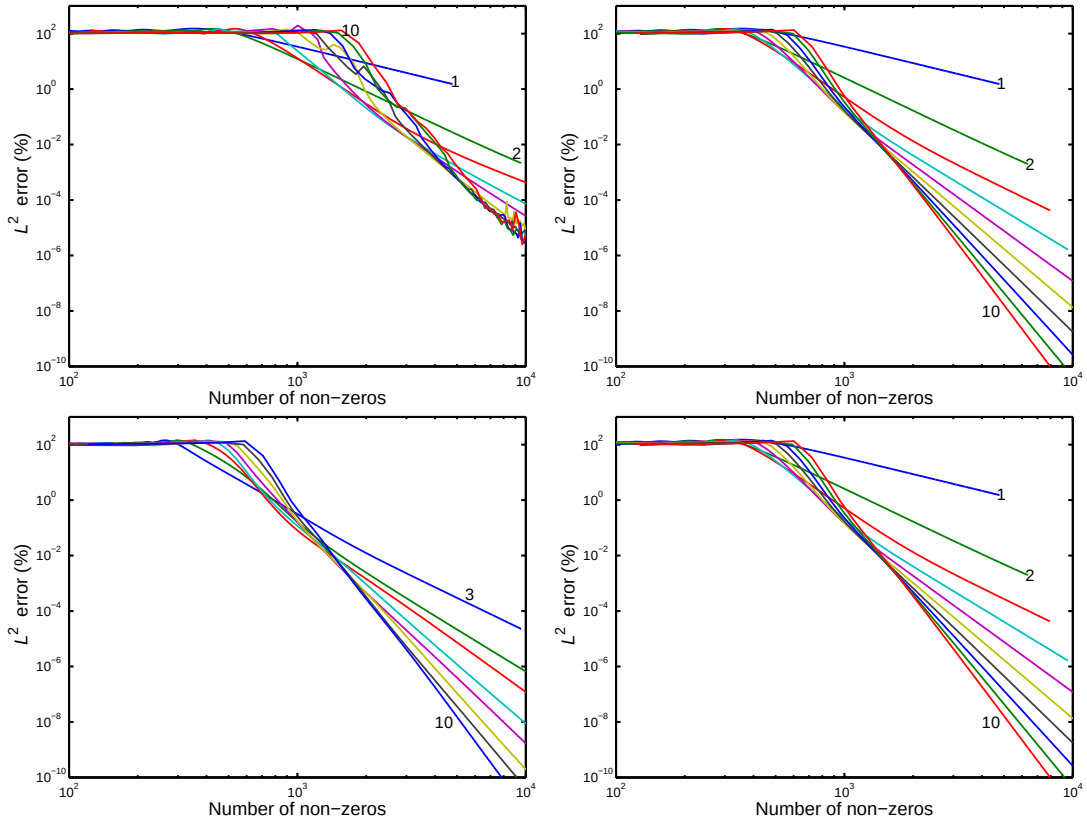

Figure 4.4: The L^2 error as a function of the number of non-zero entries ($\omega = 20, M = -0.6$). Top left: partition of unity, top right: Bernstein, bottom left: Hermite, and bottom right: Lobatto.

We see that, although the shape functions are different (see Sections 3.4 and 3.6), the methods behave in the same way because their shape functions are linear combinations of each other. Asymptotically, these shape functions produce numerical solutions which converge as expected, *i.e.* like $O\left(D_\lambda^{-(P+1)}\right)$. We note that when using order 10, for example, an error level of 1 % is obtained using approximately 5 degrees of freedom per wavelength, while in comparison more than 100 degrees of freedom would be needed to reach the same level of error using linear elements.

The Hermite method error behaves like $O\left(D_\lambda^{-(P+1)}\right)$, and they also appear to demonstrate the most efficient convergence. We take this opportunity to reiterate that the lowest order Hermite polynomials are cubic - not linear.

4.2.1.2 Error Against Number of Non-Zero Entries

Next, we evaluate the computational cost of each set of shape functions by comparing the L^2 error to the number of non-zero entries in the global matrix. The results of this analysis are given in Figure 4.4.

The polynomial partition of unity shape functions display the most expensive solutions. As the order is increased error peaks begin to appear in the plots; this is caused by the ill-conditioning of the global matrix.

Once again, the Bernstein and Lobatto results are identical. Both of the global stiffness matrices generated by the methods require the same amount of storage memory, and so the Bernstein and Lobatto shape functions have an identical error convergence as a function of the number of non-zero entries.

Using this measure, the Hermite shape functions provide the most efficient solutions.

A general observation is that the convergence plots exhibit a 'crossover region', below which (fewer non-zero entries) higher order functions are more expensive, but above which increasingly higher orders provide more efficient solutions. In comparison with the results presented in Figure 4.3 we note that changing the measure of cost from the number of degrees of freedom per wavelength to the number of non-zero entries reduces the perceived benefit of increasing the polynomial order. However, asymptotically higher order shape functions still provide the most efficient solutions.

4.2.1.3 Condition Number Against Number of Degrees of Freedom

Our next comparison is between the condition number of the global matrix and the number of degrees of freedom per wavelength. A low condition number is desirable, as the accuracy of the numerical solution can be reduced by poor conditioning of the system. The results for this comparison are given in Figure 4.5.

The polynomial partition of unity results are plotted using a different scale to that used for the other shape function results, due to the very high condition numbers obtained. It can be seen that as the polynomial order is increased the condition number rapidly increases, this is a consequence of the linear dependency issue (discussed in Section 3.3.3). The conditioning of the matrix degrades the numerical solution as the order is increased. This effect is clearly observed in the results presented in Sections 4.2.1.1 and 4.2.1.2.

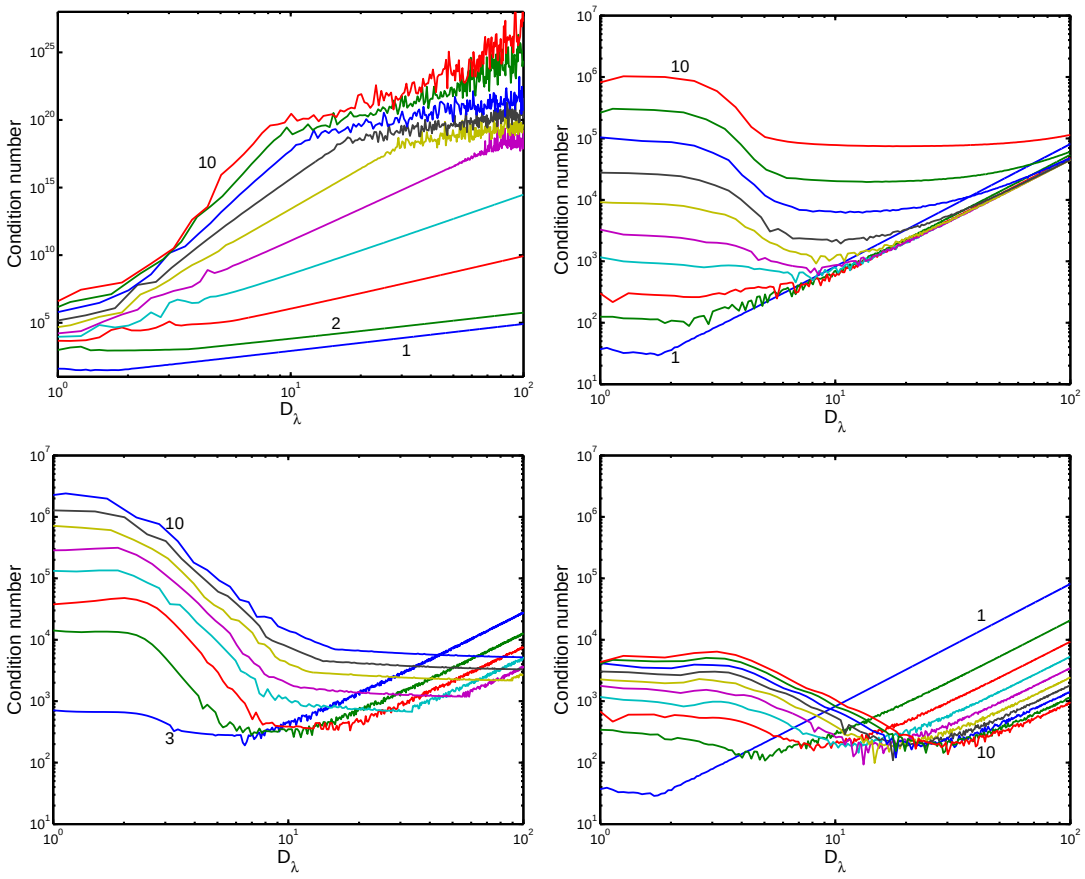

Figure 4.5: The condition number as a function of the number of non-zero entries ($\omega = 20, M = -0.6$). Top left: partition of unity, top right: Bernstein, bottom left: Hermite, and bottom right: Lobatto.

The condition number of the Bernstein method increases with polynomial order in the oscillatory region. In the asymptotic region the condition number is slightly reduced. The Hermite method demonstrates similar trends to the Bernstein method in the oscillatory region, although the condition numbers are lower. In the asymptotic region the Hermite method is better conditioned.

The Lobatto method produces the lowest condition numbers of all of the methods considered. In the oscillatory region the condition number increases with polynomial order, although it is still very low. In the asymptotic region the condition number actually decreases with increasing order (which is noteworthy, but is unique to the one dimensional case).

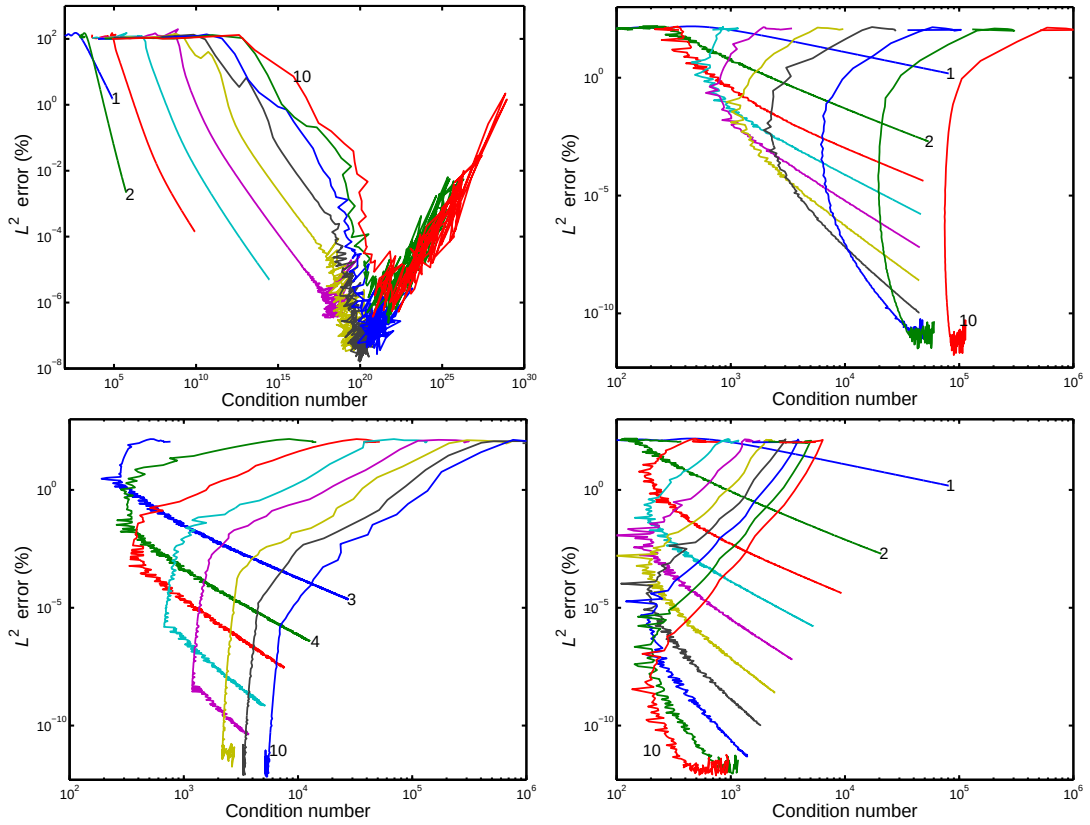

Figure 4.6: The L^2 error as a function of the condition number ($\omega = 20, M = -0.6$). Top left: partition of unity, top right: Bernstein, bottom left: Hermite, and bottom right: Lobatto.

These results show a marked difference between the methods. The partition of unity method is ill-conditioned, and even though the error convergences of the Bernstein and Lobatto methods are identical, the Lobatto method is better conditioned. It is interesting to compare the Bernstein and Lobatto results; in Section 4.2.1.2 we showed the coefficient matrices of the shape functions, (4.2) and (4.3), respectively. The sample Bernstein coefficient matrix (4.2) has a condition number of 7.7, while the Lobatto has a number of 2.5. Also, we note purely out of interest that the Bernstein matrix has real eigenvalues and eigenvectors, whereas the Lobatto values and vectors are complex.

In conclusion, the Lobatto method provides the lowest condition numbers. Similar results are presented in [32, 154, 163]. We note that changing the measure of cost from the degrees of freedom to the number of non zero entries does not change these observations.

4.2.1.4 Error Against Condition Number

For our final comparison we present the error as a function of the condition number of the sparse matrix. The comparison is given in Figure 4.6.

The partition of unity method results demonstrate the ill-conditioning of the functions. Note the scale is different to the other scales used in the figure. We see that as the condition number increases the error decreases - except at higher orders where the error begins to increase with condition number.

The condition number of the Bernstein method increases with polynomial order, and the error decreases with increasing condition number. For the highest orders the condition number is nearly constant below an error level of 1 %. The Hermite method has a high error level for a high condition number, however as the condition number decreases the error decreases.

The condition number of the Lobatto method decreases with increasing polynomial order. The best system conditioning is obtained using this method.

4.2.2 Engineering Accuracy Analysis

In this section, we use an engineering approach to identify the method with the lowest condition number and the lowest number of non-zero entries needed to solve the test case to within an accuracy of 1 %.

For these results an upstream flow is used ($M = -0.6$), and three frequencies are considered: $\omega = 1$, 20, and 40. The number of elements in the 1D domain is gradually increased, and the L^2 error of the numerical solution is successively calculated. When the error is equal to or below 1 % the condition number and number of non-zero entries for the corresponding global matrix are recorded. This process is repeated for all polynomial orders, *i.e.* from 1 to 10 (except in the case where Hermite functions are used, then the polynomial order ranges from 3 to 10). The results are presented in Figure 4.7. Note that no data is given for the case in which the frequency is 40 and the linear shape functions are used, this is due to the excessive computational effort required to obtain such data.

We shall first consider the condition numbers of the global matrices. It can be seen that the condition number of the polynomial partition of unity matrices increases rapidly with both polynomial order and frequency. For the highest order, and highest

frequency, the condition number is in excess of 10^{20}. The global matrix constructed using these functions is highly ill-conditioned. The matrices calculated using the Bernstein and Hermite functions are better conditioned, but the conditioning still increases with polynomial order and frequency. The Lobatto functions produce the best conditioned matrices. The condition number does not markedly increase with order, that is above order 1, but does still depend on frequency.

If we now consider the number of non-zero entries in the global matrix, we see that the system constructed using the partition of unity functions is the most expensive to store. The number of non-zero entries of the Bernstein and Lobatto matrices are identical. When considering the global trend of the Bernstein, Hermite and Lobatto data it can be seen that they provide approximately the same efficiency, that is in terms of matrix storage requirements.

4.2.3 Summary of One-Dimensional Analysis

From the analysis of the convergence and conditioning properties we can see that the partition of unity method is the most inefficient, and that it produces matrices that are highly ill-conditioned. The remaining methods converge like $O\left(D_\lambda^{-(P+1)}\right)$, and they do not suffer from conditioning problems. The Hermite method appears to be the most efficient, while the Lobatto method has the best conditioning.

The engineering accuracy analysis has confirmed these observations, but has also shown that the efficiencies of the Bernstein, Hermite and Lobatto functions are very similar.

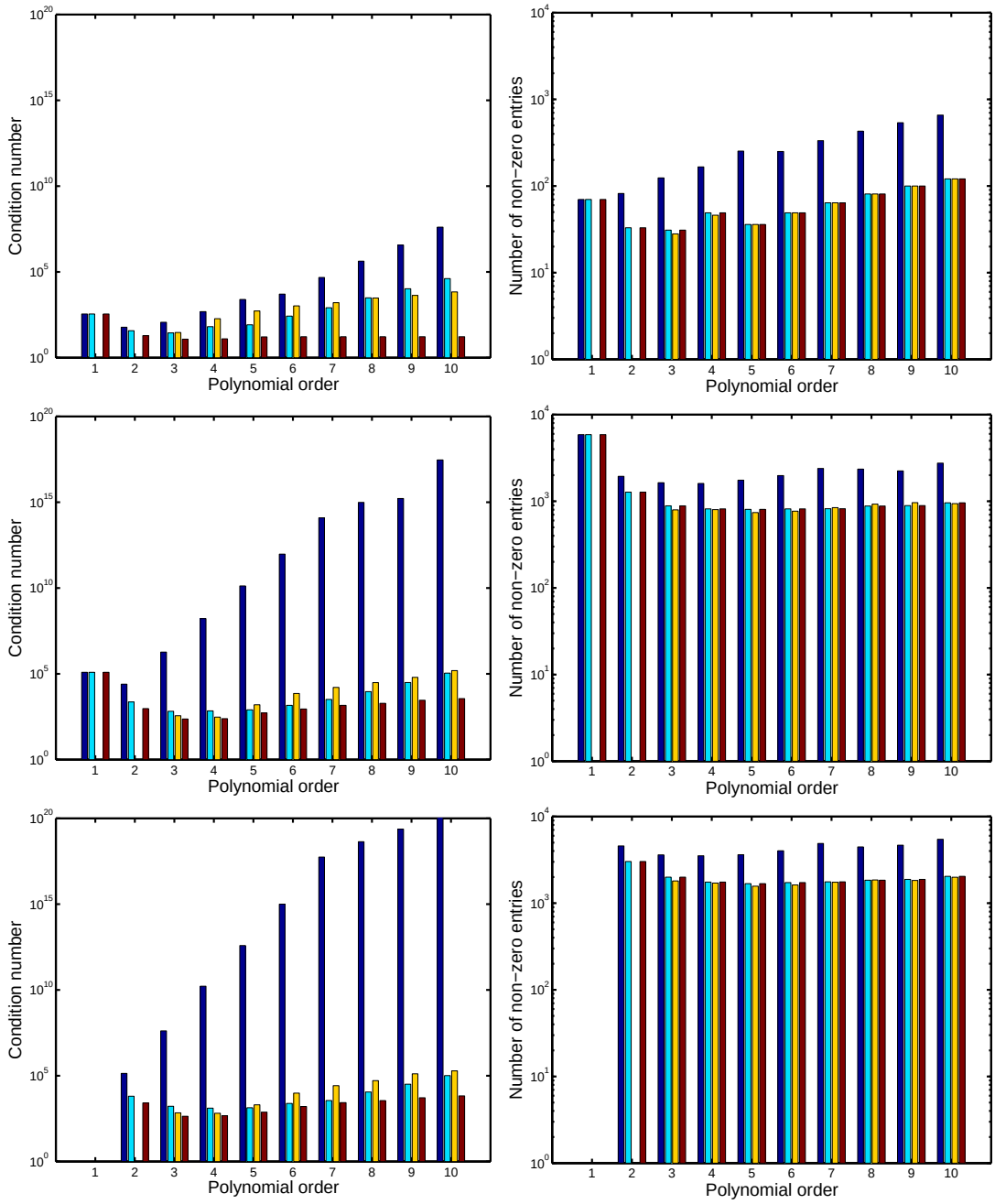

Figure 4.7: The number of non-zero entries required to reach 1% error (for $M = -0.6$), and the corresponding condition number. For each order, the data is presented from left to right as follows: polynomial partition of unity, Bernstein, Hermite and Lobatto. Top row: $k = 1$, middle row: $k = 20$, and bottom row: $k = 40$.

4.3 Two-Dimensional Analysis

In this section, we verify that the conclusions made in the one-dimensional analysis extend to the two-dimensional case. The test case is solved using quadrilateral and triangular elements. The quadrilateral element mesh is structured, which provides an illustration of the aliasing error. For the analyses which follow, both downstream flow and upstream flow cases are considered. The downstream data demonstrates the aliasing affect, but is provided mostly for the sake of interest. The upstream case must generally be accounted for when designing finite element models of aeroacoustic problems, due to the shorter wavelengths that are present. Selection of the preferred method for further development will depend on the upstream analysis. Examples of the meshes used are given in Figure 4.8.

The L^2 error, condition number, and number of non-zero entries are used as measures of performance. For the data that follows only the cubic order ($P = 3$) has been analysed, the reason being that only this order of the Hermite shape functions is available in 2D. This section will be concluded with the identification of the method chosen for further development.

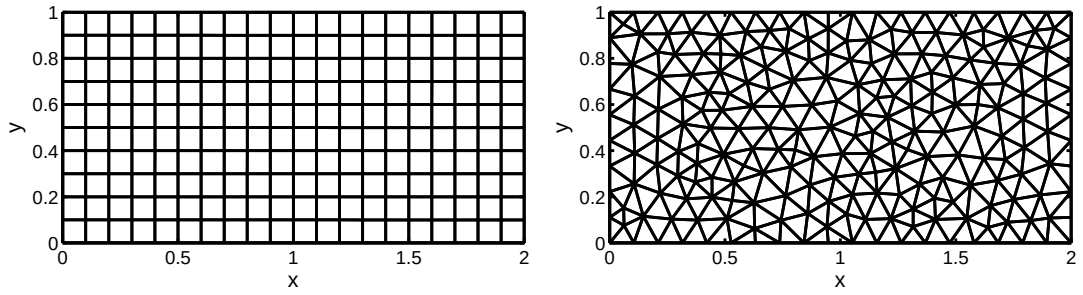

Figure 4.8: Examples of meshes used for the two dimensional analysis: $h = 0.1$. Left: Structured quadrilateral mesh. Right: unstructured triangular mesh.

4.3.1 Downstream Flow Case

To generate the data presented here the quadrilateral and triangular meshes given in Figure 4.8 are used. To demonstrate the aliasing effect, and the behaviour of the methods when subjected to a downstream flow ($M = 0.6$), the frequency of interest is gradually varied from $\omega = 7$ to 40. The results are presented in Figure 4.9.

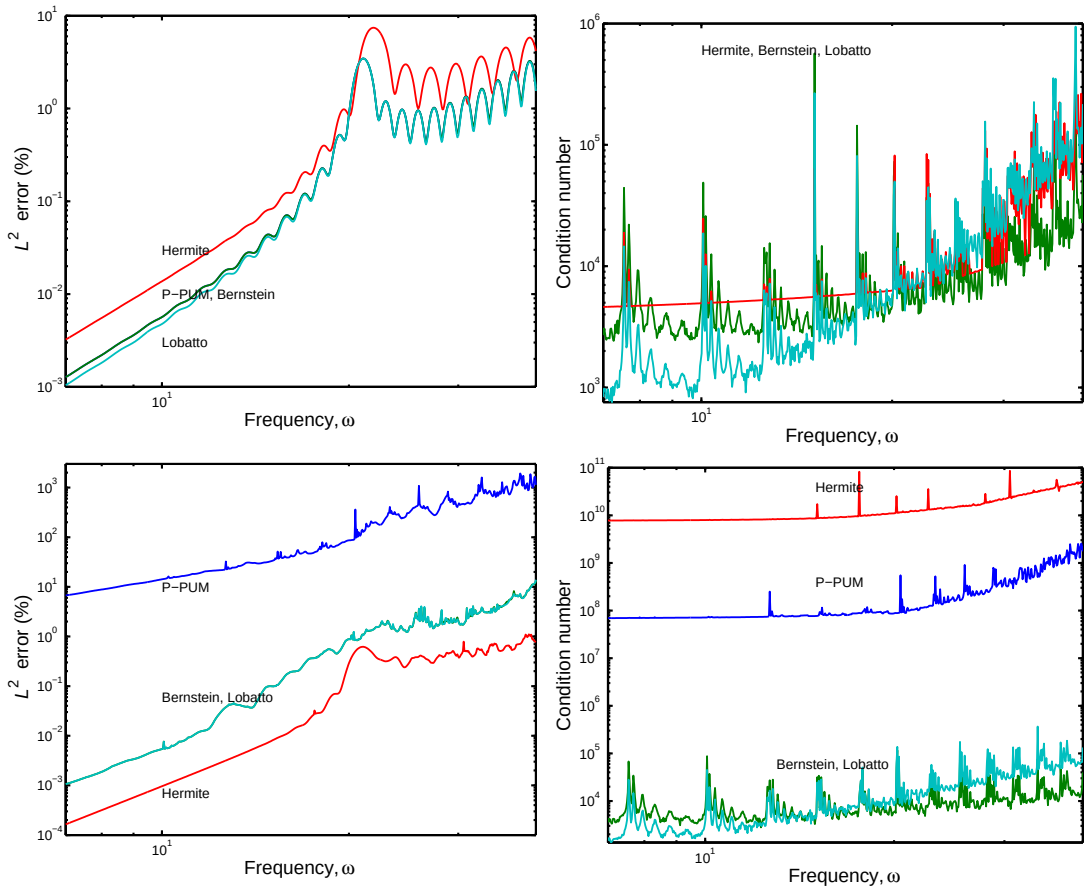

Figure 4.9: Convergence and conditioning properties of the methods, for the downstream flow case: $M = 0.6$, $h = 0.1$, $c_0 = 1$, $\rho_0 = 1$. Top: quadrilateral elements. Bottom: triangular elements.

4.3.1.1 Quadrilateral Elements

It can be seen that the convergence plots exhibit peaks. The peaks correspond to internal numerical resonances within the elements. This is the aliasing error which was introduced in Section 4.1.2.

In the asymptotic region the L^2 error of the methods converges like $O\left(\omega^{P+1}\right)$. The Hermite method returns the highest levels of error, the polynomial partition of unity and Bernstein methods give identical error levels, and the Lobatto method provides the lowest error levels.

The condition number of the polynomial partition of unity matrix is highest, as

expected from the 1D observations (see Section 4.2.3). For clarity, the condition number of the polynomial partition of unity method is not included here as it has a level of 10^{20}. We note that, when using a structured mesh the linear dependency issue reported in Section 3.3.3 is not remedied by the removal of the enrichment functions at the boundary. The condition numbers of the remaining methods are quite similar, although asymptotically the Bernstein method produces the best conditioned systems.

4.3.1.2 Triangular Elements

If we now consider the convergence plots obtained using the triangular mesh we see that the error peaks are not as pronounced as they were in the quadrilateral data. This is due to the non-uniformity of the unstructured triangular mesh, which tends to broaden and flatten the peaks. However, the effect of the aliasing error is still observable.

The L^2 error of the partition of unity method behaves like a linear polynomial system. The Bernstein and Lobatto systems produce identical error levels, but the Hermite system incurs the lowest level of error.

The condition number of the Hermite matrix is the highest, closely followed by that of the polynomial partition of unity matrix. The condition numbers of the Bernstein and Lobatto matrices are similar, but in the asymptotic region the Lobatto matrix is the best conditioned.

4.3.2 Upstream Flow Case

The convergence and conditioning plots for the upstream case (where $M = -0.6$) are given in Figure 4.10. To obtain these plots the frequency is kept constant ($\omega = 20$) and the number of quadrilateral and triangular elements is gradually increased. Dashed lines are included on the plots to indicate the orders of convergence of the various methods investigated. Note that in the upstream case there is no aliasing error [28], as the waves are well resolved in all directions (which is not true for the downstream case).

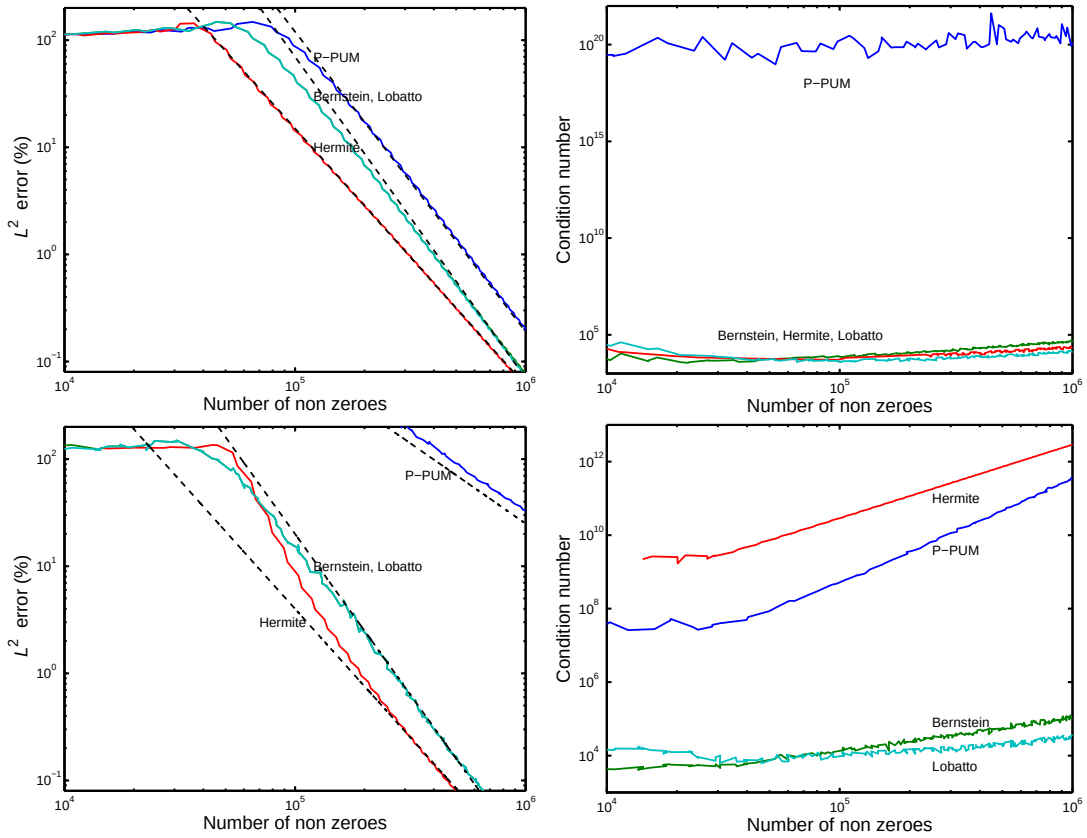

Figure 4.10: Convergence and conditioning properties of the third order functions, for the upstream flow case: $M = -0.6$, $\omega = 20$, $c_0 = 1$, $\rho_0 = 1$. Top: quadrilateral elements. Bottom: triangular elements.

4.3.2.1 Quadrilateral Elements

From the error convergence plots we see that the partition of unity system is the most expensive to store. The Bernstein and Lobatto systems return identical error levels as a function of the number of non-zero entries. For the range of numbers of elements considered, the Hermite system is the most efficient, at least in terms of matrix storage requirements.

We see that the Bernstein and Lobatto solutions converge like $O\left(N_{nz}^{-3}\right)$, where N_{nz} is the number of non zero entries. The partition of unity error converges like $O\left(N_{nz}^{-2.8}\right)$, while the Hermite error converges like $O\left(N_{nz}^{-2.4}\right)$. As expected, the partition of unity matrix is severely ill-conditioned, whereas, in the asymptotic region, the Lobatto matrix is the best conditioned.

4.3.2.2 Triangular Elements

The error of the partition of unity system converges like $O\left(N_{nz}^{-1.5}\right)$. The Bernstein and Lobatto error convergence plots are identical and converge like $O\left(N_{nz}^{-3}\right)$. For the range of non-zero entries considered, the Hermite system is the most efficient, in terms of storage requirements. Asymptotically, it converges like $O\left(N_{nz}^{-2.4}\right)$.

The Hermite matrix has the highest condition number, followed by the partition of unity matrix. In the asymptotic region the Lobatto matrix has the lowest condition number.

4.3.3 Summary of Two-Dimensional Analysis

Based on the upstream flow case analysis, it can be concluded that for the quadrilateral elements the polynomial partition of unity method produces systems which are inefficient and ill-conditioned. For triangular elements the system is better conditioned (perhaps due to the unstructured nature of the mesh, which reduces the effect of the linear dependency issue) but it does not converge as expected. These shape functions will not be considered for further development.

The Hermite elements appear to be the most efficient in terms of matrix storage, but they have a high condition number when triangular elements are used. Furthermore, this analysis has considered only one polynomial order ($P = 3$), due to the limited availability of higher order triangular Hermite functions, and without linear or quadratic functions any adaptive scheme based on these functions may be needlessly expensive when accurate geometry description is required. These functions, despite their elegance, will not be considered any further.

In the upstream case, the Bernstein and Lobatto systems produce identical error levels. However, the Lobatto elements are better conditioned. (Note that this differs from the findings of Petersen [121], however, they use an iterative solver and do not include flow.) The Lobatto functions are hierarchic, which enables efficient system assembly when using an adaptive order process to set-up a model, and there are readily available functions for all commonly used element types. The Lobatto functions have been chosen for further development.

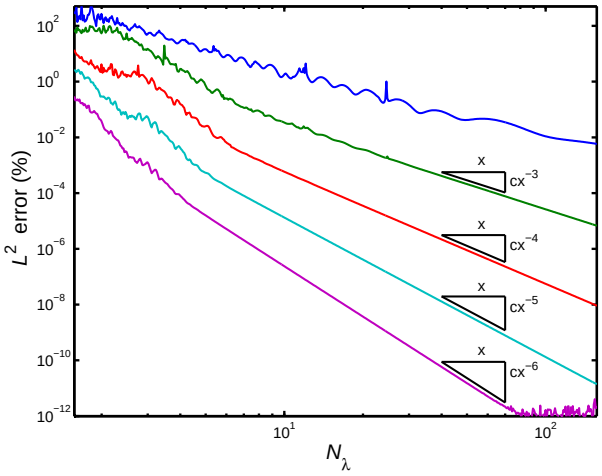

Figure 4.11: The L^2 error as a function of the number of elements per wavelength (flow effect not included) on an unstructured triangular mesh: $M = 0.6$, $h = 0.1$. The lowest polynomial order can be found at the top of the graph, and the highest order at the bottom.

4.4 Analysis of Lobatto Shape Functions

Firstly, we present a more detailed two-dimensional analysis, considering both downstream and upstream flows, to demonstrate the behaviour of the method as the polynomial order is varied. A three-dimensional analysis is then presented. For this we consider the computational resources required by the Lobatto system. This has been made possible through the implementation (by the sponsoring company, LMS International) of the Lobatto method into a commercial code, which provides more information about the system being solved than is available when using Matlab.

4.4.1 Two-Dimensional Analysis

The length of the test case geometry (see Figure 4.1) is extended ($L = 3$) to ensure that pollution error is present in the problem. The geometry is discretised using triangular elements (but note that the observations presented here are also found when quadrilateral elements are used). Both downstream flow ($M = 0.6$) and upstream flow ($M = -0.6$) cases are considered. The element size is kept constant ($h = 0.1$), and the frequency is varied from $\omega = 0.4$ to 40. The polynomial order is varied from 1 to 5; higher order data is not presented due to the unavailability of sufficient resources to calculate this data. The L^2 error as a function of the number of elements per wavelength is

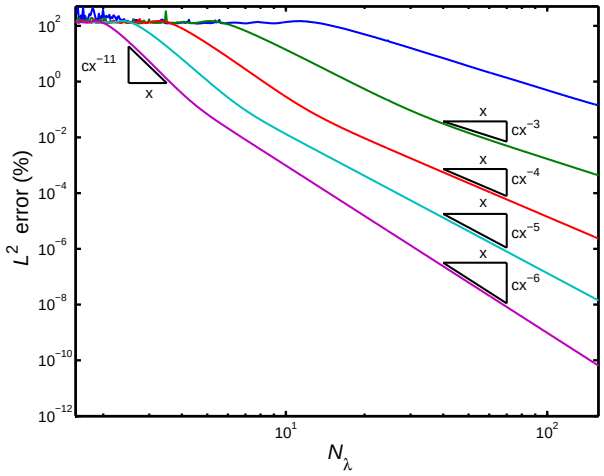

Figure 4.12: The L^2 error as a function of the number of elements per wavelength (flow effect not included) on an unstructured triangular mesh: $M = -0.6$, $h = 0.1$. The lowest polynomial order can be found at the top of the graph, and the highest order at the bottom.

given in Figure 4.11 for the downstream flow case, and in Figure 4.12 for the upstream flow case. Note that using the number of elements per wavelength, $N_\lambda = 2\pi/(k_0 h)$ is not an accurate measure of the actual cost of the method; it is only used as it lends itself easily to the demonstration of the system's behaviour.

In the downstream Flow Case the numerical solution converges as expected. In the low discretisation regime error peaks are noticeable. These are associated with internal resonances of the elements [28], *i.e.* the phenomenon termed aliasing error [108], as referred to in Section 4.1.2. In the high discretisation regime, for $P = 5$, the convergence is limited by the machine's precision. Reference triangles are included on the plot to indicate the order of convergence of the data. In the asymptotic region the method converges like $O\left(N_\lambda^{-(P+1)}\right)$.

In the upstream Flow Case the numerical solution converges as expected. However, in this case no aliasing peaks are present, this is because the shortest wavelength has been adequately resolved. Distinct regions in the convergence plots now become visible. For a low number of elements per wavelength an oscillatory region is observed. The transition region associated with the dispersion error, in which pollution effect dominates, appears as the number of elements per wavelength is increased. In this region the error converges like $O\left(N_\lambda^{-(2P+1)}\right)$. In the asymptotic region, which is associated with the interpolation error, the error converges like $O\left(N_\lambda^{-(P+1)}\right)$.

4.4.2 Performance of the Lobatto Method in Three Dimensions

In this section the test case and measures of cost used to assess the performance of the Lobatto functions in 3D are introduced. Performance results without any flow, and in the presence of an upstream flow, are presented. The computational cost of storing and factorising the global matrix as a function of polynomial order is investigated.

4.4.2.1 Test Case and Measures of Cost

A three-dimensional version of the test case (presented in Section 4.1.1) is used. The test case is a duct, which carries flow along the z-axis. The test case geometry is given in Figure 4.13. It is discretised using hexahedral and tetrahedral elements.

The Mach number is zero, in the case without any flow, and $M = -0.6$ in the upstream flow case. An acoustic plane wave is excited at the $z = 0$ plane; it propagates along the z-axis, and is acoustically terminated at the plane $z = 1$. Characteristic boundary conditions (see Section 2.4.3.1) are used to impose the incoming and outgoing waves. On the hard walls the gradient of the velocity potential is zero. The results presented here have been generated by holding the Helmholtz number constant ($kH = 50$), while the number of elements in the 3D domain is varied.

To assess the performance of the Lobatto method in three dimensions, an implementation of the method has been provided by LMS International. Their code provides information of the computational resources used when a problem is solved. Thus, the measures used here are: the L^2 error, the number of non-zero entries in the sparse matrix (this is directly related to the amount of memory needed to store the matrix), the memory needed to factorise the matrix, and the number of floating point operations (flops) used to factorise the matrix. The time needed to solve the linear system will also be presented, but only for the sake of interest as this is not a dependable measure of cost.

4.4.2.2 Performance Without Flow

At the time of writing, static condensation could not be applied to the solver with flow. As a demonstration of the effect of static condensation, we begin with an analysis of the performance without flow.

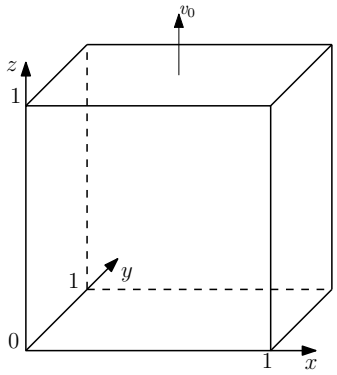

Figure 4.13: Geometry of the three-dimensional test case.

The polynomial order has been varied from 1 to 10, using both hexahedral element and tetrahedral element meshes. First, the error convergence of the numerical solution as a function of the memory required to factorise the matrix is presented, and then an analysis of the actual cost of storing and factorising the linear system is given. The presented data which follows has been obtained using a machine with 48 GB of memory, and 8 cores. Note that in this section (only) an impedance boundary condition ($\nabla\phi \cdot \boldsymbol{n} = \mathrm{i}\omega\rho_0/Z$ where $Z = \rho_0 c_0$) has been used at the duct exit.

1. Error vs. Factorisation Memory:

   The L^2 error as a function of the factorisation memory is given in Figure 4.14. A general observation is that the tetrahedral elements are more efficient than the hexahedral elements. Note that the linear order functions are too costly, in terms of time, to solve using all of the available resources. It can be seen that the static condensation reduces the computational cost, although this effect is more noticeable when using hexahedral elements. The reason for this is the greater number of bubble functions, for a fixed order, when using hexahedral elements instead of tetrahedra. As a demonstration of this, consider the formulae used to calculate the number of functions for a single element, given in Table 4.1.

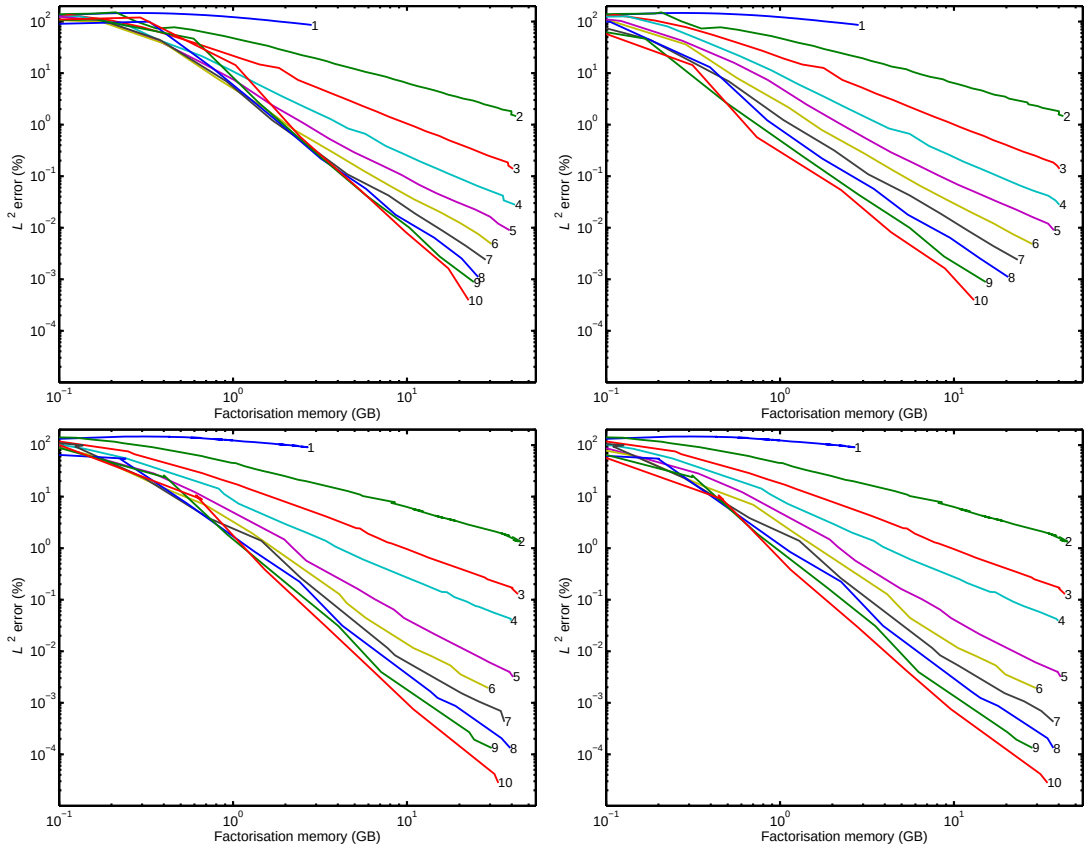

Figure 4.14: The L^2 error as a function of the amount of memory required to factorise the system ($kH = 50, M = 0$). The polynomial order is indicated by a corresponding number at the end of each data line. Top: hexahedral elements. Bottom: tetrahedral elements. Left: no static condensation. Right: static condensation applied.

Function	Hexahedral	Tetrahedral
Vertex	8	4
Edge	$12(P-1)$	$6(P-1)$
Face	$6(P-1)^2$	$2(P-1)(P-2)$
Bubble	$(P-1)^3$	$(P-1)(P-2)(P-3)/6$

Table 4.1: Number of Lobatto shape functions on a single element.

If the number of bubble functions per single element, and per polynomial order, is quantified (shown in Table 4.2), we see that the hexahedral elements always produce many more bubble functions than the tetrahedral elements.

Order	1	2	3	4	5	6	7	8	9	10
Hexahedral	0	1	8	27	64	125	216	343	512	729
Tetrahedral	0	0	0	1	4	10	20	35	56	84

Table 4.2: Number of bubble functions on a single element.

As an example of the computational saving offered by static condensation, consider the Hexahedral element convergence plots. Using polynomial order 10 without condensation requires 20 GB of memory to obtain an error level of 1×10^{-3} %, whereas using static condensation requires only 10 GB. We observe that the most efficient solution, for an error level of 1 % or less, is provided by the tetrahedral elements of polynomial order 10 with static condensation applied. For an error level of 1 % order 3 requires 9.6 GB of memory, while using order 10 requires 0.87 GB - this is an order of magnitude difference. From these results it is suggested that, once the problem geometry has been adequately described using small elements, the most efficient solutions are obtained when large tetrahedral elements with the highest available order are used inside the domain.

2. Analysis of Computational Resources:

   It has been shown that higher order systems require less factorisation memory. To investigate this observation we now compare the factorisation memory, the time to solve, and the number of floating point operations used for factorisation, to the size of the sparse matrix (quantified by its number of non-zero entries). These comparisons are given in Figure 4.15.

   It can be seen that for a fixed number of non-zero entries the factorisation memory needed reduces with increasing polynomial order. For example, when the number of non-zero entries in the sparse matrix is 1×10^6 a solution obtained using linear elements requires 1.8 GB, but using functions of polynomial order 10 requires only 72 MB. The same trend is observed in the time taken to solve the linear system. For the same number of non-zero entries, order 1 takes $17s$, while order 10 takes $0.69s$. Thus, we see that higher order functions are indeed more efficient, with the caveat that time is not a completely reliable measure of cost. The number of floating point operations carried out to factorise the matrix have been obtained

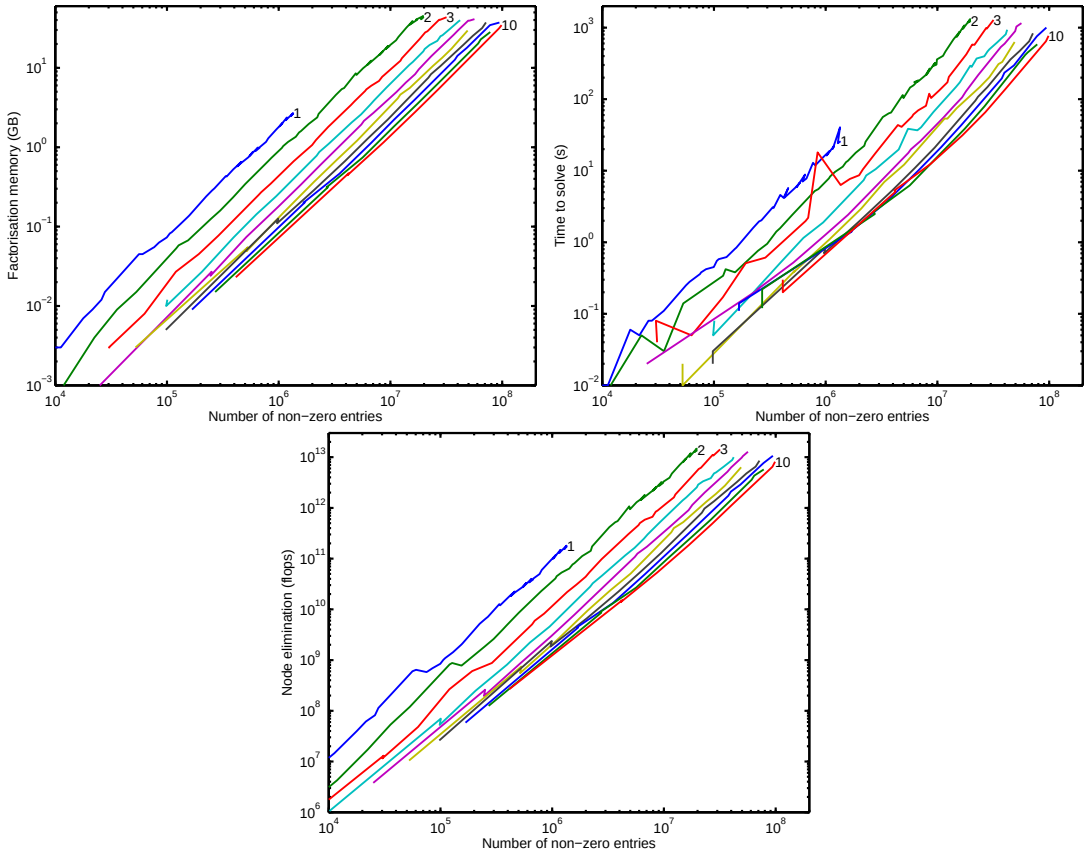

Figure 4.15: Measures of the computational cost as a function of the number of non-zero entries ($kH = 50, M = 0$). Data obtained using tetrahedral elements with static condensation. The trend of the polynomial orders is indicated.

from the linear system solver MUMPS [7, 8]. Once again the same trend in the data is observed; a lower number of floating point operations is required to factorise a matrix with a fixed number of non-zero entries when higher order polynomials are used. This data suggests that higher order matrices have a reduced number of fill-in entries (which are generated during the factorisation process). It is often remarked that higher order matrices have a greater bandwidth than lower order ones, and it is thus expected that they will be as, or even more, expensive to solve than standard finite elements. However, these results show that this is definitely not the case when hierarchic Lobatto shape functions are used. Evidence of this is shown in [134], Figure 10, although the significance of this result is not discussed in the referenced text.

4.4.2.3 Performance With Flow

The test case (with characteristic boundary conditions) has been solved using tetrahedral element meshes on a cluster computer with four nodes (2 of 32 GB, and 2 of 16 GB). An upstream flow with a Mach number of $M = -0.6$ is considered, and the polynomial order is varied from 1 to 9 (at the time of writing polynomial order 10 was not available). Note that static condensation has not been applied in this instance. The L^2 error, factorisation memory required and time taken to solve as a function of the number of non-zero entries are plotted in Figure 4.16.

For a fixed error level, polynomial order 9 gives the most efficient solution. For an error level of 1 %, 6.4 GB of memory are needed to factorise the matrix constructed using functions of order 3, while using order 9 requires 550 MB. As was shown in the case without flow, for a fixed number of non-zero entries the amount of memory used to factorise the matrix is reduced when the polynomial order is increased. For example, when the number of non-zero entries in the sparse matrix is 2×10^6 a solution obtained using linear elements requires 910 MB, whereas using functions of polynomial order 9 requires 32 MB. The same trend is observed in the time taken to solve the linear system. For the same number of non-zero entries, order 1 takes $46s$, while order 9 takes $9.8 \times 10^{-2}s$. The observations made here are the same as those made for the case without flow. The highest order provides the most efficient solution. This observation is confirmed by the comparisons of the factorisation memory and time to solve to the number of non-zero entries on the sparse matrix. Higher order matrices require increasingly less factorisation, and are thus solved faster than lower order ones.

Lastly, the effect of the mean flow on the resources required is considered. In Figure 4.17 it can be seen that the inclusion of flow increases the number of non-zero entries in the global matrix. This is expected, as in the no flow case the matrix being solved is complex symmetric, but when flow is present the matrix is complex unsymmetric. Thus in the no flow case only half of the matrix needs to be stored - the matrix with flow is twice as costly to store. Surprisingly, when flow is present the amount of factorisation memory required is reduced. The algorithms used by MUMPS to solve symmetric and unsymmetric matrices are different, but it is still expected that the matrix with flow will be more costly to solve. This is a strange result.

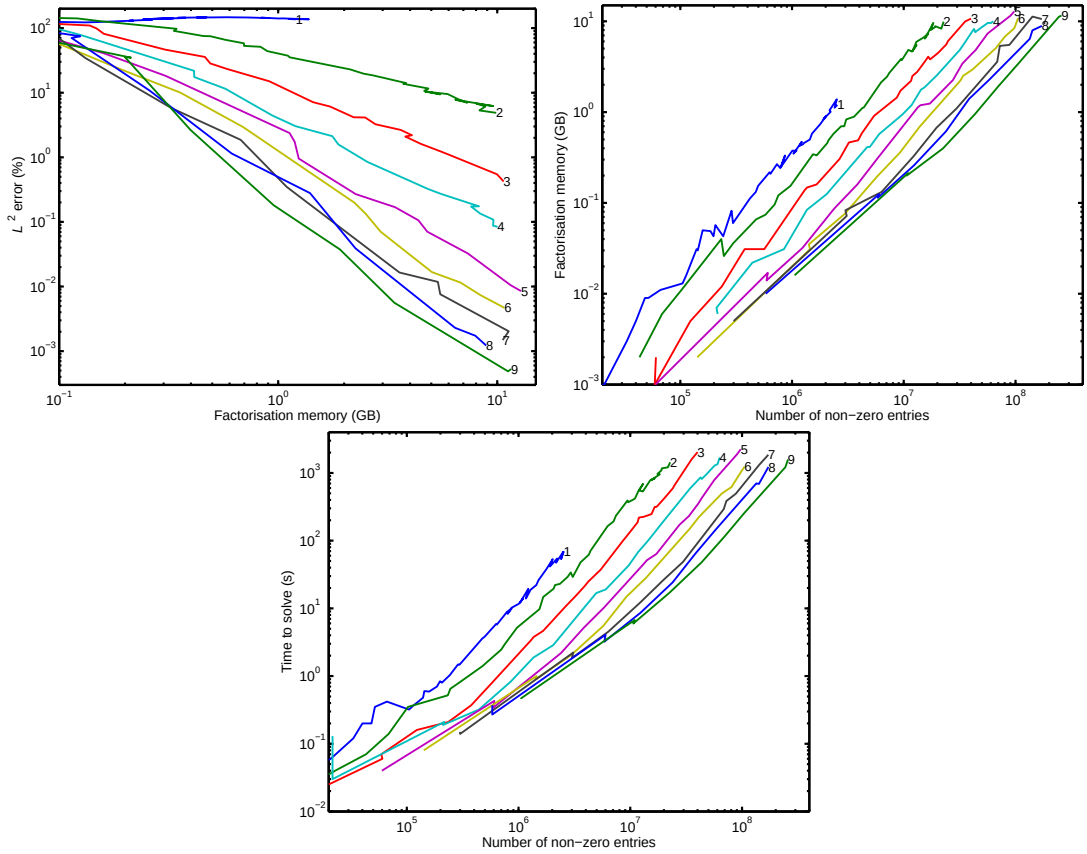

Figure 4.16: Error and measures of computational cost when an upstream flow is present ($kH = 50, M = -0.6$).

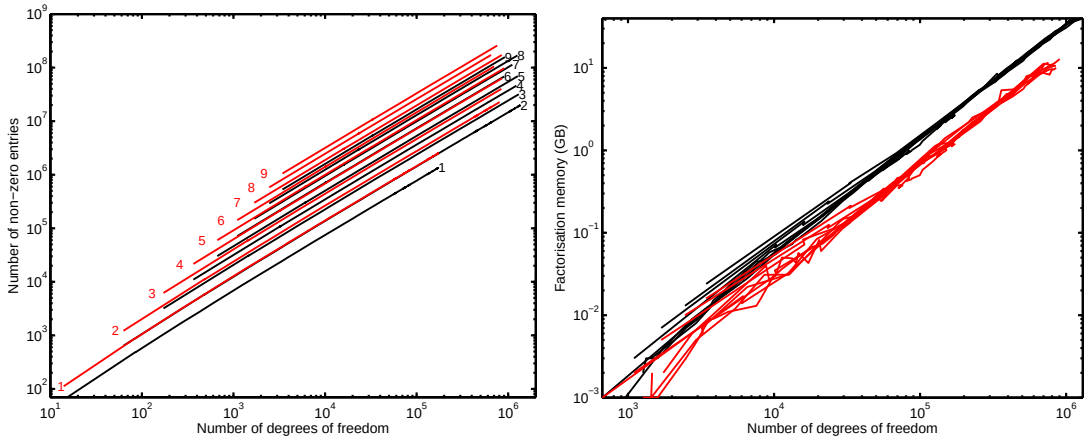

Figure 4.17: Comparison of storage (left) and solving memory (right) requirements for $kH = 50$: without flow ($M = 0$) is given in black, and with flow ($M = -0.6$) is given in red. Note that the figure on the right includes all orders, from 1 to 9.

4.5 Summary of Conclusions

The polynomial partition of unity method is inefficient and ill-conditioned. The third order triangular functions exhibit linear order convergence. The Hermite method is as efficient as the Bernstein and Lobatto methods, in 1D, and performs well in 2D for polynomial order 3. However, it is not as well conditioned as the Lobatto method, and variable order functions are not available. Furthermore, it may be of limited use for adaptive methods, as there are no linear or quadratic functions. The Bernstein method is as efficient as the Lobatto method, but it is not as well conditioned. Also, it is not hierarchic.

The Lobatto method is efficient and well conditioned. It is hierarchic, which can enable faster matrix assembly, and facilitates faster frequency sweeps. Also, shape functions are available for all commonly used element types. In three dimensions it has been found that matrices constructed using higher-order Lobatto functions require less factorisation memory than lower-order ones, due to a reduced number of fill-in entries. It is suggested that once the boundaries of a problem geometry have been properly described, large elements with high order functions should be used to obtain the most efficient solutions. In the next chapter we will focus on the development of an adaptive order version of the method, which makes use of the element size, and the flow speed and input frequency of a problem, to determine the most efficient order for a specific element.

5

Development of an Adaptive Order Scheme

To take full advantage of the efficiency of the higher order polynomials, an adaptive order scheme is required. The scheme should analyse the finite element model and choose the optimal polynomial order for each element in the mesh, based on the input frequency of the problem, the size of each element, and the medium properties on each element. In this work, an *a priori* error estimation is used to find the optimal polynomial order. Existing *a priori* estimators are first introduced and assessed. A new estimator is then proposed, and used to solve problems on non-uniform meshes, in 2D and 3D, for a wide range of frequencies.

5.1 Test Case and Measures of Error

The test case used in this chapter is identical to the test case used in Chapter 4. The 2D and 3D versions are shown in Figure 5.1. The test case is a duct that carries a uniform flow with velocity v_0. An acoustic plane wave is excited at one end of the duct, and is anechoically terminated at the opposite end. Equation (3.1) is solved on the computational domain, and characteristic boundary conditions (see Section 2.4.3.1) are used to impose the incoming and outgoing waves. This simple test case allows us to accurately quantify the behaviour of the proposed adaptive order scheme.

To measure the error incurred by the adaptive order scheme we will use the H^1

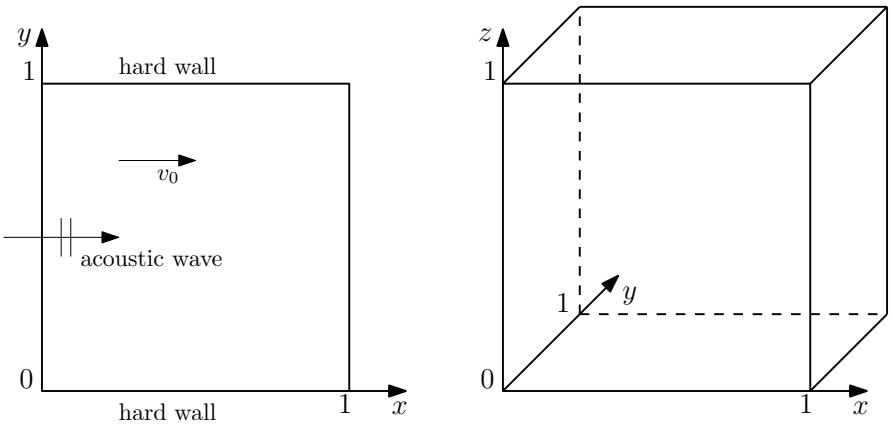

Figure 5.1: Test case geometries. Left: unit square for two-dimensional tests, right: unit cube for three-dimensional tests.

error:

$$E_{H^1} = 100\,\frac{\|\phi_a - \phi_h\|_{H^1}}{\|\phi_a\|_{H^1}}\,, \qquad \text{where} \qquad \|f\|_{H^1} = \left(\int_\Omega |f|^2 + \frac{|\nabla f|^2}{k^2}\,\mathrm{d}\Omega\right)^{1/2}, \quad (5.1)$$

and the L^2 error:

$$E_{L^2} = 100\,\frac{\|\phi_a - \phi_h\|_{L^2}}{\|\phi_a\|_{L^2}}\,, \qquad \text{where} \qquad \|f\|_{L^2} = \left(\int_\Omega |f|^2\,\mathrm{d}\Omega\right)^{1/2}. \quad (5.2)$$

The effective wavenumber, k, includes the effect of flow (which in this work is either upstream or downstream). For a plane wave in uniform flow, the k^2 coefficient in the H^1 norm ensures that the norm is proportional to the acoustic energy.

5.2 Error Estimation

Estimation of the error, incurred by the finite element model, may be carried out using either *a posteriori* or *a priori* methods. *A posteriori* methods estimate the error based on full solutions of the method, whereas *a priori* methods attempt to predict the error before solving the full problem. In this section, we briefly discuss *a posteriori* methods, but will focus mainly on *a priori* methods.

Error estimation of the finite element solution has a history which stretches back at least 35 years. Babuška & Rheinboldt [17] were the first to introduce *a posteriori* estimates. They provided asymptotic estimates for second order problems in one dimension. Ainsworth & Oden [6] presented an error estimator based on an element

residual method, and used it in the context of higher order methods. They found the residuals on single elements, and used them to approximate the actual error of the full solution. A different approach was used by Zienkiewicz & Zhu [162]; they presented a super-convergent patch recovery method. This method makes use of the behaviour of the gradient of the solution, which in general is discontinuous at interelement boundaries. The solution gradient is post-processed to generate a smooth gradient, and the post-processed gradient is compared to the actual gradient. Whether or not to refine an element is based on this comparison.

The convergence of the finite element method exhibits asymptotic and pre-asymptotic ranges. In the pre-asymptotic range, pollution error is more significant than interpolation error. Deraemaeker *et al.* [44] found that local estimators do not account for pollution error, and thus always underestimate the global error. Furthermore, according to Ainsworth [4], *a posteriori* estimators fail in the presence of pollution error, and thus *a posteriori* estimation is only reliable in the asymptotic range [88]. However, when designing a mesh it is common to base the design on the behaviour of the method in the pre-asymptotic range, as the asymptotic range is generally computationally too expensive to solve.

In general, *a posteriori* methods are computationally expensive, as the full problem must be solved before an error estimate can be obtained, and they are only reliable in the asymptotic range. In this work, only *a priori* estimators will be considered.

According to a review of estimation methods by Gräsch & Bathe [67], practical estimation techniques do not provide error bounds which are mathematically proven. They go on to provide a list of requirements of an error estimator, which are reproduced here for later analysis of the proposed estimation method. An error estimator should:

1. be accurate in the sense that the predicted error is close to the actual error;
2. be asymptotically correct;
3. yield sharp upper and lower bounds of the actual error;
4. be simple and inexpensive;
5. be robust, *i.e.* have a wide range of applications.

5.2.1 Existing *A Priori* Estimators

A priori estimators aim to predict the global error of a system based on parameters of the model. Parameters may include: domain size, element size, polynomial order, frequency of interest, and properties of the medium. Here we introduce two existing estimators, and evaluate their performance when used to solve the test case.

Ihlenburg & Babuška [87] considered higher order finite elements for the solution of Helmholtz problems at high wavenumbers. They introduced the following *a priori* error estimate:

$$E \leq C_1 \left(\frac{kh}{2P}\right)^P + C_2 k \left(\frac{kh}{2P}\right)^{2P}, \tag{5.3}$$

where C_1 and C_2 are constants. Both constants may depend weakly on the polynomial order, and the constant C_2 may also depend on the length of the domain. The first term of inequality (5.3) represents the interpolation error, while the second term represents the pollution error (thus the dependence on domain length). This estimate is based on the H^1_s semi-norm: $\|f\|_{H^1_s} = \left(\int_\Omega |\nabla f|^2 \, \mathrm{d}\Omega\right)^{1/2}$.

Ainsworth [5] designed an *a priori* guideline for choosing the order of the shape functions on an element based on the element size and the input frequency of the problem to be solved. The guideline is:

$$2P + 1 > kh + C_3 (kh)^{1/3}, \tag{5.4}$$

where C_3 is a constant, which according to Ainsworth may in practice be unity. This guideline aims to ensure that the dispersion error is negligible in the final solution.

5.2.1.1 Predicting the Optimal Order of an Element

It is possible to write (5.3) and (5.4) in terms of the polynomial order, and thus to predict the optimal polynomial order for a given element, based on the element size and input frequency, but this involves problem dependent, empirical constants.

An expression for the optimal polynomial order of an element, P_{opt}, can be derived from (5.3) by noting that the constants are weak functions of P, and thus by assuming that the dependence on P can be neglected. We can then write:

$$P_{\mathrm{opt}} = \frac{1}{2} \exp\left\{ W_0 \left[\frac{2}{hk} \left(2\mathrm{i}\pi + \log \frac{C_1 + \sqrt{C_1^2 + 4C_2 E_\tau k}}{2E_\tau} \right) \right] \right\} hk, \tag{5.5}$$

where W_0 is the Lambert function (defined by $W(z)\mathrm{e}^{W(z)} = z\,, z \in \mathbb{C}$, the subscript 0 indicates that the principal branch of the solution is to be used) and E_τ is the desired error. It may be possible to include the dependence of the constants on the polynomial order, and make use of a non-linear solution method to obtain a numerical solution, but this path has not been taken here. Inequality (5.4) can also be rewritten in terms of the polynomial order to give the optimal order:

$$P_{\text{opt}} = \frac{kh + C_3(kh)^{1/3} - 1}{2} + E_\tau\,. \tag{5.6}$$

Using a given element size and frequency, the optimal order to maintain an error level of $E_\tau = 1\%$ is predicted using (5.5) and (5.6). The optimal orders for a range of element sizes and frequencies are plotted onto the one-dimensional H^1 error convergence plots, given in Figures 5.2 and 5.3, respectively. The values of constants C_n have been adjusted empirically to tune the estimators to give the best frequency response. Good choices for the constants, at least for the test case considered, are: $C_1 = 33$, $C_1 = 6.28$ and $C_3 = 4.45$. We observe that the error levels oscillate around 1% when using the H^1_s estimator (5.3), and around 0.1% when using Ainsworth's guideline (5.4).

5.2.1.2 Performances of the Existing Estimators

As an investigation into the performance of the existing estimators, equations (5.5) and (5.6) have been used to predict the optimal order of each element in an unstructured two-dimensional mesh. The constants, C_n, are tuned to give an accuracy of 1 %. The mesh was composed of triangular elements with an element size of 0.15. The input frequency was varied from $\omega = 1$ to 50. The convected wave equation (3.1), with characteristic boundary conditions, was solved on the domain, and the H^1 and L^2 errors of the resulting solutions were calculated. Plots of the errors of the resulting solutions are given in Figure 5.4. It can be seen that both estimators are unsatisfactory as they provide errors that are much lower than the desired level. Adaptivity schemes based on these estimators will require empirical constants, and will be problem dependent. They will be too conservative, and will thus introduce unnecessary computational expense. Furthermore, the desired level of error cannot be easily changed, and upper and lower error bounds for the actual error cannot be established.

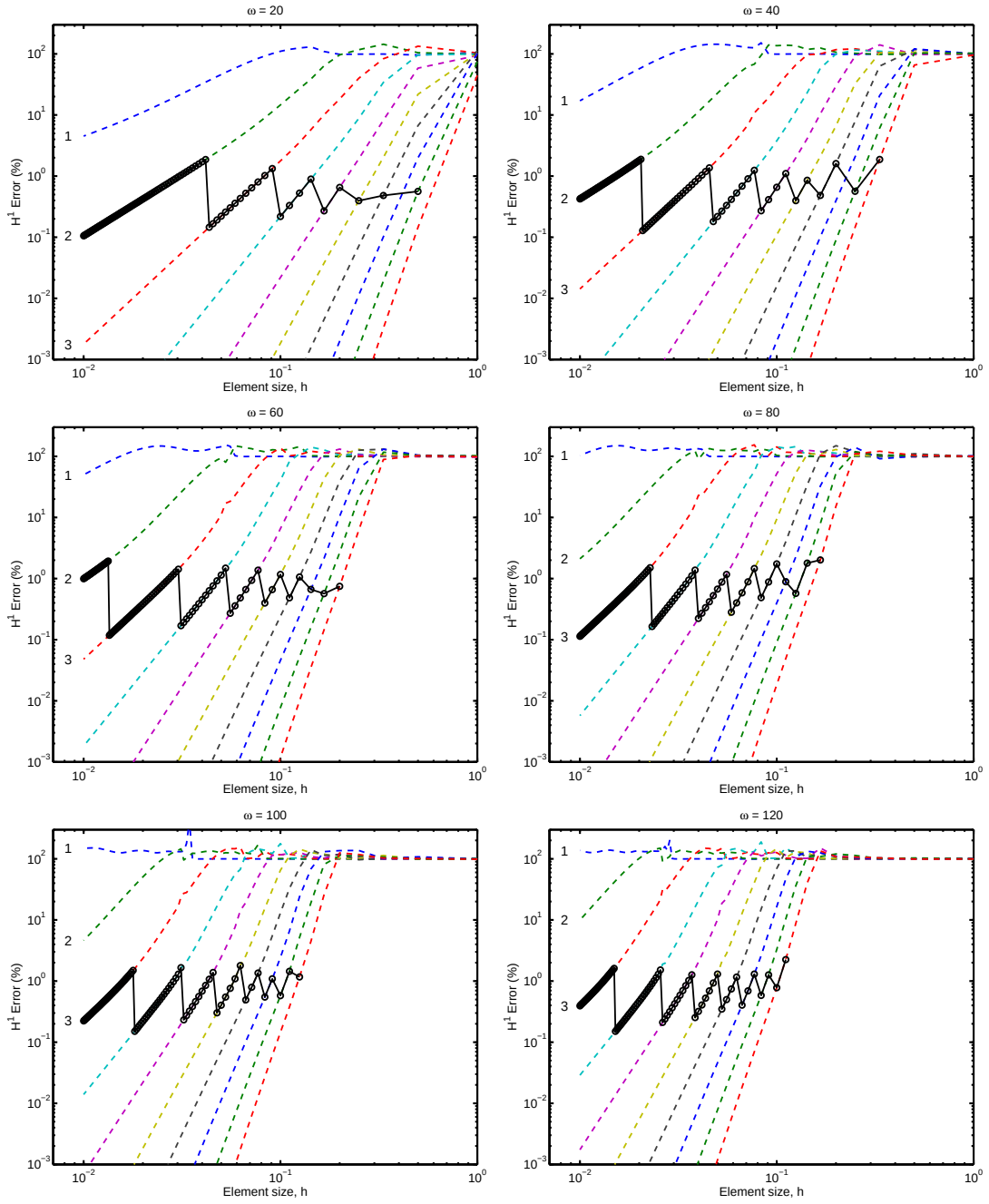

Figure 5.2: The H^1 error as a function of the element size (dashed lines). The predicted optimal order to maintain an accuracy of 1% obtained from the H^1_s error estimator (5.3) constants is shown using the marked solid line.

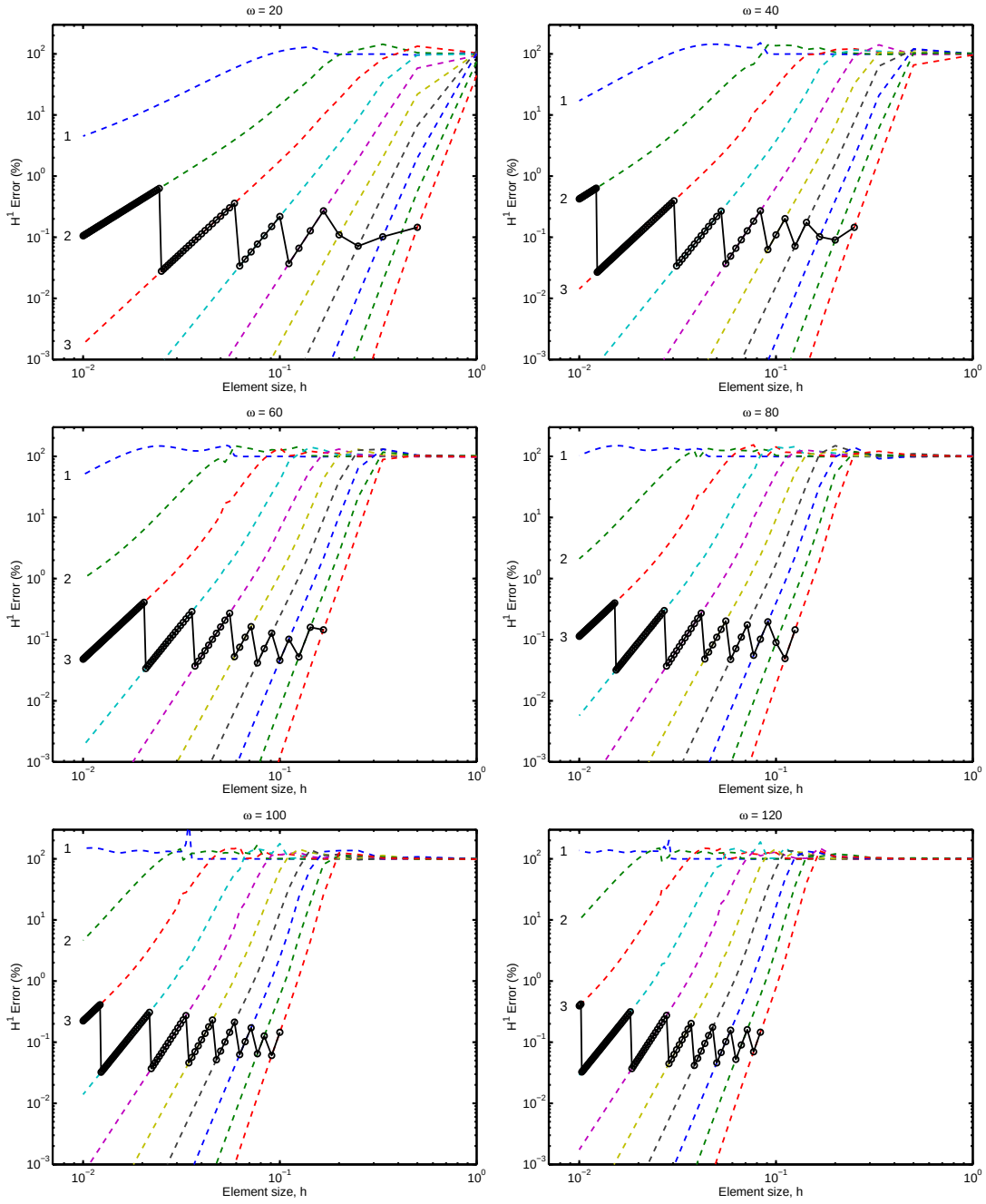

Figure 5.3: The H^1 error as a function of the element size (dashed lines). The predicted optimal order to maintain an accuracy of 1% obtained from the H^1_s error estimator (5.4) constants is shown using the marked solid line.

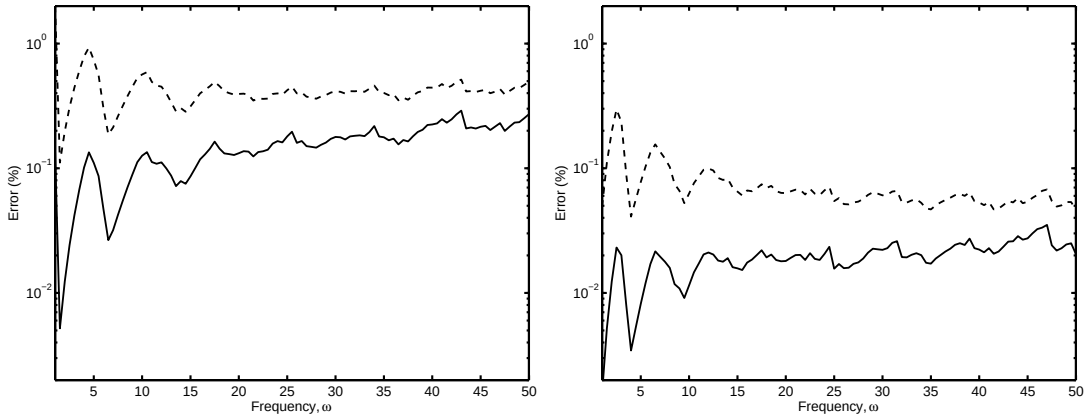

Figure 5.4: Comparison of the performances of the asymptotic error estimator (5.3) (left) and Ainsworth's guideline (5.4) (right). Shown is the actual solution error as a function of input frequency. H^1 error (---), L^2 error (—).

5.2.2 Proposed *A Priori* Estimator

In this section we propose a new *a priori* error estimator. We begin by describing the main assumption made of the method, and by introducing the operation of the estimator. The available measures of error and definitions of element size are investigated. Lastly, guidelines for the efficient implementation of the method, and for mesh design, and discussed.

5.2.2.1 Main Assumption of the Estimator

We begin by assuming that a higher-dimensional element can be related to a one-dimensional element, and that solving the convected wave equation on a single 1D element provides a reasonable prediction of the error on the higher dimensional element. On each one-dimensional element the following system is solved:

$$\int_{\Omega_e} -\frac{\rho_0}{c_0^2}\frac{\overline{\mathrm{d}_0 W}}{\mathrm{d}t}\frac{\mathrm{d}_0\phi}{\mathrm{d}t} + \rho_0\frac{\mathrm{d}\overline{W}}{\mathrm{d}x}\frac{\mathrm{d}\phi}{\mathrm{d}x}\,\mathrm{d}\Omega_e = \left[-\frac{\rho_0}{c_0^2}\boldsymbol{v}_0\cdot\hat{n}\left(\overline{W}\frac{\mathrm{d}_0\phi}{\mathrm{d}t}\right) + \rho_0\overline{W}\frac{\mathrm{d}\phi}{\mathrm{d}\hat{n}}\right]_0^h. \qquad (5.7)$$

Characteristic boundary conditions are used to close the right-hand side of Equation (5.7). The size of the 1D element is h, which may be the minimum, average, or maximum edge length of the higher dimensional element. A depiction of the analytic and numeric wave propagation along the single element (used for the estimation) is provided in Figure 5.5. In essence, the estimator predicts the average error incurred by each element of a given mesh.

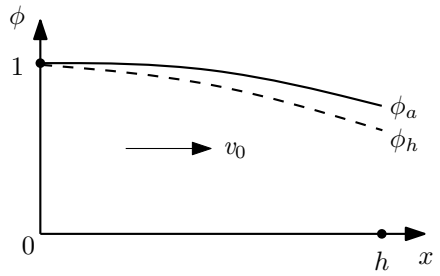

Figure 5.5: The one-dimensional element used to approximate the higher dimensional element. Analytic solution: ϕ_a, numeric solution: ϕ_h.

5.2.2.2 Operation of the Estimator

The operation of the estimator scheme is as follows: for each element in a given mesh, equation (5.7) is solved using linear shape functions. The error is calculated, and compared to a predefined error threshold, E_τ. If the error is higher than the predefined error, the polynomial order of the shape functions is increased by one. This process is repeated until the calculated error is lower than, or equal to, the predefined error. The required order for that specific element is then stored. This is repeated for every element in the mesh, thus providing the predicted optimal polynomial order on each element. The scheme can account for all of the local variables and medium properties. This procedure is depicted by the flowchart given in Figure 5.6. The scheme can be made more efficient by hard-coding pre-integrated element matrices for all orders. Then, the adaptivity scheme requires the calculation of one element matrix, and one matrix inversion per error estimate.

A 2D version of the test case has been solved using the proposed adaptive scheme. The unstructured triangular mesh used has a maximum element size of $h = 0.3$, and a minimum element size of $h = 0.07$. The 2D elements are approximated using 1D elements with a length equal to the average of the 2D element size (the average length is given by the sum of the lengths of the edges, divided by the number of edges). The L^2 error was used as the measure of the error incurred on the one-dimensional elements. The problem is solved for a frequency of $\omega = 10$, with a desired accuracy level of 1%.

The results are given in Figure 5.7. The estimation of the error on each element is shown. Note that this is not the actual error, it is instead the L^2 error levels of the 1D element solutions. Included in the figure is the predicted optimal polynomial order to use on each element; the edge functions are not shown, but take on the highest order

of the surrounding elements. The actual error of the 2D problem was 0.26%, in the L^2 norm, and 0.96% in the H^1 norm.

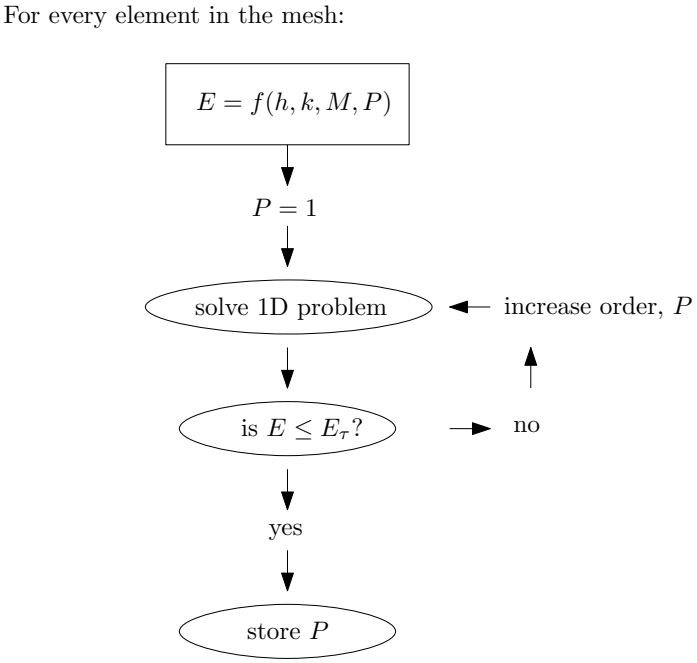

Figure 5.6: Flowchart of the operation of the adaptive order scheme that is applied to each element of the higher-dimensional element.

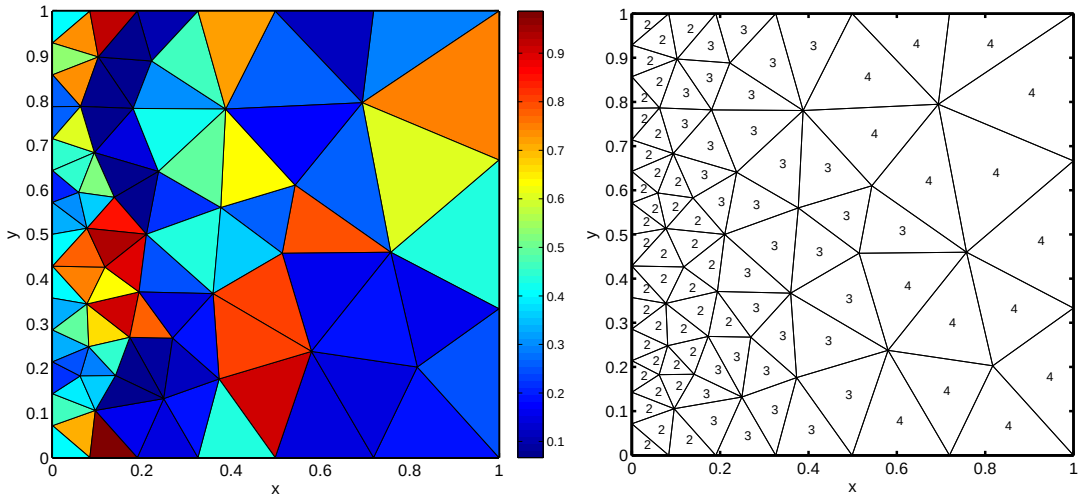

Figure 5.7: Demonstration of the predictions of the adaptive order scheme when applied to a two-dimensional problem. Left: predicted L^2 error (%) on each element, right: predicted optimal order of each element ($\omega = 10, c_0 = 1, \rho_0 = 1, M = 0, E_\tau = 1\%$).

5.2.2.3 Measure of Error and Element Size Definition

The framework of the estimator has been established, the choices of the most applicable measure of error and definition of element size still remain. In this section we compare the various measures of error available, and the best element size definition is considered. The behaviour of the estimator with the preferred measure and definition will then be demonstrated. The section will close with a discussion of the use of the estimator for the design of optimal meshes.

- Measures of Error

Four measures are considered: the H^1 error, the L^2 error, the dispersion error, and the interpolation error. The H^1 and L^2 errors have already been introduced (see Section 5.1). To define the dispersion error we begin by calculating the numerical wavenumber. Noting that the numerical solution is of the form: $\phi_h \sim \exp(-\mathrm{i}k_h h)$, the numerical wavenumber is given by:

$$k_h = \ln\left(\frac{\phi_h(h)}{\phi_h(0)}\right)\frac{\mathrm{i}}{h} + \frac{2n\pi}{h}\,,$$

where the numeric solution at the second node is normalised by the solution at the first node to ensure that both the analytic and numeric solutions have the same magnitude and phase at the first node of the element (at $x = 0$). The additional term involving π accounts for the infinite number of possible solutions; a range of n solutions are chosen, and of this range the wavenumber which best approximates the exact solution is used. The estimated dispersion error is:

$$E_d = 100\,\frac{\|k - k_h\|_2}{\|k\|_2}\,,$$

where the 2-norm ($\|x\|_2 = \left(\sum_{i=1}^{n}|x_i|^2\right)^{1/2}$) has been used. Using the numeric wavenumber, the interpolation error can be obtained using:

$$E_i = 100\,\frac{\|\phi_a(k_h) - \phi_h\|_2}{\|\phi_a(k_h)\|_2}\,.$$

A single 1D problem has been solved in order to compare the measures of error. The input frequency was held constant, $\omega = 10$, and a no-flow case was considered, $M = 0$. The number of degrees of freedom per wavelength was varied, and the error levels were recorded. The convergence results for four orders (P =1, 2, 3, and 10) are presented in Figure 5.8.

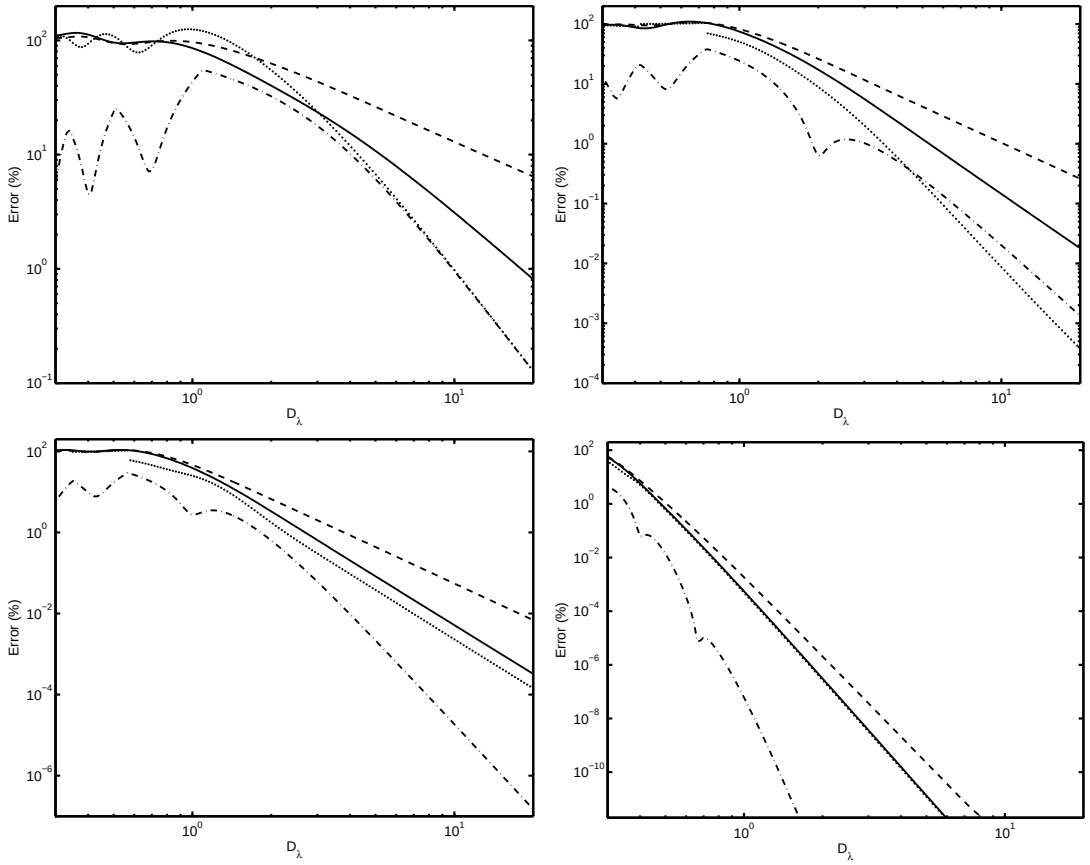

Figure 5.8: Comparisons of the measures of error on a single one-dimensional element, for polynomial orders 1 (top left), 2 (top right), 3 (bottom left), and 10. H^1 error (- - -), L^2 error (—), dispersion error (- · -), and interpolation error (· · ·).

For the first polynomial order the interpolation error is the highest in the very low discretisation region (approximately 1 or 2 degrees of freedom per wavelength) but as the element size is reduced the H^1 measure reports the highest levels of error. For all polynomial orders higher than one, the H^1 error is the highest. The L^2 error is always less than the H^1, but always greater than the dispersion and interpolation errors (except when very low discretisation with linear elements is used, but this case is uninteresting). The dispersion and interpolation errors tend to vary with the number of degrees of freedom, and the polynomial order. As the actual error of the finite element method is a combination of these two types of error, choosing one over the other may be short-sighted. The choice of best measure of error must be made between the H^1 and L^2 errors.

- Element Size Definition

The performance of the proposed error estimator depends on the way in which the 1D element approximates the behaviour of 2D or 3D elements. This is far from obvious, especially when considering unstructured meshes (for which the element size h is not well defined). Let us consider a propagation problem with triangular elements. Three different measures of the element size are used, and their influence on the accuracy of the error estimator is assessed.

A comparison of the performance of the error estimator, when used to solve the 2D problem presented in Section 5.2.2.2, for the two measures of error (H^1 and L^2) and the three element size definitions (minimum, average, and maximum), is given in Figure 5.9. Included on the plots are the maximum and minimum error levels predicted by the one-dimensional error estimator (as an example consult Figure 5.7). These indicators can be understood as numerical upper and lower error bounds. The upper and lower bounds can be viewed as indicators of the accuracy and efficiency of the error estimator, respectively. A general observation is that the upper bounds (the maximum predicted error of the mesh for each desired error) are almost identical. This seems to imply that the upper bound does not depend significantly on the choice of the measure of error, or on the element size definition. The lower bounds match very closely, but do depend on the choice of error and element size definition. If we consider the L^2 error results we see that the L^2 error is bounded for all choices of element size definition - except for very low accuracies, in which case the pollution error becomes significant. The H^1 error is bounded only when the average and maximum element size definitions are used. When the H^1 error is used as a measure we observe that the H^1 error is always bounded, and the L^2 error is bounded for the minimum element size definition only. When the definition is based on the average or maximum edge length the L^2 error is below the lower bound. We see that using the L^2 error and average edge length provides the most accurate and efficient estimates.

It is possible to define an effectivity index: $\eta = E_\tau / E$, which should ideally be close to, or equal to, 1. A value of 1 indicates that the actual error is identical to the desired error. Effectivity indices that correspond to the data presented in Figure 5.9 are given in Figure 5.10. It can be seen that using H^1 error provides solutions which are too conservative, *i.e.* using this norm incurs unnecessary computational expense, since

the effectivity index is much greater than unity. The choice of the most appropriate element length definition remains.

When using the minimum edge length, the effectivity index of the measured H^1 error is close to zero. Using the minimum edge length may give solutions which exceed the predefined error threshold. Using the maximum edge length produces solutions which are too conservative. The best solutions are obtained using the average edge length, in which case the effectivity index of the measured H^1 error is closest to unity.

In summary, using the L^2 error and the average edge length for the error estimation should provide the most efficient solutions; by using the minimum computational resources to ensure an upper bound is placed on the error of the higher-dimensional system.

- Behaviour of Estimator

We now consider the behaviour of the actual error when the proposed error estimator is used to solve the test case given above for four different frequencies, $\omega = 1$, 10, 20, and 50. The results are given in Figure 5.11.

A general observation is that in all cases the L^2 error is bounded - except at very low accuracy, which is suspected to be an effect of the pollution error that is not accounted for by the error estimator. For the low frequency case where $\omega = 1$ the H^1 error is out of bounds. A plateau is observed for low accuracies, corresponding to the lowest order elements, thus the error does not increase as the mesh adequately resolves the propagating wave. As the desired accuracy is increased, the order of the elements is increased and the error converges. For $\omega = 10$ the H^1 error is close to the upper bound. A plateau in the lower bound is observed for low accuracies; for lower accuracies the mesh resolution has reached a limit. For $\omega = 20$ the H^1 error is bounded. Again a plateau is observed, which corresponds to the resolution limit of the system. For the highest frequency, $\omega = 50$ the H^1 error is bounded, and the plateau in the upper bound and actual error indicate that the maximum resolution of the mesh has been reached. To achieve higher accuracy the element size must be reduced, or the polynomial order must be increased (a maximum order of 10 has been used in this work). We see that the behaviour of the error estimator is a function of frequency.

In summary, the largest predicted error of the mesh acts as an upper bound, until either the mesh resolution is reached, or pollution error becomes significant.

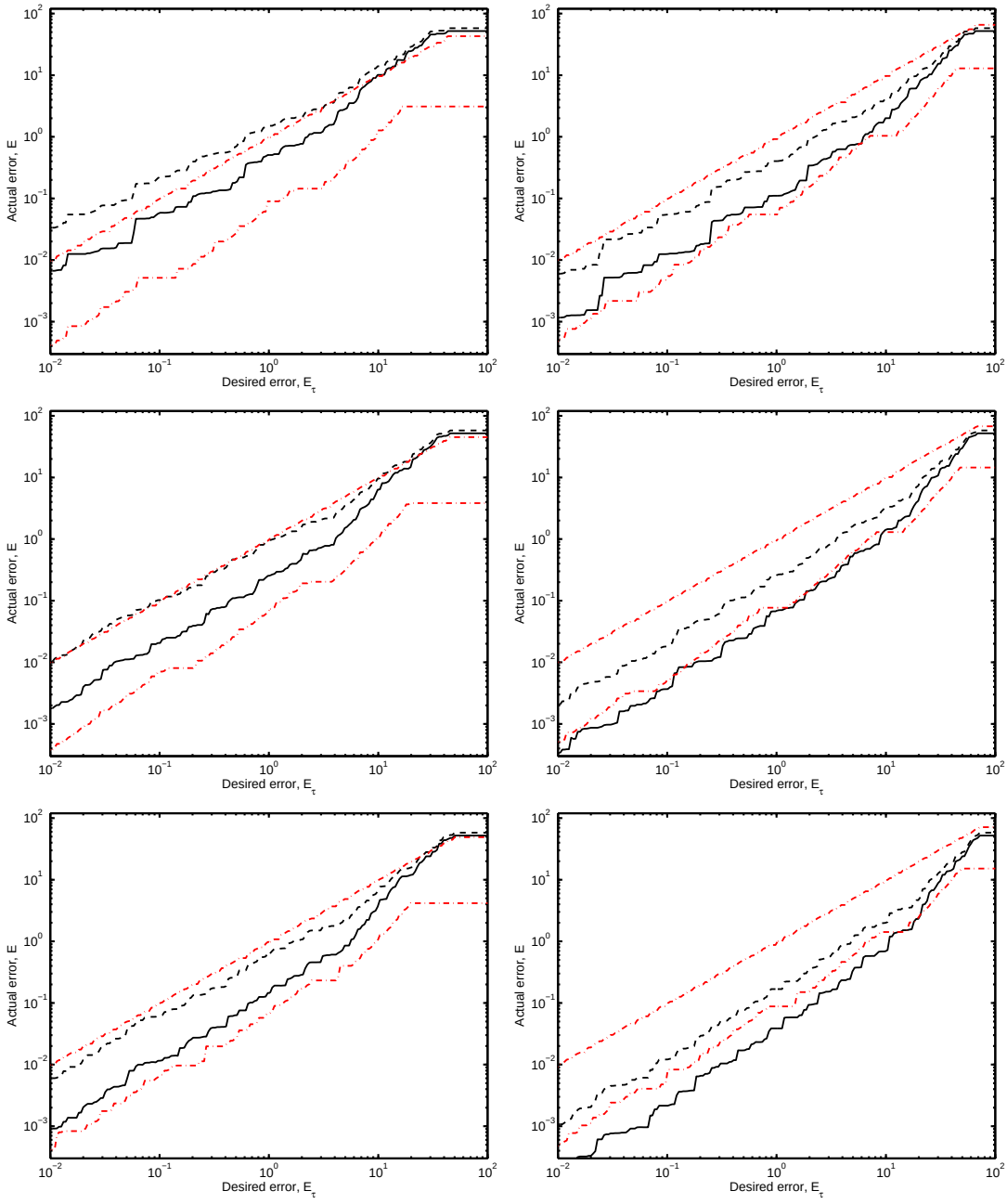

Figure 5.9: Actual error as a function of the desired error, obtained using two measures of error, and three element size definitions. Left: L^2 error measure, right: H^1 error measure. Top: minimum edge length, middle: average edge length, bottom: maximum edge length. H^1 error (- - -), L^2 error (—), max. and min. predicted errors (-·-).

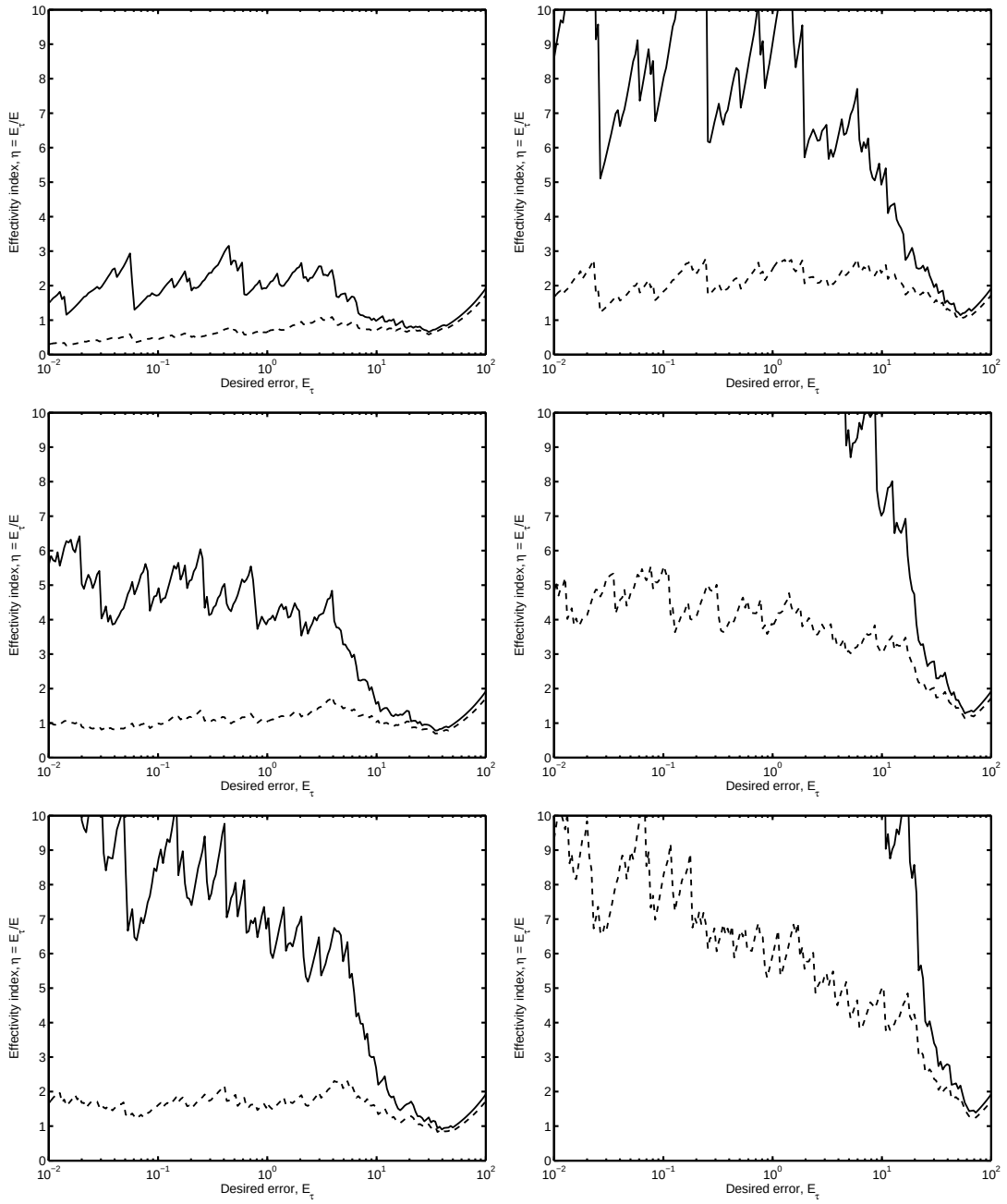

Figure 5.10: Effectivity index (measured in both the H^1 and L^2 norms) as a function of the desired error. Left: L^2 error used to estimate 1D error, right: H^1 error used to estimate 1D error. Top: minimum edge length, middle: average edge length, bottom: maximum edge length. Effectivity index of actual H^1 error (- - -), and actual L^2 error (—).

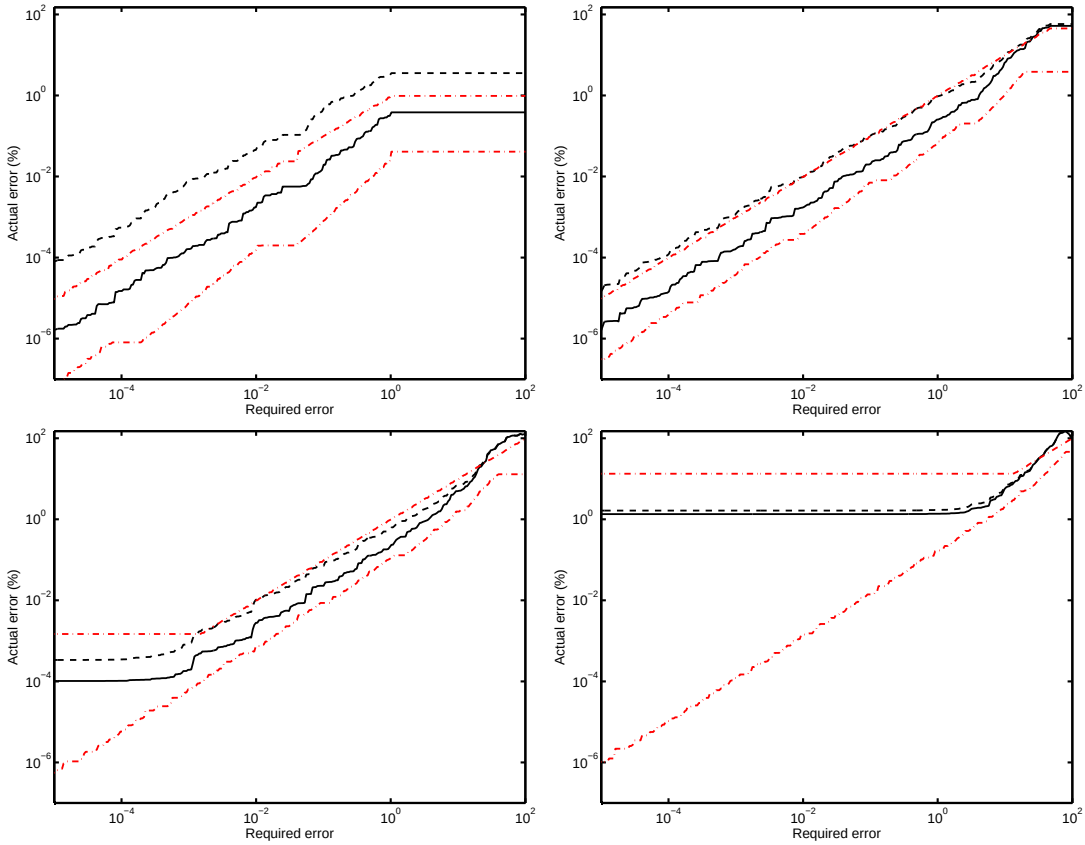

Figure 5.11: Actual error as a function of the desired error, obtained using the L^2 error and the average element size. Top left: $\omega = 1$, top right: $\omega = 10$, bottom left: $\omega = 20$, bottom right: $\omega = 50$. H^1 error (- - -), L^2 error (—), max. and min. predicted errors (-·-).

5.2.2.4 Pollution Error

It has been noted that the estimator does not make provision for the effect of pollution error (which is the domain length dependent accumulation of dispersion error). In this section the performance of the estimator when used to provide accurate solutions for problems in which the pollution error is increasing is investigated.

An re-meshed version of the geometry presented in Figure 5.7 is used, and the length of the domain is varied; one example of the meshes used is presented in Figure 5.12. The size of the elements in each mesh ranges from 0.07 to 0.3. The wavenumber limit of the mesh can be determined using: $k = 2\pi P/(h\, D_\lambda)$. For a desired accuracy of 1%, using seven degrees of freedom per wavelength and the highest polynomial order gives an upper limit on the resolvable wavenumber of the mesh of approximately $k = 30$.

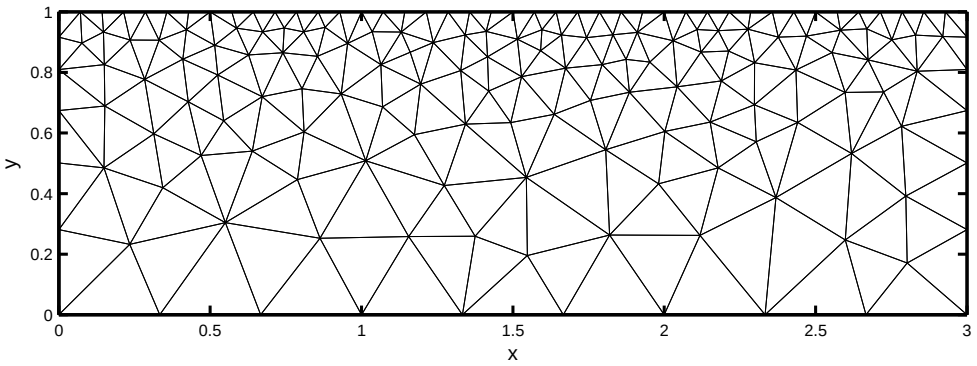

Figure 5.12: Example of mesh used to investigate behaviour of error estimator as the pollution effect becomes significant. Max. element size: 0.3, and min. element size: 0.07.

The proposed error estimator was used to predict the required polynomial order on each element to achieve an accuracy of 1%, and the H^1 and L^2 errors of the full solution were calculated. This was carried out for frequencies ω= 1, 5, 10, 20, 30 and 40. For the longest domain length used, $x = 20$, these frequencies correspond to the following numbers of wavelengths in the domain: 3.18, 15.9, 31.8, 63.7, 95.5, and 127.

The results of this investigation are presented in Figure 5.13. The pollution effect is clearly visible; as the length of the domain is increased, the level of the actual error increases while the maximum predicted error remains constant. If we consider the results obtained for frequency $\omega = 1$ we see that the estimator fails to contain the error as the length of the domain is increased, as expected. However, as the frequency is increased we observe that the L^2 error remains bounded until the frequency limit of the mesh is exceeded. The reason for this is that at very low frequencies the error estimator chooses the lowest polynomial order on the elements. It is well known (see *e.g.* [44]) that higher-order elements control dispersion error more effectively than lower-order elements, and this is what we observe in these results. As the frequency increases, the orders of the elements increase, and the dispersion error is minimised. Thus, up to some undefined maximum domain length, the highest polynomial order elements of a given mesh control the pollution error. Note that when the upper frequency limit of the mesh is exceeded, the estimator fails, but this is to be expected.

We conclude that the proposed error estimator has a frequency range of applicability, in which it performs well. Although it does not account for pollution error, the use of the higher order polynomials does, to some extent, control the pollution error.

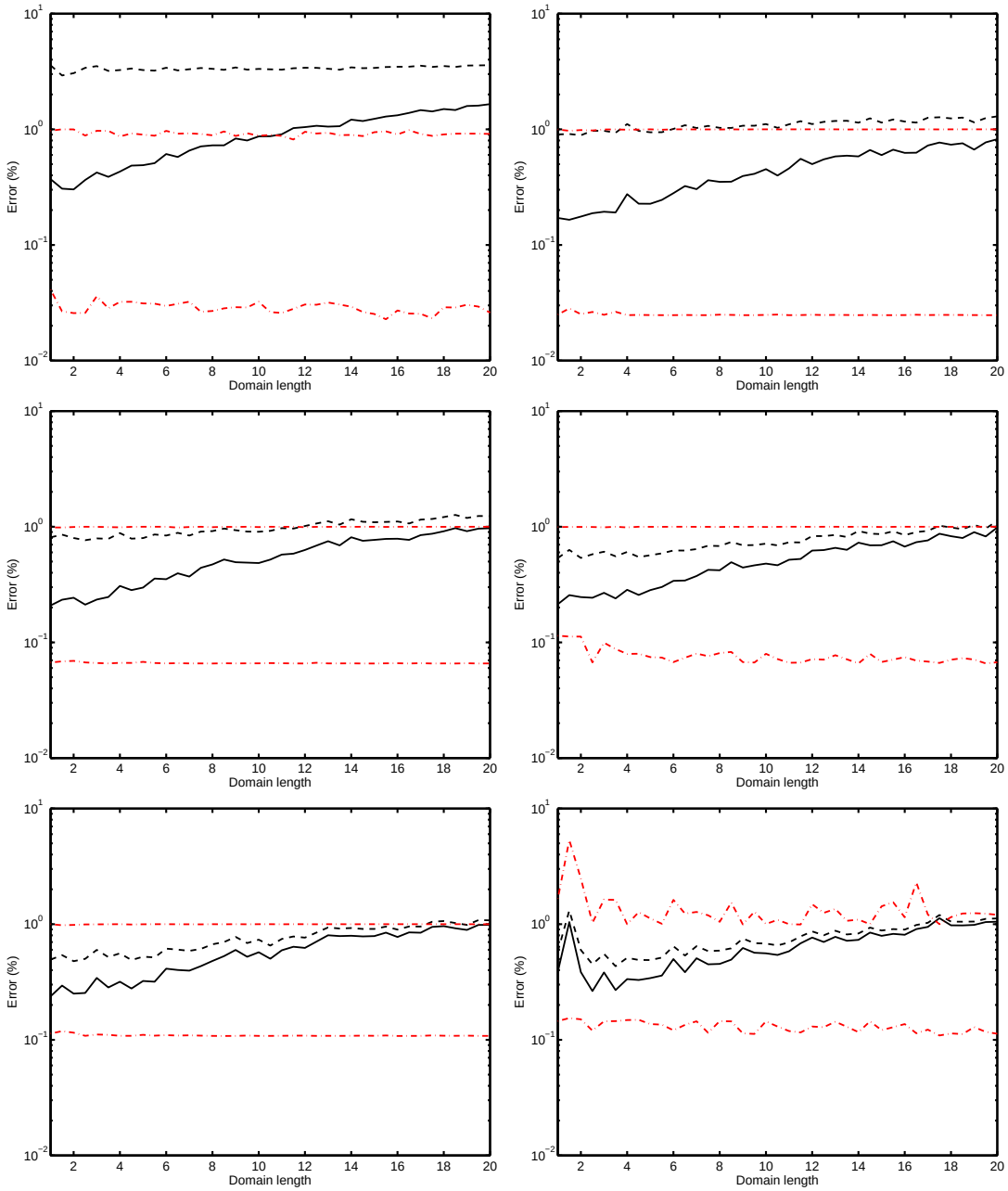

Figure 5.13: The actual error as a function of the length of the domain. Top left: $\omega = 1$, top right: $\omega = 5$, middle left: $\omega = 10$, middle right: $\omega = 20$, bottm left: $\omega = 30$, and bottom right: $\omega = 40$ (note: mesh limit has been exceeded). H^1 error (- - -), L^2 error (—), predicted error bounds (-·-).

5.2.2.5 Efficient Choice of Optimal Order

It is interesting to consider the behaviour of the L^2 error on the single element, as the polynomial order is varied.

Firstly, we analyse the L^2 error as a function of the number of elements per wavelength - this data is presented on the left panel of Figure 5.14. For these results the flow is zero. Convergence data for frequencies $\omega = 1$ and 100 are plotted. It can be seen that the error is identical for both frequencies. The reason for this is that the interpolation error is the dominant source on the single one-dimensional element, and so keeping kh constant controls the error. This is quite beneficial, as it means that for a desired error and a given element size the optimal polynomial order can be determined from the input frequency. Furthermore, a 'look-up' table which contains the optimal order for a pre-defined error level and for a given value of kh can be created, and stored. Using such a table can make the method even more efficient, by not actually requiring the solution of the single element problem on each high-dimensional element.

Next, we consider the L^2error as a function of the number of degrees of freedom per wavelength. For these results the frequency is held constant, $\omega = 100$, and the no flow and upstream cases are compared. We see that in the upstream case slightly more degrees of freedom are needed to maintain a given level of error - this is more noticeable in the low discretisation region. This is an artefact of the boundary conditions used. This behaviour means that when flow is present using a 'look-up' table is not advised. Instead the adaptivity scheme should be used to compute the optimal polynomial order for a given element.

Ultimately, the estimator requires the analysis of every element in the higher-dimensional mesh. Although this is an additional expense, the evaluation time is insignificant compared to the cost of solving the full system, especially in light of the fact that it enables more efficient solutions.

5.2.2.6 Mesh Design

As shown in Section 4.4.2, using polynomial order $P = 10$ requires the least amount of factorisation memory, for a given accuracy, when compared to lower orders. It is expected that this trend will continue for orders higher than 10, but this has not been confirmed in this work. With this in mind, the formula for the number of degrees of

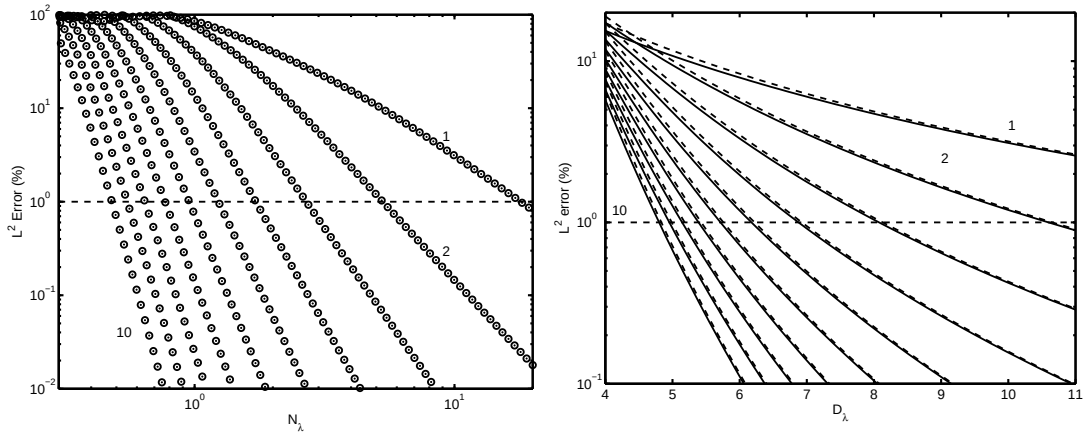

Figure 5.14: The L^2 error on a single one-dimensional element as a function of the number of elements per wavelength (left) and as a function of the number of degrees of freedom per wavelength (right). Polynomial orders 1 to 10 are presented. Left: $\omega = 1$ ($\cdot$), $\omega = 100$ ($\circ$). Right: $M = 0$ (—), $M = -0.6$ (- - -).

freedom per wavelength (4.1) can be used to determine an optimal element size for mesh design. The optimal element size is given by:

$$h_{\text{opt}} = \frac{20\pi}{kD_\lambda}\,, \tag{5.8}$$

where the optimal polynomial order 10 has been used. The wavenumber is dictated by the input frequency and Mach number of the problem. The number of degrees of freedom per wavelength to be used is determined from the accuracy required, *e.g.* for an accuracy of 1% 4.8 degrees of freedom per wavelength are needed when using polynomial order 10 (see Figure 5.14). Once a desired accuracy has been chosen, a mesh designer should aim to create elements with a size dictated by (5.8). However, as meshes of complex geometries will be composed of elements of varying sizes, and thus varying orders, it has been found that using a more conservative value for the number of degrees of freedom per wavelength is advisable. For an accuracy of 1% using the traditional rule of 6 degrees of freedom is suggested.

Formula (5.8) can be rewritten in terms of the wavenumber in order to determine the upper frequency limit of a given mesh:

$$\omega = \frac{20\pi\,(c_0 - |u_0|)}{h_{\text{opt}} D_\lambda}\,. \tag{5.9}$$

5.3 Illustration of Performance of Proposed Estimator

Assessments of the performance of the proposed error estimator are presented here. For both two-dimensional and three-dimensional problems, the non-uniform meshes used are given, and followed by the error results of frequency sweep tests.

5.3.1 Performance in Two Dimensions

In this section we demonstrate the ability of the adaptive order scheme to properly define the mesh resolution required to generate solutions which are very close to a predefined error level. The two-dimensional analysis that follows shows the behaviour of the scheme when subjected to frequency sweeps. Up to the frequency limit of the mesh, the solutions obtained are bounded by the required accuracy, and show very little variation with frequency. Four meshes have been constructed, and used to demonstrate the scheme's performance; these are presented in Figure 5.15. Note their increasing non-uniformity, *i.e.* the meshes become less uniform as the smallest size of the elements is decreased. The largest element size used is 0.15, which gives an upper frequency limit (given in terms of the wavenumber) of $k = 100$ (obtained using formula (5.9)), for both $M = 0$ and $M = -0.6$.

5.3.1.1 No Flow Case

The standard wave equation was solved using the adaptive scheme on the four different meshes, for a range of frequencies from $\omega = 1$ to 100. The adaptive scheme was used to predict the optimal polynomial order based on the element size and input frequency. The resulting errors as a function of frequency are given in Figure 5.16. We begin with a few general observations. All of the L^2 errors are bounded by the maximum and minimum predicted errors provided by the adaptive order scheme. The upper frequency limit of each mesh is exceeded, but before this occurs the maximum predicted error goes above the required error level. This serves as an indicator that the mesh limit is close to being exceeded. We also note that for higher frequencies, and in all cases, there

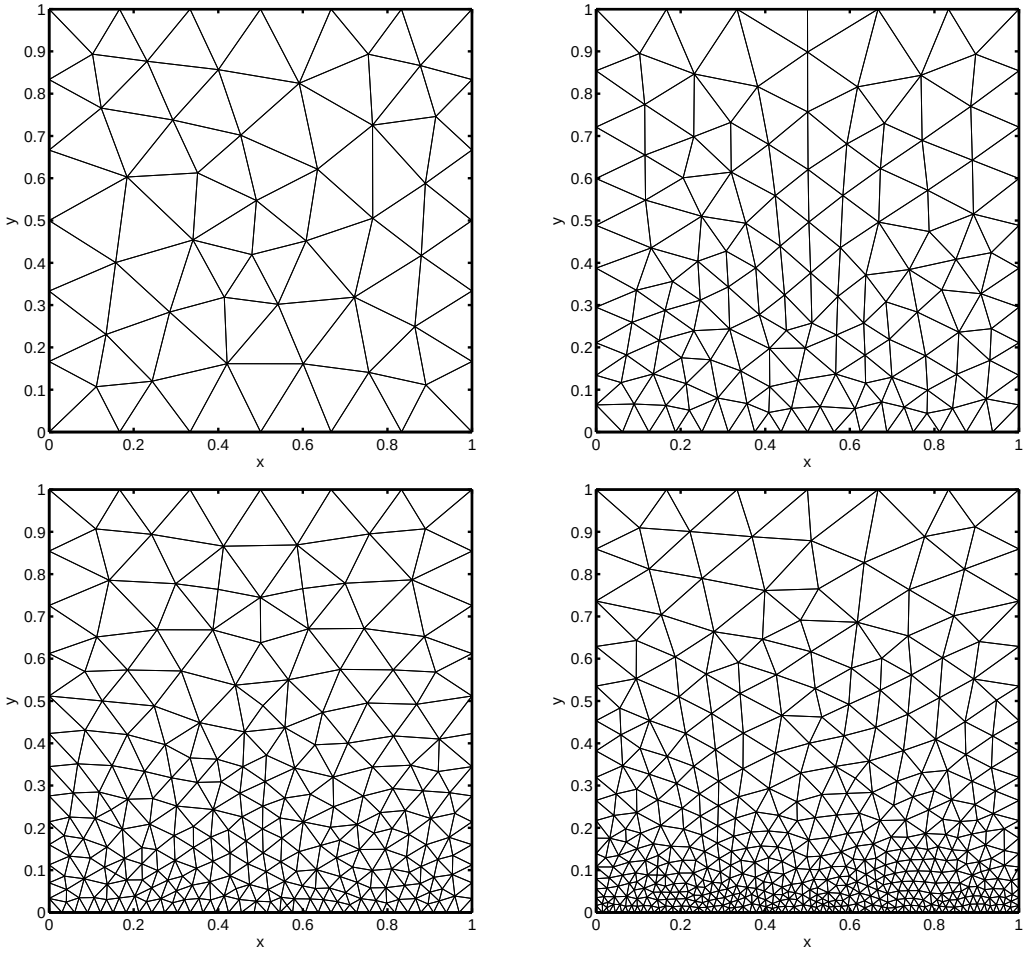

Figure 5.15: Meshes used to test the adaptivity scheme in 2D. Top left: $h = 0.15$, top right: $h_1/h_2 = 0.15/0.06$, bottom left: $h_1/h_2 = 0.15/0.03$, bottom right: $h_1/h_2 = 0.15/0.015$.

is relatively little variation in the actual error obtained for the resolvable frequencies considered. Consider the results obtained for the mesh with a ratio of $1:1$. There are noticeable dips in the error plots. As the mesh is composed of elements with approximately the same size, as the orders of the elements change the error levels exhibit an associated sudden change. These dips are still noticeable in the results obtained from the mesh with a ratio of $2.5:1$, but they are smaller. This is due to the increasing range of orders across the elements, which tend to average out the associated error dips, *i.e.* as the mesh ratio is increased, the range of orders is increased, and the error plots become much smoother.

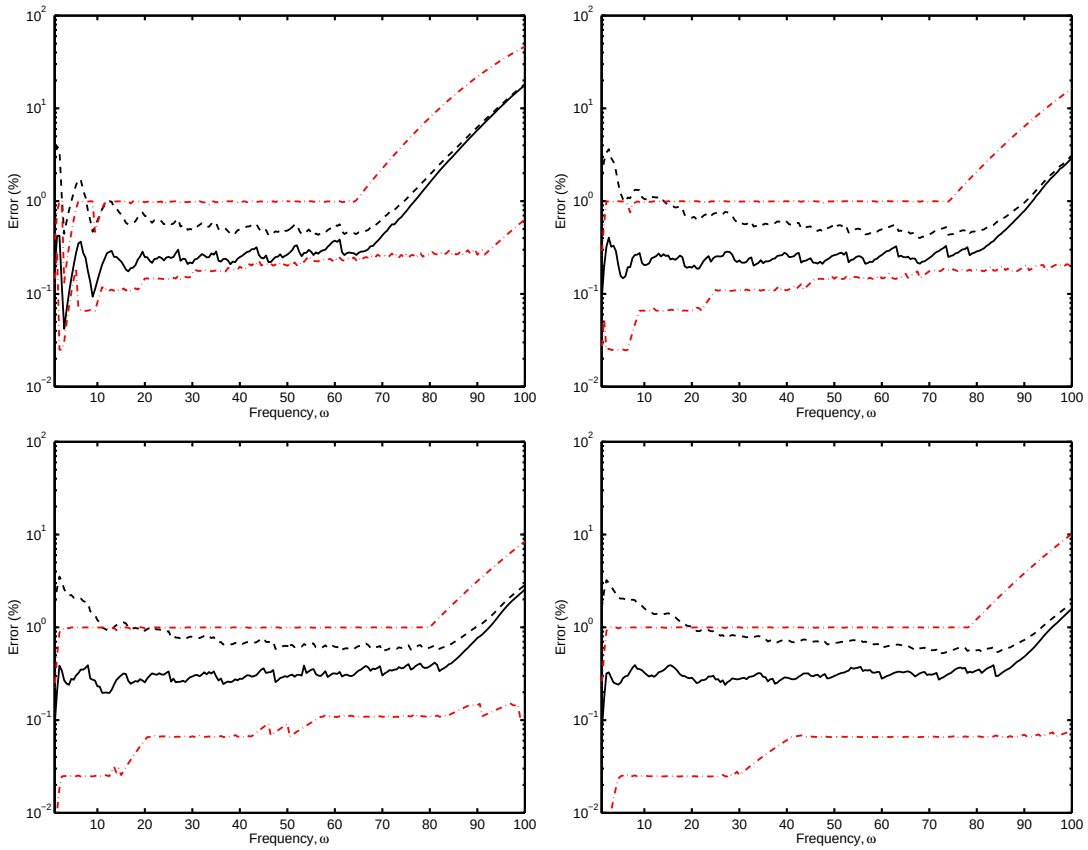

Figure 5.16: Measures of error as a function of frequency, for the 2D test case, without flow. Mesh ratios: top left: 1:1, top right: 2.5:1, bottom left: 5:1, and bottom right: 10:1. H^1 error (- - -), L^2 error (—), max. and min. predicted error (-·-).

It can be seen that beyond an upper frequency limit the proposed method fails to keep the actual error below the desired level. However, in these examples the maximum frequency resolved is higher than the limit given by (5.9), that is $k = 60$. The predicted (obtained from the one-dimensional single-element solutions) and actual maximum resolvable frequencies are given in Table 5.1. Also included are the number of degrees of freedom per wavelength which would give such frequencies. We see that using the 6 degrees of freedom per wavelength that is suggested in Section 5.2.2.6 is slightly conservative, but also that the number needed is dependent on the non-uniformity of the mesh.

If we consider all of the error plots, we observe that the *a priori* estimator places an upper bound on the L^2 error below the upper frequency limit of the mesh. Note

Mesh ratio	1:1	2.5:1	5:1	10:1
Predicted max. ω.	64	74	80	78
Predicted required D_λ	6.5	5.7	5.2	5.4
Actual max. ω.	77	92	93	96
Actual required D_λ	5.4	4.6	4.5	4.4

Table 5.1: Maximum resolvable frequencies of the meshes, and the corresponding numbers of degrees of freedom required to resolve the frequencies.

that, for higher frequencies, only the use of higher order elements or smaller elements will keep the error bounded. It is interesting to see that the maximum frequency limit of each mesh increases with the increasing non-uniformity. This is caused by the increased number of smaller elements, on which the order can still be increased for greater accuracy. These results are very encouraging as they suggest that the error estimator maintains a bounded error level, even when the mesh is non-uniform, and that the error levels obtained exhibit very little variation with frequency.

5.3.1.2 Flow Case

The convected wave equation has been solved for a range of frequencies, from $\omega = 1$ to 40, with a flow of Mach number -0.6. The resulting errors as a function of frequency are given in Figure 5.18. A general observation is that the L^2 error is always bounded by the maximum and minimum predicted errors of the mesh. We note also that the maximum frequency limit of the meshes has been exceeded in each case, but that the predicted and actual limits of the meshes are higher than the value given by (5.9) - this is due to the use of a conservative value for the number of degrees of freedom required.

Essentially the results are the same as the results given in the case without any flow ($M = 0$), albeit the frequency limit of the meshes is reduced due to the shortening of the wavelengths by the flow. For the uniform mesh (ratio 1 : 1) dips in the error are noticeable. They are caused by the improved accuracy of higher order functions which is brought about by the simultaneous increments of polynomial order of each element with increasing wavenumber. We see that as the mesh non-uniformity increases, the error plots become smoother, and exhibit less variation with frequency. This is due to the increasing range of orders on the elements.

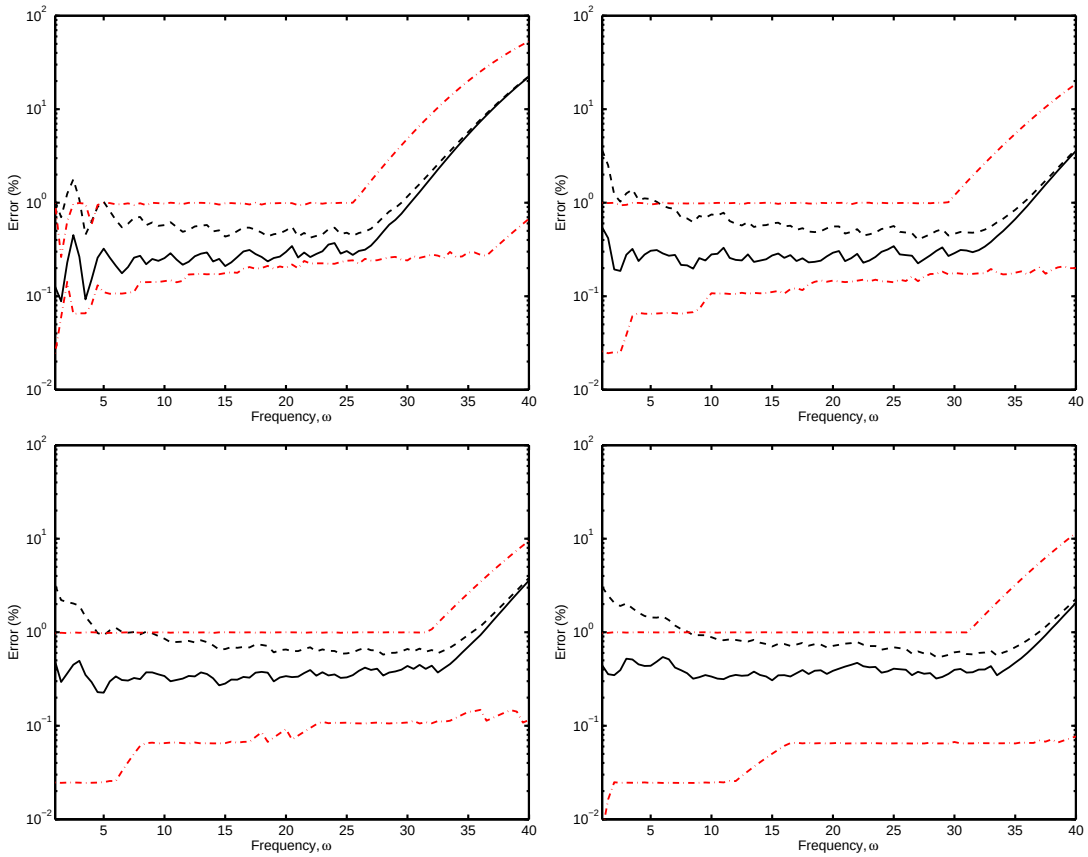

Figure 5.17: Measures of error as a function of frequency, for the 2D test case, with Mach number −0.6. Mesh ratios: top left: 1:1, top right: 2.5:1, bottom left: 5:1, and bottom right: 10:1. H^1 error (- - -), L^2 error (—), max. and min. predicted error (-·-).

To further demonstrate the behaviour of the adaptive scheme, the most common and maximum polynomial orders of each mesh, for each input frequency, are presented in Figure 5.18. It can be seen that for the uniform mesh (ratio 1:1) the most common order of the elements is much higher than the non-uniform meshes, and is at most three orders below the maximum polynomial order (in this case 10). This is the underlying reason for the appearance of the dips in the error plots shown in Figure 5.17; the size of the elements tends to be the same, and as the frequency increases the orders increase in union. In contrast, the largest difference between the most common and maximum polynomial orders of the most non-uniform mesh (ratio 10:1) is seven orders, which explains the much smoother error plots. In general, we can see that once the maximum order available has been reached, the upper frequency limit is close to being exceeded.

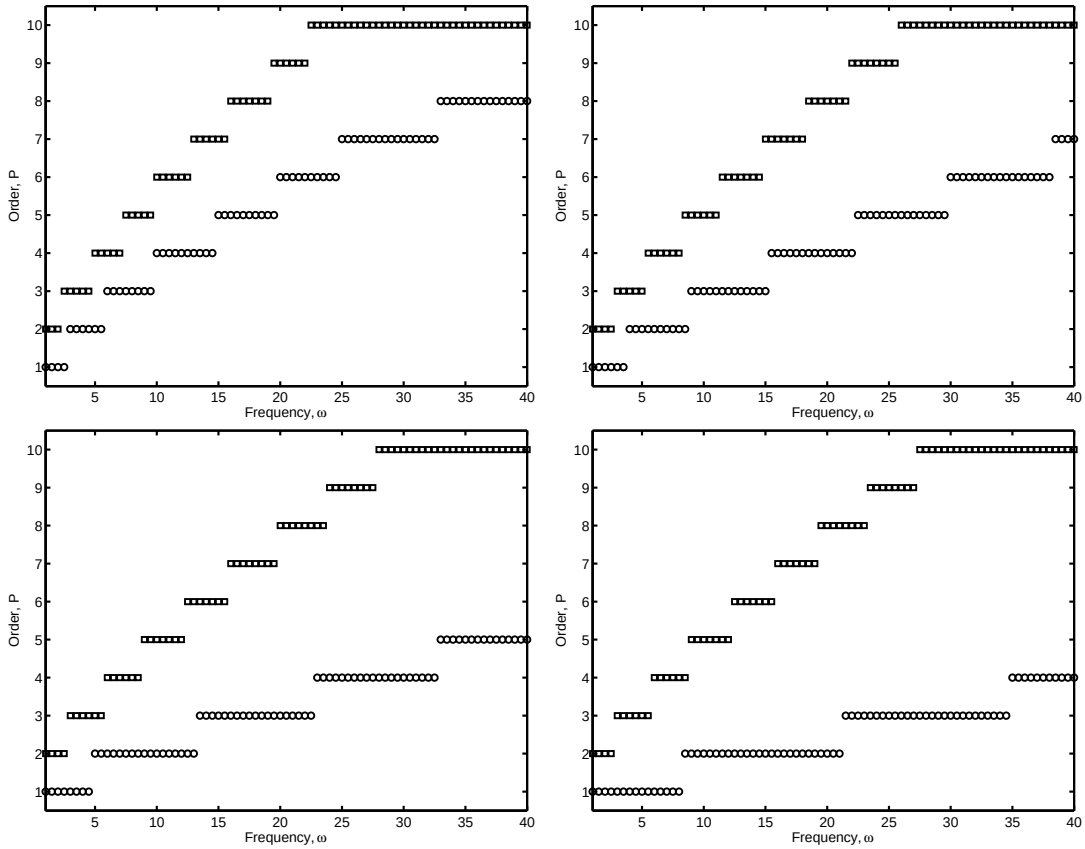

Figure 5.18: Most common (○) and maximum polynomial (□) orders as a function of frequency, for the 2D test case with a flow Mach number of -0.6. Mesh ratios: top left: 1:1, top right: 2.5:1, bottom left: 5:1, and bottom right: 10:1.

5.3.2 Performance in Three Dimensions

The company sponsoring this project, LMS International, have implemented the proposed adaptive order scheme into their aeroacoustic solver, SysNoise. This has enabled tests of the performance of the adaptive scheme in three dimensions. The results of these tests are presented in this section. Four meshes with increasing non-uniformity have been generated, and are used to test the adaptive scheme's ability to handle distorted meshes. The meshes are presented in Figure 5.19. Three predefined error levels were chosen to provide users of the solver with coarse (15%), standard (5%), and fine (0.5%) resolution options. Look-up tables for these levels were created using the data presented in Figure 5.14.

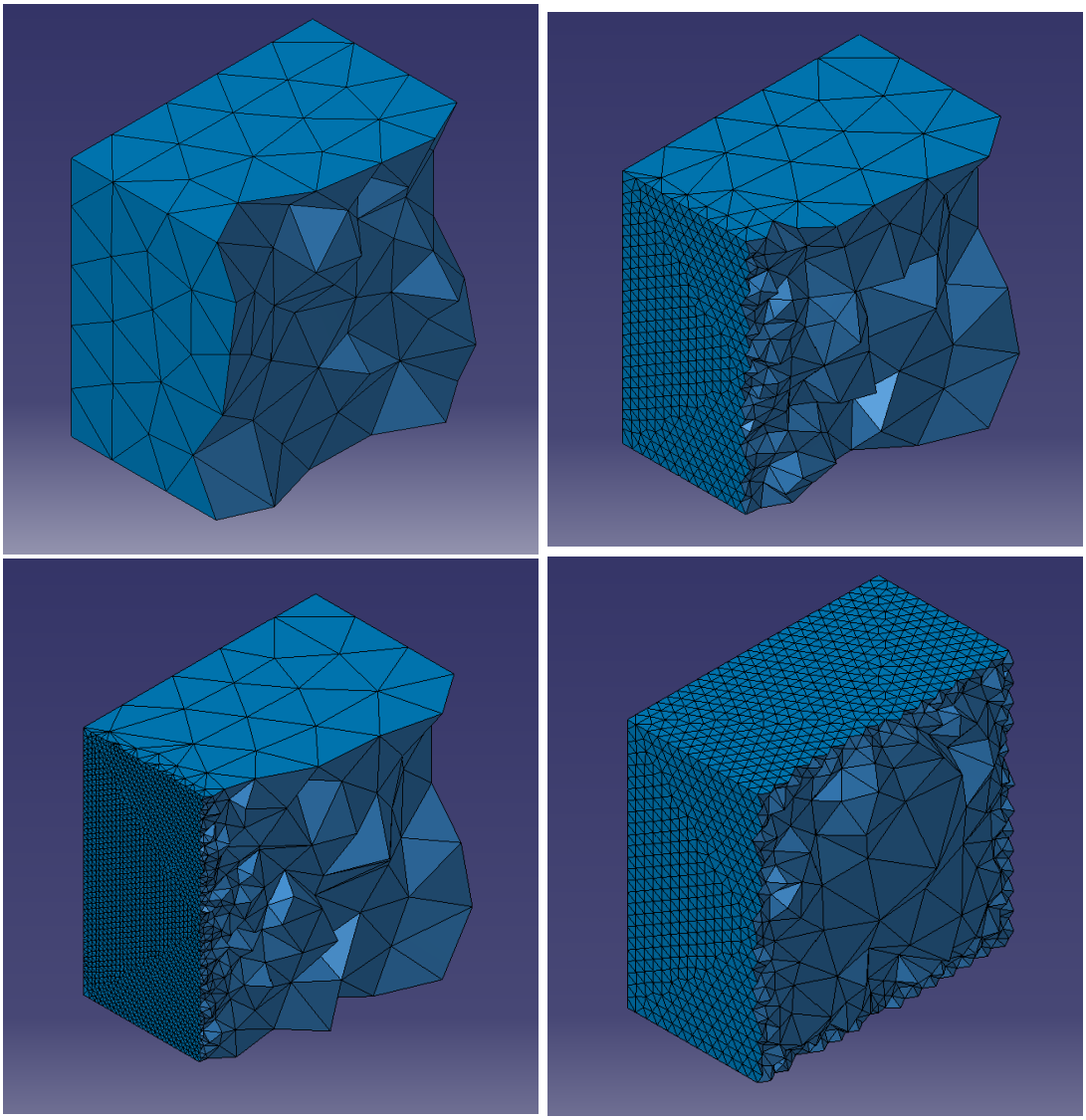

Figure 5.19: Meshes used to test the adaptivity scheme in 3D. Top left: $h = 0.2$, top right: $h_1/h_2 = 0.2/0.04$, bottom left: $h_1/h_2 = 0.2/0.02$, and bottom right: $h_1/h_2 = 0.2/0.05$

5.3.2.1 No Flow Case

The unconvected wave equation has been solved. The L^2 error as a function of the frequency is given in Figure 5.20. A general observation is that the actual error, for all meshes and for each of the accuracies (coarse, standard, and fine), is bounded by the desired error level. It can be seen that the error plots exhibit very little variation with frequency, until the mesh frequency limit is exceeded.

We observe that this limit depends on the accuracy chosen, which is expected as a higher accuracy will require elements with higher orders, and thus the highest available order will be required on a majority of the elements at high frequencies. The flat error plots also indicate that a minimal amount of unnecessary computational effort has been incurred. As was observed for the 2D results, the error levels produced by the uniform mesh exhibit dips; these are caused by the uniformly increasing polynomial order of the elements with increasing frequency. The results obtained from the mesh with an element size ratio of 4:1 exhibit 'bumps' in the error. This mesh has a much higher number of small elements than the other meshes (as the entire boundary is composed of small elements), and thus the changing of the polynomial order of these smaller elements causes the bumps in the error.

In Figure 5.21 the maximum, most common, and minimum polynomial orders used to solve the system, to a 'standard' accuracy, are given as a function of frequency. For the uniform mesh (ratio 1:1) we note that the order is not always the same on every element. Since this is an unstructured mesh the elements are not all exactly the same size. In the case of the mesh with an element size ratio of 4:1, we see that the maximum order is much higher than the most common and minimum orders. This is due to the high number of the smaller elements in the mesh, which are able to give good accuracies using lower orders. Note that the incremental changes of the minimum and most common orders coincide with the bumps in the error (referred to in the previous paragraph).

In Figure 5.22 the memory required for matrix factorisation as a function of frequency is given. As expected, the uniform mesh requires the least amount of memory, and this is because the uniform mesh has the highest number of large elements. This in turn means it has the lowest number of elements, but also that the order on those elements is higher. As already shown, using higher orders is optimal due to the reduced factorisation memory requirements. For the highest frequencies the mesh limit is reached, as indicated by the plateau in the memory needed. The distorted mesh requires the most memory, as it has the highest number of low-order elements. This comparison confirms the efficiency of using higher order elements. In Figure 5.23 the time required to solve the system is given as a function of frequency. The same conclusion can be drawn as for the memory requirements - it is most efficient to use large elements with higher order interpolation functions.

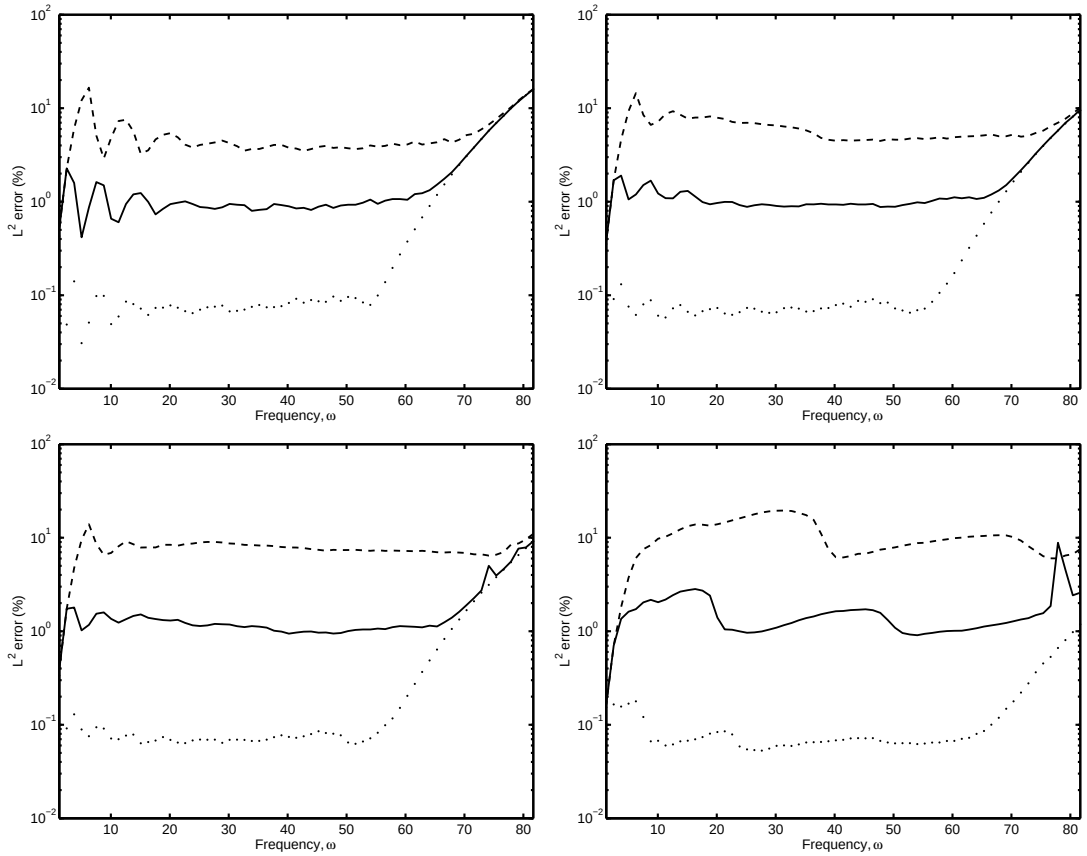

Figure 5.20: L^2 error as a function of frequency. Coarse (---). Standard (——). Fine (...). Mesh ratios: top left: 1:1, top right: 5:1, bottom left: 10:1, and bottom right: 4:1.

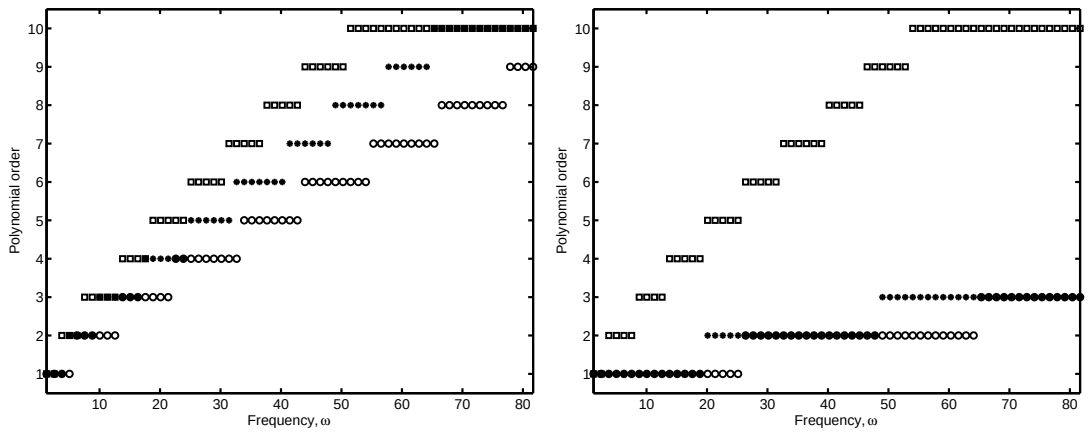

Figure 5.21: Order as a function of frequency. Maximum order (□). Most common order (●). Minimum order (○). Mesh ratios: left: 1:1, right: 4:1.

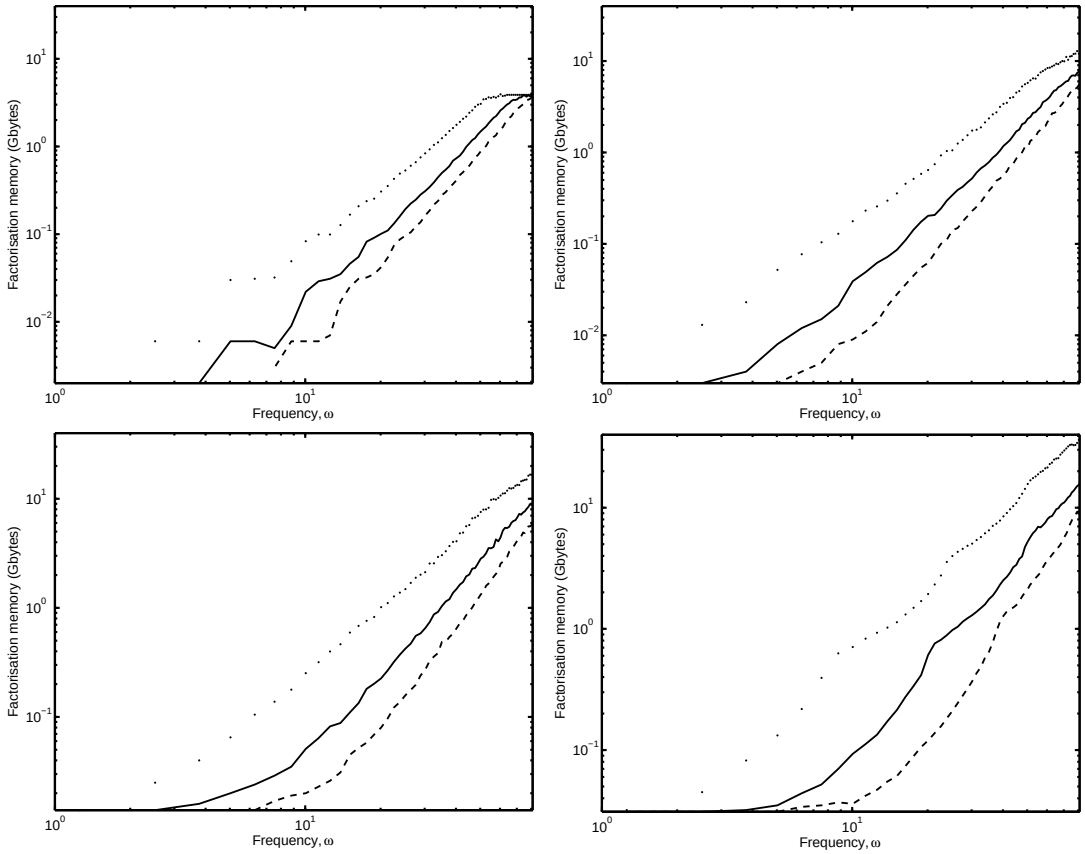

Figure 5.22: Memory as a function of frequency. Coarse (- - -). Standard (——). Fine (...). Mesh ratios: top left: 1:1, top right: 5:1, bottom left: 10:1, and bottom right: 4:1.

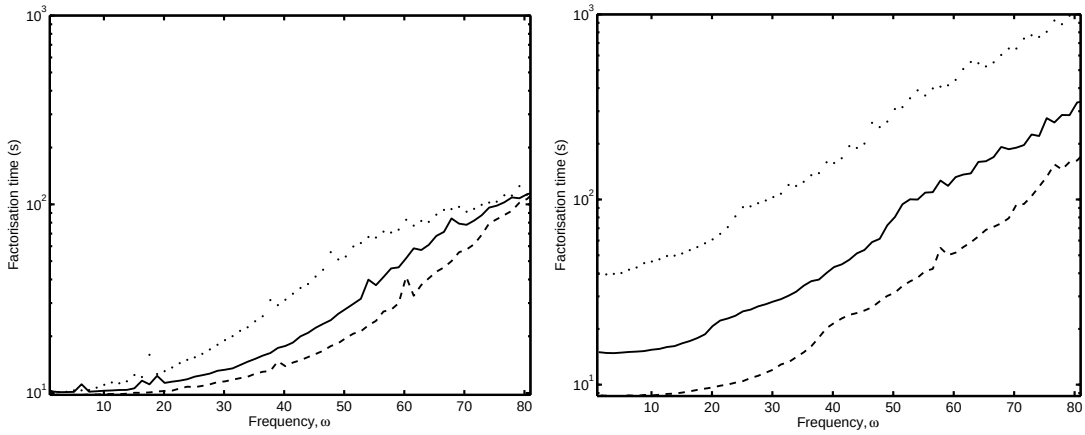

Figure 5.23: Time as a function of frequency. Coarse (- - -). Standard (——). Fine (...). Mesh ratios: left: 1:1, right: 4:1.

5.3.2.2 Flow Case

In this section the flow case is solved using the adaptive scheme with the standard accuracy (5%), for flows with Mach numbers 0.4, 0.2, −0.2, −0.4, and −0.6. The resulting L^2 errors are given as functions of the wavenumber in Figure 5.24.

A general observation is that the upstream error levels are very similar in level, although there is a noticeable increase in error with increasing Mach number. This slight increase may be caused by either pollution error or the boundary conditions of the problem - neither of these possible errors are accounted for by the adaptive order scheme. Furthermore, the scheme does not account for the wave direction across an element, which means that in the presence of flow the worst case scenario must be accounted for, which is the upstream flow case. A consequence of this is that in the presence of downstream flow the method becomes inefficient. This can be seen in the error plots shown. Waves in the downstream case are over-resolved, and thus incur unnecessary computational expense.

As in the no flow case, the uniform mesh error exhibits dips which are associated with the uniformly changing orders of the elements. In the downstream case this mesh is more expensive to solve than the other meshes due to the increased order of the element. The remaining meshes exhibit similar results; the upstream cases exhibit little variation in error with frequency, while the downstream cases are computationally expensive. The only way to make the adaptive scheme more efficient on elements that are subject to both upstream and downstream flow is to have advanced knowledge of the wave direction across each element. However, this is no trivial task, and is left for future work.

The factorisation times as a function of the wavenumber for the uniform mesh and the mesh with an element size ratio of 4:1 are presented in Figure 5.25. These results support the observations already made: the upstream cases take similar amounts of time to be solved, while the downstream cases are inefficient, and incur unwanted additional computational expense.

5.4 Discussion

In order to obtain the most efficient solutions for the higher-order finite element method, a scheme which automatically chooses the optimal order of an element is required.

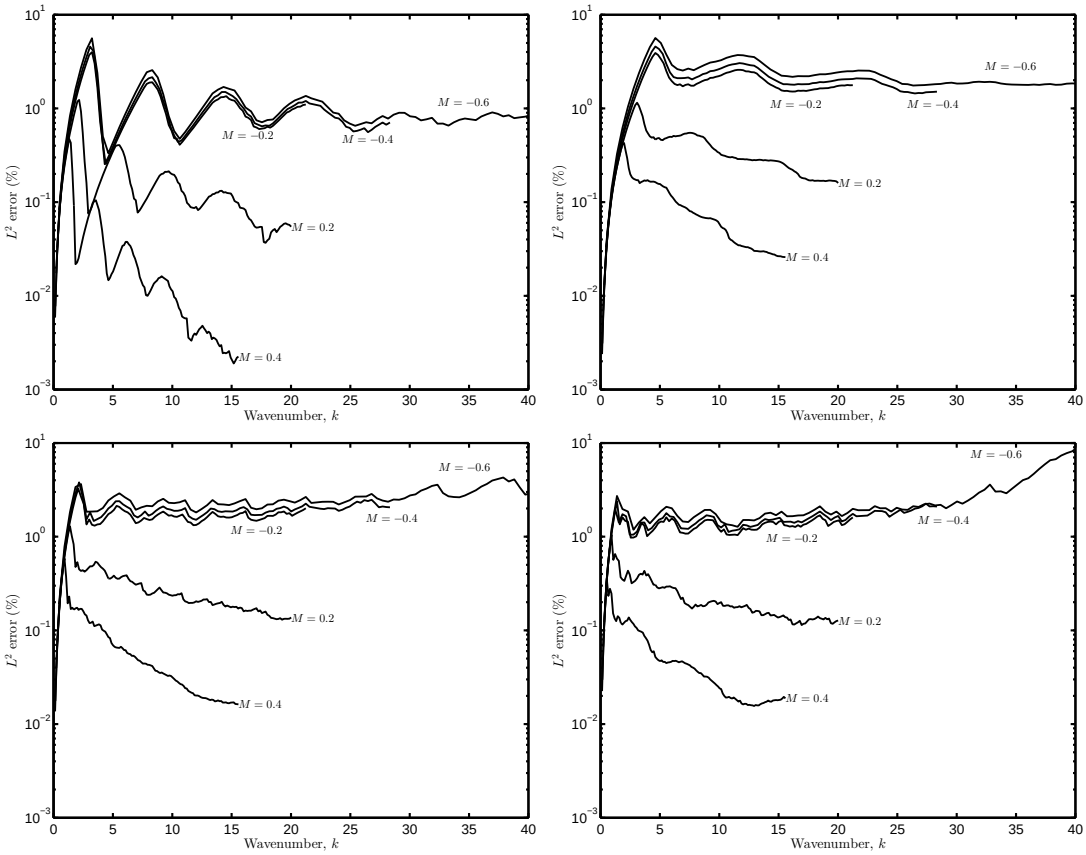

Figure 5.24: L^2 error as a function of wavenumber, for an increasing flow speed. Mesh ratios: top left: 1:1, top right: 5:1, bottom left: 10:1, and bottom right: 4:1.

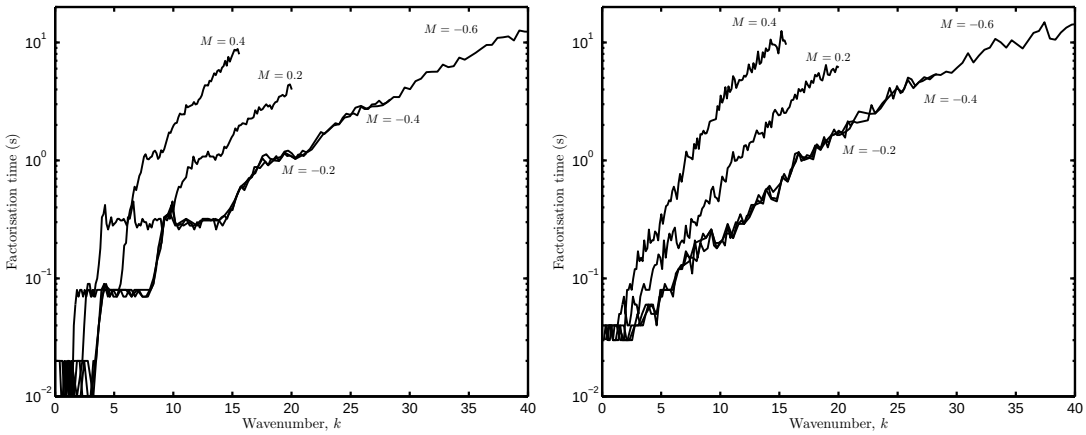

Figure 5.25: Factorisation time as a function of frequency. Mesh ratios: left: 1:1, right: 4:1.

Two existing *a priori* error estimators have been introduced, and their abilities to provide efficient solutions have been assessed. However, both estimators require empirical constants, which are problem and frequency dependent. There is no clear way to generalise these estimators for different problems. Furthermore, for the problem and frequencies considered, it has been shown that these estimators are too conservative, and thus incur unnecessary computational expense.

A new *a priori* error estimator scheme has been proposed. The scheme does not depend on constants, and is robust. It is based on solutions of one-dimensional versions of higher-dimensional elements. The proposed adaptive order scheme has been tested in two and three dimensions, and it has been shown that the scheme enables efficient solutions by placing an upper bound on the L^2 error incurred by the higher-order finite element method. The scheme produces error levels with very little variation with frequency, over a wide range of frequencies. It is remarkable that the one-dimensional estimations provide such good predictions of the error on higher-dimensional elements.

The proposed scheme has also been tested for problems which include flow. For upstream flow fields the results are excellent. However, for downstream flow, propagating waves are over-resolved, making the method very inefficient. The inclusion of flow/wave direction information into the adaptive order scheme is the subject of future work (in which case aliasing error will become an important issue [28]). Note that this adaptive scheme does not account for pollution error (as expected, see Deraemaeker *et al.* [44]). The domain size dependent pollution effect would also be considered in future work.

Considering the requirements of an error estimator [67], presented in Section 5.2, the proposed scheme controls the error in each element very well. (However, it does not account for the pollution error; for very large domains the estimator may fail. In such cases the threshold should be adjusted.) As the desired error level is reduced, the actual error converges (within the limits of the mesh). The scheme provides upper and lower bounds on the actual error (again, within the limits of the mesh, but also only in the absence of significant pollution error). The scheme is simple and inexpensive. With respect to the range of frequencies considered, the scheme appears to be quite robust. In the next section the reliability of the adaptive scheme to produce optimised meshes for a typical aircraft engine intake noise problem will be investigated.

6

Application to an Intake Noise Problem

In this chapter the standard quadratic finite element method, and the proposed higher-order finite element method are used to predict the noise radiated from a generic turbofan engine intake. The problem is introduced, as are the generic geometry, the source model, the characteristic flow field, and the typical liner model. The standard finite element method is used to solve the problem, and the cost of solving the problem using the standard method is investigated. A simplified version of the problem is then solved using the adaptive high-order method (presented in Chapter 5). The cost of the standard method is compared to that of the higher-order method, and the improvement in terms of efficiency of the proposed higher-order method over the standard method is demonstrated.

6.1 Turbofan Intake Noise

Aircraft noise is generated by many different mechanisms, but can be generally categorised into airframe noise and engine noise. An example of the contribution of both sources to the total aircraft noise is shown in Figure 6.1. Although great advances have been made in the reduction of engine noise, it is still a significant component of the total noise output.

The high-bypass ratio engine, commonly found on modern commercial aircraft, is considered. It takes its name from the fact that a large proportion of the air drawn in

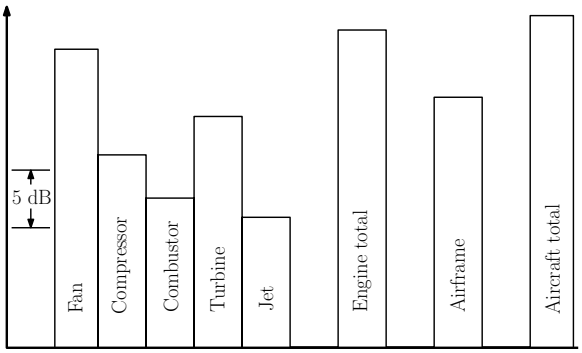

Figure 6.1: An example of the contribution of aircraft noise sources to the total noise output, given for the approach condition (adapted from [96]).

by the fan bypasses the internal workings of the engine. The high-bypass ratio engine has a large fan at the intake, and a small jet engine at the rear. The larger fan enables a lower exhaust jet velocity, while maintaining the thrust given by early engine designs. As the jet mixing noise is related to the jet velocity (to the eighth power of the velocity) the exhaust noise of the high-bypass ratio engine is reduced. This design has enabled significantly quieter aircraft. A comparison of the noise signatures produced by early and modern engine designs is given in Figure 6.2. It can be seen, however, that the cost of the reduction in exhaust noise is an increase in fan noise.

The large fan has implications for numerical modelling. The bigger the domain becomes, the greater the computational cost. However, this increased cost is slightly offset by the generation of lower blade passing frequencies, due to a reduced number of blades. Solutions of lower frequencies require less resources.

The available aeroacoustic code, SysNoise, solves the convected wave equation in terms of the velocity potential field. Using potential flow theory precludes exhaust noise predictions, as it does not account for the vorticity which is present in the exhaust noise problem. Outside of any boundary layers which may be present, the flow field of the intake problem can be assumed to be irrotational. In this chapter, the prediction of intake noise will be presented, while exhaust noise predictions will be considered in Chapter 7.

When noise certification tests of new aircraft entering service are made, three flight conditions are measured. These are take-off (often referred to as sideline), cutback (when the engine power is reduced after take-off), and approach.

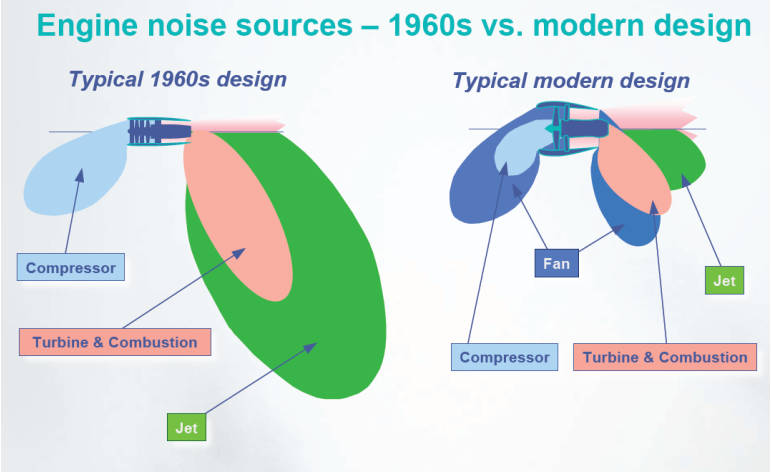

Figure 6.2: Comparison of early and modern aircraft engine designs [69]. Note the reduction in jet noise due to the high bypass ratio design.

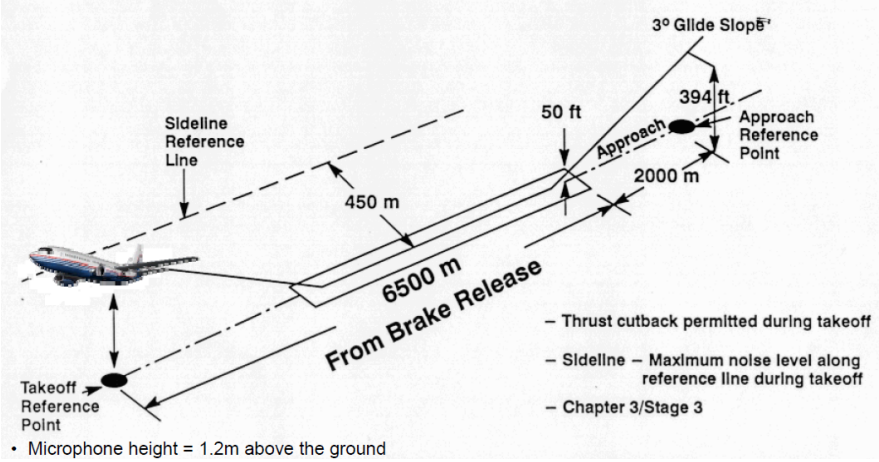

Figure 6.3: Noise Certification measurement positions [103].

The certification measurement positions are depicted in Figure 6.3. In this work we have chosen to investigate only the approach condition. Admittedly, this is the least computationally demanding condition to solve, but it allows improvements of performance to be easily demonstrated, and its use does not change the conclusions found.

In this section the physical problem is introduced, by describing the engine operation and the engine noise sources. A model of the problem will then be introduced. A generic axisymmetric intake geometry, source spectra used to model the noise source at the fan

plane, and flow field characteristics typical of the approach operating condition are presented. Lastly, a model of a typical acoustic liner is given.

6.1.1 Engine Operation and Sources of Noise

A labelled diagram of the inner workings of a typical high-bypass ratio turbofan engine is given in Figure 6.4. A large shrouded fan draws air into the engine. Two pathways are available to the inflowing air: the bypass flow, and the core flow. The bypass flow interacts only with the fan and the outlet guide vanes, it then travels along the bypass duct, and exits at the rear of the engine. Alternatively, the core flow interacts with the fan, and is then compressed, mixed with fuel, and burned in a combustion chamber. The hot air of the core jet then moves through the turbine stage, in which power is extracted from the flow for driving the compression stage. The hot air is then expelled from the engine exhaust. Air expelled from the bypass and core ducts form coaxial jets at the rear of the engine, which mix with the exterior flow.

The noise emitted from a high-bypass turbofan engine comprises fan, core and jet noise. Fan noise is caused by the displacement of the air by the blades, and by the lift and drag on the blades. The wakes produced by the blades interact with the outlet guide vanes, also creating noise. The periodicity of the rotating blades creates tonal noise with a blade passing frequency: $f = nB\Omega_s$, where n is the set of positive integers which account for harmonics of the fundamental frequency ($n = 1$), B is the number of fan blades, and Ω_s is the shaft rotation frequency. In the case of supersonic fan-tip speeds, buzz-saw noise is generated, which comprises multiple pure tones. The fan noise propagates out of the engine inlet and exhaust.

The core noise is composed of compressor, combustion, and turbine noise. Compressor noise is generated by interactions between adjacent blade rows. The spectrum of compressor noise has both broadband and tonal components. Combustion noise is caused by the rapid expansion of small packets of heated air, and has a broadband spectrum. Turbine noise is tonal with a broadband component. The core noise radiates from the exhaust nozzle, where it refracts through the shear layers, which develop between the core and bypass jets, and between the bypass jet and the cool air surrounding the exhaust. As the noise traverses the bypass shear layer spectral broadening of the harmonic tones occurs. Lastly, broadband jet noise is generated by the turbulent mixing of the hot core jet with the bypass jet and the surrounding atmosphere.

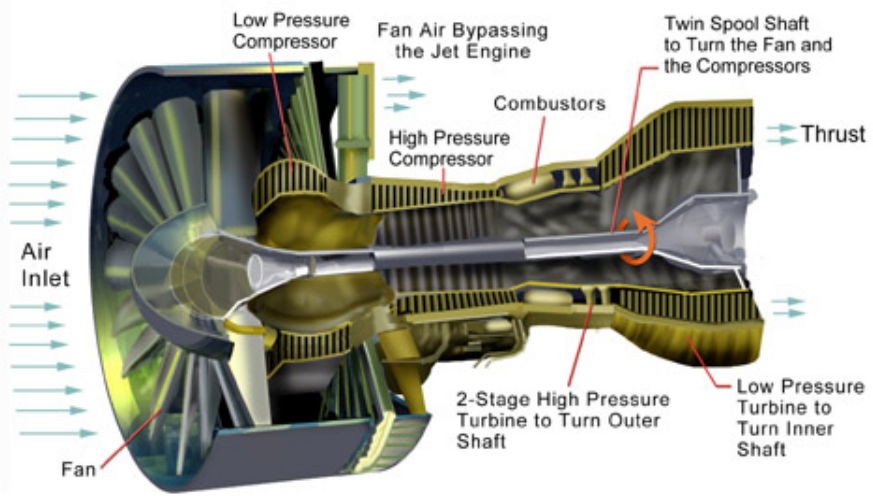

Figure 6.4: High-bypass ratio turbofan engine [113].

The noise generated by the engine propagates to the far-field, and as it does it is subjected to frequency dependent atmospheric absorption, and atmospheric effects brought about by wind, temperature, and humidity gradients. Although these phenomena are of significant importance when determining the sound pressure levels which are observed in the far-field, they are not explicitly dealt with in this work.

6.1.2 Definition of a Generic Intake

The test case used in this work is introduced here. This is a generic engine intake geometry, with typical acoustic source and flow field characteristics. An acoustic liner model is also presented.

6.1.2.1 Engine Intake Geometry

The generic, axisymmetric engine intake geometry used in this work is given in Figure 6.5. The geometry is revolved to generate a fully three-dimensional intake geometry. The spinner has a radius of 0.36 m, and the fan has a radius of 1.2 m. The noise emitted from the fan plane is described using duct modes, which are defined for a uniform duct. Thus, a source plane has been positioned behind the fan plane, at $z = -0.24$ m, to ensure the duct is uniform. An acoustic liner is placed along the interior wall of the intake, between $z = 0.07$ m and $z = 1.15$ m.

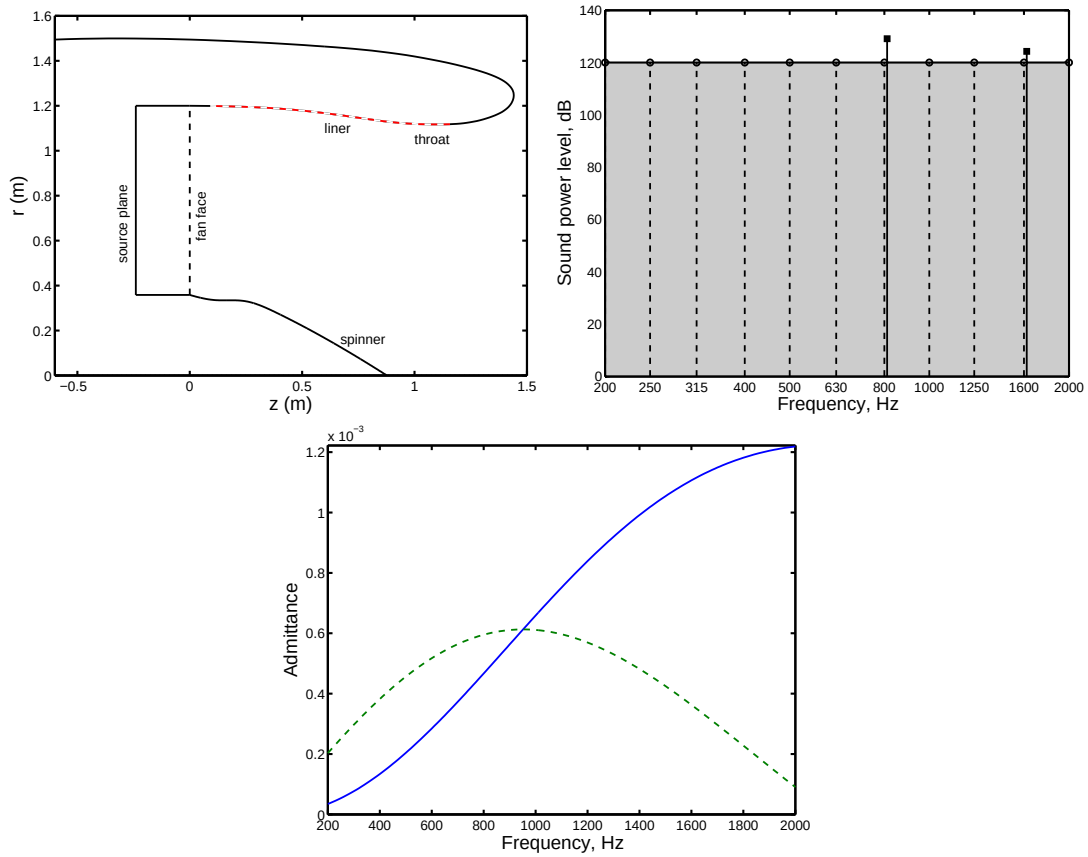

Figure 6.5: Test case. Top left: generic axisymmetric aero-engine intake geometry. Top right: source spectrum for the approach condition. BPF tones (—□), third octave frequency bands (- - -). Bottom: frequency dependent acoustic liner admittance, real (—) and imaginary (- - -) parts.

6.1.2.2 Noise Source Spectra

The noise source spectrum is described using the duct mode definition given in Section 2.4.2. The source is composed of tonal and broadband components.

Tones are present at the blade passing frequency and its harmonics. It is assumed that for a given frequency all cut-on modes have an equipartition of power. The sound power levels at the blade passing frequency and its harmonics are approximated using the formula:

$$L_w = -0.006f + 134.$$

The blade passing frequency is $f = 811$ Hz ($B = 24, \Omega_s = 2028$ rpm).

It is assumed that the broadband noise has a flat frequency response (when using third octave bands), with a sound power level of $L_w = 120$ dB. The broadband noise is assumed to be composed of uncorrelated modes with the same power in each third octave frequency band. A plot of the source spectrum is given in Figure 6.5.

6.1.2.3 Flow Field Characteristics

The flow field is non-uniform within the problem domain. Typically, low flow velocities are expected in the free stream surrounding the engine, while higher velocities will be found at the throat and fan-face of the engine. Flow field characteristics are needed to generate numerical solutions of the flow field.

The following stagnation variables are used: the density is 1.2 kg/m^3, the sound speed is 340 m/s, and the temperature is 20° Celsius. The ratio of specific heats is $\gamma = 1.4$. The engine is assumed to be moving, and the free stream flow surrounding the engine has a Mach number of 0.25. At the engine fan face the Mach number is 0.3. A numerical solution of the flow field will be given in Section 6.2.1.

6.1.2.4 Sound Absorbing Acoustic Liner

Acoustic liners are strategically placed along the interior surfaces of the engine in order to attenuate acoustic emissions. Liners placed in the intake section of a turbofan engine typically have a honeycomb structure, and are covered with a perforated face sheet. The liner begins at the throat of the nacelle and runs along the interior intake wall towards the fan (this can be see in Figure 6.5). It has a length of $0.9r$, where r is the nacelle radius,

The typical impedance of such a liner can be modelled using the formula [107]:

$$\frac{Z}{\rho_0 c_0} = \frac{R}{\rho_0 c_0} - \mathrm{i}\frac{\cot(k_0 h)}{\rho_0 c_0} + \mathrm{i}\frac{k_0 M_f}{\rho_0 c_0},$$

where $R = 2$ Pa·s/m^3 is the resistance, $h = 0.02$ m is the cavity depth, and $M_f = 0.02286$ Pa·s/m^3 is mass reactance. The admittance of the liner is given by the inverse of the impedance. A plot of the frequency dependent acoustic admittance of the typical liner described above is given in Figure 6.5.

6.2 Application of the Standard Finite Element Method

Solutions of the three-dimensional turbofan intake noise radiation problem using the standard finite element method are presented. The flow field calculation is described. The acoustic model is established, and solved using quadratic elements. The numerical results are presented, and the computational costs of the method are discussed.

6.2.1 Flow Field Calculation

The flow field will refract acoustic waves propagating through it, and will vary the acoustic wavelength. A realistic description of the flow field is needed for accurate noise predictions. Thus, FLUENT has been used to compute the flow field around the turbofan intake. A calculation of the steady inviscid compressible flow has been made by solving the Euler equations (2.3,2.4).

The engine intake geometry given in Figure 6.5 is used. The rear of the intake is extruded to form a cylinder, to avoid any unwanted wave reflections. A sphere with a radius of 5 m is placed around the intake. This new geometry is discretised for the flow field computations. Small quadratic elements with a size of 30 mm are used close to the intake to ensure that features of the flow are correctly captured. Larger elements with a size of 500 mm are used in the free field, where it is assumed that the field variables are almost constant. The resulting mesh is given in Figure 6.6, and is composed of approximately 4.3 million cells.

The flow field characteristics for the approach condition (presented in Section 6.1.2.3) are used to provide input data to the fluid dynamics solver. However, other input parameters are required. The static pressures at the boundary of the domain and at the source plane are calculated using the formula:

$$p = p_0 \left(1 + \frac{\gamma - 1}{2} M^2\right)^{-\frac{\gamma}{\gamma - 1}}$$

(taken from the FLUENT manual [58]). The stagnation pressure, p_0, is calculated using the equation of state, $p_0 = \rho_0 R_g T_0$, where R_g is the ideal gas constant (taken to be 287 J/(kg K)), and T_0 is the temperature in Kelvin. The calculated stagnation pressure is 1.01×10^5 Pa, the static pressure at the far-field boundary is 9.67×10^4 Pa, and the pressure at the source plane is 9.47×10^4 Pa. The static temperature at the

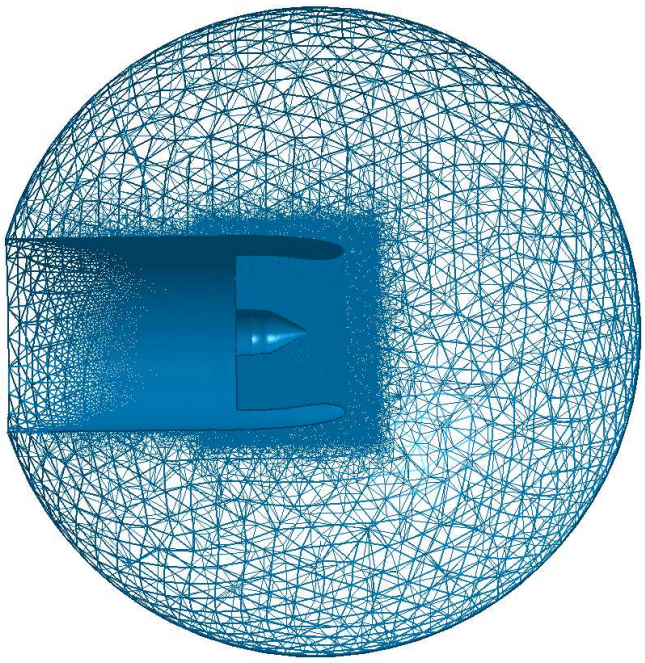

Figure 6.6: The flow mesh.

source plane is also required; it is computed using the formula:

$$T = T_0 \left(1 + \frac{\gamma - 1}{2} M^2\right).$$

The static temperature is $T = 290.4$ K. The mass flow rate at the source plane is obtained from the product of the local density, source surface area, and the local flow speed, yielding 504 kg/s.

The results of the flow computation is given in Figure 6.7. If we consider the velocity field, we see that the highest velocity ($M \approx 0.5$) is found at the engine throat and halfway along the spinner. The flow velocity is the lowest at the leading edge of the engine casing, *i.e.* at the lip of the nacelle. Close to the tip of the spinner the flow has a Mach number of $M \approx 0.2$. The higher velocities, found at the engine throat and at the base of the spinner, shorten the acoustic wavelength. Thus, when designing the acoustic mesh, these regions will require greater resolution. This can be achieved in two ways: the sizes of the elements in that region can be reduced, or the order of the interpolation functions can be increased. The resolution requirements are more relaxed at the lip of the engine and at the tip of the spinner.

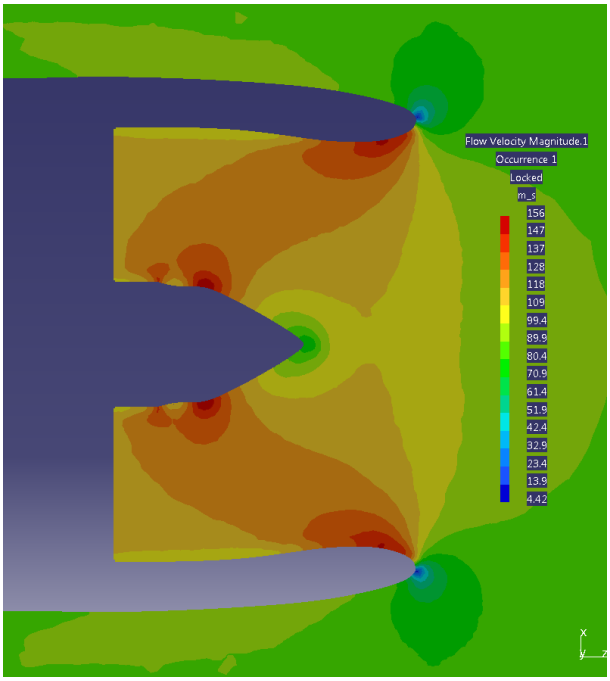

Figure 6.7: The computed velocity field.

6.2.2 Establishment of the Acoustic Model

The convected wave equation written in terms of velocity potential (2.13) is solved in SysNoise using standard quadratic finite elements. The boundary conditions and acoustic meshes are presented in this section.

6.2.2.1 Boundary Conditions

The noise source spectrum given in Section 6.1.2.2 is imposed at the source plane. The boundary condition in this region is a perfectly matched layer (see Section 2.4.3.2), which imposes the source condition, and guarantees that waves reflected back into the intake fan from the sound field are completely absorbed.

The frequency dependent absorption characteristics of the liner surface, expressed in terms of its admittance, A, are related to the wall normal displacement, ξ, (pointing into the wall) through the relation: $Ap = \mathrm{i}\omega\xi$. The acoustic liner admittance (given in Section 6.1.2.4) is included in the model using the Myers boundary condition (2.15). To avoid the second order derivative of the velocity potential which arises in the formulation, the condition is implemented using a technique proposed by Eversman [50].

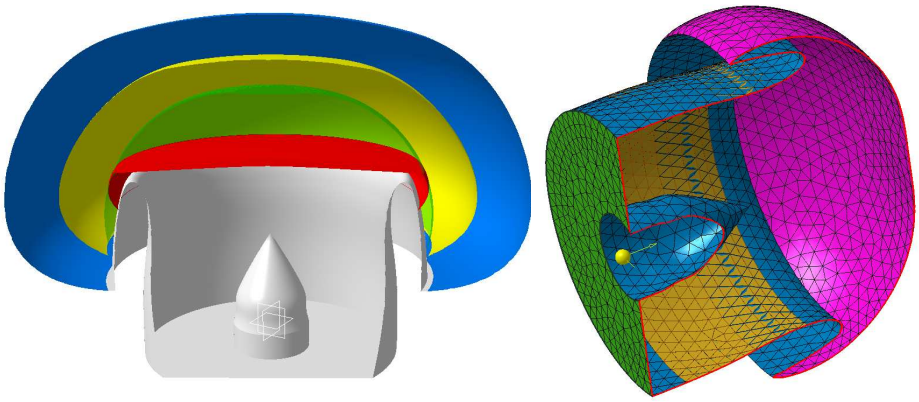

Figure 6.8: Left: boundary truncation study, four acoustic domains: Domain I (blue), Domain II (yellow), Domain III (green) and Domain IV (red). Right: coarse mesh of acoustic Domain III with the source plane (green), the liner (yellow) and non-reflecting boundary condition (pink).

A perfectly matched layer is used at the computational boundary to impose a non-reflecting boundary condition. The far-field is computed using the Kirchhoff integral formulation (Section 2.4.4). The remainder of the geometry is composed of hard walls, at which the velocity potential gradient normal to the surface is set to zero.

6.2.2.2 Acoustic Meshes

The size of the computational domain has a significant effect on the computational resources needed to solve the problem. It is desirable to have as small a domain as possible, but care must be taken so as not to sacrifice the accuracy of the solution. Thus, four domains of varying sizes are presented in this section, which are used in the next section to investigate the effect on the solution of moving the artificial boundary closer to the intake geometry. The four domains are shown in Figure 6.8. It can be seen that the boundary is placed increasingly closer to the lip of the intake. Domain I represents a reference domain, its boundary is positioned in a region where the flow values are close to the free stream quantities (given in Section 6.1.2.3). Domain IV represents an extreme truncation, the boundary is positioned in a region of significant flow variations.

The four domains are discretised using quadratic elements. Each domain is discre-

tised using large elements, with a size of 120 mm, to create a coarse, low frequency mesh, and also with small elements, with a size of 60 mm, to create a fine, higher frequency mesh. Using a resolution of 7 degrees of freedom per wavelength (eq. (4.1)) gives the maximum attainable frequencies of each discretisation; these are 567 Hz and 1.13 kHz, respectively.

Each acoustic mesh is locally refined at the engine throat, due to the increased flow velocity in this region, and locally relaxed on the far-field (perfectly matched layer) boundary, where the flow velocity is lower. The coarse mesh is refined to give a local element size of 102 mm, and relaxed to give elements with an average size of 128 mm. The fine mesh is refined to give a size of 52 mm, and relaxed to give a size of 64 mm. The coarse mesh of acoustic Domain III is shown in Figure 6.8. The three regions in which the boundary conditions are imposed are highlighted.

6.2.3 Numerical Results

In this section we present the post-processed results of the numerical solutions. The values of the interpolated flow field are given, the transmission loss and far-field directivities of the different acoustic domains are compared, and the far-field noise spectrum is considered.

6.2.3.1 Interpolated Flow Field

The flow speed and density, obtained from the flow field computation, are interpolated onto the acoustic domains. The average interpolated values are compared to the computed values, for each of the four coarsely meshed acoustic domains, in Table 6.1. The values at the source plane, and on the far-field (Kirchhoff) surface, are presented. The values on the Kirchhoff surface are used as input parameters to the Kirchhoff integral formulation (see Section 2.4.4), which calculates the acoustic far-field. Thus, it is important that these values agree well with the computed flow field values. Upon comparison, the computed flow field data and the averaged interpolated data are in good agreement, even for the smallest domain, IV. Note that only averaged values are available from the acoustic solver, and so this comparison does not take into account the any fluctuations of the values that may be present on the Kirchhoff surface. Fluctuations can have a significant affect on the far-field calculation, as the integral formulation is based upon the assumption that the flow field does not vary.

	Computed	Interp. I	Interp. II	Interp. III	Interp. IV
Kirchhoff surface					
c_0 (m/s)	343	343	343	343	343
ρ_0 (kg/m^3)	1.14	1.15	1.15	1.15	1.15
u_{0x} (m/s)	0	-0.2$\times 10^{-2}$	-0.1	-0.1$\times 10^{-1}$	-0.5$\times 10^{-3}$
u_{0y} (m/s)	0	-0.6$\times 10^{-2}$	-0.2$\times 10^{-2}$	0.2	-0.8$\times 10^{-2}$
u_{0z} (m/s)	-85.0	-85.0	-84.4	-83.0	-83.8
Source plane					
c_0 (m/s)	341	341	341	341	341
ρ_0 (kg/m^3)	1.11	1.12	1.12	1.12	1.12
M	-0.338	-0.332	-0.331	-0.331	-0.332

Table 6.1: Comparison of the averaged Kirchhoff surface and source plane values with the computed flow field values. Data for each of the coarsely meshed acoustic domains is presented.

6.2.3.2 Transmission Loss

The transmission loss quantifies the power loss of the sound field between the source plane and the far-field. Here, the transmission loss is used to compare the numerical solutions obtained from the different domains, and thus to determine the effect on the accuracy of moving the artificial boundary closer to the engine intake.

The transmission loss is given by:

$$TL = 10 \log_{10} \left(\frac{\mathcal{P}_i}{\mathcal{P}_o} \right),$$

where $\mathcal{P}_i$ is the input power prescribed at the source plane and $\mathcal{P}_o$ is acoustic power radiated to the far-field. The input power is 120 dB (which is divided equally between all cut-on modes), and the output power is calculated on the Kirchhoff surface. The transmission loss as a function of frequency is shown in Figure 6.9. The coarse meshes are used to generate solutions for a range of third-octave band centre frequencies from 50 Hz to 630 Hz. The fine meshes are used to solve the third-octave frequencies ranging from 800 Hz to 1.6 kHz.

Good agreement between the transmission losses given by each domain is found. For the low frequency results the maximum observable difference between Domain I and Domain IV is 0.2 dB. For the higher frequency range it was only possible to solve

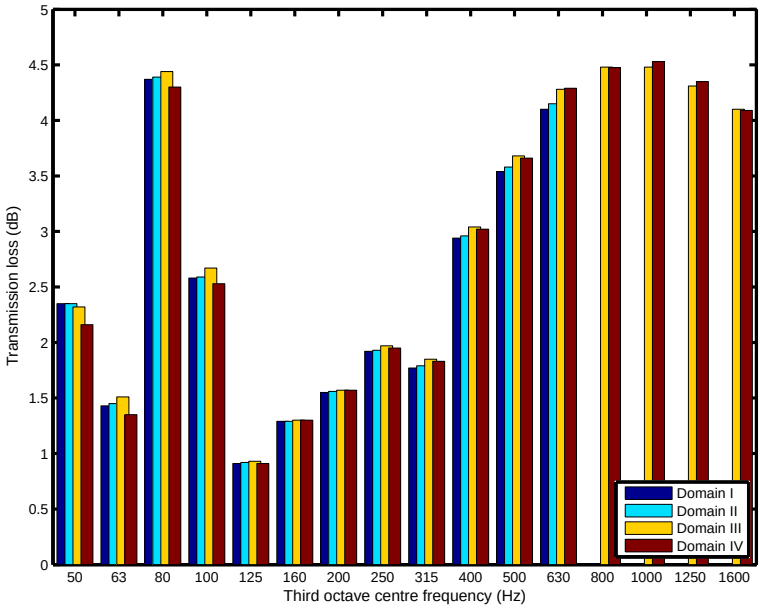

Figure 6.9: Comparison of the transmission losses obtained for the lined inlet duct, for the third-octave band centre frequencies ranging from 50 Hz to 1.6 kHz.

the two smallest domains with the available computational resources. The results given by these two domains are also in good agreement. The comparison of the transmission losses seems to suggest that using the smallest domain (IV) does not reduce the accuracy of the solution.

6.2.3.3 Far-Field Directivity

To assess the influence of the domain truncation on the far-field results, the directivity plots obtained on the different domains are compared between 0° to 120°. Beyond 120° little significant information is expected to be found, as in the rear arc the sound field will be weakest. The directivity plots at 315 Hz and 500 Hz for a multimode noise source on the coarse meshes are given in Figure 6.10. Domains I and II show close agreement along the full arc, while differences of up to 2 dB at 315 Hz, and up to 3 dB at 500 Hz, are observed for Domain IV. This shows that the boundary of Domain IV is too close the nacelle lip. The results for the fine meshes of Domains III and IV are given in Figure 6.11 at 1 kHz and 1.25 kHz. Noticeable differences are observed, and thus it is assumed that the boundary truncation used to generate Domain IV is too crude for accurate predictions, as it is in a region of significant flow variation.

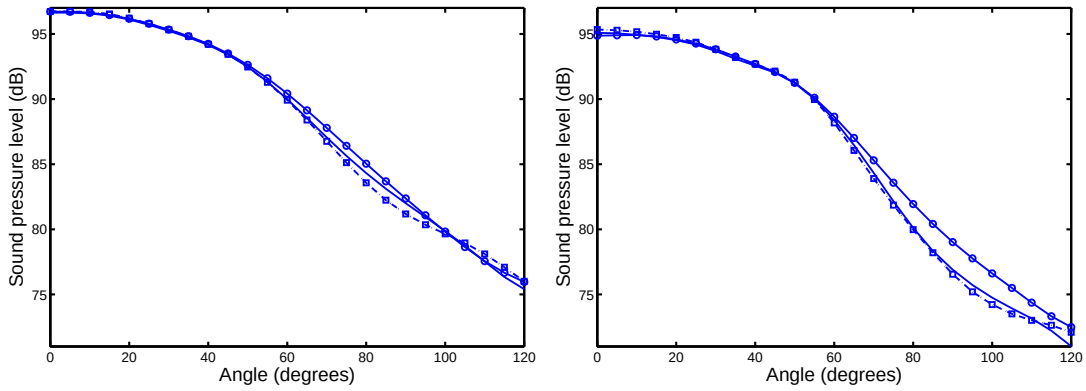

Figure 6.10: Comparison of the far-field pressure directivities at 10 meters, obtained using the coarse meshes, with a multimode noise source at 315 Hz (left) and 500 Hz (right). Domains: I (- - -), II ($\cdots\square$), III (—), and IV (–○).

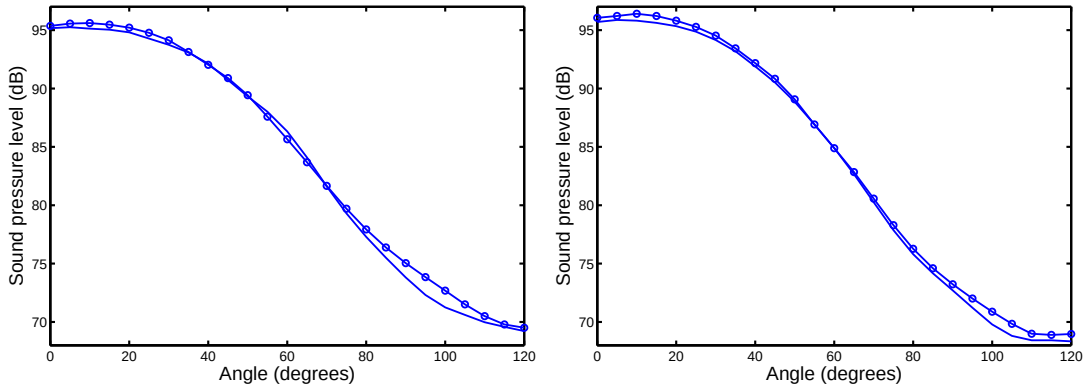

Figure 6.11: Comparison of the far-field pressure directivities at 10 meters, obtained using the fine meshes, with a multimode noise source at 1 kHz (left) and 1.25 kHz (right). Domains: III (—), and IV (–○).

6.2.3.4 Far-Field Spectrum

The complete radiation of the turbofan engine is considered. The coarse and fine meshes of Domain III are used to predict the sound pressure levels at 10 m from the source plane, for the set of third-octave band centre frequencies ranging from 50 Hz to 1.6 kHz, and at various angles to the centreline axis. The sound pressure level is given as a function of frequency, and of angle, in Figure 6.12. The source comprises the broadband noise, and fundamental tone at 1 BPF.

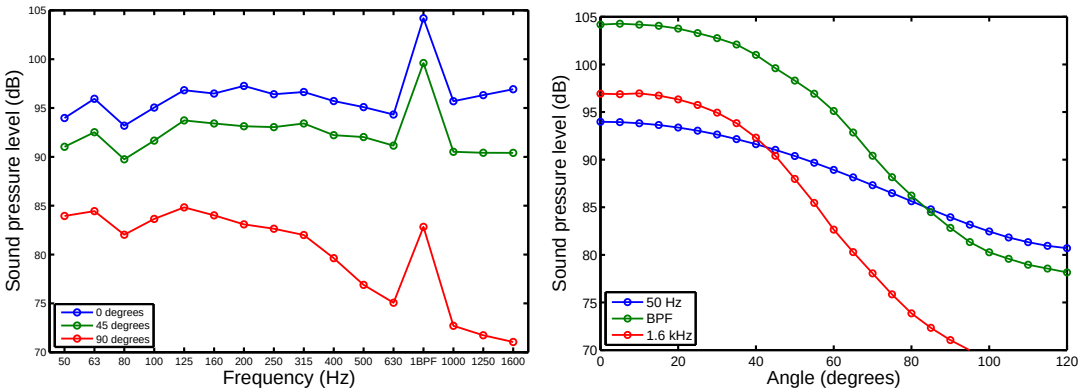

Figure 6.12: Left: complete radiation spectrum of the turbofan engine at 10 meters, at three different angles, in the approach condition over the frequency range [50, 1600] Hz. Both the contribution of the broadband noise and of the BPF tones are included. Right: Directivity patterns for three frequencies.

The broadband pressure level at 0° is almost constant with frequency. It varies by approximately ±2 dB about a level of 95 dB. For the largest angle considered, 90°, the low frequency components play a much more significant role. The noise spectrum is clearly dominated by the 1 BPF tone, which is about 10 dB higher than the average broadband noise. At larger angles this is less obvious, and the 1 BPF pressure levels are comparable to those recorded in the low frequency regime. The directivity of the turbofan changes significantly with the frequency. Radiation differences between the duct axis and the largest angle range from, approximately, 13 dB at 50 Hz to 27 dB at 1.6 kHz.

6.2.4 Computational Costs

The computational costs of the prediction of the noise radiated from the generic engine intake are discussed here. The cost of the low frequency solution (coarse mesh) is compared to the high frequency cost in Table 6.2. The number of nodes, elements, and degrees of freedom are included in the table for the sake of interest, but it is more informative to consider the number of non-zero entries in the global matrix instead. This number quantifies the amount of memory required to store the matrix. The global matrix must be assembled and factorised for every frequency considered. For each cut-on mode (for a given frequency) a new right hand side term for the linear system to be solved must be assembled. The cost of solving the system for each mode

	Coarse (low freq.)	Fine (high freq.)
Number of nodes	103 131	707 362
Number of elements	72 348	511 754
Number of degrees of freedom	153 266	875 618
Number of non-zero entries	5 015 063	27 275 355
Factorisation memory used (GB)	4.31	41
Time per factorization (s)	63.9	707
Solve time per mode (s)	1.37	5.48
Post-process time per mode (s)	1.88	28.7

Table 6.2: Computational costs of the noise solutions using Domain III.

is also included. Finally, a post -processing stage is carried out (for every mode) in which the nodal pressure values and velocity vectors are evaluated, and the Kirchhoff integral is solved.

From the table it can be seen that, between the coarse and fine meshes, the number of non-zero entries increases by a factor of approximately five. The memory and time needed to factorise the global matrix, for each frequency, goes up by an order of magnitude. The time needed to solve the system for each mode increases by a factor of four, while the post-processing goes up by a factor of fifteen.

It can be seen that the time taken to factorise the system for all of the twelve low frequencies (ranging from 50 Hz to 630 Hz) is 12.8 minutes, where as for the four high frequencies the time taken is 47.1 minutes. However, as the frequency increases, so does the number of cut-on modes. The number of cut-on modes as a function of frequency is shown in Figure 6.13. As the number of modes increases, the post-processing becomes the most computationally expensive stage. To cover the twelve low frequencies the total computational time (including matrix assembly) is 25.2 minutes. Due to the very high number of cut-on modes, the total time taken to cover the four high frequencies is 10.3 hours.

The mesh refinement used in this example of the performance of the standard quadratic finite element method doubles the maximum resolvable frequency. However, it can be seen in these results that the factorisation memory and time requirements increase by approximately an order of magnitude between the two meshes; clearly the

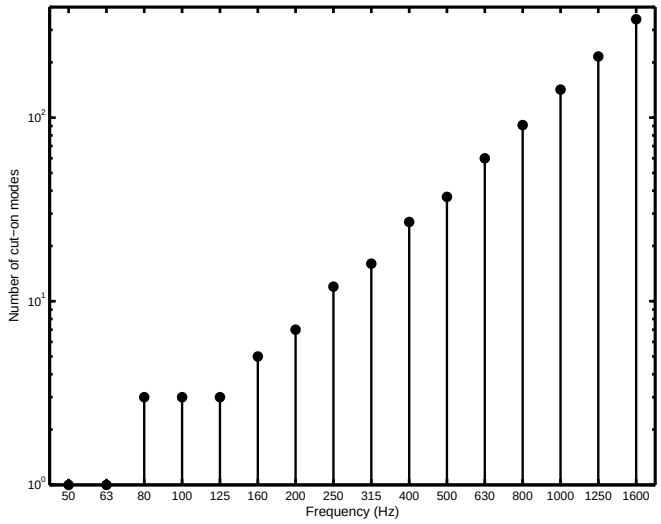

Figure 6.13: Number of cut-on modes per third octave band frequency.

relation between the resolvable frequency and the computational resources required is not linear. Higher frequencies will become increasingly more computational expensive due to this relation, and the total computational time needed will increase dramatically with frequency due to the increasing number of cut-on modes.

6.3 Application of Proposed Adaptive-Order Method

The proposed adaptive higher-order finite element method has been implemented in the commercial software SysNoise (by the sponsoring company, LMS International). Unfortunately, at the time of writing the implementation did not yet provide for the inclusion of a flow field, or the use of a modal source condition. Thus, a version of the model without a flow field is used in this section to demonstrate the efficiency gains afforded by the new method. The plane wave mode only is considered. Using this simplified test case does not affect the performance gains demonstrated in this Chapter.

6.3.1 Meshes

In total, ten meshes have been created. All of the meshes use quadratic elements to describe the geometry. Eight of the meshes are designed for solution using the standard quadratic finite element method, while the remaining two meshes are designed for the

Max. frequency (Hz)	h (mm)	nodes	elements	degrees of freedom
315	310	8 593	5 611	15 563
400	240	17 911	12 002	29 906
500	190	32 570	22 201	51 300
630	150	72 043	50 465	103 428
800	120	129 587	91 691	177 727
1000	97	249 400	178 629	322 475
1250	78	517 945	375 492	630 610
1600	60	1 053 697	769 074	1 243 087

Table 6.3: Data of the meshes used for the standard quadratic finite element method.

Max. frequency (Hz)	h (mm)	nodes	elements	degrees of freedom
1600	300	9 492	6 226	frequency dependent
2300	200	24 363	16 185	frequency dependent

Table 6.4: Data of the meshes used for the adaptive higher-order finite element method.

adaptive order finite element solutions. Details of the meshes used for the quadratic finite element method are presented in Table 6.3, while mesh details for the adaptive order finite element method are presented in Table 6.4.

Meshes which are intended to be used for the quadratic method have been created for each of the third-octave centre frequencies, ranging from 315 Hz to 1.6 kHz. The desired element size of each mesh has been determined using seven degrees of freedom per wavelength (eq. (4.1)). In this section solutions are obtained for the case when the flow is zero, thus the meshes are approximately uniform (as no regions which require refinement exist). The most refined mesh ($h = 60$ mm) is used to provide reference solutions with which to confirm the validity of solutions obtained using coarser meshes.

Of the two meshes created for the polynomial finite element solutions, one is used to investigate the efficiency gain made possible by the adaptive higher-order elements, while the other is used to investigate the highest achievable frequency with the available resources. The sizes of the elements have been chosen to resolve frequencies of 1.6 kHz and 2.3 kHz, respectively, again by ensuring that seven degrees of freedom per wavelength are used.

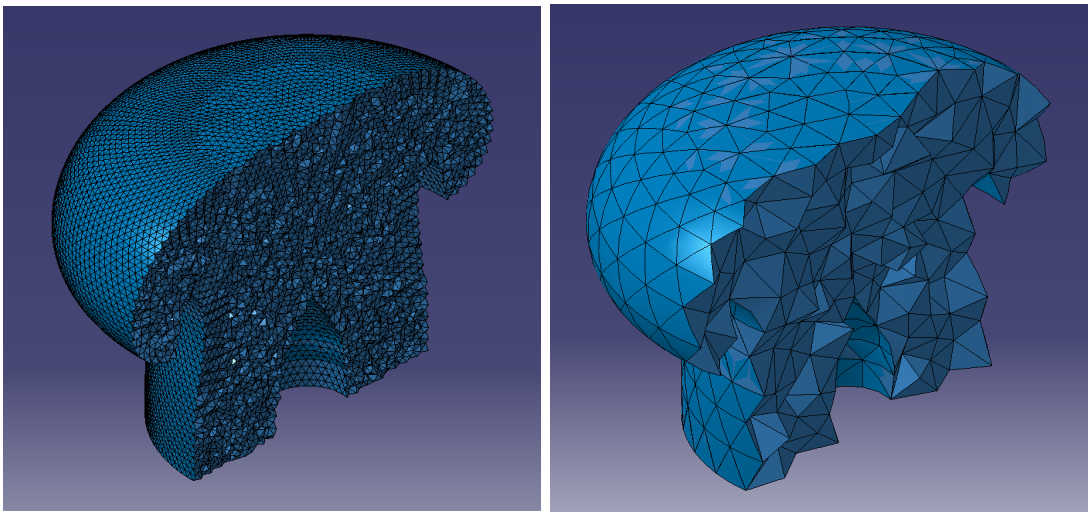

Figure 6.14: Examples of the meshes used for intake noise propagation predictions. Left: quadratic FEM (reference) mesh: $h = 60$ mm, right: adaptive order FEM mesh: $h = 300$ mm.

Examples of the meshes are given in Figure 6.14. It can be seen that the adaptive higher-order method mesh is much coarser than the quadratic method mesh. The geometry of the problem is still respected by making use of quadratic geometry elements. Furthermore, from a practical point of view, the coarser mesh is much less demanding of resources when pre-processing the model, *i.e.* when meshing, selecting boundary condition surfaces, or mapping the flow.

6.3.2 Far-Field Directivities

In this section the directivities of the plane wave mode emitted from the generic lined turbofan engine, predicted using quadratic elements and higher-order elements, are compared. This comparison aims to confirm that the problem geometry is properly respected by the coarse mesh. The predicted directivities at 10 m from the fan plane for each of the third-octave frequencies are given in Figures 6.15 and 6.16. It can be seen that for all solutions the main lobes of the directivity patterns are in good agreement. At larger off-axis angles the agreement is not as good, but these sound pressure levels are very low in comparison to the maximum levels, and thus these differences should not have a noticeable effect on the accuracy of the predictions. These results imply that the problem geometry is respected by the coarse mesh, and that the higher-order

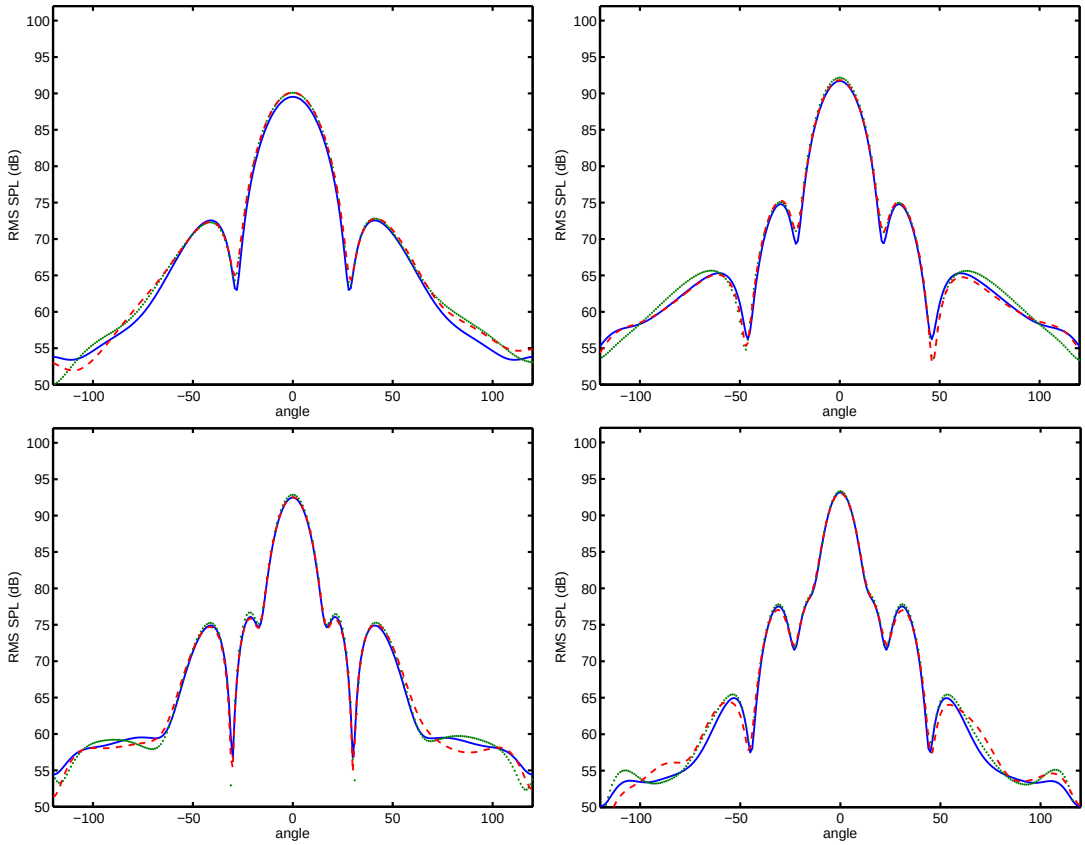

Figure 6.15: Sound pressure level of the plane wave mode as a function of polar angle. Top left: 315 Hz, top right: 400 Hz, bottom left: 500 Hz, and bottom right: 630 Hz. Reference solution (—), standard quadratic solution (...), higher order solution (- - -)

solutions agree with the reference solution.

6.3.3 Memory and Time Requirements

The standard method and the higher-order method are used to solve the problem on a machine with 48 GB of memory, operating at 2.53 GHz, with 8 cores. The computational resources required to factorise the global matrix are investigated. In Figure 6.17 the memory and time requirements of the quadratic finite element method are compared to those of the higher-order finite element method. A general observation is that both measures of cost exhibit the same trend, in that the higher-order solutions are increasingly more efficient than the standard finite element solutions with increasing frequency. This is due to the reduced factorisation memory needed by higher-order

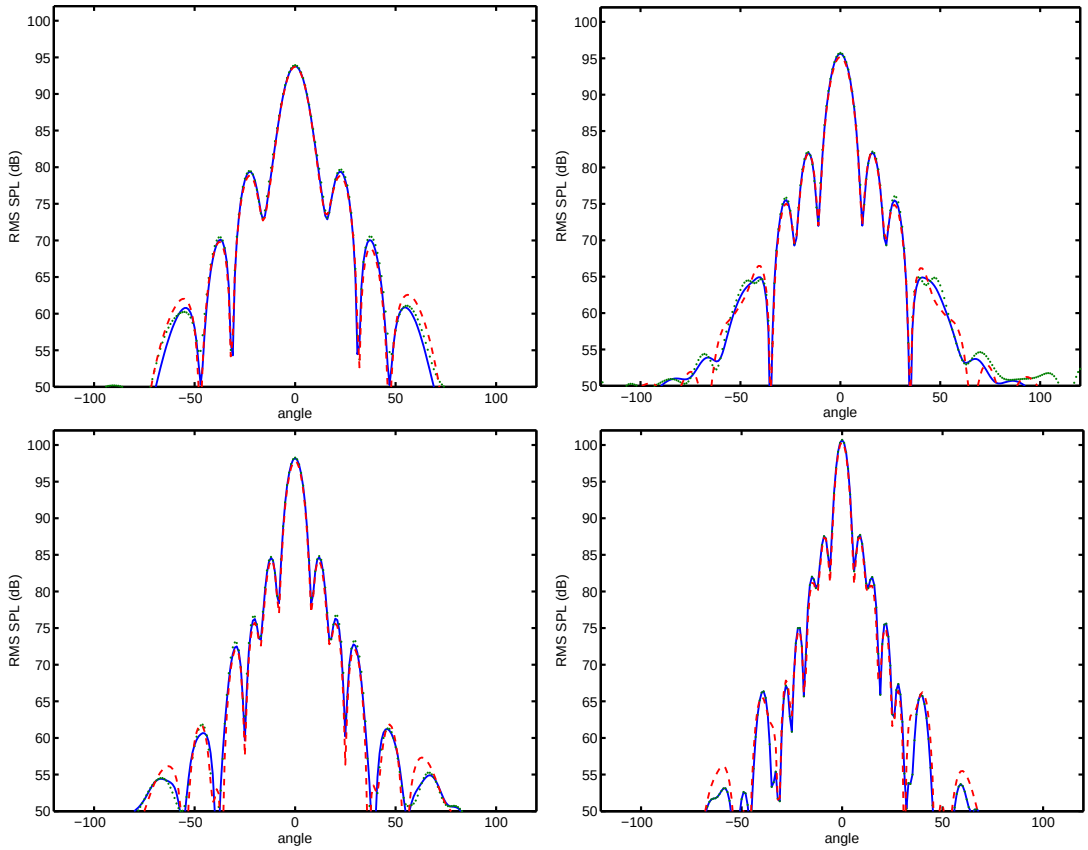

Figure 6.16: Sound pressure level of the plane wave mode as a function of polar angle. Top left: 800 Hz, top right: 1 kHz, bottom left: 1.25 kHz, and bottom right: 1.6 kHz. Reference solution (—), standard quadratic solution (...), higher order solution (- - -)

functions. At low frequencies both methods require, roughly, the same amount of memory and time. This is as expected since they both use low order elements. However, as the frequency is increased the higher-order method becomes increasingly more efficient. For a frequency of 1.6 kHz the standard quadratic method requires approximately 40.7 GB of memory, whereas the polynomial order method requires only 11.5 GB. The total time spent factorising the matrices using the standard quadratic method was 27.2 minutes, while the total time spent factorising the matrices when using the higher-order element method was 5.17 minutes. It is worth noting that each quadratic element solution requires a new mesh and problem definition, which consumes a great deal of time for the end-user. Furthermore, the higher-order method will maintain the accuracy of the solution at much higher frequencies than the standard method, as higher-order

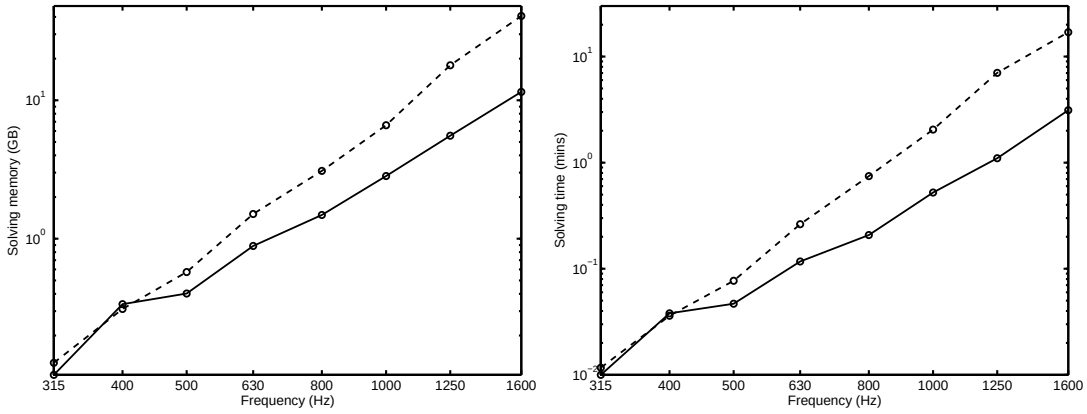

Figure 6.17: Resources required to solve the linear system, as a function of frequency. Standard quadratic solution (- - -). Higher order solution (—).

functions tackle dispersion error more effectively than lower-order functions. It is clear that a significant gain in efficiency has been achieved.

To reduce operator time in industry it is not uncommon to generate a single mesh and solve the linear system for a range of frequencies. This technique is reproduced here for further comparison. The quadratic element reference mesh is compared to the more refined ($h = 200$ mm) higher-order element mesh. The memory requirements of both solutions are given as a function of frequency in Figure 6.18. It can be seen that the higher-order method provides more efficient solutions. The standard quadratic solutions require about 40.7 GB of memory for every frequency (as the same mesh is used for each frequency) whereas the higher-order element requirements vary with frequency. The higher order solution at 1.6 kHz requires approximately 14 GB. Furthermore, the maximum resolvable frequency has been raised from 1.6 kHz (obtained using the most refined standard quadratic mesh) to 2.3 kHz when using the higher-order method, for approximately the same amount of available memory (the higher-order element method requires 36.8 GB at 2.3 kHz). This is an increase of maximum resolvable frequency of 43.8 %. The total time taken to solve the standard finite element problem was 5 hours and 9 minutes, whereas only 37 minutes were needed to solve the higher order problem. In this instance, the higher-order method is 13.7 times faster than the standard quadratic method. Included in Figure 6.18 are the minimum, most common and maximum polynomial orders of the adaptive order method, as a function of frequency. We observe that, qualitatively, the maximum order exhibits the same trend as seen in

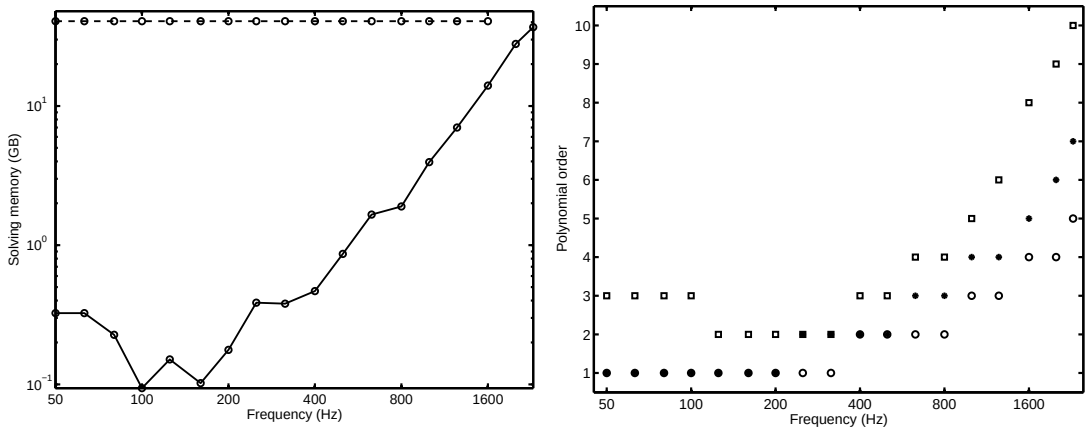

Figure 6.18: Comparison of reference mesh ($h = 60$ mm, quadratic elements) and refined pFEM mesh ($h = 200$ mm). Standard quadratic solution (- - -). Higher order solution (—). Maximum order (□). Most common order (●). Minimum order (○)

the plot of the factorisation memory given as a function of the frequency.

6.4 Summary of Conclusions

A generic model of a turbofan engine intake noise problem has been presented. The standard quadratic method has been compared to the proposed higher-order method, using a version of the physical problem which omits the flow field (as at the time of writing this feature was not available in the prediction software used). It has been shown that the cost of solving this problem is greatly reduced when the proposed higher-order method is used instead of the standard quadratic method. When solving the problem for eight third-octave centre frequencies, ranging from 315 Hz to 1.6 kHz, the factorisation time is reduced from 27.2 minutes (using quadratic elements) to 5.17 minutes. Note that this saving will be even more significant when all cut-on modes are solved for. For the highest frequency solvable by both methods, *i.e.* 1.6 kHz, the factorisation memory requirement has dropped from 40.7 GB (standard FEM) to 11.5 GB. The higher-order method presented in this work is significantly more efficient than the standard method, and can be used to solve problems at higher frequencies than can the standard quadratic method.

7

Exhaust Noise Prediction

In the preceding chapters work concerning the development of a more efficient computational method for convected wave problems was presented. In this chapter we consider a reformulation of the potential flow problem to predict the noise radiated from turbo-fan engine exhausts. Solving these problems for a potential flow is considerably less computationally expensive than solving the linearised Euler equations, but the assumption of potential perturbations excludes the vorticity from the mean flow; this is an essential feature of sheared flow acoustic problems, as the acoustic field becomes coupled to the flow field.

7.1 Background and Motivation

Exhaust noise predictions are generally obtained by solving the Linearised Euler Equations (LEE) in the time domain. Finite-difference methods are commonly used for this purpose, typically with compact schemes or dispersion-relation-preserving schemes, see for instance the work by Panek *et al.* [119], and Chen *et al.* [39]. When using unstructured grids, the discontinuous Galerkin methods (DGM) seem to be the method of choice [30, 40, 127]. Using these computational approaches, solutions have been obtained for axi-symmetric and three-dimensional models of turbofan exhausts at realistic frequencies.

A specific issue associated with time-domain solutions of the LEE is that they can include Kelvin–Helmholtz instabilities which develop along the jet shear layer. This part of the solution can, in some cases, overwhelm the acoustic solution. In practice the

growth of these instabilities is limited by the development of the shear layer thickness and is saturated by non-linearities. Several methods have been proposed to suppress or control these instabilities. Bogey *et al.* [33] used a technique called Gradient Term Suppression (GTS) to remove the terms associated with the instabilities. The Acoustic Perturbation Equations (APE) have been introduced to remove the hydrodynamic part of the solutions [52]. Huang *et al.* [79] compared GTS and the APE and found that they provide similar results, while Tester *et al.* [145] have shown that suppressing gradient terms has a small but measurable effect on the acoustic far-field. Bailly & Juvé [21] modified the LEE by introducing non-linear terms to saturate the instability waves. The full non-linear Euler equations are also used, for instance by Redonnet *et al.* [125].

An alternative approach is to solve the LEE in the frequency-domain. It has been suggested that solutions obtained in the frequency domain using a direct solver are free of instability waves [2]. Zhao & Morris [159] and Rao & Morris [124] used a DGM and a Streamlined Upwind Petrov-Galerkin finite element method to solve the LEE in the frequency-domain, and produced solutions which were not polluted by instability waves. Özyörük [117, 118] used a finite difference scheme to make turbofan exhaust predictions in the frequency domain using a direct solver.

Frequency-domain solutions of the LEE using direct solvers can be computationally expensive, as four or five unknowns must be solved for and a fine grid must be used to resolve the hydrodynamic waves. A simpler model can be used if one assumes that the total flow, i.e. mean flow and perturbed flow, is irrotational. The benefit of the linearised potential theory is that it only involves a scalar convected wave equation and is therefore much cheaper and faster to solve [132]. This model is now well established in industry and is valid for several applications, such as noise radiation from turbofan inlets. However, by definition it cannot be applied to cases with shear flows or thick boundary layers. Note that it may also be possible to make use of the Möhring equation [101], but (to date) validations of this equation have not been published.

The main objective of this investigation is to extend the linearised potential theory to include shear layers so as to represent the refraction effects. Previous attempts have been made to represent shear layers with linearised potential theory. Eversman & Okunbor [51] modelled the shear layer using a vortex sheet across which the continuity of acoustic particle velocity and continuity of pressure are imposed. The convected wave equation is solved using standard finite elements. More recently, Manera *et al.* [95]

compared time-domain LEE and potential flow solutions for exhaust noise problems. They also used a vortex sheet, but enforced the continuities of normal displacement and of pressure instead.

In this chapter we revisit the models previously proposed in references [51, 95] and we address several outstanding issues: the application of a Kutta condition at the beginning of the vortex sheet, the discretisation of the vortex sheet, and a quantitative validation and comparison of these finite element models. In particular, we explicitly include the Kutta condition, an upwinding method is proposed to discretise the vortex sheet, and finally the different finite element formulations are validated against a semi-analytic model.

This chapter is structured as follows: we introduce the physical problem, by describing the vortex sheet, the Kutta condition, and the Kelvin-Helmholtz instability. We review the governing equations, derive the potential theory model, and present the necessary continuity conditions. We derive the existing formulations, the proposed formulation, and we introduce a novel streamline upwind Petrov-Galerkin method. Details of the implementation of the method to a benchmark problem are given, and the results are discussed. Finally, a summary of the main findings is presented.

7.2 Description of the Problem

An example of the jet exhaust of a turbofan engine exhaust is illustrated in Figure 7.1. Coaxial jets issue from the bypass and core ducts, and shear layers develop at the interface between these jets, and between the bypass jet and the free stream flow. Broadband noise and tonal noise are generated upstream of the core and bypass ducts. This noise propagates along the ducts and radiates through the jets and into the far field. The sound waves will be diffracted by the trailing edges of the ducts, and refracted by the mean flow gradient as it propagates through the shear layers. It is essential to capture these effects to accurately predict the sound radiated to the far field.

7.2.1 Vortex Sheet

The shear layer of a jet is initially very thin close to the nozzle and gradually grows in the downstream direction. The convected wave equation (2.13) does not allow sheared flows, such as a mixing layer, to be included as a base flow. Instead we implement a

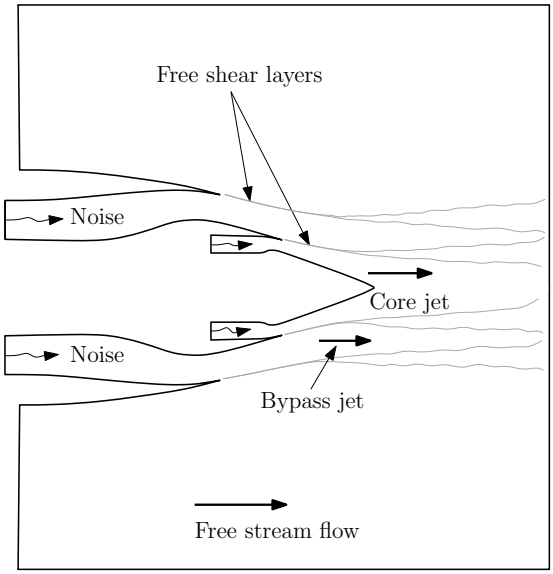

Figure 7.1: Diagram of the engine exhaust problem.

vortex sheet, which is essentially a surface of discontinuity in the mean flow representing an infinitely thin shear layer. This approximation is only valid when the acoustic wavelength is much larger than the shear layer thickness. This is the case either close to the nozzle and/or at low frequencies.

To fix ideas, let us consider two different flow regions Ω_1 and Ω_2 separated by a vortex sheet Γ, as shown in Figure 7.2. The trailing edge of the nozzle, from which the vortex sheet originates, is labelled Γ_0. The flow properties in each region are denoted by subscripts 1 and 2. On Γ the mean flow is tangential: $\boldsymbol{v}_{01} \cdot \mathbf{n} = \boldsymbol{v}_{02} \cdot \mathbf{n} = 0$, where $\mathbf{n}$ is the unit normal to Γ pointing into Ω_2. The solutions on either side of the vortex sheet are coupled by imposing kinematic and dynamic conditions [149].

For an inviscid fluid, the dynamic condition is the continuity of pressure:

$$p_1 + \xi \frac{\partial p_{01}}{\partial n} = p_2 + \xi \frac{\partial p_{02}}{\partial n}, \tag{7.1}$$

where ξ is the normal displacement of the vortex sheet. Note that the terms involving mean pressure gradients are present because the continuity of pressure for the total flow is imposed on a surface which oscillates with displacement ξ. Using Euler's equation for the base flow we can write:

$$\frac{\partial p_0}{\partial n} = -\rho_0 \left[(\boldsymbol{v}_0 \cdot \nabla) \boldsymbol{v}_0 \right] \cdot \mathbf{n} \, . \tag{7.2}$$

Thus we see that the second terms on both sides of Equation (7.1) are related to the change in direction of the fluid elements along the vortex sheet.

The kinematic condition derived by Myers [110] is obtained by linearising the continuity of total normal velocity along a moving interface:

$$\boldsymbol{v}_1 \cdot \mathbf{n} = \frac{\mathrm{d}_{01}\xi}{\mathrm{d}t} - \xi \mathbf{n} \cdot [(\mathbf{n} \cdot \nabla)\boldsymbol{v}_{01}] \quad \text{and} \quad \boldsymbol{v}_2 \cdot \mathbf{n} = \frac{\mathrm{d}_{02}\xi}{\mathrm{d}t} - \xi \mathbf{n} \cdot [(\mathbf{n} \cdot \nabla)\boldsymbol{v}_{02}] \ , \tag{7.3}$$

where the terms involving normal gradients account for the curvature of the vortex sheet. This condition can be understood to represent the continuity of the normal acoustic displacement across the vortex sheet [149].

As an alternative to (7.3), the continuity of normal acoustic velocity has sometimes been used. This can be written as:

$$\boldsymbol{v}_1 \cdot \mathbf{n} = \boldsymbol{v}_2 \cdot \mathbf{n} \ , \quad \text{or} \ , \quad \frac{\partial \phi_1}{\partial n} = \frac{\partial \phi_2}{\partial n} \ . \tag{7.4}$$

7.2.2 Trailing Edge

The behaviour of the fluid at the trailing edge has a noticeable effect on the acoustic far field. The acoustic and hydrodynamic fields are coupled at the trailing edge, and, as a consequence, the amount of vorticity shed from the trailing edge and the behaviour of the sound field at that point are closely linked.

A basic physical property of the problem is that the streamline at the trailing edge is continuous, which amounts to requiring that the normal displacement of the vortex sheet at the trailing edge must be zero.

A stronger constraint is the Kutta condition, for which the normal acoustic velocity should also vanish at the trailing edge. Since we have $\boldsymbol{v} \cdot \mathbf{n} = \mathrm{d}_0\xi/\mathrm{d}t$ the streamwise gradient of the normal displacement at the trailing edge vanishes. The Kutta condition indicates that all the vorticity is shed from the trailing edge and, in that case, that the acoustic pressure vanishes with $p \sim \sqrt{r}$ near this point where r is the distance from the trailing edge. If the Kutta condition is not satisfied, the acoustic pressure is singular at the trailing edge and behaves like $p \sim 1/\sqrt{r}$.

This condition has been included in analytic models of exhaust duct problems. Rienstra [128] introduced a complex parameter which could be continuously varied to control the amount of vorticity shedding. Gabard & Astley [62] used this method when modelling the noise radiating from a jet pipe (the so-called Munt problem [109]).

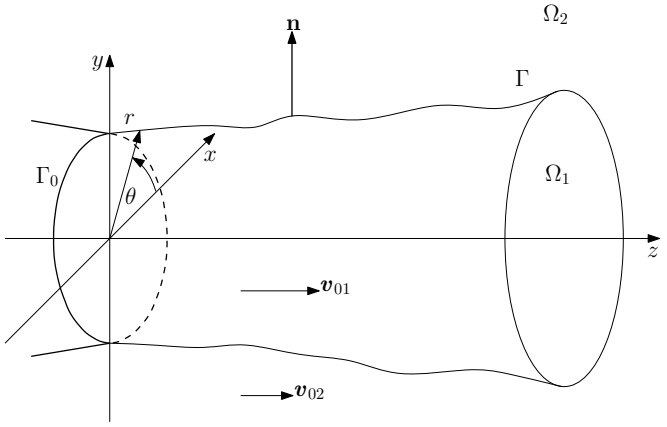

Figure 7.2: A schematic of a three-dimensional vortex sheet Γ emanating from the trailing edge Γ_0 of a nozzle.

They observed that vorticity shedding has no significant effect on the main lobe in far-field directivities, but did find that vorticity shedding noticeably affects the pressure amplitude in the rear arc.

An example of vortex shedding from a trailing edge, in the case of a uniform mean flow with an imposed Kutta condition, is given in Figure 7.3. Also included in the figure is a solution of the velocity potential field in the presence of non-uniform mean flow, but without any Kutta condition, note the refraction of the wave as it propagates the vortex sheet. This data has been obtained using the analytic solution which will be used to test the numerical predictions, yet to be presented.

7.2.3 Kelvin–Helmholtz Instability

The shear layer can exhibit Kelvin–Helmholtz instabilities. The onset of this hydrodynamic instability is characterized by the Strouhal number $St = f\delta/\Delta u$, where f is the frequency, δ the shear layer thickness and Δu is the velocity difference [89].

The instability wave will initially grow exponentially along the shear layer. If included, non-linear effects will saturate the growth of this instability. Even in a linear model, the gradual increase of the shear layer thickness will turn the instability wave into a decaying wave. When approximating the shear layer by a vortex sheet model, it is important to recognise that the vortex sheet model is unstable at any frequency since we take $\delta \to 0$ [48]. Furthermore, since the growth of the shear layer thickness is

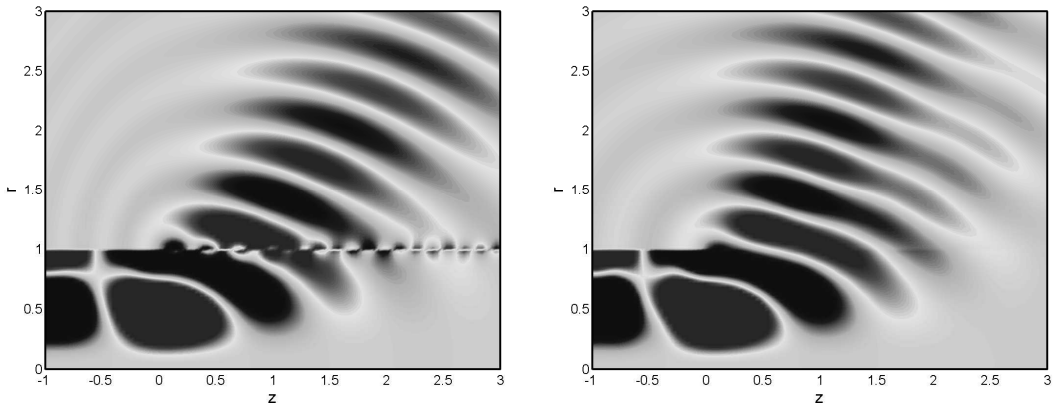

Figure 7.3: An analytic solution of a straight vortex sheet leaving a straight duct, the duct is found at $r = 1$, and ends at $z = 0$. The Helmholtz number kR (where $k = \omega/c_0$ is the wavenumber, $c_0 = 1$ and R is the duct radius) is 10. The excitation source is the second radial mode with azimuthal order $m = 3$. Left: Uniform mean flow ($v_{01} = v_{02} = 0.45$) with Kutta condition imposed at the trailing edge. Note the vorticity shedding. Right: Non-uniform mean flow ($v_{01} = 0.45$, $v_{02} = 0.1$) without the Kutta condition. Note the acoustic refraction across the vortex sheet.

not included the instability wave will grow indefinitely along the vortex sheet. This introduces significant challenges for numerical predictions inasmuch as such instabilities may obscure the acoustic part of the solution. Finally, the causal solution for the initial value problem does include the instability [42]. However, when solved in the frequency domain it is expected that a non-causal solution excluding the instability is obtained [2]. We will comment further on this issue when we discuss the properties of the finite element models presented.

7.3 Finite Element Models

The wave equation (2.13), written in terms of velocity potential, is solved on each acoustic domain, Ω_1 and Ω_2, using a standard finite element method based on the usual variational formulation (3.1).

The integral on the boundary $\partial\Omega$ is modified to incorporate the appropriate boundary conditions. Here we concentrate on the implementation of the vortex sheet at the surface Γ, as presented in Section 7.2. In the following discussion, we denote by A all the terms involved in the formulation of the vortex sheet. Since the mean flow is

parallel to the vortex sheet, the initial definition of these terms is:

$$A = -\int_\Gamma \rho_{01}\overline{W_1}\frac{\partial\phi_1}{\partial n} - \rho_{02}\overline{W_2}\frac{\partial\phi_2}{\partial n}\,\mathrm{d}\Gamma\ . \tag{7.5}$$

7.3.1 Existing Formulations

The rationale for the formulation proposed by Eversman & Okunbor [51] is (i) to allow for a discontinuity in the velocity potential along Γ, and (ii) not to introduce other additional degrees of freedom. In this formulation the integral in (7.5) vanishes, which requires a continuous mean density across Γ (e.g. an isothermal jet), and the continuity of normal velocity (7.4).

The continuity of pressure is enforced by means of a Lagrange multiplier, that is by adding the following term to the variational formulation (3.1):

$$A = -\lambda\int_\Gamma \overline{\left(\rho_{01}\frac{\mathrm{d}_{01}W_1}{\mathrm{d}t} - \rho_{02}\frac{\mathrm{d}_{02}W_2}{\mathrm{d}t}\right)}\left(\rho_{01}\frac{\mathrm{d}_{01}\phi_1}{\mathrm{d}t} - \rho_{02}\frac{\mathrm{d}_{02}\phi_2}{\mathrm{d}t}\right)\mathrm{d}\Gamma\ , \tag{7.6}$$

where λ is the Lagrange multiplier. Note that the terms involving the displacement ξ in (7.1) are not included since the formulation was developed for a cylindrical vortex sheet. The term under the overbar is the test function suggested in [51].

It is possible to extend this formulation to the case with different mean densities across the vortex sheet. To that end, we have to introduce a variable ν such that

$$\frac{\partial\phi_1}{\partial n} = \frac{\partial\phi_2}{\partial n} = \mathrm{i}\omega\nu\ .$$

This variable can be interpreted as the normal displacement that would be observed in the absence of mean flow and we denote the corresponding test function by η. Instead of a Lagrange multiplier for the continuity of pressure, we write equation (7.1) as the following variational formulation:

$$\int_\Gamma \overline{\eta}\left[\left(\rho_{01}\frac{\mathrm{d}_{01}\phi_1}{\mathrm{d}t} - \xi\frac{\partial p_{01}}{\partial n_1}\right) - \left(\rho_{02}\frac{\mathrm{d}_{02}\phi_2}{\mathrm{d}t} - \xi\frac{\partial p_{02}}{\partial n_2}\right)\right]\mathrm{d}\Gamma = 0\ , \quad \forall\eta\ , \tag{7.7}$$

where the terms between parentheses represent the acoustic pressure on either side of the vortex sheet. When considering a straight vortex sheet, the terms in equation (7.7) involving ξ vanish since they describe the change in direction of the fluid elements, see equation (7.2). The variational formulation (7.7) is solved alongside equation (3.1).

Therefore, for a straight vortex sheet the relevant terms in the modified variational formulation are:

$$A = -\int_\Gamma (\rho_{01}\overline{W_1} - \rho_{02}\overline{W_2})\mathrm{i}\omega\nu + \overline{\eta}\left[\left(\rho_{01}\frac{\mathrm{d}_{01}\phi_1}{\mathrm{d}t}\right) - \left(\rho_{02}\frac{\mathrm{d}_{02}\phi_2}{\mathrm{d}t}\right)\right]\,\mathrm{d}\Gamma\,. \tag{7.8}$$

Eversman & Okunbor suggest that the test function η should be constructed by taking the material derivative of the standard finite element shape function. We follow their example by replacing η with $\mathrm{d}_0\eta/\mathrm{d}t$, where standard shape functions are used for η.

Manera *et al.* [95] proposed an alternative formulation based on the continuities of pressure and of normal displacement, the latter being also introduced as a variable in the model. Equation (7.3) is used to write the continuity of displacement ξ in terms of the velocity potential. Using equation (7.3) the integral in (7.5) becomes

$$\int_\Gamma \rho_{01}\overline{W_1}\left\{\frac{\mathrm{d}_{01}\xi}{\mathrm{d}t} - \xi\mathbf{n}\cdot[(\mathbf{n}\cdot\nabla)\boldsymbol{v}_{01}]\right\} - \rho_{02}\overline{W_2}\left\{\frac{\mathrm{d}_{02}\xi}{\mathrm{d}t} - \xi\mathbf{n}\cdot[(\mathbf{n}\cdot\nabla)\boldsymbol{v}_{02}]\right\}\,\mathrm{d}\Gamma. \tag{7.9}$$

The continuity of pressure is enforced by adding the variational statement (7.7) where η is now the test function associated with ξ. The corresponding terms in the variational formulation are therefore as follows:

$$\begin{aligned} A = &-\int_\Gamma \rho_{01}\overline{W_1}\left\{\frac{\mathrm{d}_{01}\xi}{\mathrm{d}t} - \xi\mathbf{n}\cdot[(\mathbf{n}\cdot\nabla)\boldsymbol{v}_{01}]\right\} - \rho_{02}\overline{W_2}\left\{\frac{\mathrm{d}_{02}\xi}{\mathrm{d}t} - \xi\mathbf{n}\cdot[(\mathbf{n}\cdot\nabla)\boldsymbol{v}_{02}]\right\} \\ &+ \overline{\eta}\left[\left(\rho_{01}\frac{\mathrm{d}_{01}\phi_1}{\mathrm{d}t} - \xi\frac{\partial p_{01}}{\partial n_1}\right) - \left(\rho_{02}\frac{\mathrm{d}_{02}\phi_2}{\mathrm{d}t} - \xi\frac{\partial p_{02}}{\partial n_2}\right)\right]\,\mathrm{d}\Gamma\,. \end{aligned} \tag{7.10}$$

The addition of the normal displacement as additional degrees of freedom on Γ does not represent a noticeable cost compared to the discretisation of the acoustic field.

Note that in the formulations described so far no attempt has been made to control the behaviour of the solution at the trailing edge (for instance, for (7.10) there is no mention in [95] of the displacement being set to zero at the trailing edge, although technically it is possible to do so directly since the displacement ξ is an explicit variable in this formulation). Furthermore, it is not possible in these formulations to enforce the Kutta condition. These issues will be revisited in Section 7.5, where the constraints imposed at the trailing edge will be discussed and their effects compared.

7.3.2 Proposed Formulation

The new formulation is also based on the continuity of pressure and normal displacement across the vortex sheet. In addition, it attempts to provide an explicit description of the Kutta condition at the trailing edge.

First we introduce the normal velocity on the vortex sheet as an independent variable. Two distinct velocities are defined since this quantity is not necessarily continuous across the vortex sheet:

$$v_1 = \frac{\partial \phi_1}{\partial n} , \quad \text{and } v_2 = \frac{\partial \phi_2}{\partial n} . \tag{7.11}$$

These additional variables only represent a very small increase in the total number of degrees of freedom in the numerical model. The advantage of having v_1 and v_2 as explicit variables is that one can directly impose the Kutta condition by setting $v_1 = v_2 = 0$ at the trailing edge.

Secondly, the normal velocities on either side of Γ are related to the displacement ξ of the vortex sheet by using the kinematic condition (7.3) derived by Myers. This is achieved by the following variational statement:

$$\int_\Gamma \overline{\sigma_1} \left(v_1 - \frac{\mathrm{d}_{01}\xi}{\mathrm{d}t} + \xi \mathbf{n} \cdot [(\mathbf{n} \cdot \nabla)\boldsymbol{v}_{01}] \right) + \overline{\sigma_2} \left(v_2 - \frac{\mathrm{d}_{02}\xi}{\mathrm{d}t} + \xi \mathbf{n} \cdot [(\mathbf{n} \cdot \nabla)\boldsymbol{v}_{02}] \right) \mathrm{d}\Gamma = 0 , \tag{7.12}$$

where the test functions σ_1 and σ_2 are associated with the velocity variables v_1 and v_2. The displacement is still an explicit variable, and this allows the trailing edge displacement to be set to zero directly.

Thirdly, we use equation (7.1) for the continuity of pressure formulated in the same way as in equation (7.7). When put together, the proposed formulation corresponds to:

$$\begin{aligned} A = &- \int_\Gamma \rho_{01} \overline{W_1} v_1 - \rho_{02} \overline{W_2} v_2 + \overline{\eta} \left[\left(\rho_{01} \frac{\mathrm{d}_{01}\phi_1}{\mathrm{d}t} - \xi \frac{\partial p_{01}}{\partial n_1} \right) - \left(\rho_{02} \frac{\mathrm{d}_{02}\phi_2}{\mathrm{d}t} - \xi \frac{\partial p_{02}}{\partial n_2} \right) \right] \\ &+ \overline{\sigma_1} \left\{ v_1 - \frac{\mathrm{d}_{01}\xi}{\mathrm{d}t} + \xi \mathbf{n} \cdot [(\mathbf{n} \cdot \nabla)\boldsymbol{v}_{01}] \right\} + \overline{\sigma_2} \left\{ v_2 - \frac{\mathrm{d}_{02}\xi}{\mathrm{d}t} + \xi \mathbf{n} \cdot [(\mathbf{n} \cdot \nabla)\boldsymbol{v}_{02}] \right\} \mathrm{d}\Gamma . \end{aligned}$$

The first two terms originate from (7.5) and represent the forcing of the acoustic fields in Ω_1 and Ω_2 by the vortex sheet. The next term enforces the continuity of pressure across Γ. The last two terms relate the acoustic normal velocities on either sides of Γ to

the normal displacement of the vortex sheet. For a straight vortex sheet the proposed formulation reduces to

$$A = -\int_\Gamma \rho_{01}\overline{W_1}v_1 - \rho_{02}\overline{W_2}v_2 + \overline{\eta}\left(\rho_{01}\frac{\mathrm{d}_{01}\phi_1}{\mathrm{d}t} - \rho_{02}\frac{\mathrm{d}_{02}\phi_2}{\mathrm{d}t}\right) + \overline{\sigma}_1\left(v_1 - \frac{\mathrm{d}_{01}\xi}{\mathrm{d}t}\right) + \overline{\sigma}_2\left(v_2 - \frac{\mathrm{d}_{02}\xi}{\mathrm{d}t}\right)\mathrm{d}\Gamma\,. \tag{7.13}$$

7.3.3 Streamline Upwind Petrov-Galerkin

Oscillations of the vortex sheet will be caused not only by acoustic waves propagating through it but also by the vorticity shedding from the trailing edge. The latter is hydrodynamic in nature and has quite different properties from the acoustic field. In particular, its wavelength is smaller and given by v_0/f. There are two acoustic wavelengths $\lambda = (c_0 \pm v_0)/f$, *i.e.* downstream and upstream waves, and there are therefore the factors $M/(1 \pm M)$ between the acoustic and hydrodynamic wavelengths. These hydrodynamic oscillations are simply convected by the mean flow along the vortex sheet.

It is well-known that standard finite elements are particularly inefficient at representing such solutions due to the lack of upwinding. Finite elements tend to produce node-to-node oscillations when attempting to solve convection-dominated problems, see for example the standard textbook by Zienkiewicz *et al.* [161].

Brooks & Hughes [35] introduced the Streamline Upwind Petrov-Galerkin (SUPG) method which can result in nodally exact solutions for the one-dimensional advection-diffusion equation. This upwinding method is based on the idea that information will propagate in the direction of the convection velocity, and it reduces the need for severe mesh refinement by weighting the solution upstream of a node more heavily than the solution downstream.

SUPG methods are used extensively for convection-dominated problems in the time domain [161]. They are not so common for time-harmonic problems, one exception being the work of Rao & Morris on a finite element model for the LEE [123, 124]. They showed that the method was suitable for aeroacoustic problems with rotational mean flow. In the present work, a SUPG method is proposed to discretise equations (7.1) and (7.3). Results presented in section 7.5 will demonstrate the benefit of this approach.

SUPG methods use test functions of the form $\eta + h\beta\partial\eta/\partial z$ where η is a standard shape function, and h is the element size. The addition of the gradient term to the test function stabilises the Galerkin method, and then the parameter β can be adjusted to optimize the accuracy of the numerical scheme.

7.3.3.1 Model Problem

The oscillations of the vortex sheet are fully coupled with the sound fields on either side of Γ, and it is not possible to write a simple convection equation for the displacement of the vortex sheet. As a consequence it is not practical to use the full formulations described in Sections (7.3.1) and (7.3.2) to choose the value of the upwinding parameter β. Instead we consider a simple model problem to identify a suitable value for β, which we will then use for the full formulation with the vortex sheet. The model problem considered is the one-dimensional 'one-way' wave equation in the frequency domain:

$$\mathrm{i}\omega\zeta + v\frac{\partial\zeta}{\partial z} = 0\,, \tag{7.14}$$

where ζ is a physical quantity, and v is a convection velocity, which may take on a complex value. The imaginary part of this velocity may be used to generate solutions which either grow or decay. Solutions to the model problem behave like $\zeta \sim e^{-\mathrm{i}\tilde{k}z}$, where $\tilde{k} = \omega/v$ is the wavenumber. As will be shown in Section (7.5) this simple model adequately captures the behaviour of the oscillations of the vortex sheet in the problem of interest (7.13).

Solving Equation (7.14) with the SUPG method leads to a variational statement of the form:

$$\int \overline{\left(\eta + h\beta\frac{\partial\eta}{\partial z}\right)}\left(\mathrm{i}\omega\zeta + v\frac{\partial\zeta}{\partial z}\right)\,\mathrm{d}z = 0\,. \tag{7.15}$$

To obtain β we consider a uniform mesh with elements of size h with quadratic shape functions[1]. We then require that the exact solution $\zeta \sim e^{-\mathrm{i}\tilde{k}z}$ be also a solution of the numerical model. This leads to two distinct equations:

$$K_{3,1}\mathrm{e}^{-\mathrm{i}\tilde{k}(-h)} + K_{3,2}\mathrm{e}^{-\mathrm{i}\tilde{k}(-h/2)} + (K_{3,3} + K_{1,1}) + K_{1,2}\mathrm{e}^{-\mathrm{i}\tilde{k}(h/2)} + K_{1,3}\mathrm{e}^{-\mathrm{i}\tilde{k}(h)} = 0\,, \tag{7.16a}$$

$$K_{2,1}\mathrm{e}^{-\mathrm{i}\tilde{k}(-h/2)} + K_{2,2} + K_{2,2}\mathrm{e}^{-\mathrm{i}\tilde{k}(h/2)} = 0\,, \tag{7.16b}$$

[1] We will also use quadratic elements when solving the full problem in Sections 7.4 and 7.5. The procedure described here to obtain β can also be applied to linear elements.

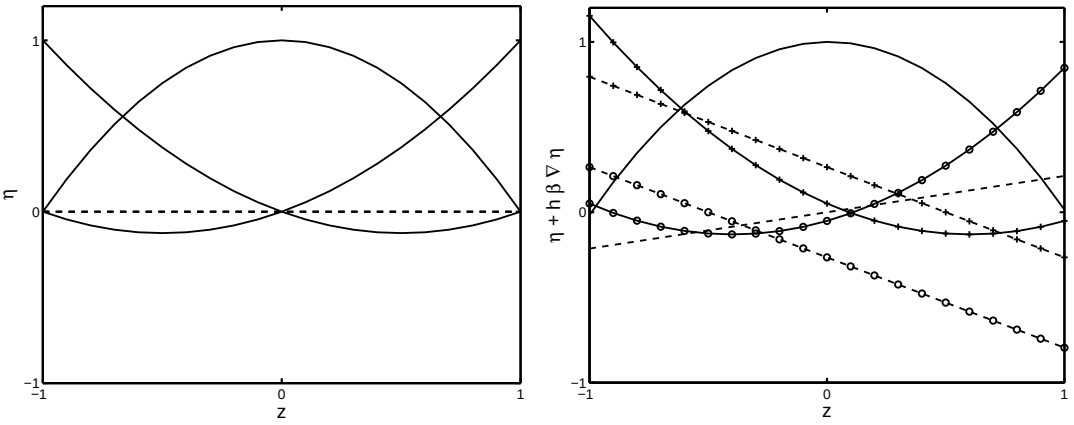

Figure 7.4: Comparison of standard test functions and the SUPG test functions, on a reference element. For the SUPG functions, $h = 0.5$, and $v = 0.45 - 0.1\mathrm{i}$. Left: Standard quadratic test functions. Right: SUPG test functions. Real part (—), imaginary part (- - -).

where the coefficients K, originating from the element matrix, can be written in closed-form (these expressions are not given here for the sake of brevity). Equation (7.16a) corresponds to the difference equation for the nodes between two elements (i.e. the adjacent shape functions) while equation (7.16b) corresponds to the internal nodes (i.e. to the internal bubble shape function). Each of these equations can be solved to obtain an optimal value for the upwinding parameter β. This implies that different values of β should be used for the adjacent shape function and for the internal bubble shape function. The closed-form expressions for β_1 and β_2 are quite complex, but using a Taylor series with respect to ωh when $\omega h \to 0$ yields the following approximations:

$$\beta_1 \simeq \frac{7\mathrm{i}h\omega}{75\overline{v}} + \frac{4\mathrm{i}\overline{v}}{5h\omega} \quad \text{(exterior nodes)}\,, \quad \text{and}\,, \quad \beta_2 \simeq \frac{\mathrm{i}h\omega}{75\overline{v}} + \frac{4\mathrm{i}\overline{v}}{5h\omega} \quad \text{(interior node)}\,. \tag{7.17}$$

A comparison of the standard test functions and the SUPG test functions is given in Figure 7.4. It should be noted that the coefficients β_1 and β_2 are imaginary, so the SUPG test functions are complex whereas the standard test functions are real. It can be seen as well that the SUPG test functions are weighted more heavily towards the upstream direction.

To illustrate the benefit of using the SUPG method with the Definitions (7.17), Figure 7.5 compares the rates of convergence of the standard quadratic test function and of the SUPG method. These results are for a simple test case with a Dirichlet

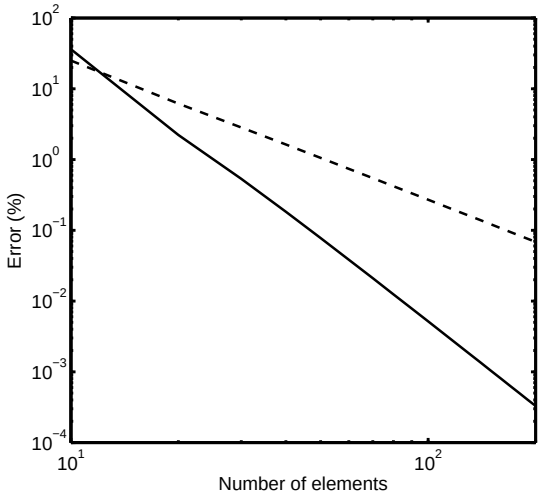

Figure 7.5: Numerical error, as a function of the number of elements, for the simple convection equation (7.14). Standard quadratic test functions (- - -), SUPG test functions (—). The numerical error is measured using the relative nodal error. Parameters are the number of elements: 10 to 200 in steps of 10, a domain size of 2, $\omega = 10$ and $v = 0.45 + 0.1\mathrm{i}$.

condition ($\zeta = 1$) at $z = 0$ and a domain of length 2. It is quite clear that the use of the SUPG test functions results in a faster convergence rate than that of the Galerkin test functions - quartic instead of quadratic.

7.3.3.2 Vortex Sheet Problem

Now that we have devised an optimal SUPG for the model problem (7.14), we discuss how it can be used for the vortex sheet model. The key is in identifying the phase velocity v which is used in Equation (7.17) to define the values of the upwinding coefficient. We therefore need to calculate the phase velocity of the hydrodynamic disturbances that can propagate along the vortex sheet.

To that end, we consider a three dimensional problem with a planar vortex sheet located at $y = 0$ and separating two uniform mean flows in the z direction (with parameters v_{01}, c_{01} and ρ_{01} for $y > 0$, and parameters v_{02}, c_{02} and ρ_{02} for $y < 0$). For a solution behaving like $\mathrm{e}^{\mathrm{i}\omega t - \mathrm{i}\tilde{k}z - \mathrm{i}\kappa r}$ (with arbitrary frequency ω and wavenumbers $\tilde{k}$ and κ) it is straightforward to solve the convected wave equation (2.13), and then to apply equations (7.1) and (7.3) for the continuity of pressure and normal displacement.

This leads to the following condition on the streamwise wavenumber $\tilde{k}$:

$$\rho_{02}\kappa_1(\omega - v_{02}\tilde{k})^2 = \rho_{01}\kappa_2(\omega - v_{01}\tilde{k})^2 \,,$$

where $\kappa_1 = \sqrt{(\omega - v_{01}\tilde{k})^2/c_{01}^2 - \tilde{k}^2}$ and $\kappa_2 = -\sqrt{(\omega - v_{02}\tilde{k})^2/c_{02}^2 - \tilde{k}^2}$. Then by writing $\tilde{k} = \omega/v$, where v is the phase velocity, this can be further simplified to give:

$$\rho_{02}[(v_{01} - v)^2 - c_{01}^2](v_{02} - v)^4 = \rho_{01}[(v_{02} - v)^2 - c_{02}^2](v_{01} - v)^4 \,. \tag{7.18}$$

This gives a polynomial equation of order 6 in v, which can be solved numerically. However, if one assumes that the density and sound speed are uniform ($c_{01} = c_{02}$ and $\rho_{01} = \rho_{02}$), then the convection velocity along the vortex sheet is given by:

$$v = \frac{v_{01} + v_{02}}{2} \pm \frac{\mathrm{i}}{2}\left[1 - \left(\sqrt{1 + (v_{01} - v_{02})^2} - 2\right)^2\right]^{1/2} , \tag{7.19}$$

where the sign of the imaginary part determines if the hydrodynamic wave oscillating along the vortex sheet is exponentially decaying or growing. This result is in fact consistent with the high-frequency approximation derived by Gabard & Astley [62] for a cylindrical vortex sheet, because at high frequency the curvature of the vortex sheet becomes negligible.

The SUPG method is applied to the variational formulation described in Section 7.3.2 by substituting η, σ_1 and σ_2 in Equation (7.13) by

$$\eta + h\beta\partial\eta/\partial z \,, \quad \sigma_1 + h\alpha_1\partial\sigma_1/\partial z \,, \quad \text{and} \,, \quad \sigma_2 + h\alpha_2\partial\sigma_2/\partial z \,,$$

respectively. The values of the upwinding parameter β are given by (7.17) with the phase velocity v given by (7.19) in the isothermal case, or by numerically solving Equation (7.18) for the hot jet case; using the positive complex part gives a decaying solution. Parameter α is calculated using the tangential mean flow velocity on either Ω_1 or Ω_2, and serves to stabilise the elements along the vortex sheet. The performance of such a formulation will be discussed in Section 7.5.

7.4 Test Case

The test case used for the validation of the finite element models is the Munt problem [109]. This test case was chosen because it contains the essential features of the physical

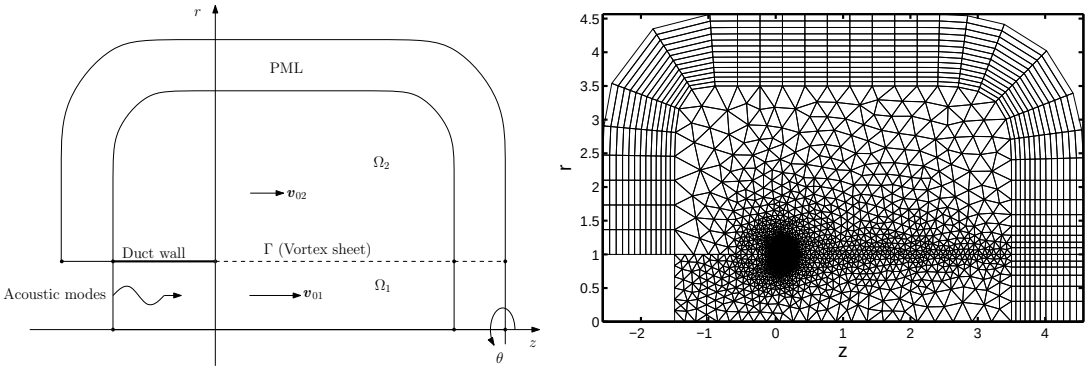

Figure 7.6: Schematic of the test case. Example of a coarse mesh. Note the refinement of the trailing edge; this is needed to predict solutions with singularities.

problem, namely: the trailing edge, the vortex sheet and the refraction through the vortex sheet, and because there is a readily available semi-analytic solution [62].

The test case geometry is shown in Figure 7.6. A semi-infinite axisymmetric straight duct carries an axial uniform mean flow with velocity v_{01}. In region Ω_2 a uniform mean flow with velocity v_{02} is present, which may be different from the jet velocity v_{01}. A vortex sheet Γ separates the two flow regions, it emanates from the nozzle lip and is parallel to the z-axis. An acoustic source is placed at the upstream end of the duct, and corresponds to an incoming acoustic mode. A hard-wall condition is imposed on the inner and outer duct walls, and the computational domain is surrounded by a perfectly matched layer (see Section 2.4.3.2).

We will consider both isothermal and hot jets. All variables are normalised by the ambient sound speed, the ambient density, and the duct radius. For the isothermal jet it is assumed that the density and sound speed are uniform. The Helmholtz number kR, where $k = \omega/c_0$ is the wavenumber and R is the duct radius, is 10, and the excitation source is the second radial mode with azimuthal order $m = 3$. The jet Mach number is 0.45 and the ambient Mach number in Ω_2 is either 0.45 or 0.1. Both uniform mean flow ($v_{01} = v_{02} = 0.45$) and non-uniform mean flow ($v_{01} = 0.45$, $v_{02} = 0.1$) are considered. Such flow conditions are typical of bypass duct exhausts on turbofan engines.

For the hot jet, in Ω_1 the density is 0.33 and the sound speed is 1.74, in Ω_2 the density and sound speed are unity. The Helmholtz number is still 10, but now the excitation source is the first radial mode with azimuthal order $m = 2$. The jet Mach number is chosen to be 0.51 in Ω_1, and the ambient Mach number is 0.1 in Ω_2. These

values were chosen as they are representative of a typical helicopter exhaust jet.

Unstructured triangular elements are used to discretise domains Ω_1 and Ω_2, and quadrilateral elements are used for the PML. Line elements are used for the vortex sheet. An example of a coarse mesh is given in Figure 7.6. As can be seen from the figure the mesh is refined along the vortex sheet, by a factor $M/(1+M)$. This is necessary for proper resolution of the hydrodynamic oscillations along the vortex sheet.

Quadratic interpolation shape functions have been used for all elements. In the acoustic domains the typical element size is 0.1. For a velocity of 0.45 this gives an approximate resolution of 18 nodes per acoustic wavelength in the downstream direction, and 7 nodes per wavelength in the upstream direction. The mesh refinement used along the vortex sheet resolves the hydrodynamic waves with approximately 11 nodes per wavelength.

7.5 Discussion of Results

In this section we compare the different formulations previously presented to the semi-analytic solution. Several quantities of interest will be considered to assess the accuracy of these formulations, including: the normal displacement of the vortex sheet, the normal acoustic velocity on either side of the sheet, and the velocity potential. The latter quantity will be assessed along the vortex sheet as well as along an observation line located at a fixed radius $r = 2.75$; this is to study the acoustic field at some distance from the vortex sheet.

We will first consider specific cases to demonstrate the properties of the vortex sheet that we are trying to capture. We will then consider the convergence tests for cases without vorticity shedding (*i.e.* no Kutta condition), and with vorticity shedding (*i.e.* with Kutta condition).

7.5.1 Preliminary Considerations

Here we will present results which demonstrate some important aspects of the problem, and which highlight the performances of the formulations considered, by comparing the numerical and analytical solutions either along the vortex sheet, or along the observation line. We will consider different flow conditions to show different but relevant

phenomena. First, we demonstrate the consequence of using displacement as an explicit variable, we then show the behaviour of the displacement at the trailing edge, without and with the Kutta condition. The efficacy of the SUPG technique is demonstrated, and the singularities which result when the Kutta condition is not imposed are presented.

7.5.1.1 Displacement as an Explicit Variable

First we compare the original formulation (7.6), where the vortex sheet displacement is treated as an implicit variable, to a variant (7.8) in which displacement is explicitly included in the formulation. We consider a uniform mean flow, with and without the Kutta condition.

Velocity potential predictions along the observation line at $r = 2.75$ are compared in Figure 7.7. The trailing edge displacement has been set to zero for these numerical results, as this is a physical requirement (see next Section). Also shown in this figure are the analytical solutions with or without Kutta condition at the trailing edge. It can be seen that the velocity potential obtained when the vortex sheet displacement is considered as an implicit variable agrees poorly with the analytic solutions. The prediction obtained using displacement as an explicit variable gives excellent agreement with the solution with Kutta condition. For this reason we shall now concentrate on formulation (7.8) instead of (7.6).

7.5.1.2 Zero Trailing Edge Displacement

Having shown that it is preferable to include the vortex sheet displacement as an explicit variable, we now discuss the impact of setting this displacement to zero at the trailing edge. As discussed in Section 7.2.2, a basic physical requirement is to have a continuous streamline at the trailing edge. To demonstrate this behaviour we consider a uniform mean flow without Kutta condition.

Shown in Figure 7.8 is the comparison of the results obtained with the formulation (7.8) and the formulation proposed by Manera *et al.* (7.10). Predictions are given both with and without the constraint $\xi = 0$ at the trailing edge, and the analytical solution without Kutta condition is included.

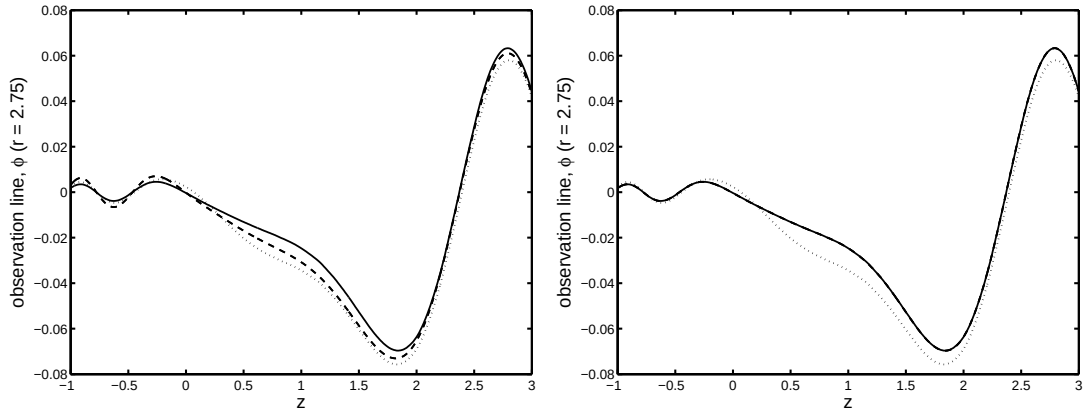

Figure 7.7: Velocity potential, in the presence of uniform mean flow, along the observation line. Left: no Kutta condition, right: Kutta condition. Comparison of formulation (7.6) with displacement as an implicit variable ($\cdots$), formulation (7.8) with displacement as an explicit variable (—)., and the analytic solution (- - -). (Explicit variable and analytic solutions agree with a Kutta condition.)

When the constraint is not applied, formulation (7.8) predicts a singularity[1] at the trailing edge, while formulation (7.10) does not yield the correct solution for the displacement along the vortex sheet.

It can be seen that imposing the constraint $\xi = 0$ improves the predictions at the trailing edge. For the formulation (7.8), there is no singularity in the solution. The small-scale oscillations (corresponding to the hydrodynamic wavelength) are initially captured but then decay progressively in the streamwise direction. Formulation (7.10) predicts the correct response at the trailing edge, but the solution grows with distance from the trailing edge. Note also the node-to-node oscillations, these are the topic of Section 7.5.1.4. The behaviours reported here show the significance of imposing the constraint $\xi = 0$ at the trailing edge.

7.5.1.3 Kutta Condition

In addition to stating that $\xi = 0$ at the trailing edge, a stronger constraint on the solution at the trailing edge is the Kutta condition, which requires that the trailing edge velocity must be zero or, equivalently, that the gradient of the vortex sheet displacement

[1]Note that when the Kutta condition is not included in the model the mesh must be refined at the trailing edge to avoid problems associated with the prediction of singularities.

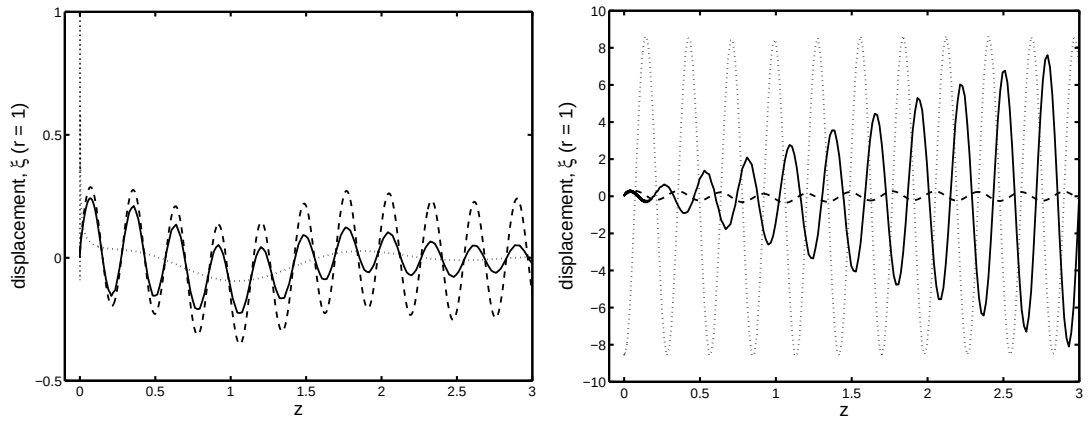

Figure 7.8: Normal displacement along the vortex sheet, in uniform mean flow without Kutta condition. Left: formulation (7.8). Right: formulation (7.10). Unconstrained normal displacement at the trailing edge ($\cdots$), trailing edge displacement set to zero (—), and analytic solution (- - -).

at the trailing edge vanishes. In Figure 7.9 we present a comparison for the vortex sheet displacement of the three formulations against the analytical solution with Kutta condition[1].

When only $\xi = 0$ is set and the gradient of ξ is not prescribed, the results in Figure 7.9 show that the formulations (7.8) and (7.10) are not able to capture the solution along the vortex sheet. However, the velocity potential along the observation line is correct for formulation (7.8). This is due to the enforced continuity of velocity, which is valid only in this specific case - that of uniform mean flow.

As explained in Section 7.3.2, imposing $\partial\xi/\partial z = 0$ at the trailing edge is easily achieved in the proposed formulation (7.13) by directly setting $v_1 = v_2 = 0$ since the velocities on either side of the vortex sheet are explicit variables. Excellent agreement with the analytical solution is observed in Figure 7.9.

In contrast, the formulations (7.8) and (7.10) only provide the displacement as explicit variable, but it is still possible to impose a zero axial gradient of ξ by introducing

[1]Note that in this analytical solution the normal velocity of the vortex sheet is of the form $e^{-\mathrm{i}\tilde{k}z}$ for $z > 0$ where $\tilde{k}$ corresponds to the hydrodynamic wavenumber. The corresponding solution for the displacement is $ze^{-\mathrm{i}\tilde{k}z}$ (for $z > 0$) which is linearly growing along the vortex sheet, as can be seen in Figure 7.9. This should not be misunderstood as an instability, since we are considering a uniform mean flow.

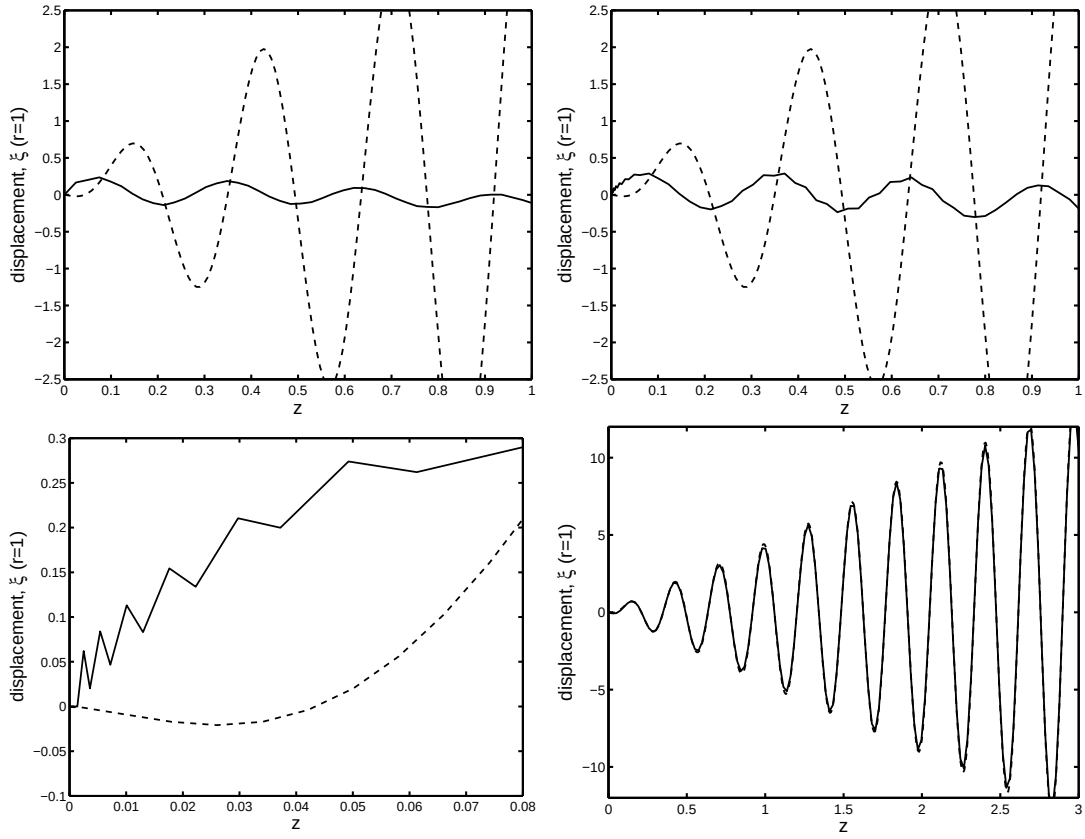

Figure 7.9: Normal displacement of the vortex sheet, in uniform mean flow with Kutta condition. Top left: Formulation (7.8). Top right: Formulation (7.10). Bottom left: Formulation (7.10) with gradient of displacement set to zero. Bottom right: Formulation (7.13). Analytic (- - -) , numeric (—).

a linear constraint to force the gradient of the displacement at the trailing edge to be zero. This is not part of the variational formulation and is implemented directly in the solution procedure. The result of formulation (7.10) in Figure 7.9 indicates that the effect of this modification is only local, and that the numerical solutions are not consistent with the Kutta condition.

7.5.1.4 Vortex Sheet Discretisation

A distinctive feature of the proposed model (7.13) is the use of an SUPG method to improve the accuracy of the numerical solution, especially for the convection of hydrodynamic disturbances along the vortex sheet. The benefit of using the SUPG test

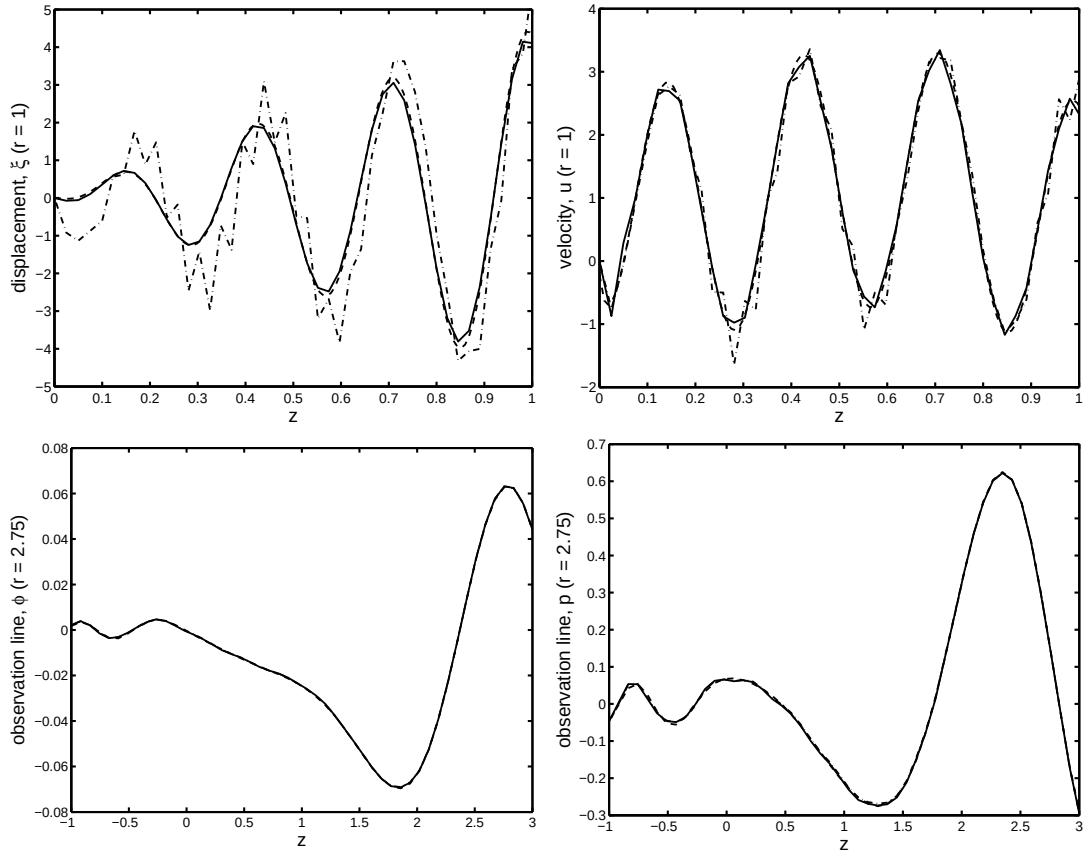

Figure 7.10: Uniform mean flow with Kutta condition. Predictions obtained using the proposed formulation (7.13). Top left: Displacement. Top right: Normal velocity along vortex sheet. Bottom left: Velocity potential along the observation line. Bottom right: Acoustic pressure along the observation line. Analytic (- - -) , numeric with SUPG (—) , numeric without SUPG (-.-) .

functions devised in section 7.3.3.1 is illustrated in Figure 7.10, where the numerical results obtained with and without SUPG test functions are compared against the analytical solution for uniform mean flow. The case with Kutta condition is considered here (so we impose $\xi = 0$ and $v_1 = v_2 = 0$ at the trailing edge in the numerical model). The results obtained when using standard test function are not as accurate as with the SUPG method. This is especially true for the vortex sheet displacement which exhibits very large, node-to-node oscillations typical of convection-dominated problem solved with standard finite elements (see [161] for other examples of this phenomenon). Although less visible for the other variables shown in Figure 7.10, the numerical error

was also found to be increased when using standard test functions. In contrast the results obtained with the SUPG method are in excellent agreement with the analytical solution.

7.5.1.5 Velocity Singularities

When the Kutta condition is not imposed the acoustic velocity at the trailing edge becomes singular. This results in a singularity in velocity potential at the trailing edge. To demonstrate this behaviour, we now present a comparison of the numerical and analytical solutions for the non-uniform flow case without Kutta condition; we consider an isothermal jet. For the isothermal jet, the density and sound speed are constant across the vortex sheet, and only the mean flow velocity changes.

Predictions obtained using the proposed formulation (7.13) are presented in Figure 7.11. The vortex sheet displacement, the normal velocities on either side of the vortex sheet, and the velocity potential on the observation line ($r = 2.75$) are presented. Excellent agreement is found for all of these variables. Note that the singularity in the normal velocity is present, as explained in Section 7.2, and it was necessary to refine the mesh at the trailing edge. This singularity also affects the upwinding provided by the SUPG shape functions at the trailing edge node, and so the standard shape functions were used, at this node only, instead.

Although not clearly visible in the Figure, the singular behaviour of the numerical solution is different to that of the singular behaviour of the analytic solution. Note that this is not an error associated with the proposed formulation, but with the inherent inability of finite element models to predict singularities.

7.5.2 Convergence Results

To further assess the consistency of the numerical results, we now present the results of convergence tests where the variation of relative error between numerical and analytical solutions is measured by varying the mesh resolution. The error is calculated for the velocity potential over the whole computational domain, but excluding the PML region. The following definition of the relative numerical error (in percent) is used:

$$E = \left\{ \frac{\sum_j |\phi_{a,j} - \phi_{n,j}|^2}{\sum_j |\phi_{a,j}|^2} \right\}^{1/2} \times 100,$$

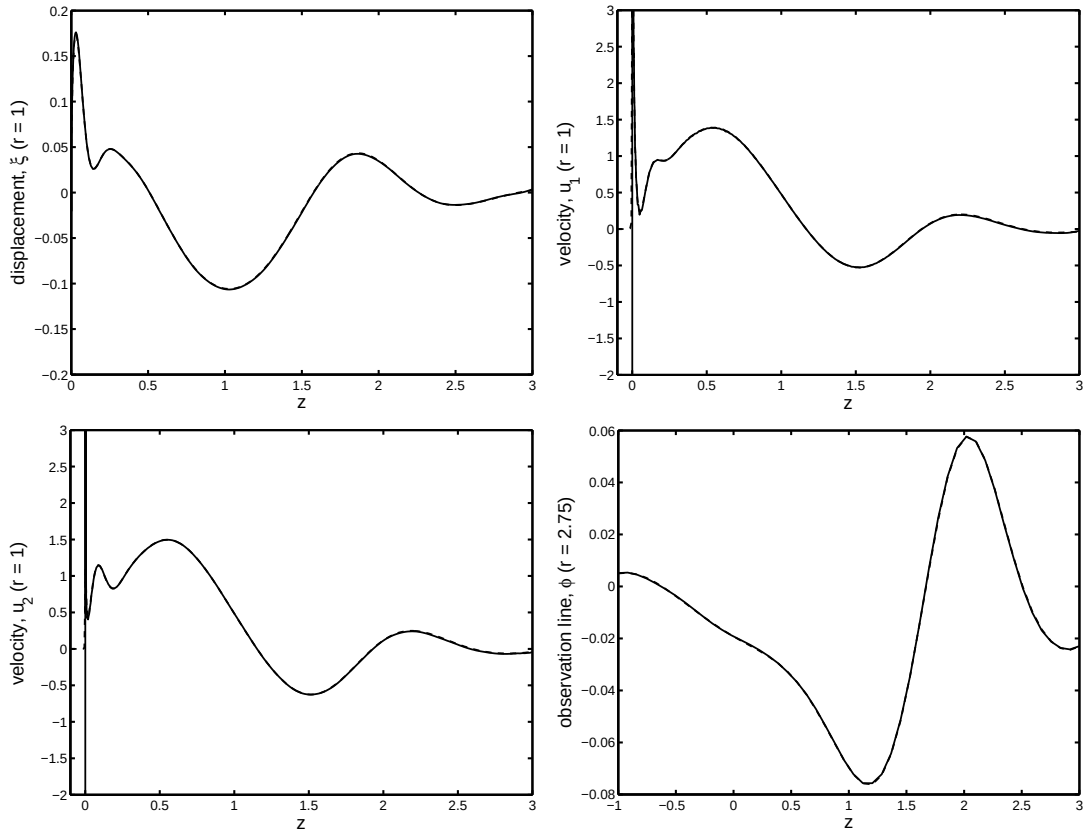

Figure 7.11: Non-uniform mean flow without Kutta condition. Predictions obtained using formulation (7.13). Top left: Displacement along the vortex sheet. Top right: Normal velocity on the duct side of the vortex sheet. Bottom left: Normal velocity on the free stream side of the vortex sheet. Bottom right: Velocity potential along the observation line. Analytic (- - -), numeric (—).

where ϕ_a is the analytic solution, ϕ_n is the numerical solution, and j is the nodal index. This error is computed by interpolating the solution over a uniform mesh, and is in effect the error in the L^2 norm. In these convergence plots the cost of the numerical model is measured by the number of elements per acoustic wavelength, $N_\lambda = 2\pi/(kh)$, note that there are twice as many grid points per wavelength due to the use of quadratic elements. These results were obtained by keeping the frequency constant and by varying the element size.

7.5.2.1 Uniform Mean Flow without Kutta Condition

We shall first present results for the case when no Kutta condition is imposed. In this case there is no vorticity shedding, which results in a singularity at the trailing edge. We begin by discussing the case with a uniform mean flow. Even though there is no refraction of acoustic waves when they propagate through the jet, the use of a vortex sheet in these cases is still useful to describe the vortex shedding from the nozzle lip. Results are presented in Figure 7.12.

Four different formulations are discussed. First, the modified formulation of Eversman & Okunbor (7.8), and that of Manera *et al.* (7.10) are considered, both of them with the vortex sheet displacement set to zero at the trailing edge. Secondly, results obtained with the proposed formulation (7.13) are also included. The condition $\xi = 0$ at $z = 0$ is always enforced. Finally, we consider the behaviour of the model without any special treatment for the vortex sheet, whereby the velocity potential is simply continuous across this surface (in other words the formulation (7.5) is solved on one single domain $\Omega_1 \cup \Omega_2$). This is included here to check whether ignoring the vortex sheet altogether is a viable option and to assess the level of error incurred by such a simplification. Note that in some industrial cases in which the vortex sheet is completely ignored error levels of around 10 % are reported.

The first observation that can be made from Figure 7.12 is that formulations (7.8) and (7.10) do not yield accurate results for either the nodal error or the error along the observation line. Neither of these formulations predicts the behaviour of the vortex sheet correctly.

More striking is the fact that in the absence of any treatment of the vortex sheet the solution converges to the analytical solution with no vorticity shedding. This can be understood by noting that this solution only contains acoustic waves, and the absence of hydrodynamic waves along the vortex sheet explains why no special treatment is required to capture the solution.

The proposed formulation (7.13) generates a solution which converges to the analytic solution without the Kutta condition. A mesh resolution of $N_\lambda = 3$, *i.e.* 3 quadratic elements per wavelength, is sufficient to achieve an error of 1%. We can observe that the numerical error reaches a plateau at 0.2% in Figure 7.12. This is due

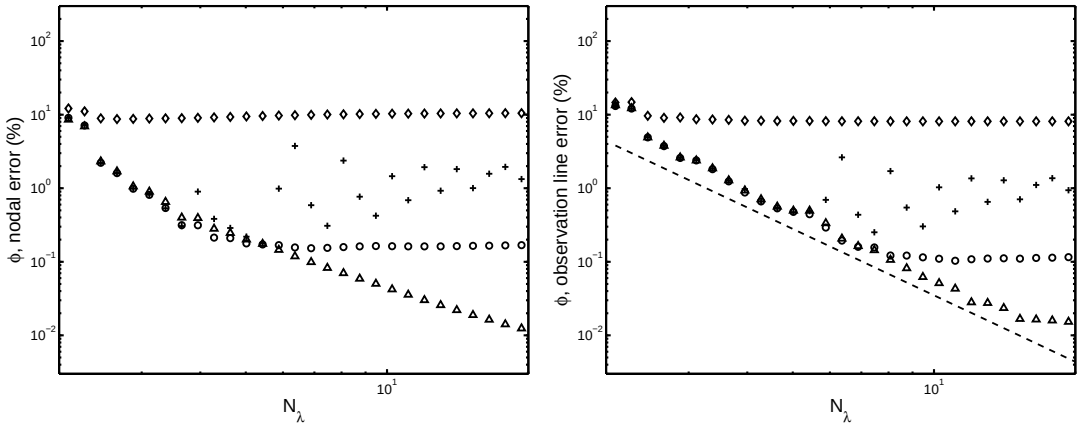

Figure 7.12: Numerical error E of the velocity potential as a function of the mesh resolution for a uniform flow without Kutta condition. No vortex sheet ($\triangle$), formulation (7.8) ($\diamond$), formulation (7.10) ($+$) and proposed formulation (7.13) ($\circ$). The 3^{rd}-order rate of convergence is shown by the dashed line.

to the singularity in velocity at the trailing edge. For finite element methods the presence of singularities in the solution can reduce the accuracy of the numerical scheme. This can be remedied by further refining the mesh in the vicinity of the trailing. This issue is therefore not due to the formulation, but to the nature of the solution that is represented by the finite element model. Such a problem is not present with the Kutta condition since the corresponding solutions for pressure, velocity and displacement are all regular.

7.5.2.2 Non-Uniform Mean Flow without Kutta Condition

We now consider a test case with non-uniform mean flow, that is when the mean flow properties are different on either sides of the vortex sheet. The test case involves a strong refraction of the acoustic waves as they propagate through the vortex sheet, as illustrated on Figure 7.3 (right). We consider the case without Kutta condition, for both isothermal and hot jets

A key feature of the test case with non-uniform flow is that the shear layer is unstable, i.e. it exhibits a physical unstable mode of oscillation that grows exponentially in the streamwise direction (see reference [62] for examples). As mentioned above in Section 7.2.3, the causal solution to the problem includes this instability, but numerical models in the frequency domain tend to provide results excluding the instability [2],

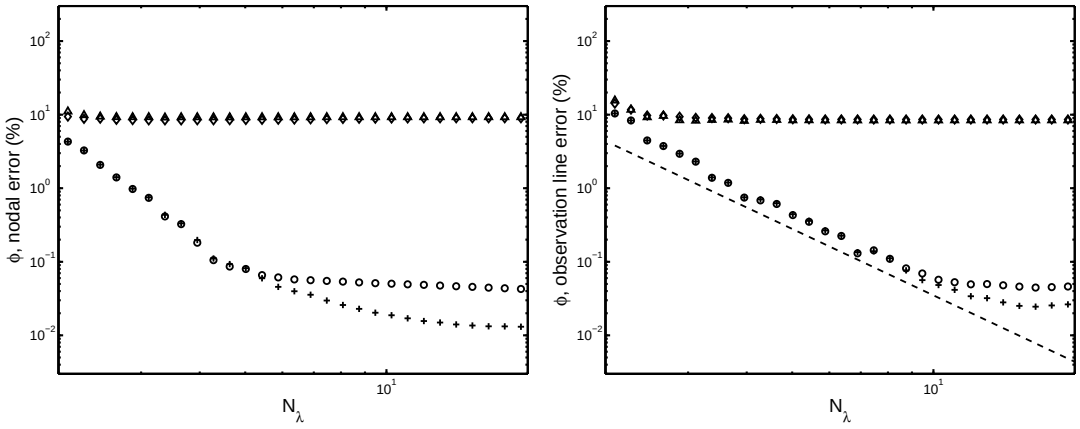

Figure 7.13: Numerical error E of velocity potential as a function of the mesh resolution for an isothermal jet flow without Kutta condition. No vortex sheet ($\triangle$), formulation (7.8) ($\diamond$), formulation (7.10) ($+$) and proposed formulation (7.13) ($\circ$). The 3$^{\text{rd}}$-order rate of convergence is shown by the dashed line.

and are therefore not causal [42] (and indeed this is the case for the finite element models discussed here). From the analysis reported in [62] it can be seen that if the Kutta condition is not imposed at the trailing edge, then it is possible to derive the corresponding, non-causal analytical solution (the details are rather lengthy and technical and are not presented here). So, we can still use the analytical model presented in [62] to obtain the reference solution.

The results of a convergence test, for the isothermal jet case, are shown in Figure 7.13. The solution with no treatment of the vortex sheet does not converge. This is expected since in the case of a non-uniform mean flow the velocity potential is not continuous. Note also that the error level is around 10 %. Similarly, the formulation by Eversman & Okunbor (7.8) does not converge to the expected solution. The formulation by Manera *et al.* (7.10) is able to achieve better levels of accuracy, and indeed converges to the analytical solution. Formulation (7.13) is also able to provide the accurate solutions, although the rate of convergence deteriorates somewhat when the error reaches level of the order of 0.06%. This is due to the velocity singularity present at the trailing edge (a similar trend can be seen in Figure 7.12).

Next we consider the case of a hot jet, without imposing the Kutta condition at the trailing edge. In this case the density and sound speed are not uniform (see Section 7.4 for details). The convergence of the numerical results is shown in Figure 7.14. Qual-

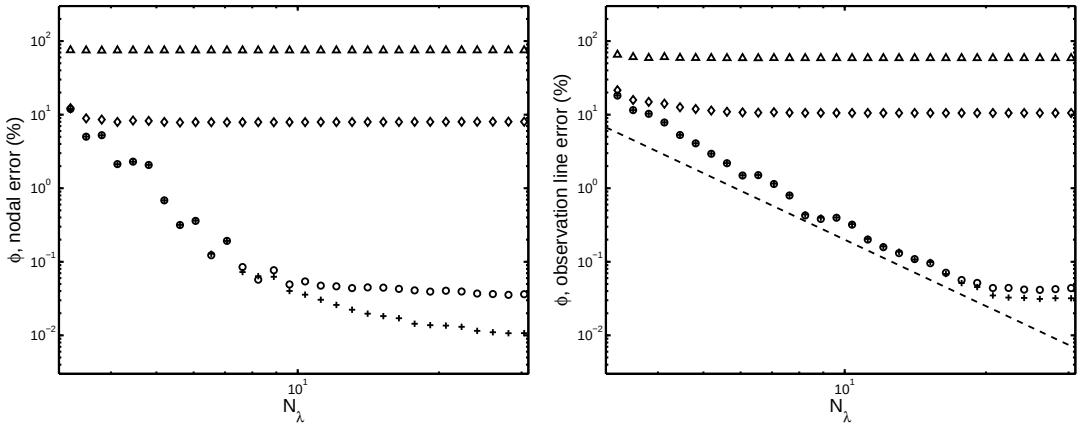

Figure 7.14: Numerical error E of velocity potential as a function of the mesh resolution for a hot jet without Kutta condition. No vortex sheet ($\triangle$), formulation (7.8) ($\diamond$), formulation (7.10) ($+$) and proposed formulation (7.13) ($\circ$). The 3$^{\text{rd}}$-order rate of convergence is shown by the dashed line.

itatively, the conclusions are similar to that of the isothermal jet. Solutions obtained in the absence of a vortex sheet, and from formulation (7.8) are unable to converge to the analytical solution; note that with no vortex sheet the error increases dramatically. The formulation (7.10) converges, but does not predict the singularity behaviour demonstrated by the analytic solution, and eventually plateaus. The proposed formulation achieves good accuracy, although the rate of convergence is reduced again by the presence of the singularity in velocity.

7.5.2.3 Uniform Mean Flow with Kutta Condition

We now consider the case in which a Kutta condition is present at the trailing edge. Even in the case of uniform flow, the Kutta condition results in vorticity shedding from the trailing edge which relieves the singularity there. Results are presented for the solutions with Kutta condition in Figure 7.15.

Again, four different formulations are discussed. The modified formulation of Eversman & Okunbor (7.8), and that of Manera *et al.* (7.10) are considered, both of them with the vortex sheet displacement set to zero at the trailing edge, but without any further treatment at the trailing edge. For the proposed formulation (7.13) the condition $\partial\xi/\partial z = 0$ at $z = 0$ is also imposed. We consider the case for which there is no special treatment for the vortex sheet.

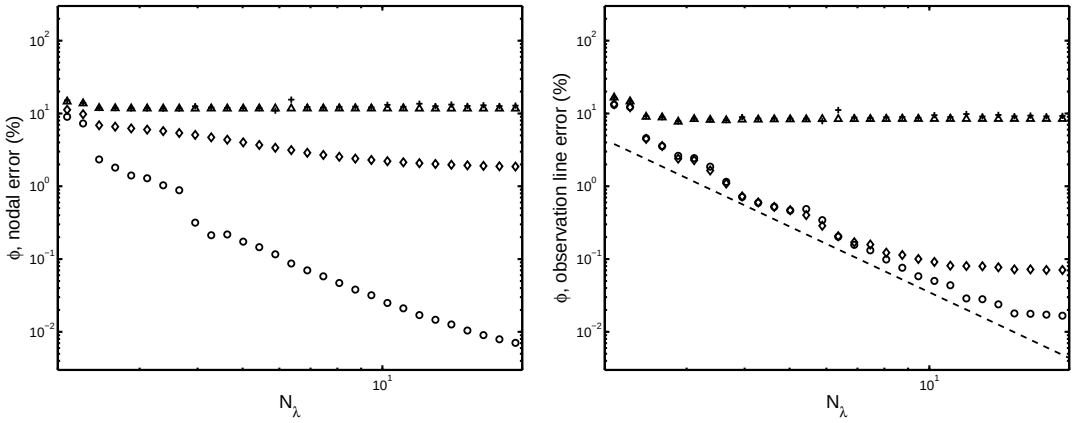

Figure 7.15: Numerical error E of the velocity potential as a function of the mesh resolution for a uniform flow with Kutta condition. No vortex sheet ($\triangle$), formulation (7.8) ($\diamond$), formulation (7.10) ($+$) and proposed formulation (7.13) ($\circ$). The 3^{rd}-order rate of convergence is shown by the dashed line.

Formulations (7.5) and (7.10) do not yield accurate results. Neither formulation correctly predicts the vortex sheet behaviour at the trailing edge.

Formulation (7.8) does not yield accurate results. However, if one considers the numerical error only on the observation line at $r = 2.75$, then this formulation is found to converge to the analytical solution with Kutta condition (i.e. vorticity shedding), despite the fact that it cannot represent the solution in the vicinity of the vortex sheet. This is due to the use of the continuity of acoustic velocity in the construction of the formulation. This specific case is the only case in which this continuity condition is valid. The result is that the observation line solution is correctly predicted. This shows the importance of the influence of the Kutta condition on the acoustic field at some distance from the trailing edge.

The proposed formulation (7.13) is able to provide the expected solution with the Kutta condition. A mesh resolution of $N_\lambda = 3.5$ is sufficient to achieve an error of 1%, but in this case the solution converges to the analytic solution without plateauing; with the Kutta condition the singularity is not present.

In Figure 7.16 we present the condition number of the algebraic systems associated with each formulation and corresponding to the convergence results presented in Figure 7.15 for the solutions with Kutta condition. The condition number is an indicator of the robustness of the numerical model and also indicates whether iterative solvers could be

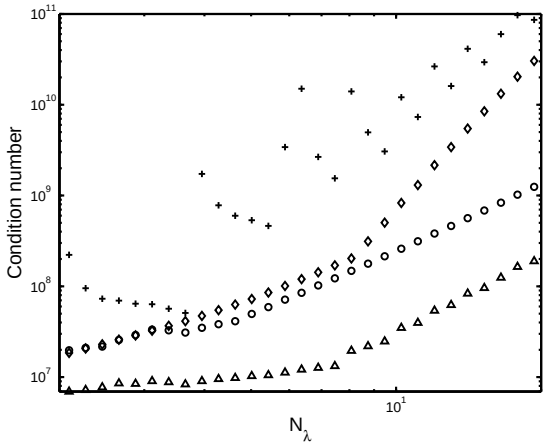

Figure 7.16: Condition number as a function of the mesh resolution for a uniform flow with Kutta condition. No vortex sheet (△), formulation (7.8) (⋄), formulation (7.10) (+) and proposed formulation (7.13) (○).

used to solve large-scale problems. It appears that the formulation (7.10) exhibits the worst conditioning, and the formulation (7.8) yields rather poorly conditioned systems, especially for high mesh resolutions. The best conditioning is found in the absence of a vortex sheet, and the second best by the proposed formulation (7.13).

7.5.2.4 Non-Uniform Mean Flow with Kutta Condition

Finally we discuss the case of a non-uniform flow with the Kutta condition applied. In this case, it is not possible to derive an analytical solution excluding the Kelvin–Helmholtz instability and satisfying the Kutta condition. The fundamental reason for this can be found in the analysis from [62]: the Kutta condition can only be applied if the instability is included as such in the solution. For this reason it is not possible to provide a reference solution to assess the finite element models. A possible way around this issue would be to modify the finite element models of the vortex sheet to allow, at least locally, for the existence of the instability. However this goes beyond the scope of the present work.

Here, we consider the velocity potential along the observation line predicted by the proposed formulation. We quantitatively compare the no Kutta solution to the non-causal Kutta solution. The results for both the isothermal jet and the hot jet cases are given in Figure 7.17. As a further investigation, results are also presented for the

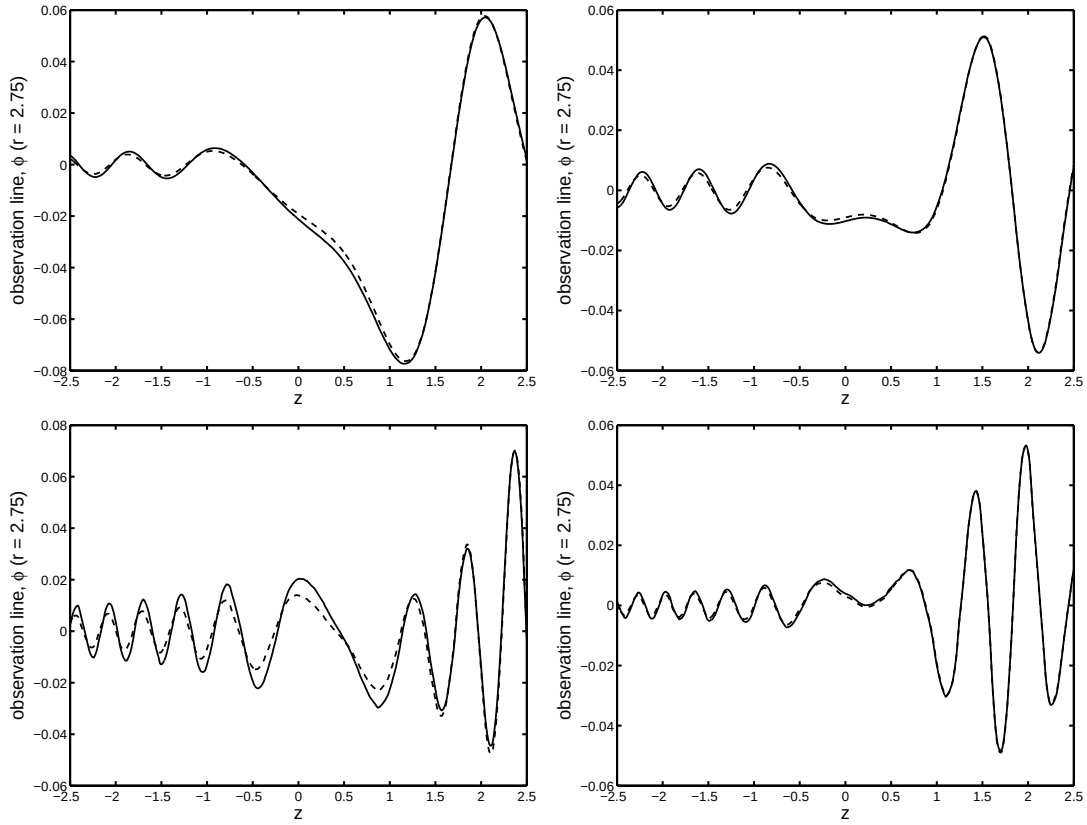

Figure 7.17: Non-uniform mean flow velocity potential solution with and without Kutta condition, along the observation line. The proposed formulation (7.13) solutions are shown. Top left: isothermal jet, $\omega = 10$. Bottom left: isothermal jet, $\omega = 20$. Top right: hot jet, $\omega = 12$. Bottom right: hot jet, $\omega = 24$. No Kutta (- - -), Kutta (—).

case in which the frequency of interest is doubled, and the observation line has been extended into the rear arc.

It can be seen that the largest differences occur in the rear arc, which is in support of the findings of Gabard & Astley [62]. For the isothermal jet the difference between the no Kutta and the Kutta solution is 4.7 % when $\omega = 10$, and 22 % when $\omega = 20$. For the hot jet case the difference is 4.5 % when $\omega = 12$, and 3.9 % when $\omega = 24$. Unfortunately, without an available analytic solution, it is not possible to provide a qualitative assessment of the non-causal Kutta condition solution.

7.6 Summary of Conclusions

Exhaust noise predictions can be obtained by solving the linearised Euler's equations, but they are computationally expensive when compared to solving models based on linearised potential theory. However, potential theory solutions do not predict shear layer refraction effects. In this chapter several finite element models, based on the linearised potential theory, have been presented and their capability to predict the noise propagation through a shear layer by implementing a vortex sheet model has been assessed.

It has been shown that it is preferable to introduce the normal displacement ξ and the normal velocities at the vortex sheet as variables in the formulation. This permits the inclusion of the constraint $\xi = 0$ at the trailing edge, as well as a Kutta condition, directly in the model. A new formulation of the vortex sheet which includes these features has been proposed. Comparisons with an analytical solution have shown that these constraints are required for the finite element model to converge to the appropriate solution. When the Kutta condition is imposed, the proposed formulation improves on previous finite element models of the vortex sheet. However, without a Kutta condition the formulation by Manera *et al.* [95] gives the best results. When the vortex sheet is omitted from the model, the error is around 10 %, or worse in the hot jet case.

Furthermore, oscillations of the vortex sheet represent hydrodynamic waves that are convected downstream; since standard finite elements are inefficient when it comes to representing convection, a new SUPG method has been introduced to obtain an accurate description of these hydrodynamic waves in the new formulation. Numerical results have shown the benefits of this approach.

The present study can be extended further, for instance by considering curved vortex sheets which would correspond more closely to the jets of turbofan engines. In this case the additional terms present in equations (7.1) and (7.3) would play a role. In extending this study two challenges will be faced; the best position for the vortex sheet will need to be defined, and a suitable, possibly experimental, reference solution will need to be used for validation.

8

Conclusions

The finite element method is relied upon to predict the behaviour of wave problems due to its robustness, and its ability to handle complex geometries and inhomogeneous media. However, to provide solutions for problems at high frequencies a great deal of computing power is required. Consequently, due to an increasing reliance upon numerical modelling, there is much interest in reducing the computational costs in order to provide solutions more efficiently. The main aim of this thesis was to develop more efficient finite element methods, with a specific focus on the prediction of turbofan engine noise propagation.

Following a review of the finite element methodology, four high order finite element methods were identified as candidates for more efficient solutions. These methods are based on high order polynomials, which make use of a modal (as opposed to a nodal) expansion of the solution over an element. The methods considered were the polynomial partition of unity method, the Bernstein method, the Hermite method, and the Lobatto method.

The polynomial functions (which give their name to each method) were implemented into an existing finite element code, and used to solve a simple test case with an available analytic solution. One-dimensional and two-dimensional (using both quadrilateral/structured and triangular/unstructured elements) analyses were carried out. It was demonstrated that the polynomial partition of unity method suffers from ill-conditioning caused by linear dependencies between the shape functions. The Hermite method proved to be the most efficient (at least in terms of storage memory requirements) but variable-order functions are currently unavailable. The Bernstein and Lo-

batto methods incur identical error levels as a function of the storage memory required, but the Lobatto method yields matrices with the best conditioning.

In general, the Lobatto method outperforms the other candidate methods. The Lobatto functions are available for all commonly used element types, and are hierarchic in nature - which enables computational savings in terms of reduced global matrix assembly time. The performance of the method was further analysed in two and three dimensions, and it was found that the use of the highest available polynomial order results in the most efficient solutions, due to a reduction of the relative amount of factorisation memory needed (which reduces with increasing order). This is brought about by a reduced number of fill-in entries during factorisation.

To take full advantage of the reduction of relative factorisation memory with order, a higher-order adaptive scheme has been proposed. This is an *a priori* scheme which assumes that the error found on a higher-dimensional element can be related to the error found on a one-dimensional element. As such, solutions obtained on the one-dimensional versions of the higher-dimensional elements are used to determine the optimal order of a given element in a mesh based on the average element size, the input frequency of interest, and the properties of the physical medium on the element. The scheme has been used to solve a test case with an analytic solution, in two and three dimensions. The error estimator which drives the adaptive order scheme provides bounded error levels over wide ranges of frequencies.

The finite element method has been applied to an industrial problem, that of the noise emitted from a turbofan engine intake. The noise predictions have been demonstrated, and the computational cost of using the standard quadratic finite element method to solve the problem has been investigated. A simplified version of the problem (in which there is no flow and only the plane wave mode is considered, due to lack of available implementation) has been solved using the proposed adaptive order method. The standard (quadratic) and proposed methods have been compared, and a significant improvement in terms of efficiency has been demonstrated. It is expected that these computational savings will extend to the case in which flow is included.

Further to this, the possibility of obtaining more efficient solutions for the turbofan exhaust noise problems has been considered. The mathematical model used for the intake noise prediction is not valid for exhaust noise predictions, due to its inability to include rotational mean flows. These solutions are an essential part of acoustic

refraction across shear layers, and the diffraction from trailing edges. Previous investigators have made use of a vortex sheet to model the problem, across which continuity conditions are applied. In this work, the existing formulations have been revisited, and an improved formulation has been proposed. It has been shown that by including the acoustic velocity along the vortex sheet as an explicit variable in the formulation, the Kutta condition can be applied to the trailing edge from which the vortex sheet issues. Good agreement with analytic solutions has been found. However, an issue still remains, and that is the inclusion of the Kelvin-Helmholtz instability in the finite element model.

8.1 Original Contributions

- Assessed the performances of four high-order finite element methods for the solution of the convected wave equation in the frequency domain. Identified a more efficient method, which is based on hierarchic Lobatto polynomials. Furthermore, it has been shown that using hierarchic high order functions is computationally less expensive than using low order functions, *i.e.* the relative computational cost reduces with increasing order. This is due to a reduction of the factorisation memory needed (due to reduced fill-in).

- Developed a simple *a priori* error estimator to obtain solutions with a pre-defined level of accuracy with minimal cost. Error levels obtained using the proposed estimator exhibit very little variation over a wide range of frequencies. The estimator also provides upper and lower bounds on the interpolation error of the finite element method. The estimator provides optimal solutions in both two and three dimensions.

- Compared the computational resources required by the standard quadratic method and the variable-order Lobatto method (steered by the proposed adaptive order scheme) when used to solve a simplified version of an industrial problem (in three dimensions). A significant improvement in terms of efficiency of the proposed higher-order method over the standard quadratic method has been demonstrated. A more efficient finite element method, for the solution of convected wave propagation problems, is now available, as can be seen in Figure 8.1.

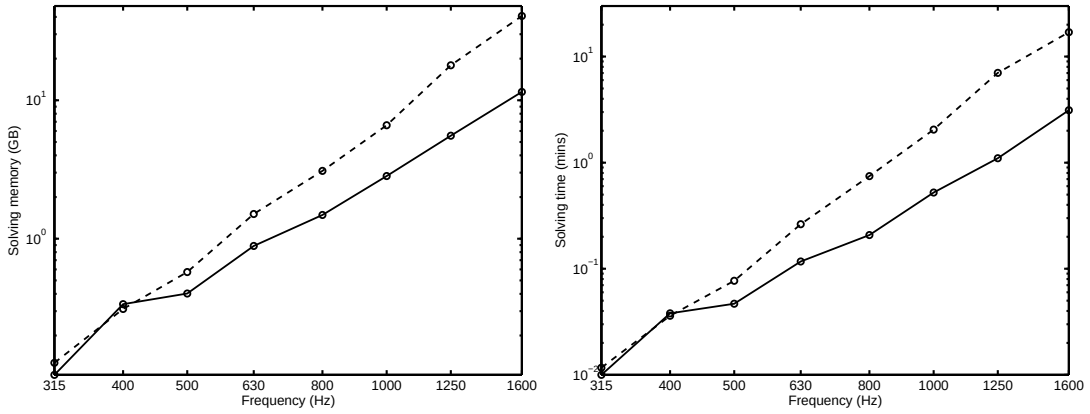

Figure 8.1: Resources required to solve the linear system, as a function of frequency. Standard quadratic solution (- - -). Higher order solution (—).

- As evidence of the quality of the work, the proposed adaptive order method has been implemented in SysNoise, one of the leading software packages for aeroacoustic solutions.

- Investigated two existing formulations for the solution of vortex sheet problems based on potential flow theory. A new formulation which allows for the inclusion of a Kutta condition at the trailing edge has been proposed. The vortex sheet has been discretised using a new SUPG method. The first quantitative assessment of the existing formulations has been carried out, and the proposed formulation's predictions have been validated using an analytic solution.

8.2 Future Work

The use of Hermite elements could be further investigated. They have been found to be quite efficient, but unfortunately there are no readily available variable order functions, for all commonly use element types. If variable order (preferably hierarchic) functions could be constructed, efficiency tests could be carried out to determine their performance in three-dimensional models. It may be that hierarchic Hermite functions are more efficient than the Lobatto functions. Such functions may also find employment in structural mechanics models, or indeed any models which require the solution of fourth-order differential equations, due to their C^1 continuity. However, as their lowest

order is cubic, models with complex geometries (thus requiring smaller elements) may still be expensive.

A limitation of the proposed higher order method is the need for small (computationally expensive) elements in the region of complex boundaries. Xue & Demkowicz [158] present a way of computing the error introduced by the finite element discretisation, with a view to controlling it. Demkowicz *et al.* [43] propose a new scheme for geometry description using sixth order polynomials based on Hermite interpolation, and use it to reconstruct the geometry of a human head from CT and MRI data. Sevilla *et al.* [135] present a finite element method which makes use of non-uniform rational b-splines (NURBS). They have found the NURBS enhanced finite element method to be an order of magnitude more precise than isoparametric finite elements. Xie *et al.* [157] present an *a posteriori* strategy which moves boundary element nodes to create curved boundaries. Another possible avenue for future studies could be the use of higher order functions for the description of complex geometries. This would allow for the use of larger elements near complex surfaces, which would permit the use of higher-order interpolation, and thus increase computational efficiency.

Polynomial order 10 may be considered as quite a high order in the finite element community, however it is quite low when compared to the orders used in the spectral element method [151]. It would be interesting to investigate the performance of the Lobatto finite element method when using orders greater than 10. Do the computational savings afforded by the reduced factorisation memory extend above polynomial order 10? Unfortunately this could not be investigated in this work due to the unavailability of higher order functions. Before this could be investigated new functions would have to be constructed.

The Lobatto method could be used for the solution of other mathematical models, like for example the linearised Euler equations (which would allow for more efficient shear layer predictions). Also, its performance in the presence of corner singularities could also be assessed.

The adaptive order scheme should be further developed. A major drawback of the scheme is that it does not account for the pollution error. It may be possible to include the pollution effect by providing the scheme with information about the longest free paths in a model to be solved. This may even lead to the development of a 'directional order scheme', which takes the longest free paths, and the direction of the flow field

into account. This would be ideal, as the current scheme considers only an upstream flow, which may lead to unnecessarily expensive solutions. It may be possible to use ray theory to predict the paths of propagating acoustic waves (in the presence of flow) and then use this information to predict the resolution requirements of each individual element. Perhaps a map of the streamlines could also be utilised.

Furthermore, the adaptive order scheme could be used for the solution of non-aeroacoustic problems, in order to determine its robustness. It could also be implemented in other numerical methods, to determine if the principle used in its construction can make other numerical methods more efficient.

When considering the application of the proposed method to the intake noise problem, it is necessary to conduct further tests of the benchmark problem with flow and a modal source condition, in order to determine the actual cost of solving the complete physical problem. Furthermore, tests should be carried out which determine the maximum resolvable frequency of the proposed higher-order element method; specifically when using a cluster computer for large scale industrial problems.

The proposed formulation for the prediction of acoustic refraction across vortex sheet could be applied to a curved vortex sheet. Predictions could then be compared to experimental data, although this data may be difficult to find. Also, the Kelvin-Helmholtz instability should be included in the proposed finite element model. It is possible to do this in an *ad hoc* way, for example by forcing the solution behaviour using the SUPG test functions, but this does not satisfy the physical requirements of the problem. Another serious issue is the need for an effective boundary condition at the vortex sheet termination. It may even be that the correct boundary condition would permit an instability wave in the frequency domain (as can be seen in [118]) Finally, it could be interesting to apply the Möhring equation [101] to the Munt problem.

Appendix A

Hermite Functions

Included in this appendix are the 1D bubble, and the 2D triangular functions.

A.1 One-Dimensional Bubble Functions

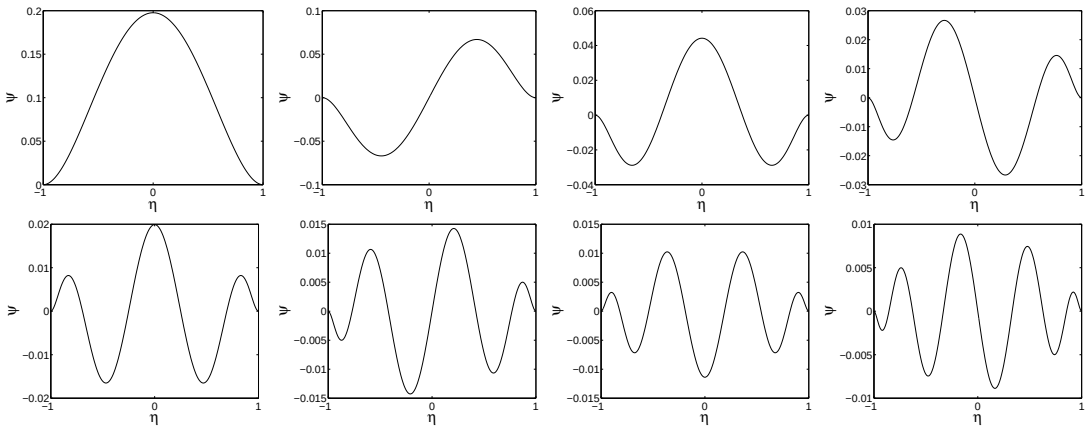

Figure A.1: One dimensional Hermite bubble functions. Top left ψ_5, bottom right: ψ_{12}.

Šolín and Segeth have designed hierarchic Hermite shape functions for 1D elements [152]. Their hierarchic 1D Hermite bubble functions, from order 5 to 12, are given by:

$$\psi_5 = \sqrt{\tfrac{5}{128}}\big(1-\eta^2\big)^2, \qquad \psi_6 = \sqrt{\tfrac{7}{128}}\big(1-\eta^2\big)^2\eta,$$

$$\psi_7 = \tfrac{1}{6}\sqrt{\tfrac{9}{128}}\big(1-\eta^2\big)^2\big(-7\eta^2+1\big), \qquad \psi_8 = \tfrac{1}{2}\sqrt{\tfrac{11}{128}}\big(1-\eta^2\big)^2\big(3\eta^2-1\big)\eta,$$

$$\psi_9 = \tfrac{1}{16}\sqrt{\tfrac{13}{128}}\big(1-\eta^2\big)^2\big(33\eta^4-18\eta^2+1\big),$$

$$\psi_{10} = \tfrac{1}{48}\sqrt{\tfrac{15}{128}}\big(1-\eta^2\big)^2\big(143\eta^4 - 110\eta^2 + 15\big)\eta,$$
$$\psi_{11} = \tfrac{1}{32}\sqrt{\tfrac{17}{128}}\big(1-\eta^2\big)^2\big(143\eta^6 - 143\eta^4 + 33\eta^2 - 1\big),$$
$$\psi_{12} = \tfrac{1}{32}\sqrt{\tfrac{19}{128}}\big(1-\eta^2\big)^2\big(221\eta^6 - 273\eta^4 + 91\eta^2 - 7\big)\eta,$$

These bubble functions can be seen in Figure A.1. The bubble functions allow for condensation of the stiffness matrix.

A.2 Triangular Hermite Functions

The triangular Hermite shape functions are not quite as easy to define as for the quadrilateral functions. The (incomplete) T3 functions are given by:

$$N_{1,1} = \zeta^2(10\zeta - 15\zeta^2 + 6\zeta^3 + 30\xi\eta(\xi+\eta)), \quad N_{1,2} = \xi\zeta^2(3 - 2\zeta - 3\xi^2 + 6\xi\eta),$$
$$N_{1,3} = \eta\zeta^2(3 - 2\zeta - 3\eta^2 + 6\xi\eta), \quad N_{1,4} = \tfrac{1}{2}\xi^2\zeta^2(1 - \xi + 2\eta),$$
$$N_{1,5} = \xi\eta\zeta^2, \quad N_{1,6} = \tfrac{1}{2}\eta^2\zeta^2(1 + 2\xi - \eta),$$
$$N_{2,1} = \xi^2(10\xi - 15\xi^2 + 6\xi^3 + 15\eta^2\zeta), \quad N_{2,2} = \tfrac{1}{2}\xi^2(-8\xi + 14\xi^2 - 6\xi^3 - 15\eta^2\zeta),$$
$$N_{2,3} = \tfrac{1}{2}\xi^2\eta(6 - 4\xi - 3\eta - 3\eta^2 + 3\xi\eta), \quad N_{2,4} = \tfrac{1}{4}\xi^2(2\xi(1-\xi)^2 + 5\eta^2\zeta),$$
$$N_{2,5} = \tfrac{1}{2}\xi^2\eta(-2 + 2\xi + \eta + \eta^2 - \xi\eta), \quad N_{2,6} = \tfrac{1}{4}\xi^2\eta^2\zeta + \tfrac{1}{2}\xi^3\eta^2,$$
$$N_{3,1} = \eta^2(10\eta - 15\eta^2 + 6\eta^3 + 15\xi^2\zeta), \quad N_{3,2} = \tfrac{1}{2}\xi\eta^2(6 - 3\xi - 4\eta - 3\xi^2 + 3\xi\eta),$$
$$N_{3,3} = \tfrac{1}{2}\eta^2(-8\eta + 14\eta^2 - 6\eta^3 - 15\xi^2\zeta), \quad N_{3,4} = \tfrac{1}{4}\xi^2\eta^2\zeta + \tfrac{1}{2}\xi^2\eta^3,$$
$$N_{3,5} = \tfrac{1}{2}\xi\eta^2(-2 + \xi + 2\eta + \xi^2 - \xi\eta), \quad N_{3,6} = \tfrac{1}{4}\eta^2(2\eta(1-\eta)^2 + 5\xi^2\zeta),$$

where $\zeta = 1 - \xi - \eta$. These functions are incomplete because they are dependent on the reference coordinate transformation used. The complete set of shape functions is given by:

$$N_i = L_i \begin{bmatrix} 1 & 0 & 0 & 0 & 0 & 0 \\ 0 & J_{11} & J_{12} & 0 & 0 & 0 \\ 0 & J_{21} & J_{22} & 0 & 0 & 0 \\ 0 & 0 & 0 & J_{11}^2 & 2J_{11}J_{12} & J_{12}^2 \\ 0 & 0 & 0 & J_{11}J_{21} & J_{12}J_{21} + J_{11}J_{22} & J_{12}J_{22} \\ 0 & 0 & 0 & J_{21}^2 & 2J_{21}J_{22} & J_{22}^2 \end{bmatrix}.$$

where $L_i = [N_{i,1}\, N_{i,2}\, N_{i,3}\, N_{i,4}\, N_{i,5}\, N_{i,6}]$, i is the node index, and J_{nm} is the coordinate transformation Jacobian with matrix indices n and m.

References

[1] S Adjerid, M Aiffa, and JE Flaherty. Hierarchical finite element bases for triangular and tetrahedral elements. *Computational Methods in Applied Mechanics and Engineering*, 190:2925–2941, 2001. 48

[2] A Agarwal, PJ Morris, and R Mani. Calculation of sound propagation in nonuniform flows: Suppression of instability waves. *AIAA Journal*, 42(1):80–88, 2004. 12, 142, 147, 166

[3] C Agut, J Diaz, and A Ezziani. A new modified equation approach for solving the wave equation. *Monografías Matemáticas, García de Galdeano*, 35:19–26, 2010. 45

[4] M Ainsworth. Identification and a posteriori estimation of transported errors in finite element analysis. *Computer Methods in Applied Mechanics and Engineering*, 176:3–18, 1999. 85

[5] M Ainsworth. Discrete dispersion relation for hp-version finite element approximation at high wave number. *Journal for Numerical Analysis*, 42(2):553–575, 2004. 56, 59, 86

[6] M Ainsworth and JT Oden. A procedure for a posteriori error estimation for h-p finite element methods. *Computer Methods in Applied Mechanics and Engineering*, 101:73–96, 1992. 84

[7] PR Amestoy, IS Duff, J Koster, and JY L'Excellent. A fully asynchronous multifrontal solver using distributed dynamic scheduling. *Society for Industrial and Applied Mathematics: Journal on Matrix Analysis and Applications*, 23(1):15–41, 2001. 79

[8] PR Amestoy, IS Duff, and JY L'Excellent. Multifrontal parallel distributed symmetric and unsymmetric solvers. *Computer Methods in Applied Mechanics and Engineering*, 184:501–520, 2000. 79

[9] XM An, LX Li, GW Ma, and HH Zhang. Prediction of rank deficiency in partition of unity-based methods with plane triangular or quadrilateral meshes. *Computer Methods in Applied Mechanics and Engineering*, 25 September 2010. 40

[10] D Appelö, M Inkman, T Hagstrom, and T Colonius. Hermite methods for aeroacoustics: recent progress. *17th AIAA/CEAS Aeroacoustics Conference, Portland, Oregon*, AIAA 2011-2757, 6-8 June 2011. 45

[11] DN Arnold, F Brezzi, B Cockburn, and LD Donatella Marini. Unified analysis of Discontinuous Galerkin Methods for elliptic problems. *Society for Industrial and Applied Mathematics Journal on Numerical Analysis*, 39(5):1749–1779, 2002. 32

REFERENCES

[12] RJ Astley. Numerical methods for noise propagation in moving flows, with application to turbofan engines. *Acoustical Science and Technology*, 30:227–239, 2009. 7, 16

[13] RJ Astley and P Gamallo. Special short wave elements for flow acoustics. *Computer Methods in Applied Mechanics and Engineering*, 194:341–353, 2005. 35

[14] CE Augarde. Generation of shape functions for straight beam elements. *Computers and Structures*, 68:555–560, 1998. 44

[15] W Babisch, D Houthuijs, G Pershagen, E Cadum, K Katsouyanni, M Velonakis, M Dudley, H Marohn, W Swart, O Breugelmans, G Bluhm, J Selander, F Vigna-Taglianti, S Pisani, A Haralabidis, K Dimakopoulou, I Zachos, and L Jarup. Annoyance due to aircraft noise has increased over the years - results of the hyena study. *Environment International*, 35:1169–1176, 2009. 1

[16] I Babuška, M Griebel, and J Pitkäranta. The problem of selecting the shape functions for a p-type finite element. Report number BN-1090, Institute of Physical Science and Technology, University of Maryland, United States of America., 1988. 35

[17] I Babuška and C Rheinboldt. A-posteriori error estimates for the finite element method. *International Journal for Numerical Methods in Engineering*, 12:1597–1615, 1978. 84

[18] I Babuška and SA Sauter. Is the pollution effect of the FEM avoidable for the helmholtz equation considering high wave numbers? *Society for Industrial and Applied Mathematics Rev.*, 42(3):451–484, 2000. 56

[19] C Bacuta, J Chen, Y Huang, J Xu, and L Zikatanov. Partition of unity method on nonmatching grids for the Stokes problem. *Journal of Numerical Mathematics*, 13(3):157–169, 2005. 35

[20] C Bacuta and J Sun. Partition of unity finite element method implementation for Poisson equation. *Advances in Applied Mathematics*, Special volume 0:57–67, 2005. 35

[21] C Bailly and D Juvé. Numerical solution of acoustic propagation problems using linearized euler equations. *AIAA Journal*, 38:22–29, 2000. 142

[22] G Bao, GW Wei, and S Zhao. Numerical solution of the Helmholtz equation with high wavenumbers. *International Journal for Numerical Methods in Engineering*, 59:389–408, 2004. 33

[23] JR Barber, KR Crooks, and KM Fristrup. The costs of chronic noise exposure for terrestrial organisms. *Trends in Ecology and Evolution*, 25(3):180–189, 2009. 1

[24] KJ Bathe. *Finite element procedures.* Prentice Hall, Englewood Cliffs, NJ, 1996. 59

[25] E Bécache, A Bonnet-Ben Dhia, and G Legendre. Perfectly matched layers for the convected Helmholtz equation. *Society for Industrial and Applied Mathematics Journal on Numerical Analysis*, 42:409–433, 2004. 18

[26] JA Benfield, PA Bell, LJ Troup, and NC Soderstrom. Aesthetic and effective effects of vocal and traffic noise on natural landscape assessment. *Journal of Environmental Psychology*, 30:103–111, 2010. 1

[27] J-P Bérenger. A perfectly matched layer for the absorption of electromagnetic waves. *Journal of Computational Physics*, 114:185–200, 1994. 18

[28] H Bériot, G Gabard, and E Perrey-Debain. Analysis of high-order finite elements for convected wave propagation. *International Journal for Numerical Methods in Engineering*, 96:665–688, 2013. 55, 70, 74, 116

[29] A Bermúdez, L Hervella-Nieto, A Prieto, and R Rodríguez. An optimal perfectly matched layer with unbounded absorbing function for time-harmonic acoustic scattering problems. *Journal of Computational Physics*, 223:469–488, 2007. 23

[30] M Bernacki, L Fezoui, S Lanterni, and S Piperno. Parallel discontinuous Galerkin unstructured mesh solvers for the calculation of three-dimensional wave propagation problems. *Applied Mathematical Modelling*, 30:744–763, 2006. 141

[31] SN Bernstein. Démonstration du théorème de Weierstrass fondée sur le calcul des probabilités. *Communications of the Kharkov Mathematic Society*, 13:1–2, 1912. 41

[32] J Biermann and O van Estorff. Higher order finite and infinite acoustical elements based on ultraspherical polynomials. *Acta Acustica United with Acustica.*, 99:759–769, 2013. 64

[33] C Bogey, C Bailly, and D Juvé. Computation of flow noise using source terms in linearized Euler's equations. *AIAA Journal*, 40:235–243, 2002. 142

[34] KS Brentner and F Farassat. An analytical comparison of the acoustic analogy and Kirchhoff formulation for moving surfaces. *AIAA Journal*, 36(8):1379–1386, 1998. 20

[35] N Brooks and JR Hughes. Streamline upwind Petrov/Galerkin formulations for convected flows with particular emphasis on the incompressible Naviers-Stokes equations. *Computer Methods in Applied Mechanics and Engineering*, 32:199–259, 1982. 31, 151

[36] YC Cai, XY Zhuang, and C Augarde. A new partition of unity finite element free from the linear dependence problem and possessing the delta property. *Computer Methods in Applied Mechanics and Engineering*, 199:1036–1043, 2010. 40

[37] LMBC Campos. On 36 forms of the acoustic wave equation in potential flows and inhomogeneous media. *Applied Mechanics Reviews*, 60:149–171, 2007. 6

[38] O Cessenat and B Després. Application of an Ultra Weak Variational Formulation of elliptic PDES to the two-dimensional Helmholtz problem. *Society for Industrial and Applied Mathematics Journal on Numerical Analysis*, 35(1):255–299, 1998. 31

[39] X Chen, X Huang, and X Zhang. Sound radiation from a bypass duct with bifurcations. *AIAA Journal*, 47:429–436, 2009. 141

[40] JF Chevaugeon, X Remacle, P Ploumhans, X Gallez, and S Caro. Efficient discontinuous Galerkin methods for solving acoustic problems. *11th AIAA/CEAS Aeroacoustics Conference, Monterey, USA*, AIAA 2005-2514, May 2005. 141

[41] CS Chien and YT Shih. A cubic Hermite finite element-continuation method for numerical solutions of the von Kármán equations. *Applied Mathematics and Computation*, 209:356–368, 2009. 45

[42] DG Crighton and FG Leppington. Radiation properties of the semi-finite vortex sheet: The initial-value problem. *Journal of Fluid Mechanics*, 64(2):393–414, 1974. 147, 167

[43] L Demkowicz, P Gatto, W Qiu, and A Joplin. G^1-interpolation and geometry reconstruction for higher order finite elements. *Computer Methods in Applied Mechanical Engineering*, 198:1198–1212, 2009. 177

[44] A Deraemaeker, I Babuška, and P Bouillard. Dispersion and pollution of the FEM solution for the Helmholtz equation in one, two and three dimensions. *International Journal for Numerical Methods in Engineering*, 46:471–499, 1999. 85, 100, 116

[45] B Després. Sur une formulation variationnelle de type ultra-faible. *Comptes Rendus de l'Académie des Sciences*, 318:939–944, 1994. 31

[46] S Dey, JJ Shirron, and LS Couchman. Mid-frequency structural acoustic and vibration analysis in arbitrary, curved three-dimensional domains. *Computers and Structures*, 79:617–629, 2001. 33

[47] G Dhatt, G Touzot, and E Lefranois. *Méthode des éléments finis*. Lavoisier, Paris, 2005. 47

[48] PG Drazin and WH Reid. *Hydrodynamic stability*. Cambridge University Press, 2004. 146

[49] CA Duarte, I Babuska, and JT Oden. Generalized finite element methods for three-dimensional structural mechanics problems. *Computers and Structures*, 77:215–232, 2000. 35

[50] W Eversman. The boundary condition at an impedance wall in a non-uniform duct with potential mean flow. *Journal of Sound and Vibration.*, 246(1):63–69, 2001. 11, 126

[51] W Eversman and D Okunbor. Aft fan duct acoustic radiation. *Journal of Sound and Vibration*, 213(2):235–257, 1998. 33, 142, 143, 148

[52] R Ewert and W Schröder. Acoustic perturbation equations based on flow decomposition via source filtering. *Journal of Computational Physics*, 188(2):365–398, 2003. 142

[53] F Farassat. The Kirchhoff formulas for moving surfaces in aeroacoustics - the subsonic and supersonic cases. NASA Technical Memorandum 110285, National Aeronautics and Space Administration Langley Research Center Hampton, Virginia 23681-0001, 1996. 20

[54] F Farassat and MK Myers. Extension of Kirchhoff's formula to radiation from moving surfaces. *Journal of Sound and Vibration*, 123:451–460, 1988. 20

[55] C Farhat, I Harari, and LP Franca. The discontinuous enrichment method. *Computer Methods in Applied Mechanics and Engineering*, 190:6455–6479, 2001. 32

[56] RT Farouki. The Bernstein polynomial basis: a centennial retrospective. *Computer Aided and Geometric Design*, 29:379–419, 2012. 41

[57] RT Farouki, TNT Goodman, and T Sauer. Construction of orthogonal bases for polynomials in Bernstein form on triangular and simplex domains. *Computer Aided and Geometric Design*, 20:209–230, 2003. 41

[58] FLUENT. FLUENT 6.3. *User's Guide*, pages 7–23, 2006. 124

[59] LP Franca and EG Dutra Do Carmo. The Galerkin Gradient Least-Squares method. *Computer Methods in Applied Mechanics and Engineering*, 74:41–54, 1989. 31

[60] LP Franca, C Farhat, AP Macedo, and M Lesoinne. Residual-free bubbles for the Helmholtz equation. *International Journal for Numerical Methods in Engineering*, 40:4003–4009, 1997. 31

[61] L Fritschi and Who Regional Office for Europe. *Burden of Disease from Environmental Noise: Quantification of Healthy Life Years Lost in Europe*. Euro Non Serial Publications Series. World Health Organization, Regional Office for Europe, 2011. 1

[62] G Gabard and RJ Astley. Theoretical model for sound radiation from annular jet pipes: far- and near-field solutions. *Journal of Fluid Mechanics*, 549:315–341, 2006. 145, 155, 156, 166, 167, 170, 171

[63] P Gamallo and RJ Astley. The partition of unity finite element method for short wave acoustic propagation on non-uniform potential flows. *International Journal for Numerical Methods in Engineering*, 65:425–444, 2006. 35

[64] D Garijo, ÓF Valencia, FJ Gómez-Escalonilla, and J López Díez. Bernstein Galerkin approach in elastostatics. *Journal of Mechanical Engineering Science*, 0:1–14, 2013. 41

[65] CI Goldstein. The weak element method applied to Helmholtz type equations. *Applied Numerical Mathematics*, 2(3-5):409–426, 1986. 30

[66] ME Goldstein. *Aeroacoustics*. McGraw International Book Company, 1976. 6

[67] T Grätsch and K-J Bathe. A posteriori error estimation techniques in practical finite element analysis. *Computers and Structures.*, 83:235265, 2005. 85, 116

[68] WW Hager. Condition estimates. *Society for Industrial and Applied Mathematics: Journal on Scientific and Statistical Computing*, 5:311–316, 1984. 57

[69] P Haley. Perspectives on noise and emissions reductions. *Aircraft Noise and Emissions Reduction Symposium*, May 2005. xv, 119

[70] W Han and WK Liu. Flexible piecewise approximations based on partition of unity. *Advances in Computational Mathematics*, 23:191–199, 2005. 36

[71] I Harari and TJR Hughes. Finite element methods for the Helmholtz equation in an exterior domain: Model problems. *Computer Methods in Applied Mechanics and Engineering*, 87:59– 96, 1991. 31

[72] CM Harris. Aircraft operations near concentrations of birds in Antarctica: The development of practical guidelines. *Biological Conservation*, 125:309–322, 2005. 1

[73] L Hazard and P Bouillard. Structural dynamics of viscoeleastic sandwich plates by the partition of unity finite element method. *Computer Method in Applied Mechanics and Engineering*, 196:4101–4116, 2007. 36

[74] R Hixon. Radiation and wall boundary conditions for computational acoustics: A review. *International Journal of Computational Fluid Dynamics*, 18:523–531, 2004. ix, 16, 17

[75] R Hixon and SH Shih. Evaluation of boundary conditions for computational aeroacoustics. *33rd AIAA Aerospace Sciences MSeeting*, AIAA 95-0160, Jan 5-12, 1995. 15, 18

[76] JT Holdeman. A Hermite finite element method for incompressible fluid flow. *International Journal for Numerical Methods in Fluids*, 00:1–33, 2009. 45

[77] FQ Hu. On absorbing boundary conditions for linearized Euler equations by a perfectly matched layer. *Journal of Computational Physics*, 129:201–219, 1996. 18

[78] FQ Hu. A perfectly matched layer absorbing boundary condition for linearized Euler equations with a non-uniform mean flow. *Journal of Computational Physics*, 208:469–492, 2005. 18

[79] X Huang, X Chen, Z Ma, and X Zhang. Efficient computation of spinning modal radiation through an engine bypass duct. *AIAA Journal*, 46(6):1413–1423, 2008. 142

[80] KH Huebner. *The Finite Element Method for Engineers*. A Wiley-Interscience publication. Wiley, 2001. 24, 26

[81] DL Huff. Noise reduction technologies for turbofan engines. *NASA Technical Report*, Report number: NASA/TM-2007-214495, 2007. ix, 4

[82] TJR Hughes. Multiscale phenomena: Green's functions, the Dirichlet-to-Neumann formulation, subgrid scale models, bubbles and the origin of stabilized methods. *Computer Methods in Applied Mechanics and Engineering*, 127:387–401, 1995. 31

[83] TJR Hughes, GR Feijóo, L Mazzei, and J-B Quincy. The variational multiscale method - a paradigm for computational mechanics. *Computer Methods in Applied Mechanics and Engineering*, 166:3–24, 1998. 31

[84] TJR Hughes, LP Franca, and GM Hulbert. A new finite element formulation for computational fluid dynamics: VIII. The Galerkin/Least Squares method for advective-diffusive equations. *Computer Methods in Applied Mechanics and Engineering*, 73:173–189, 1989. 31

[85] T Huttunen, P Gamallo, and RJ Astley. Comparison of two wave element methods for the Helmholtz problem. *ISVR Technical Report*, 307, 2006. 32, 35

[86] T Huttunen, P Monk, and JP Kaipio. Computational aspects of the Ultra-Weak Variational Formulation. *Journal of Computational Physics*, 182:27–46, 2002. 32

[87] F Ihlenburg and I Babuška. Finite element solution of the Helmholtz equation with high wave number part ii: The h-p version of the FEM. *Society for Industrial and Applied Mathematics Journal on Numerical Analysis*, 34:315–358, February 1997. 56, 86

[88] F Ihlenburg, I Babuška, and S Sauter. Reliability of finite element methods for the numerical computation of waves. *Advances in Engineering Software*, 28:417–424, 1997. 85

[89] DS Jones. The scattering of sound by a simple shear layer. *Philosophical Transactions of the Royal Society of London. Mathematical and Physical Sciences*, 284(1323):287–328, 1977. 146

[90] M Kumar, S Chakravorty, P Singla, and JL Junkins. The partition of unity finite element approach with hp-refinement for the stationary Fokker-Planck equation. *Journal of Sound and Vibration*, 327:144–162, 2009. 35

[91] O Lagrouche, P Bettess, and RJ Astley. Modelling of short wave diffraction problems using approximating systems of plane waves. *International Journal for Numerical Methods in Engineering*, 54:1501–1533, 2002. 35

[92] ZC Li, H Huang, and J Huang. Effective condition number of the Hermite finite element methods for biharmonic equations. *Applied Numerical Mathematics*, 58:1291–1308, 2008. 44

[93] E Listerud and W Eversman. Finite element modelling of acoustics using higher order elements. part i: Turbofan acoustic radiation. *International Association for Mathematics and Computers in Simulation*, 12(3):431–446, 2004. 33

[94] X Liu and K Tai. Point interpolation collocation method for the solution of partial differential equations. *Engineering Analysis with Boundary Elements*, 30:598–609, 2006. 36

[95] J Manera, R Leneveu, S Caro, and J Mardjono. Broadband turbomachinery noise: exhaust noise computations with ACTRAN/TM and ACTRAN/DGM. *15th AIAA/CEAS Aeroacoustics Conference, Miami, Florida, U.S.A.*, AIAA 2009-3292, 11-13 May 2009. 142, 143, 149, 172

[96] DC Mathews. Combustion and turbine noise work at Pratt & Whitney. *Noise Workshop at Honeywell in Phoenix, Arizona, USA. February 26-27.*, 2003. xv, 118

[97] JM Melenk. On condition numbers in hp-FEM with Gauss-Lobatto-based shape functions. *Journal of Computational and Applied Mathematics*, 139:21–48, 2002. 28

[98] JM Melenk and I Babuška. The partition of unity finite element method: basic theory and applications. *Computer Methods in Applied Mechanics and Engineering*, 139:289–314., 1996. 32, 35, 39

[99] T Mertens, P Gamallo, RJ Astley, and P Bouillard. A mapped finite and infinite partition of unity method for convected acoustic radiation in axisymmetric domains. *Computer Methods in Applied Mechanics and Engineering*, 197(49-50):4273–4283, 15 September 2008. 36

[100] MS Mohamed, O Laghrouche, and A El-Kacimi. Some numerical aspects of the PUFEM for efficient solution of 2D Helmholtz problems. *Computers and Structures*, 88(23-24):1484–1491, December 2010. 36

[101] W Möhring. A well posed acoustic analogy based on a moving acoustic medium. *Presented at the Aeroacoustic workshop SWING in Dresden*, 1999. 142, 178

[102] P Monk and D-Q Wang. A least-squares method for the Helmholtz equation. *Computer Methods in Applied Mechanics and Engineering*, 175:121–136, 1999. 31

[103] M Monsrud. Flight operations engineering. *Performance Engineering Operations Course*, September 2009. xv, 119

[104] CL Morfey. Acoustic energy in non-uniform flows. *Journal of Sound and Vibration*, 14:159–170, 1971. 10

[105] RP Morgans. The Kirchhoff formula extended to a moving surface. *Philosophical Magazine*, 9(55):141–161, 1930. 20

[106] L Moroz, P Pagur, Y Govorushchenko, and K Grebennik. Comparison of counter - rotating and traditional axial aircraft low - pressure turbines integral and detailed performances. *International Symposium on Heat Transfer*, 9-14 August 2009. 2

[107] RE Motsinger and RE Kraft. *Aeroacoustics of Flight Vehicles: Theory and Practice*, volume 2. NASA, 1991. 123

[108] WA Mulder. Spurious modes in finite-element discretizations of the wave equation may not be all that bad. *Applied Numerical Mathematics*, 30:425–445, 1999. 55, 74

[109] RM Munt. The interaction of sound with a subsonic jet issuing from a semi-infinite cylindrical pipe. *Journal of Fluid Mechanics*, 83(4):609–640, 1977. 145, 155

[110] MK Myers. On the acoustic boundary condition in the presence of flow. *Journal of Sound and Vibration*, 71:429–434, 1980. 11, 145

[111] JT Oden, CA Duarte, and OC Zienkiewicz. A new cloud-based hp-finite element method. *Computer Methods in Applied Mechanics and Engineering*, 153:117–126, 1998. 35, 39

[112] Parliamentary Office of Science and Technology. Postnote: Aircraft noise. *Number 197*, June 2003. 1

[113] Massachusetts Institute of Technology. Unified propulsion: Introduction to propulsion. *Online*, Accessed September 28 2010. xv, 121

[114] H Oh, JG Kim, and W Hong. The piecewise polynomial partition of unity functions for the generalized finite element methods. *Computer Methods in Applied Mechanics and Engineering*, 197(45-48):3702–3711, 15 Aug 2008. 36, 40

[115] HS Oh and JW Jeong. Almost everywhere partition of unity to deal with essential boundary conditions in meshless methods. *Computer Methods in Applied Mechanics and Engineering*, 198:3299–3312, 2009. 40

[116] Ö Özgün and M Kuzuoğlu. Non-Maxwellian locally-conformal PML absorbers for Finite Element Mesh Truncation. *IEEE Transactions on Antennas and Propagation*, 55:931–937, 2007. 18

[117] Y Özyörük. Numerical prediction of aft radiation of turbofan tones through exhaust jets. *Journal of Sound and Vibration*, 325:122–144, 2009. 142

[118] Y Özyörük and BJ Tester. Assessment of a frequency-domain linearised Euler solver for turbofan aft radiation predictions and comparison with measurements. *Procedia Engineering*, 6:153–162, 2010. 142, 178

[119] L Panek, N Schönwald, C Richter, and F Thiele. Simulation of the rearward propagation of fan noise through a long cowl aero-engine. *14th AIAA/CEAS Aeroacoustics Conference 2008, Vancouver, British Columbia, Canada*, AIAA 2008-2820, 5-7 May 2008. 141

[120] AT Patera. A spectral element method for fluid dynamics: Laminar flow in a channel expansion. *Journal of Computational Physics*, 54(3):468–488, 1984. 32

[121] S Petersen, D Dreyer, and O van Erstoff. Assessment of finite and spectral element shape functions for efficient iterative simulations of interior acoustics. *Computer Methods in Applied Mechanics and Engineering*, 195:6463–6478, January 2006. 41, 49, 72

[122] S Rajendran and BR Zhang. A 'FE-meshfree' QUAD4 element based on partition of unity. *Computer Methods in Applied Mechanics and Engineering*, 197(1-4):128–147, 1 December 2007. 36

[123] PP Rao. High order unstructured grid methods for computational aeroacoustics. *Ph.D. thesis, Pennsylvania State University*, 2004. 151

[124] PP Rao and PJ Morris. Use of finite element methods in frequency domain aeroacoustics. *AIAA Journal*, 44(7):1643–1652, 2006. 142, 151

[125] S Redonnet, C Mincu, and E Manoha. Computational aeroacoustics of realistic co-axial engines. *14th AIAA/CEAS Aeroacoustics Conference 2008, Vancouver, British Columbia, Canada*, AIAA 2008-2826, 5-7 May 2008. 142

[126] WH Reed and TR Hill. Triangular mesh methods for the Neutron Transport Equation. *Los Alamos Scientific Laboratory*, Tech report LA-UR-73-479, 1973. 32

[127] Y Reyman, W De Roeck, G Rubio, M Baelmans, and W Desmet. A 3D discontinuous Galerkin method for acoustic propagation in duct flows. *Euromech Colloquium 467: Turbulent Flow and Noise Generation, Marseille, France*, July 18-20, 2005. 141

[128] SW Rienstra. Acoustic radiation from a semi-infinite annular duct in a uniform subsonic mean flow. *Journal of Sound and Vibration*, 94(2):267–288, 1984. 145

[129] SW Rienstra and A Hirschberg. An introduction to acoustics. Updated version of Report IWDE 01-03 May 2001, Eindhoven University of Technology, Department of Mathematics and Computer Science, 2009. 9, 12, 22

[130] ME Rose. Weak element approximations to elliptic differential equations. *Numerische Mathematik, Springer - Verlag*, 24:185–204, 1975. 30

[131] SHM Roth. Bernstein-bezier representations for facial surgery simulation. *Ph.D. Thesis*, 2002. 41

[132] ID Roy, W Eversman, and HD Meyer. Improved finite element modelling of the turbofan engine inlet radiation problem. *NASA Report*, NASA-CR-204341, 1993. 142

[133] E Schneider, P Paoli, E Brun, European Agency for Safety, and Health at Work. *Noise in Figures*. European Agency for Safety and Health at Work. Office for Official Publications of the European Communities, 2005. 1

[134] LR Scott, A Ilin, RW Metcalfe, and B Bagheri. Fast algorithms for solving high-order finite element equations for incompressible flow. *Proceedings of the Third International Conference on Spectral and High Order Methods, University of Houston*, 1995. 79

[135] R Sevilla, S Fernández-Méndez, and A Huerta. NURBS-enhanced finite element method (NEFEM). *International Journal for Numerical Methods in Engineering*, 76:56–83, 2008. 177

[136] PA Sheikh and C Uhl. Airplane noise: a pervasive disturbance in Pennsylvania Parks, USA. *Journal of Sound and Vibration*, 274:411–420, 2004. 1

[137] SJ Sherwin, RM Kirby, J Peiro, RL Taylor, and OC Zienkiewicz. On 2D elliptic discontinuous Galerkin methods. *International Journal for Numerical Methods in Engineering*, 65:752–784, 2006. 30

[138] D Shi and H Liang. Convergence and superconvergence analysis of a new quadratic Hermite-type triangular element on anisotropic meshes. *Applied Mathematics and Computation*, 212:257–269, 2009. 45

[139] D Stanescu, D Ait-Ali-Yahia, WG Habashi, and MP Robichaud. Spectral element method for linear fan tone noise radiation. *AIAA Journal*, 42(4):696–705, 2004. 33

[140] T Strouboulis, I Babuska, and K Copps. The design and analysis of the generalized finite element method. *Computer Methods in Applied Mechanics and Engineering*, 81:43–69, 2000. 32

[141] M Tabata and Y Ueda. A set of variant Hermite tetrahedral elements for three-dimensional problems. *Journal of Math for Industry*, 1:131–138, 2009. 45

[142] CKW Tam. Computational aeroacoustics: issues and methods. *AIAA Journal*, 33:1788–1796, 1995. 18

[143] K W Tam and Z Dong. Radiation and outflow boundary conditions for direct computation of acoustic and flow disturbances in a nonuniform mean flow. *Journal of Computational Acoustics*, 04(02):175–201, 1996. 16

[144] RL Taylor, OC Zienkiewicz, and E Onãte. A hierarchical finite element method based on partition of unity. *Computer Methods in Applied Mechanics and Engineering*, pages 73–84, 1998. 35, 39

[145] BJ Tester, G Gabard, and Y Özyörük. Influence of mean flow gradients on fan exhaust noise predictions. *14th AIAA/CEAS Aeroacoustics Conference, Vancouver, Canada*, AIAA 2008-2825, 2008. 142

[146] KW Thompson. Time dependent boundary conditions for hyperbolic systems. *Journal of Computational Physics*, 68:1–24, 1987. 16

[147] LL Thompson and PM Pinsky. Complex wavenumber fourier analysis of the p-version finite element method. *Computational Mechanics*, 13:255–275, 1994. 48

[148] R Tian, G Yagawa, and H Terasaka. Linear dependence problems of partition of unity-based generalized FEMs. *Computer Methods in Applied Mechanics and Engineering*, 195:4768–4782, 2006. 40

[149] F Treyssède and M Ben Tahar. Jump conditions for unsteady small perturbations at fluid-solid interfaces in the presence of initial flow prestress. *Wave Motion*, 46(2):155–167, 2009. 144, 145

[150] T Vejchodsky. On efficient solution of linear systems arising in hp-fem. *Numerical Mathematics and Advanced Applications PSroceedings of ENUMATH 2007*, pages 199–205, 2007. 30

[151] PEJ Vos, SJ Sherwin, and RM Kirby. From h to p efficiently: Implementing finite and spectral/hp element methods to achieve optimal performance for low- and high- order discretisations. *Journal of Computational Physics*, 229:5161–5181, 2010. 48, 177

[152] P Šolín and K Segeth. Towards optimal shape functions for hierarchical Hermite elements. *Proceedings of the SANM Conference, Srni, Czech Republic*, 2005. 44, 46, 179

[153] P Šolín and K Segeth. Hierarchic higher-order Hermite elements on hybrid triangular/quadrilateral meshes. *Mathematics and Computers in Simulation*, 76:198–204, October 2007. 44

[154] P Šolín, K Segeth, and I Doležel. Higher-order finite element methods. *Chapman and Hall / CRC*, ISBN 1-58488-438-X, 2004. 49, 51, 64

[155] P Šolín and T Vejchodský. Continuous hp finite elements based on generalized eigenfunctions. *University of Texas, Department of mathematical sciences, Research Report Series*, 2006-08, 2006. 48

[156] P Šolín, T Vejchodský, M Zítka, and F Ávila. Imposing orthogonality to hierarchic higher-order finite elements. *Mathematics and Computers in Simulation*, 76:211–217, 2007. 48

[157] ZQ Xie, R Sevilla, O Hassan, and K Morgan. The generation of arbitrary order curved meshes for 3D finite element analysis. *Computer Mech*, 51:361–374, 2013. 177

[158] D Xue and L Demkowicz. Control of geometry induced error in hp finite element (FE) simulations. *International Journal of Numerical Analysis and Modeling*, 2(3):283–300, 2005. 177

[159] Y Zhao and PJ Morris. The prediction of fan exhaust noise propagation. *11th AIAA/CEAS Aeroacoustics Conference, Monterey, USA*, AIAA 2005-2815, May 2005. 142

[160] OC Zienkiewicz and YK Cheung. The finite element method in continuum and structural mechanics. *McGraw-Hill, New York*, 1967. 30

[161] OC Zienkiewicz, RL Taylor, and P Nithiarasu. The finite element method for fluid dynamics. *Butterworth-Heinemann*, 6th edition.(ISBN 0 7506 6322 7), 2006. 151, 162

[162] OC Zienkiewicz and JZ Zhu. The superconvergent patch recovery (SPR) and adaptive finite element refinement. *Computer Methods in Applied Mechanics and Engineering*, 101:207–224, 1992. 85

[163] GW Zumbusch. Symmetric hierarchical polynomials for the h-p version of finite elements. *Technical Report SC-93-32, Konrad-Zuse-Zentrum, Berlin, Germany*, 1993. 41, 64